Changes in the proglacial landscape of the Antarctic Peninsula and sub-Antarctic islands during the 21st century

Christopher David Stringer

Submitted in accordance with the requirements for the degree of Doctor of Philosophy

The University of Leeds

School of Geography

March 2024

Publication Statement

I confirm that the work submitted is my own, except where work which has formed part of jointly authored publications has been included. My contribution and the other authors to this work has been explicitly indicated below. I confirm that appropriate credit has been given within the thesis where reference has been made to the work of others.

The work in Chapter 2 and Chapter 3 of the thesis has been submitted as a single paper for publication:
Stringer, C.D., Carrivick, J.L., Quincey, D.J., Nývlt, D., Comber, A. (*in review*) Contemporary (2016–2020) land cover and 21st-century change across the major proglacial regions of West Antarctica and the McMurdo Dry Valleys. *Arctic, Antarctic, and Alpine Research.*
CS produced the data, conducted the analysis and wrote the manuscript, supported by JC, DQ, and DN. All authors contributed to the writing.

The work in Chapter 4 of this thesis has been published:

Stringer, C.D., Boyle, J.F., Hrbáček, F., Láska, K., Nedělčev, O., Kavan, J., Kňažková, M., Carrivick, J.L., Quincey, D.J., Nývlt, D. (2024) Quantifying sediment sources, pathways, and controls on fluvial transport dynamics on James Ross Island, Antarctica. *Journal of Hydrology*.

CS produced most of the data, conducted the analysis and wrote the manuscript. JFB supported CS with the interpretation of geochemistry data. FH supplied active layer measurements. KL supplied meteorological measurements. ON supported CS in collecting river samples. MK provided images of the region collected from UAV. All authors contributed to the writing.

The work in Chapter 5 has been submitted for publication:

Stringer C.D., Macfee, M.W., Carrivick, J.L., Engel, Z., Matějka, M., Harpur, C., Nývlt, D., Quincey, D.J., Davies, B. (*in review*) Accelerated glacier changes on the James Ross Archipelago, Antarctica, from 2010 to 2023. *Journal of Glaciology*.

CS designed and led the study, produced the albedo results and prepared the manuscript. MWM produced the SLA results. JC produced area results, provided ongoing advice to CS, and with DN edited the first full draft of the manuscript. ZE produced the ablation results. KL and MM produced the meteorological results. CH provided velocity data. DN, DQ and BD edited the manuscript before submission. All authors contributed to writing the final version of the manuscript.

Acknowledgements

I would like to thank my supervisory team of Jonathan Carrivick, Duncan Quincey and Daniel Nývlt for their excellent support. Their backing has allowed me to undertake research of which I am deeply proud. They have also supported me in my personal dream of working in Antarctica; an experience I will never forget.

It has been a privilege to work alongside colleagues in the School of Geography, particularly in the River Basin Processes and Management cluster. I am especially grateful to those colleagues that made an effort to ensure I felt welcomed when I started this PhD online during the height of the COVID-19 pandemic.

It was an honour to join the Český antarktický výzkumný program (Czech Antarctic Research Programme) on an expedition to the J.G. Mendel Station on James Ross Island. It was a pleasure to spend Christmas 2021, as well as 2 ½ productive months in Antarctica with Zbyněk Engel, Filip Haiduk, Jana Smolíková, Filip Hrbáček, Lucia Pastíriková-Kaplan, Kamil Láska, Lucia Ráčková, Peter Škamrala, Vendula Koublová, Michael Matějka, Ondřej Nedělčev, Michaela Kňažková, Peter Váczi, František Vorel, and Jaroslav Gerža. Thank you also to Pavel Kapler for his logistical support.

I am grateful to the co-authors of several papers that are either accepted or in review - they have been great to work with and have aided my personal development: Alexis Comber, John Boyle, Filip Hrbáček, Kamil Láska, Zbyněk Engel, Michael Matějka, Ondřej Nedělčev, Michaela Kňažková, Mia Macfee, Connie Harpur, and Bethan Davies. I would also like to thank those organisations that have financially supported me: Leeds-York-Hull NERC Doctoral Training Partnership (DTP) Panorama (NE/S007458/1), the Czech Antarctic Research Programme, and the Czech Antarctic Foundation.

Through this PhD, with the support of NERC Panorama DTP and the Český antarktický nadační fond (Czech Antarctic Foundation), I was also honoured to join the Czech Antarctic Research Programme, alongside colleagues from Ulusal Antarktika Bilim Seferi (Seventh Turkish Antarctic Expedition, TAE-VII) on a placement as part of their expedition to the Cz*Eco Nelson field camp in the South Shetland Islands. I learnt a lot from my colleagues as I supported their technical and scientific work: Václav Pavel, Jenik Havránek, Ondřej Stanický, Ondřej Zvěřina, Alp Unal, Göksu Uslular, David Jindra, and Anton Puhovkin.

Lastly, I would like to thank my family. My wonderful fiancé, Eszter Kovacs, has been by my side through this process and I am immensely grateful to her for supporting me through the

tough times, as well as my siblings: Matthew Turner-Allen and Louise Stringer. From an early age, my mum, Maggie Stringer, has fostered a love of science and encouraged me to explore my curiosities in the world. For that, I am eternally grateful. Finally, I would like to thank my dad – David Stringer. Although he passed away before I started this PhD, the trips I took with him following Oldham Athletic around the country first sparked my interest in geography and geomorphology.

Abstract

Proglacial systems are among the most dynamic landscapes on Earth and are important habitats and sources of nutrients. They are predominantly shaped by the interplay of meltwater from glaciers and sediment supplied by slope failures. This thesis describes the composition and ever-evolving dynamics of the Antarctic Peninsula and sub-Antarctic islands' proglacial environment, making use of remote sensing and field techniques. First, a land cover map of major proglacial sites is presented with ten land cover classes describing the extent of water, sediment, bedrock, and vegetation at 30 m spatial resolution (77 % accuracy). Vegetation and coarse/wet sediment are observed to be more abundant in northerly sites. Building on this, change-vector analysis is used to investigate how Antarctic proglacial regions have evolved in the 21st Century (80 % accuracy). Ice loss is shown to be a key driver of land cover change, with extensive change occurring on South Georgia and Alexander Island, where melt was widespread. An analysis of river water discharge and sediment transport from two neighbouring catchments on Ulu Peninsula, James Ross Island, is also presented. Stream monitoring and provenance techniques highlight that catchments on James Ross Island are sensitive to changes in air temperature (specifically in melting ice and snow) for their water delivery, whilst the supply of sediment is largely controlled by underlying lithology. Finally, the role of recent warming (0.24 ± 0.08 ^{o}C yr^{-1}) on deglaciation on the James Ross Archipelago between 2010 and 2023 is described. Over this period, the rate of glacier area reduction increased six-fold, and glacier ablation prevailed (up to -1.5 m yr^{-1}). Together, these findings highlight that glaciers and proglacial systems are rapidly changing in the Antarctic Peninsula and sub-Antarctic, and further research is required to understand how the interaction between these systems will affect the future evolution of its glaciers, landscape, and habitats.

Table of contents

List of figures

List of tables

Abbreviations

AC	Algal Catchment
AL	Algal Lower
ALOS	Advanced Land Observing Satellite
APR	Antarctic Peninsula Region
ASPA	Antarctic Specially Protected Areas
AU	Algal Upper
BAS	British Antarctic Survey
BC	Bohemian Catchment
BL	Bohemian Lower
BTC	Bedrock To Coarse/wet sediment (land cover change class)
BU	Bohemian Upper
CTB	Coarse/wet sediment To Bedrock (land cover change class)
CTF	Coarse/wet sediment To Fine & dry sediment (land cover change class)
CTT	Coarse/wet sediment To Turbid water (land cover change class)
CTV	Coarse/wet sediment To Vegetation (land cover change class)
CTWI	Coarse/wet sediment To Wet Ice (land cover change class)
CVA	Change Vector Analysis
ClTCl	Class To Class (change)
DA	vector Direction Angle
DEM	Digital Elevation Model
DS	Dirty Stream
DSM	Digital Surface Model
ED	Euclidean Distance
ELA	Equilibrium Line Altitude

ETM+	Enhanced Thematic Mapper Plus
FTB	Fine & dry sediment To Bedrock (land cover change class)
FTC	Fine & dry sediment To Coarse/wet sediment (land cover change class)
GCOS	Global Climate Observing System
GLAMOS	GLAcier MOnitring in Switzerland
GLIMS	Global Land Ice Measurements from Space
GEE	Google Earth Engine
IAA	Instituto Antarctico Argentino (Argentine Antarctic Institute)
IRS	InfraRed Spectrometry
ITF	Ice To Fine & dry sediment (land cover change class)
ITT	Ice To Turbid water (land cover change class)
JGM	Johann Gregor Mendel Station (CZ)
MAAT	Mean Annual Air Temperature
MAP	Mean Annual Precipitation
MSI	MultiSpectral Instrument
NDSI	Normalised Difference Snow Index
NDVI	Normalised Difference Vegetation Index
NDWI	Normalised Difference Water Index
NIR	Near InfraRed
OLI	Optical Land Imager
PCA	Principal Component Analysis
PCC	Post Classification Change
PDD	Positive Degree Days
REMA	Reference Elevation Model of Antarctica
RGI	Randolph Glacier Inventory
RMSE	Root Mean Squared Error

SAM	Spectral Angle Mapper
SCAR	Scientific Committee on Antarctic Research
SCR	Snow Cover Ratio
SLA	SnowLine Altitude
SMB	Surface Mass Balance
SRTM	Shuttle Radar Topography Mission
SR	Surface Reflectance
SSC	Suspended Sediment Concentration
SWIR	Short-Wave InfraRed
TOA	Top-Of-Atmosphere
USGS	United States Geological Survey
UTC	Coordinated Universal Time
WITC	Wet Ice To Coarse/wet sediment (land cover change class)
WMO	World Meteorological Organisation
XRF	X-Ray Fluorescence

1. Introduction

Until the start of the 21st century, the Antarctic Peninsula was one of the most rapidly warming places on Earth with temperature rises of 1.5 ^{o}C observed since the 1950s (Vaughan et al., 2003; Bentley et al., 2009; Mulvaney et al., 2012). Following a hiatus in warming at the start of the 21st Century, there is now evidence that temperatures are once again warming (Carrasco et al., 2021). Consequently, glacier mass loss is occurring at an enhanced rate in the region, with small glaciers particularly vulnerable (Engel et al., 2018; Rosa et al., 2020; Engel et al., 2024). This loss of glacier mass is leading to an increase in proglacial area and changes how water and sediment is delivered to the Southern Ocean, much like in other parts of the world (Carrivick et al., 2018; Carrivick and Tweed, 2021).

Small glaciers and ice caps (hereafter referred to as glaciers) cover 132 900 km^2 around the periphery of Antarctica and represent 18 % of global glacier area, excluding the major ice sheets (Pfeffer et al., 2014). Increased meltwater from glaciers has contributed to the enlargement of fluvial systems, whilst the degradation of permafrost has also increased meltwater availability, and led to greater hillslope activity (Decaulne et al., 2005; Kavan et al., 2017; Kňažková et al., 2021). Both of these processes act to increase sediment discharge from catchments.

Understanding the make-up of Antarctica's proglacial regions (**Figure 1**), and how they are changing and operating, is vital because they are an important source of water, sediment and solutes. The quantity and spatio-temporal pattern of sediment discharged from Antarctica has profound effects on the ecosystem of the Southern Ocean and polar lakes, with particular impacts seen in benthic communities (Friedlander et al., 2020). The majority of sediment enters these ecosystems via rivers (Overeem et al., 2017) and suspended sediments impact the feeding behaviour of marine and lacustrine organisms (Cloern, 1987). Additionally, proglacial environments are important refuges for several species of flora and fauna, including seals, penguins, and rare species of moss, lichen, and vascular plants (Lee et al., 2017; Colesie et al., 2023, **Figure 1.1 C, D**). This thesis will explore the themes of water and sediment in the Antarctic Peninsula Region and sub-Antarctic; in particular, it will consider the distribution and transportation of sediments.

Whilst the mechanisms that affect water and sediment discharge from rivers are well understood, and despite the importance of proglacial regions as sediment sources in sub-polar environments (Syvitski, 2002; Overeem et al., 2017; Carrivick and Tweed, 2021), studies from the Southern Hemisphere are sparse. Furthermore, there is limited land cover data for Antarctica, with disparate geological and geomorphological maps having been produced over a

period of several decades lacking a common classification system (e.g. Heywood et al., 1977; British Antarctic Survey, 1981; Jennings et al., 2021). Additionally, “global” land cover products typically do not include Antarctica (cf. Chen et al., 2015; Brown et al., 2022). Similarly, there has been a dearth of research investigating rivers in Antarctica. Of the studies that do consider rivers in Antarctica (e.g. Gooseff et al., 2007; Chinn and Mason, 2016; Kavan et al., 2017; Kavan et al., 2021; Kavan et al., 2023), none explored the spatio-temporal variability in sediment deliver and they typically do not take a holistic approach to the factors controlling sediment discharge.

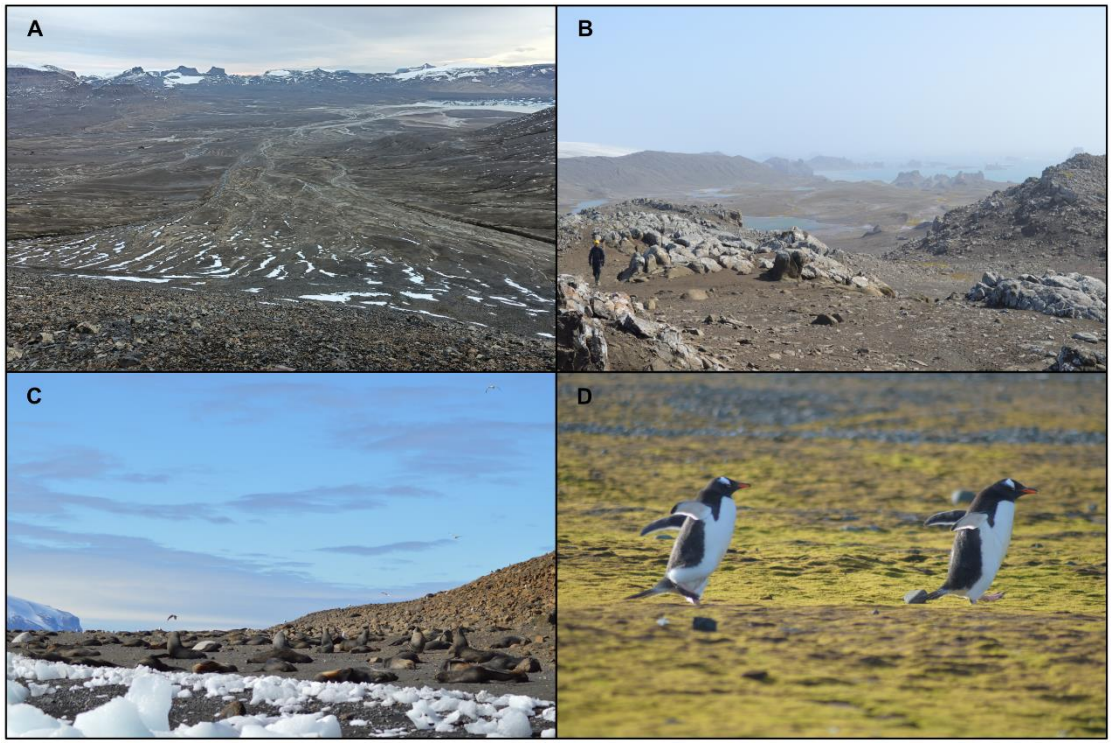

Figure 1.1: A) *A typical proglacial environment for James Ross Island’s semi-arid Ulu Peninsula. Photo taken at Crame Col, looking east over Abernethy Flats;* ***B)*** *The humid, maritime environment of the South Shetland Islands. Photo taken on Stansbury Peninsula (Nelson Island), 1 km south of Cz*Eco Nelson, looking south west;* ***C)*** *An example of some of James Ross Island’s wildlife, including Fur Seals and Kelp Gulls. Photo taken at Cape Lachman, looking north east;* ***D)*** *An example of flora and fauna in the South Shetland Islands, including Gentoo Penguins and extensive moss mats, taken on a beach to the north east of Edgell Bay, Nelson Island, looking west .*

Antarctica is a dynamic continent, which is undergoing profound changes as a consequence of warming temperatures (Davies et al., 2013; Carrasco et al., 2021). Therefore, to understand what the future may bring, this thesis also seeks to quantify how land cover and glacier masses have changed in the recent past, and the environmental factors that drive these. There are very few, if any, studies that quantify proglacial land cover change in Antarctica, and, despite their large areal coverage, few glaciological observations for land-terminating glaciers in Antarctica compared to other world regions.

This thesis aims to investigate the dynamics and evolution of proglacial systems across the Antarctic Peninsula and sub-Antarctic islands during the 21st Century.

1.1. An overview of proglacial environments

Since the end of the Little Ice Age, glaciers around the world have been receding (Matthews and Briffa, 2005), and this recession has accelerated in recent years as temperatures have increased (Hugonnet et al., 2021). Whilst evidence for the occurrence of a Little Ice Age glacier advancement is limited to just a handful of sites in Antarctica (e.g. Simms et al., 2021), there has certainly been an acceleration of glacier recession in recent decades (Rosa et al., 2020; Engel et al., 2024). Consequently, proglacial regions have increased in size. Proglacial systems are amongst the most dynamic landscapes on Earth and are predominantly shaped by the interplay of meltwater from glaciers, which erodes, transports and deposits sediment, and hillslope activity, which largely acts to supply new sediment into the system during mass transport events (Carrivick and Heckmann, 2017). Permafrost-affected soils can also be extensive in proglacial environments, and these are an additional and important water and sediment source on days when ground temperatures exceed 0 °C (Humlum et al., 2003; Łepkowska and Stachnik, 2018). In a warming climate, the increased activity of water and increased mass movements result in greater stream discharge and, therefore, increases sediment transport (Huss and Hock, 2018; Carrivick and Tweed, 2021).

Proglacial regions are natural laboratories for biologists and ecologists, as they provide an insight into ecological succession and how “pristine” environments can become colonised by vegetation and other organisms (e.g. Klaar et al., 2015). In many parts of the world, proglacial regions and the associated unstable slopes of proglacial landforms (e.g. moraines, steep valley walls) can be potential natural hazards (Motschmann et al., 2020). Whilst this has not specifically been raised as a concern in Antarctica (at an official level), many research stations are built on permafrost-affected ground or close to slopes that may be vulnerable to failure in the coming decades.

1.1.1. Water and sediment transport

In drainage basins that are not directly affected by human activity, there are two primary factors affecting stream discharge (Syvitski, 2002): **i)** the size of the basin, and; **ii)** the air temperature of the basin. To account for the effect of basin size, it is typical to normalise sediment loads (cf. Carrivick and Tweed, 2021). Air temperature is correlative with glacier and snow melt (**Figure 1.2**), as well as an increase in active layer thickness, and is therefore the primary driver of variability in water supply (Oliva, Hrbacek, et al., 2017; Hrbáček et al., 2020; Siegert et al., 2023; Engel et al., 2023). In those catchments dominated by glaciers, radiation is

also an important factor (Huss et al., 2009), however, it is negligible in those catchments that are dominated by permafrost-affected soils (Kavan et al., 2017; Hrbáček and Uxa, 2020). Additional water may be sourced from proglacial lakes (Carrivick et al., 2022).

Carrivick and Heckmann (2017) proposed three main sources of sediment in proglacial systems:

1) Sediment derived from glacial erosion and subglacial sediment storage.
2) Debris from slope failures of steep, deglaciated bedrock
3) Glacigenic debris in proglacial forelands, including fluvial terraces, moraines, and debris cones. This may also include aeolian sediment.

The first of these mechanisms is controlled by the erosional power of a glacier, which is itself primarily controlled by the glacier's thermal regime (and, therefore, velocity) and the erodibility of the subglacial bedrock (Chakrapani and Subramanian, 1990; Moosdorf et al., 2018; Lai and Anders, 2021). Slope failures in steep valleys (**Figure 1.2**) are controlled one of two mechanisms: **i)** retreat of a glacier causing debuttressing of slopes, increased vertical shear stress, and the amplification of tectonic activity (Ballantyne et al., 2014), or: **ii)** permafrost degradation (Ballantyne et al., 2014; Kňažková et al., 2021). These mechanisms supply coarse (cobble to boulder size) sediment to valley floors in the form of scree. Scree is typically quite resistant to erosion, and it often supplies coarser, less mobile sediments to streams (Mosley, 1980; Attal et al., 2015).

In proglacial forelands, the flow of meltwater can entrain sediments. The force of water (shear stress) acting upon a sediment grain controls its entrainment. If the discharge of water at a point generates a shear stress that is sufficient to exceed the forces of gravity and cohesion that hold a grain in place, sediment will be transported (Paola and Voller, 2005). This can be considered as the critical threshold for sediment transport, which may be raised by the presence of vegetation increasing sediment cohesion (Brooks et al., 1995; Klaar et al., 2015). The primary sources of sediment in proglacial environments are glacial depositional landforms (e.g. moraines, drift sheets), scree, and fluvial terraces/floodplains, which are often abundant in poorly consolidated sediments (Schrott et al., 2003; Davies et al., 2013; Carrivick and Heckmann, 2017). Another important source of sediment to proglacial forelands are aeolian sediments. These sediments are typically fine-grained, easily transported by streams, and may have been transported many hundreds of kilometres from their source (Bullard et al., 2016; Kavan et al., 2017; Kavan, Láska, et al., 2020).

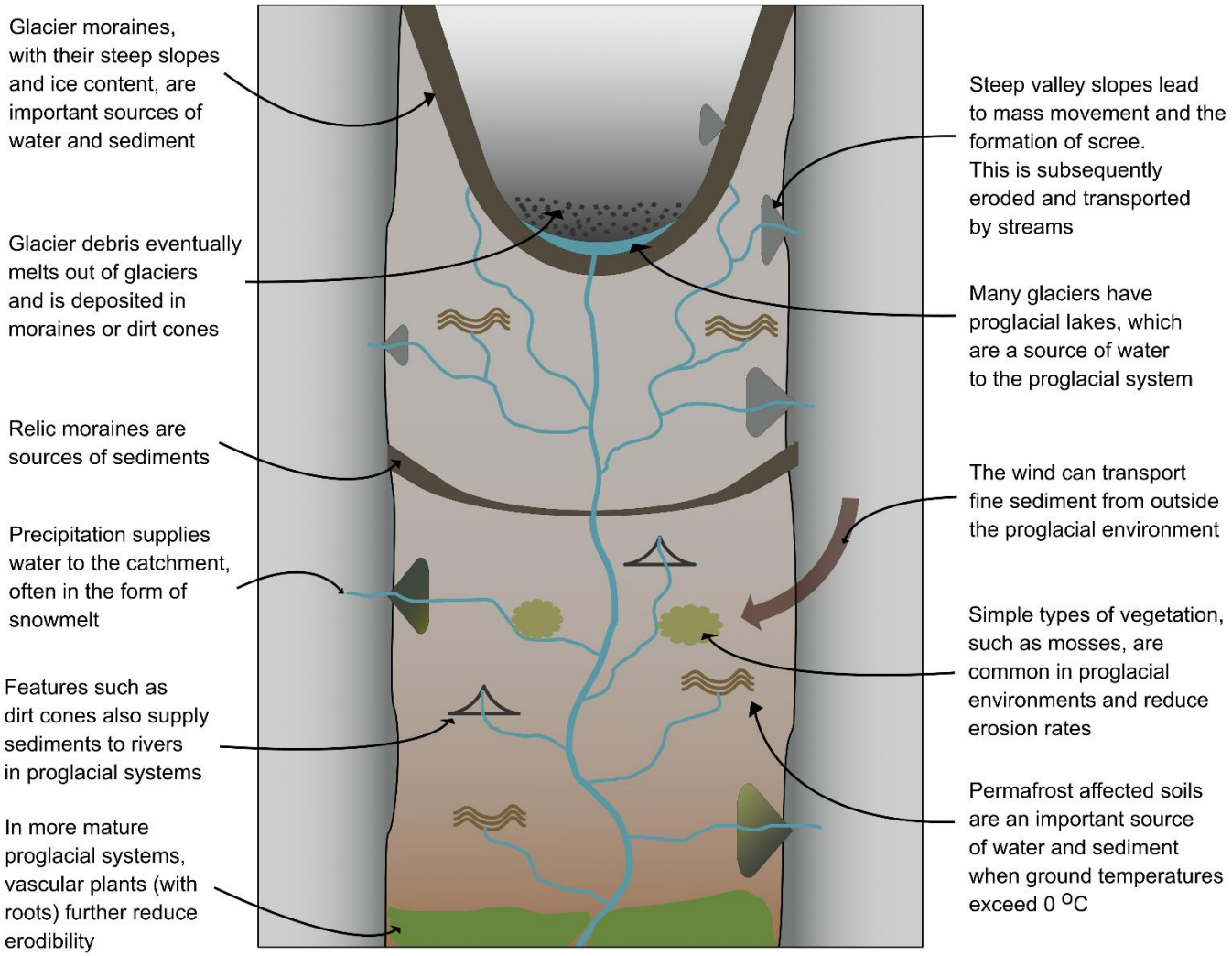

Figure 1.2: *An idealised proglacial system, which describes how water and sediment is delivered to streams.*

In brief, the variability of stream discharge and sediment load in a proglacial drainage system is controlled by the spatial variability in sediment delivery, and the spatio-temporal variability in precipitation, glacier melt, and permafrost-affected soil melt/degradation (**Figure 1.2**). This variability is important to consider because large quantities of sediment increase the turbidity of the water. When this sediment is output into the ocean or lakes, it can negatively affect biota, by preventing photosynthesis or causing mechanical damage if organisms ingest the sediment (Cloern, 1987; Maat et al., 2019; García-Rodríguez et al., 2021). Sediment is a nutrient source for many organisms, and the quantity of sediment entering polar waters in the summer months is thought to play a role in the size of phytoplankton blooms (Arrigo et al., 2017; Righetti et al., 2019; Leeuwe et al., 2020). In turn, this can alter the quantity of carbon that is sequestered from the atmosphere by these organisms (Brussaard et al., 2008; Maat et al., 2019).

1.2. Proglacial regions in the Antarctic Peninsula Region

The majority (99.8 %) of Antarctica is covered by ice, with the remaining 0.2 % characterised as nunataks (i.e. mountain peaks that penetrate the ice sheet) or as proglacial regions (Burton-Johnson et al., 2016). The largest, and perhaps most famous, of Antarctica's proglacial regions is the McMurdo Dry Valleys (78 ^{o}S, **Figure 1.3**). Other important proglacial sites are present along the Antarctic Peninsula, such as Alexander Island and West Palmer Land (hereafter referred to simply as "Alexander Island" 71 ^{o}S), and James Ross Island (64 ^{o}S) (**Figure 1.3**). Respectively, they host major proglacial sites such as Fossil Bluff and the Ulu Peninsula (**Figure 1.1A**). Additionally, the milder climates of the sub-Antarctic islands have also created a suitable environment for proglacial regions to exist, with major proglacial areas in the South Shetland Islands (62 ^{o}S, **Figure 1.1B**) and, further north, on South Georgia (54 ^{o}S) (**Figure 1.3**). This thesis primarily focuses on the Antarctic Peninsula Region and sub-Antarctic Islands but also includes a land classification (and analysis of change) of the McMurdo Dry Valleys, since it is the largest proglacial region in Antarctica (**Figure 1.3**).

The sites selected for study in this thesis were informed by the British Antarctic Survey's (BAS) rock outcrop datasets (Burton-Johnson et al., 2016; Gerrish et al., 2020). Nunataks in the interior of the ice sheets were excluded because they are disconnected from the coastline and can be assumed to be largely unimportant as sediment sources to the Southern Ocean. Fossil Bluff and other coastal regions in Alexander Island and Palmer Land were included and are interesting for their proximity to George VI Sound. These regions may become important sediment sources in the near future, as exceptional melting in this region appears to have increased the likelihood of the George VI ice shelf collapsing (Banwell et al., 2021). Site selection was further narrowed to only consider those regions with cloud-free Landsat-8

Operational Land Imager (OLI) images. These sites are: **i)** the McMurdo Dry Valleys; **ii)** Alexander Island and west Palmer Land (referred to hereafter as "Alexander Island"); **iii)** Deception Island; **iv)** southern Livingston Island and Snow Island (referred to hereafter as Byers Peninsula); **v)** James Ross Archipelago, and; **vi)** South Georgia. The sites chosen follow a latitudinal gradient (**Figure 1.3**), which acts as a space-for-time substitute, i.e. changes observed in more northern sites will theoretically propagate south with warming temperatures, and covers a range of lithologies and climatic environments (**Table 1.1**). An overview of site characteristics are available in **Table 1.1**, with a more detailed description in sections 1.2.1 to 1.2.6.

Table 1.1: *The sites studied in this thesis, including key climate, surface, and wildlife information. The information in this table is based on the descriptions in sections 1.2.1 to 1.2.6 and references therein.*

Site	*Location*	*MAAT (°C)*	*MAP (mm)*	*Dominant lithology/surface cover*	*Wildlife*
South Georgia	54° S, 37°W	2	>1500	Metasedimentary and volcanoclastic sediments	High biodiversity: seal, penguins and other sea birds, extensive vegetation coverage (including vascular plants), some invasive
Byers Peninsula	62° S, 61°W	-3	>500	Marine and volcanoclastic mud and sandstones, with intrusions of basalt and andesite	Moderate: Penguins and other sea birds, seals, large area of mosses and lichens, but few vascular plants
Deception Island	62° S, 61°W	-3	>500	Volcanically active. Basaltic/andesitic lava flows, volcanoclastic sediments	Fairly sparse: Penguins and other sea birds, seals, some mosses, lichens
James Ross Island	54° S, 58°W	-7	400 to 700	Cretaceous sediments, hyaloclastite breccia, basalt	Fairly sparse: Penguins and other sea birds, seals, mosses, lichens
Alexander Island	71° S, 68°W	-9	~200	Jurassic/Cretaceous marine sediments and metasediments with plutonic intrusions	Sparse: mosses, lichens, some fish in coastal lakes
McMurdo Dry Valleys	78° S, 18°W	-20	<100	Gravelly sediments, with large exposures of volcanic bedrock	Sparse: very small patches of moss and lichens

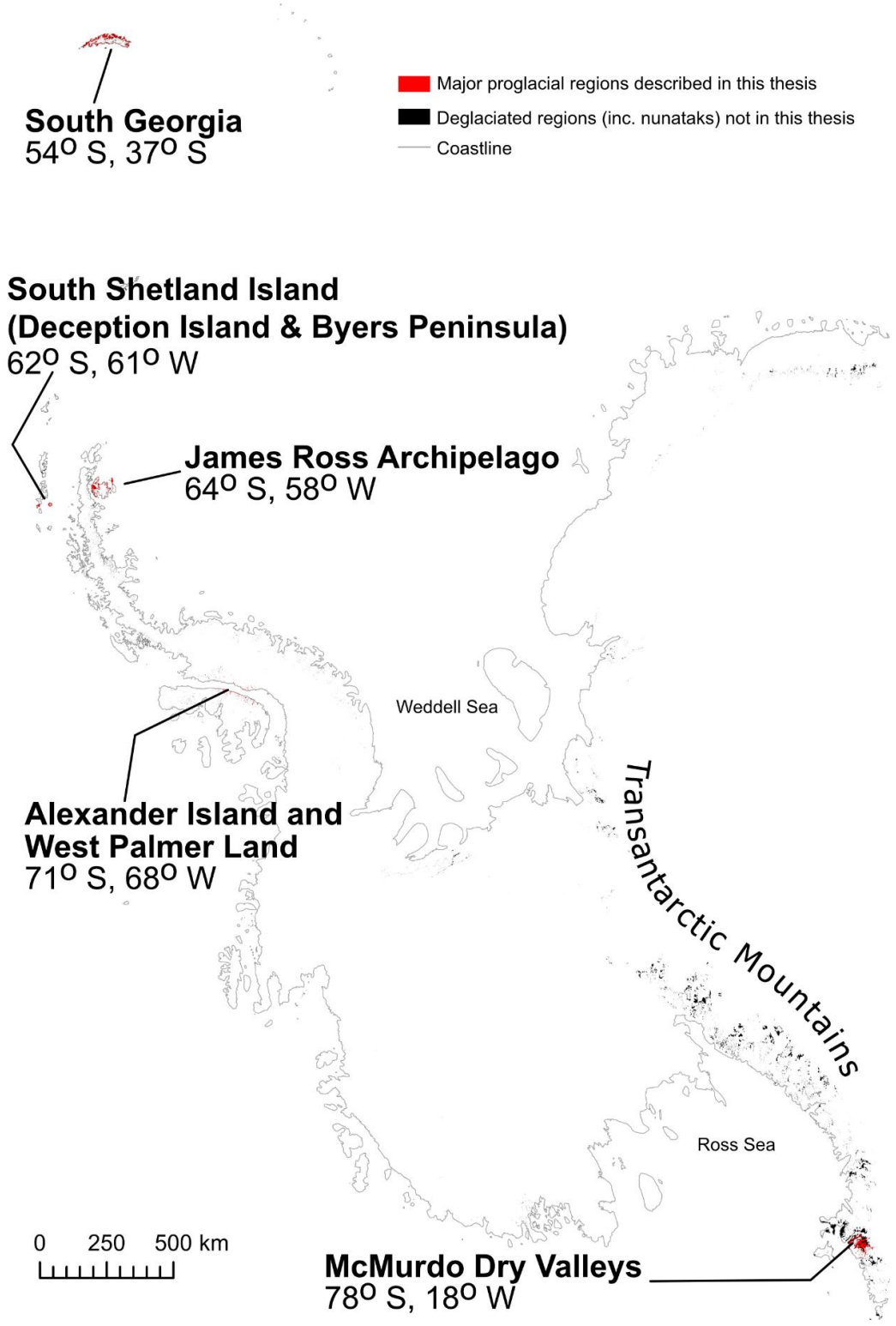

Figure 1.3: *Location of study sites. The areas analysed in this thesis have been highlighted in red and span a latitudinal gradient from 54°S to 78°S . Proglacial regions not analysed in this thesis have been highlighted in black (Burton-Johnson et al., 2016) and are primarily mountains (e.g. Transantarctic Mountains) or are frequently covered by extensive cloud-cover (e.g. King George Island).*

1.2.1. McMurdo Dry Valleys

The McMurdo Dry Valleys, often referred to simply as "The Dry Valleys", are composed of ~ 3000 km^2 proglacial terrain between McMurdo Sound and the Transantarctic Mountains (Levy, 2013, **Figure 1.3**). The Dry Valleys have received extensive research over the years owing to their size and proximity to the United States' McMurdo Station. Its high-relief terrain is primarily covered by sandy, gravelly soil, with ice-covered lakes and large exposures of bedrock of volcanic origin (e.g. basement sills), as well as glacial and periglacial landforms, such as moraines, solifluction lobes and thermokarst features (Fountain et al., 2014; Petford and Mirhadizadeh, 2017, **Figure 1.4**). It is the coldest proglacial site discussed in this thesis, with a polar-continental climate and a mean annual air temperature (MAAT) of -20 ^{o}C, according to data from 15 stations with elevations ranging from 20 to 1870 m a.s.l. (Obryk et al., 2020) . Its climate is "hyper-arid", with low humidity a product of the orographic blocking effect of the Transantarctic Mountains (**Figure 1.3**), combined with drying katabatic and Foehn winds (Nylen et al., 2004; Speirs et al., 2010). With these cold temperatures and low humidity, The Dry Valleys are categorised as a polar desert and receive a mean annual precipitation (MAP) of less than 100 mm.

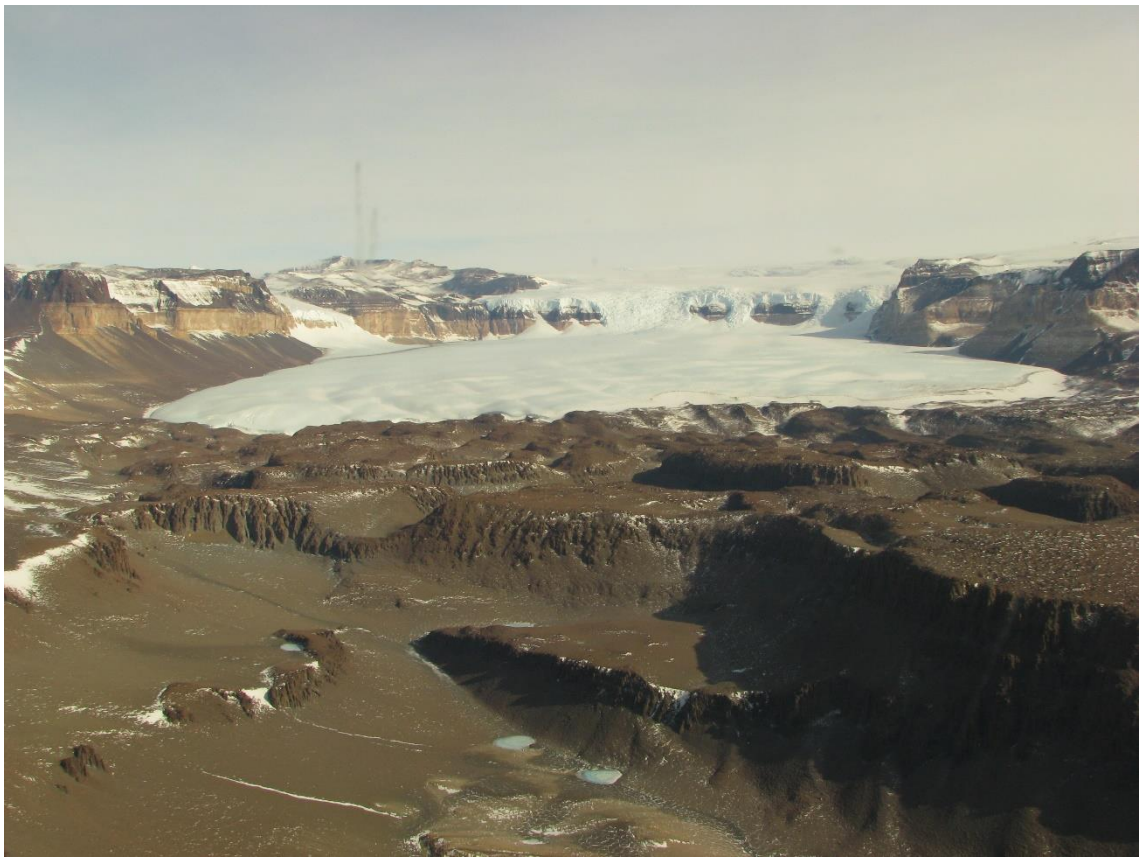

Figure 1.4: *The Wright Valley of the McMurdo Dry Valleys (looking west towards Wright Upper Glacier) in 2013. Note the high relief, hummocky ground, and lack of vegetation. Photograph sourced from* ***Wikimedia Commons*** *(CC BY-SA 4.0), taken by "Turkish D.".*

The Dry Valley's very low air temperature and hyper aridity, and very high wind speeds create a hostile environment for life to exist (Nylen et al., 2004; Speirs et al., 2010). Consequently, there are few biological communities and those that do exist are limited to microbial life (i.e. bacteria and algae) and non-vascular plants (e.g. mosses), that primarily inhabit wetted areas produced by the radiative melting of snow patches and the alpine glaciers which flow into the valley (Pannewitz et al., 2003; Cary et al., 2010; Obryk et al., 2020). These wetted areas include streams such as the Onyx River, which is the longest river in Antarctica (cf. Gooseff et al., 2011; Chinn and Mason, 2016).

1.2.2. Alexander Island

Alexander Island is situated across the Antarctic Peninsula from Palmer Land (**Figure 1.3**) and has a polar continental climate, with a MAAT recorded at Fossil Bluff of approximately -9 °C (780 m a.s.l) and receives approximately 200 mm MAP (Harangozo et al., 1997; Morris and Vaughan, 2003; Davies et al., 2017). The proglacial areas of this region are limited to the small rocky outcrops on Alexander Island and Palmer Land are primarily composed of Upper Jurassic/Lower Cretaceous marine sediment, plutonic intrusions and gneisses (British Antarctic Survey, 1981). The high relief of the region has resulted in several scree slopes being formed, primarily of fine material (**Figure 1.5**), whilst the cold temperatures mean that only a few, small streams can form (Heywood et al., 1977).

Figure 1.5: *The central station of Fossil Bluff on Alexander Island in 2003. Note the relatively fine sediments of the scree slopes (appearing smaller than cobble-sized), and exposed strata further up the hill, as well as the lack of surface water or vegetation. Photo sourced from* ***Wikimedia Commons*** *(Public Domain) and taken in 2003 by "Apacheeng lead".*

There are very few studies of the landscape around Alexander Island, with the most recent geological map having been produced in 1981 (British Antarctic Survey, 1981), and has since been reinterpreted and incorporated into the Scientific Committee on Antarctic Research's (SCAR) GeoMAP (Cox et al., 2023). Similarly, there are very few descriptions of the landscape or land cover are available, with limited descriptive accounts (e.g. Heywood et al., 1977) and only very limited geomorphology maps of the region available (e.g. Salvatore, 2001). Much like The Dry Valleys, Alexander Island is a harsh place for life to exist and biological communities are largely confined to microbial communities and small patches of moss, though some fish species have been observed in coastal lakes (Heywood et al., 1977).

1.2.3. James Ross Archipelago

The James Ross Archipelago is situated 10 km eastward of the north east coast of the Antarctic Peninsula (**Figure 1.3; Figure 1.6**). The largest islands of the archipelago are James Ross Island, Vega Island, Snow Hill Island, and Seymour Island. The bedrock across the archipelago is primarily composed of Cretaceous to Paleogene mudstones and sandstones, with upland regions of Neogene basalts, hyaloclastite breccias and tuffs (Smellie, 2013; Mlčoch et al., 2020). The region has a semi-arid polar continental climate, with a MAAT of -7 °C recorded at the Johann Gregor Mendel Station (JGM, 10 m a.s.l) (Kaplan Pastíriková et al., 2023). MAP is estimated at between 400 and 700 mm (Palerme et al., 2017), although high wind speeds mean the effective precipitation is lower than this (Nývlt et al., 2016), resulting in it being considered semi-arid. Snow cover observations at JGM indicate considerable inter-annual variability in snowfall but with a snow depth rarely exceeding 0.35 m (Hrbáček et al., 2021) at JGM.

The archipelago has several large proglacial regions, owing to its semi-arid climate (Davies et al., 2013). These include Seymour Island and the Ulu Peninsula (**Figure 1.6**), the latter of which is considered to be the second largest proglacial region in Antarctica, after The Dry Valleys, and the largest in the Antarctic Peninsula Region, covering more than 300 km^2 (Kavan et al., 2017). The Ulu Peninsula is home to the Czech Antarctic Research Programme's research station (JGM), and, combined with efforts from the British Antarctic Survey (BAS) and the Argentine Antarctic Institute (Instituto Antártico Argentino**,** IAA), has thus been subject to extensive research. This work includes several geological and geomorphological surveys, though these studies are either limited to the Ulu Peninsula (e.g. Davies et al., 2012; Mlčoch et al., 2020; Jennings et al., 2021) or lack detail on land cover information beyond the geology (e.g. Smellie, 2013). Although the archipelago has several "rich oases" of vegetation, these are restricted to relatively small areas of moss, microbial mats, algae, and lichen (Barták et al., 2015; Váczi and Barták, 2022).

Figure 1.6: *Abernethy Flats on James Ross Island's Ulu Peninsula, as viewed from Lachman Crags, above Triangular Glacier (looking West). Note the large streams; those in the foreground are glacier-sourced, whilst those in the middle-ground and to the right of the photo are soil/precipitation sourced. Also note the lack of vegetation. The landmass furthest away in the photo is Trinity Peninsula. Photo taken by Christopher Stringer in 2022.*

Located in the Weddell Sea, the archipelago is home to several aquatic mammals and sea birds, including several species of penguins, seals, and seabirds (Pavel and Weidinger, 2013; Nývlt et al., 2016; Schiel et al., 2019), with lakes also acting as important habitats for bacterial mats, algae, and small invertebrates (Nedbalová et al., 2017; Roman et al., 2019). There are also several streams on the Ulu Peninsula, including the Bohemian Stream, Dirty Stream (**Figure 1.1A**) and Algal Stream, which have been the subject of research in recent years (Kavan et al., 2017; Sroková and Nývlt, 2021; Kavan, 2021).

1.2.4. Deception Island

Deception Island is a volcanic island situated with the South Shetland Islands archipelago (**Figure 1.3**), with a proglacial area of ~ 50 km^2 (Smellie et al., 2002). Its climate is polar maritime, with a MAAT of -3^oC (85 m a.s.l.) (Tejedo et al., 2015). Summer temperatures regularly exceed 0^oC in the summer, resulting in a MAP of 510 mm, often falling as rain (Smellie et al., 2002; Bañón et al., 2013). As one of only two active volcanoes in Antarctica, it geology is primarily basaltic lava flows, with volcanoclastic sediments (**Figure 1.7**) and tuffs also present (Smellie et al., 2002).

There are also a number of glacial and periglacial landforms, including solifluction lobes, moraines and permafrost-affected soils. Positive air temperatures in the summer, combined with regular rainfall, means there are several small rivers and drainage networks (**Figure 1.7**) on the island (Smellie et al., 2002).

Figure 1.7: *Telefon Bay (background), as viewed from the rim of a crater on Deception Island. Note the dark, volcanic rocks and the variability of sediment grain sizes, as well the small-scale drainage channels, frozen lake, and lack of vegetation. Photo sourced from* ***Wikimedia Commons*** *(CC BY-SA 4.0), taken in 2020 by Espen Mills.*

Deception Island is a hotspot for wildlife activity, and indeed it was historically a centre of the commercial whaling and seal hunting industries in the early 20th Century (Dibbern, 2010). It is home to a Chinstrap Penguin colony, as well as Fur Seals and Elephant Seals, as well as a number of other seabirds (Kendall et al., 2003; Dibbern, 2010; Naveen et al., 2012). Whilst several species of plants are present on the island (i.e. mosses), there are fewer than other islands owing to its ongoing volcanism (Smith, 1988; Smith, 2005)

1.2.5. Byers Peninsula

Byers Peninsula is approximately 40 km to the north east of Deception Island (**Figure 1.3**) and, thus, shares many of its climatic characteristics. Excluding Snow Island, Byers Peninsula has a proglacial area of ~ 60 km^2 and, much like Deception Island, has a polar maritime climate with a MAAT of -3^{o}C (70 m a.s.l.) (Bañón et al., 2013). Air temperature regularly exceeds 0 ^{o}C in summer, resulting in liquid precipitation. MAP typically exceeds 500 mm (Bañón et al., 2013), which allows several streams to form (**Figure 1.8**). The geology is where the characteristics of Deception Island and Byers Peninsula differ; Byers Peninsula is largely formed of marine and volcanoclastic mud and sandstones, with only limited intrusions of basalt and andesite (Gao et

al., 2018). There are also a number of glacial and periglacial features, including patterned ground, moraines and blockfields (Moura et al., 2012).

Figure 1.8: *Camp Byers (ESP) on South Beach, Byers Peninsula. Note the extensive drainage network, appearing to be sourced from snow patches and soils. These streams are surrounded by a large expanse of moss and other vegetation. Photo sourced from* ***Wikimedia Commons*** *(CC BY-SA 4.0) and taken in 2017 by "Inoceramid bivalves".*

Byers Peninsula has relatively high biological diversity (compared to other Antarctic regions), with species of lichens and mosses, as well as birds and seals being present (Quesada et al., 2013). This includes Skuas, Chinstrap Penguins, Gentoo Penguins, and Elephant Seals (Gil-Delgado, Villaescusa, et al., 2013; Gil-Delgado, González-Solís, et al., 2013). Researchers from across the globe regularly visit both Byers Peninsula and Deception Island. Deception Island was home to several research stations, though these were abandoned in the 1960s following volcanic eruptions on the island (Bartolini et al., 2014). Nevertheless, both Deception Island and Byer's Peninsula host field campaigns, either on-site in the form of seasonal field camps (e.g. Spanish Antarctic research and IAA, **Figure 1.8**), or more ad-hoc trips from stations on other parts of Livingston Island (Bulgarian, Spanish, Argentinian), or from neighbouring islands (e.g. King George Island).

1.2.6. South Georgia

The most northerly site in this thesis is the sub-Antarctic island of South Georgia (**Figure 1.3**). Its geology is dominated by metasedimentary and volcanoclastic sediments, with some mafic volcanic outcrops and basement accretionary prism sediments to the south of the island. Its northerly position means it has the mildest climate of all the study sites, with a MAAT of 2 °C. As an isolated South Atlantic island it has a very wet maritime climate with a MAP of more than 1500 mm (Bannister and King, 2015; Bannister and King, 2020). Whilst much of this falls as rain, its high relief (the Allardyce and Salvesen Mountain Ranges that dominate the island have elevations > 2000 m) means there is ample snowfall for glaciers to persist on the island, though these have retreated substantially since the 1950s (Bentley et al., 2007; Bannister and King, 2015).

Due to its relatively mild climate, it has an abundance of wildlife along its coastal regions. It hosts the largest breeding populations of Antarctic fur seals, elephant seals and King Penguins, as well as having large populations of albatross and other seabirds (Dickens et al., 2021). South Georgia's coastal regions are extensively covered by vegetation (**Figure 1.9**), some of which is invasive, and includes several vascular plants including grasses, herbs, and shrubs (Strother et al., 2015). Indeed, there were also some invasive mammals; including reindeer, rats, and mice (Cook et al., 2010), though they have since been eradicated (Martin and Richardson, 2019).

***Figure 1.9**: Grytviken on South Georgia. Note the metasedimentary and sedimentary rocks on the beach, high relief landscape, large-scale scree slopes, and extensive vegetation coverage. Photo sourced from **Wikimedia Commons** (CC BY-SA 2.0), taken by Simon Murgatroyd in 2009.*

Although there has been a human presence on the island since the 18th Century, following its first reordered discovery by British sailors in the 17th Century, the population has dwindled in recent decades following the end of the seal and whaling industry in the 1960s (Headland, 1984). Today, human populations are centred around research stations on King Edwards Point and Bird Island, and tourist sites in Grytviken (**Figure 1.9**). Although there has been extensive research of glaciers and wildlife on the island (e.g. Farías-Barahona et al., 2020; Dickens et al., 2021), there has been little analysis of land cover, geomorphology or geology in recent years, particularly outside of regions adjacent to permanent stations on the island.

1.3. Research objectives

Given the clear importance of land cover, and more specifically sediment dynamics, to the functioning of Antarctic ecosystems, this thesis aims to describe the landcover of the Antarctic Peninsula and sub-Antarctic Islands, and how it has changed in recent decades. Furthermore, it will investigate how proglacial river catchments operate in Antarctica. With this in mind, four objectives will guide this research and the structure of this thesis:

1. Use the existing maps of Antarctica to design the first unified **land cover classification of the major proglacial regions of the Antarctic Peninsula and sub-Antarctic islands** (Chapter 2) using optical satellite images.
2. Investigate how the **land cover has changed on Antarctic Peninsula and sub-Antarctic islands during the 21st century** (Chapter 3).
3. Explore how different **environmental factors and ground conditions influence sediment export from two river catchments on James Ross Island.** (Chapter 4)
4. Quantify how **glaciers have changed in recent decades on the James Ross Archipelago** (Chapter 5).

1.4. Thesis structure

This thesis is structured to describe: **i)** how proglacial regions in Antarctica look today; **ii)** how these regions have changed since the early 2000s; **iii)** how environmental conditions affect sediment transport in an Antarctic proglacial environment; **iv)** how the glaciers of the James Ross Archipelago have changed since 2010. These results chapters are designed to give a holistic view of proglacial landscape evolution. This introduction has provided the relevance and importance of studying proglacial environments in Antarctica. The findings of this thesis will be discussed in the context of the future evolution of the Antarctic Peninsula and sub-Antarctic Islands, and their proglacial regions. This thesis is structure as follows:

1. Introduction

2. Classifying the contemporary land cover of major proglacial regions across the Antarctic Peninsula, sub-Antarctic Islands and the McMurdo Dry Valleys
3. Land cover change of major proglacial regions across the Antarctic Peninsula, sub-Antarctic Islands and the McMurdo Dry Valleys during the 21st Century
4. Quantifying sediment sources, pathways, and controls on fluvial transport dynamics on James Ross Island, Antarctica
5. Accelerated glacier changes on the James Ross Archipelago, Antarctica, since 2010
6. Discussion and outlook for the future
7. Summary and conclusions

2. Classifying the contemporary land cover of major proglacial regions across the Antarctic Peninsula, sub-Antarctic Islands and the McMurdo Dry Valleys

2.1. Introduction

Land cover information is essential to furthering our understanding of terrestrial environments, ecological niches and the atmosphere, especially across sensitive regions of Earth (Raup et al., 2007; Ban et al., 2015; Chen et al., 2019; Gong et al., 2020). Additionally, land cover maps are a critical resource required to support the research of climate change: particularly those that include information on vegetation coverage (Bojinski et al., 2014). Owing to the frequent return period and extensive areas covered by satellite images, land cover maps are increasingly being produced using remote-sensing (Friedl et al., 2010; Brown et al., 2022). Several global land cover products have been released in recent years (e.g. Brown et al., 2022) but they typically do not include Antarctica or sub-Antarctic Islands (e.g. South Georgia), leaving a gap in our understanding of Earth's southernmost continent.

Maps of land cover are particularly important for Antarctica , owing to its dynamic landscape and rapid environmental change (Davies et al., 2013). Unlike most other regions on Earth, human activities are not the major control on land cover type in Antarctica, and the footprint of anthropogenic activities is limited to relatively small areas (Tejedo et al., 2016; Tejedo et al., 2022). Until the start of the 21st century, the Antarctic Peninsula Region (APR) was one of the most rapidly warming places on Earth with a temperature rise of 1.5 °C observed since the 1950s (Vaughan et al., 2003; Mulvaney et al., 2012). Following a hiatus in warming at the start of the 21st century, there is evidence that this trend has resumed (Carrasco et al., 2021) and glaciers have continued to respond to the temperature increases of the 20th century and subsequent warming since 2015 (Oliva, Navarro, et al., 2017; Engel et al., 2023). This ice mass loss has resulted in the enlargement of proglacial regions, and they will continue to expand as both land and marine-terminating glaciers continue to retreat with a warming climate (Lee et al., 2017; Bosson et al., 2023).

Given the importance of land cover to the functioning of Antarctic ecosystems, the aim of this chapter is to produce a land cover map with a unified classification scheme of several key proglacial regions across the APR, sub-Antarctic and the McMurdo Dry Valleys (see section 1.2.). Since land cover mapping involves a combination of observation and interpretation, the spatial variability in land cover, as well as potential reasons for their patterns, are described and discussed in a combined "Results and Discussion" section.

2.2. Methodology

Landsat-8 Optical Land Imager (OLI) top-of-atmosphere (TOA) images were processed in Google Earth Engine (GEE), with intermediate steps of interpretation taking place in ArcGIS Pro (v2.6.0).

2.2.1. Image selection and pre-processing

Landsat-8 OLI TOA imagery (30 m resolution) was chosen for analysis, rather than higher-resolution images (such as Sentinel-2), because of its extensive archive dating back to 1972. This allows for a direct comparison with older images in future studies. Specifically, TOA images were chosen over surface reflectance (SR) because the US Geological Survey (USGS) states the efficacy of surface reflectance correction is reduced in regions with extensive snow cover, hyper-aridity, low sun angles, or in coastal regions (USGS, 2024); factors that affect all of the study sites in this thesis (section 1.2).

The Landsat-8 OLI images were processed in GEE (**Table 2.1**), a cloud-based platform that allows for the analysis of large datasets in higher speeds than can be done locally on a traditional home computer (Gorelick et al., 2017). GEE gives access to petabytes of Earth observation data from a multitude of satellites, including optical images (including the entire Landsat catalogue) and digital elevation models (DEMs) (including those used in this chapter), and removes the need to download these images locally.

Table 2.1: *Images used to produce land cover classification*

Site	**Image**	**Date**	**Cloud cover %**
McMurdo Dry Valleys	LANDSAT/LC08/C02/T2_TOA/LC08_056116_20191217	17/12/2019	0
Alexander Island	LANDSAT/LC08/C02/T2_TOA/LC08_218110_20200117	17/01/2020	0
	LANDSAT/LC08/C02/T2_TOA/LC08_217111_20191107	07/11/2019	1
	LANDSAT/LC08/C02/T2_TOA/LC08_216110_20191218	18/12/2019	0
James Ross Island	LANDSAT/LC08/C02/T2_TOA/LC08_215105_20170204	04/02/2017	6
	LANDSAT/LC08/C02/T2_TOA/LC08_215105_20160202	02/02/2016	6
Deception Island	LANDSAT/LC08/C02/T2_TOA/LC08_219104_20200209	09/02/2020	21
Byers Peninsula	LANDSAT/LC08/C02/T2_TOA/LC08_219104_20200209	09/02/2020	21
South Georgia	LANDSAT/LC08/C02/T1_TOA/LC08_206098_20180328	28/03/2018	2
	LANDSAT/LC08/C02/T1_TOA/LC08_207098_20180404	04/04/2018	47

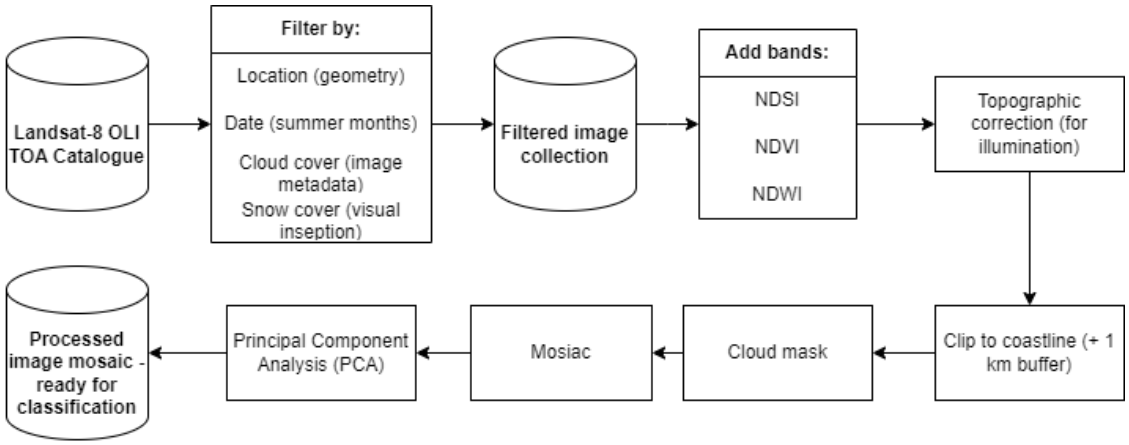

Figure 2.1: *The workflow to select and process images in GEE*

Images that were suitable for analysis had low cloud cover (less than 20 % over land) and limited snow cover, meaning that some sites were limited to a single image for analysis. To ensure consistency with older Landsat images, only six bands were selected. These represent the visible and infrared wavelengths (red, green, blue, near infrared, shortwave infrared 1, and shortwave infrared 2, ranging from 0.45 to 2.29 µm), but excludes the thermal infrared bands that are only available for the most recent Landsat sensors (i.e. the optical land imager on board Landsat 8 and 9). Three further bands were added to the image: **i)** normalised difference snow index (NDSI, **Eq. 2.1**); **ii)** normalised difference vegetation index (NDVI, **Eq. 2.2**); **iii)** normalised difference water index (NDWI, **Eq. 2.3**). NDSI is effective at highlighting areas of snow and ice cover, and also allows sub-categories of these surfaces (e.g. snow, bare ice, wet ice) to be identified (Selkowitz and Forster, 2016). NDVI is a well-established indicator of vegetation cover, and is highly effective at discriminating areas of vegetation from other areas of land (Carlson and Ripley, 1997). NDWI is effective at identifying open water features, and does this by exploiting the high reflectance by green wavelength, and high absorption by near infrared (Xu, 2006).

$$NDSI = \frac{green\ -\ swir1}{green\ +\ swir1} \quad (\mathbf{2.1})$$

$$NDVI = \frac{nir\ -\ red}{nir\ +\ red} \quad (\mathbf{2.2})$$

$$NDWI = \frac{green - nir}{green + nir} \quad (\mathbf{2.3})$$

Where:

- green = band 3 of Landsat 8 OLI, wavelength (λ) = 0.53–0.59 µm
- swir1 = shortwave infrared 1, band 6, λ = 1.57–1.65 µm

- red = band 4, λ = 0.64–0.67 µm
- nir = near-infrared, band 5, λ = 0.85–0.88 µm

Once these bands were added to the image, they were topographically corrected to adjust for the effect of relief on the illumination of images using the Sun Canopy Sensor + C method (Soenen et al., 2005), as previously used for mapping other polar regions (Grimes et al., 2024). REMA DSM (Reference Elevation Model of Antarctica Mosaic Digital Surface Model) (Howat et al., 2019) was used as reference elevation data at 30m resolution (equivalent to the resolution of Landsat-8 OLI multispectral bands) for all sites except South Georgia. Since South Georgia is not covered by REMA, SRTM DEM (Shuttle Radar Topography Mission) was used, also at 30m resolution (Farr et al., 2007). Subsequently, images were mosaicked and clipped to a 1 km buffer around their coastline (Gerrish, L., Fretwell, P., & Cooper, 2021). This buffer was to account for any errors that may be present in the coastline, but had the added benefit of giving confidence in the ability of the classifier to differentiated ice (i.e. icebergs) from liquid water. Lastly, a principal component analysis (PCA) of the images was conducted to reduce the dimensionality of the data and improve the ultimate quality of the classifier by reducing noise (Frohn et al., 2009; Chasmer et al., 2020). The first three components, containing 99.6 % (± 0.3 %) of the data, were selected for classification.

2.2.2. Classification

As established in Chapter 1 of this thesis, there are is a dearth of available data available with which to produce an independent training data set necessary for a supervised classification approach to be produced (e.g. Random Forest Classification, Support Vector Machine) (Rodriguez-Galiano et al., 2012). Therefore, an unsupervised classification approach was used (Duda and Canty, 2002; Mohd Hasmadi et al., 2009; Grimes et al., 2024). Unsupervised approaches do not require training datasets, and instead use the structure of an image to identify spectrally homogeneous pixels. Pixels are then grouped together based on a user-defined number of clusters. K-means is a relatively simple yet effective and widely-used unsupervised land classification algorithm (Phiri and Morgenroth, 2017). Given land cover data are disparate and incomplete over the study sites, it has the added benefit that knowledge of relatively small areas (see **Table 2.2**) could be used to interpret clusters that cover much wider areas.

Table 2.2: *Resources used to interpret clusters and assign them to a land class*

Location	**Resources**
James Ross Island	Geomorphology map (Jennings et al., 2021)
	Geomorphology map (Davies et al., 2013)
	Geological map, British Antarctic Survey (Smellie, 2013)
	Geological map, Czech Geological Survey (Mlčoch et al., 2020)
	Vegetation map (Barták et al., 2015)
Dry Valleys	Interactive geological map, SCAR (Cox et al., 2023); primarily using a beta version (Cox et al., 2019)
Alexander Island	Geological map (British Antarctic Survey, 1981)
Deception Island	Geology and geomorphology map, BAS (Smellie et al., 2002)
	Map of vegetation, ASPA 140 (Secretariat of the Antarctic Treaty, 2022)
Livingston Island	Geomorphological map (Lopez-Martinez et al., 1996)
	Map of vegetation (Ruiz-Fernández et al., 2017)
South Georgia	Geomorphology map (Clapperton, 1971)

A hierarchical approach was taken to classify the image mosaics of each site:

1) A first-order land classification of “land”, “ice”, and “water” informed the subdivision of each of these classes in a second, more detailed, analysis of the dominant land cover classes.
2) A second-order classification made of sub divisions of the first-order classes.

The first-order land classification was produced using 75 clusters (K = 75), which are determined using 500,000 training points. Whilst others have used statistical methods, such as the ‘Elbow Method’, to determine the number of clusters for analysis (Syakur et al., 2018), in this study the threshold was established through trial-and-error, and was found to minimise the area which was misclassified, based on a visual inspection of satellite images and a comparison with published information (**Table 2.2**). The K value chosen ultimately affects the accuracy of the output (Ahmed et al., 2020) and it is, therefore, essential to assess the accuracy of the final product using independent datasets.

In a minority of cases, a cluster could not be assigned to a first-order class. This was usually because a cluster had conflated shadow with dark seawater. To address this, these clusters were split using a slope threshold of 3°, with pixels <3° being assigned as water. Where this process resulted in obvious misclassification a random forest classifier to differentiate between water, land and ice, using user-defined training data and 100 decision trees. Some pixels were covered entirely by very dark shadows or clouds and, therefore, could not be classified; these were assigned “No data”.

The second-order classification was produced by clipping the image to the three first-order land types and running a further clustering of K = 40. These clusters were inspected and then manually assigned a final land classification. Ten different land cover classes were identified by reviewing the available maps of Antarctica (**Table 2.2**) and finding commonalities between them. Although each map used its own nomenclature, their different land classes followed similar themes, primarily centred on vegetation, bedrock outcrops, and landforms made of unlithified sedimentary rocks that are often defined by their grain size. The first-order “land” class was subset into five classes “Bedrock”, “Coarse/wet sediment”, “Fine & dry sediment”, “Vegetation”. In cases where clouds partially obscured land, pixels were assigned to the more general class of “Land (undifferentiated)”. The first-order “Water” class subset into “Water” and “Turbid water”, while the ice class subset into “Ice” and “Wet ice”. Therefore, ten land classes that describe eight distinct surface types, plus partially obscured land (Land (non-differentiated)) and surfaces totally obscured by clouds or shadows (No data). The largest of these examples are on South Georgia and James Ross Island. To the north west of South Georgia (Cape Alexandra and Bird Island), a large area of land was classified as “No data”, since it was entirely obscured by thick clouds in images. Similarly, the south east of James Ross Island is classified as “Land (undifferentiated)”. This region was covered by thin clouds in the imagery, which allowed land to be differentiated from ice and water, but it could not assigned a second-order class with any confidence.

Of the proglacial land classes, the two sedimentary classes (Coarse/wet sediment and Fine & dry sediment) are the dominant land classes. During the clustering process, these sedimentary classes were separated based on the observation that pixels containing wet sediments (such as rivers) or blocky superficial sediments, such as scree, clustered distinctly from those pixels that contain sediments smaller than cobbles in size and fissile sedimentary rocks. This grain size threshold was derived from information on geomorphological maps for the region (Jennings et al., 2021), and observations made on James Ross Island during the 2022 field season. It is emphasised that the first of these two classes describe pixels that contain sediment that may

be coarse, wet, or both. The second of these classes describes surfaces with fine sediments with minimal water content.

2.2.3. Accuracy assessment

Having used the limited pre-existing land cover data to inform the interpretation of the K-means clusters, finer-resolution imagery was determined to be the optimal source of independent validation data. To ensure the accuracy assessment was robust, and following recommended best practice, 3000 random points were generated and stratified by the area of each land class (Olofsson et al., 2013; Olofsson et al., 2014). These points were visually compared them to 10 m resolution Sentinel-2 MultiSpectral Instrument (MSI) images. Sentinel-2 images were used as an independent data source for validation as they are higher resolution than Landsat images, thus giving a better indication of the "true" land cover.

Throughout this assessment, the terms "accuracy" and "uncertainty" are used. The terms used are defined by Olofsson et al. (2014). Accuracy is defined as the degree to which the map produced agrees with the reference point. Uncertainty is defined as the variability of an estimated land area for a given class. The term "error" is also used; this term is specifically used to refer to the likely (95 % confidence interval) difference between the measured land area and the error-adjusted area, as defined by Eq. 2.10. The error is also referred to as a percentage; this is to indicate its magnitude of it relative to the area of the class.

Given the dominance of the ice class in the classification, this meant most of the stratified sample points landed on ice. Therefore, a second level of accuracy assessment was conducted on just the proglacial classes using 1000 points to ensure their accuracy was adequately calculated.

Accuracy was assessed using an error matrix, following equations**,** as defined by Olofsson et al. (2014). This involves calculating the proportional area of each class (i,j) within the matrix.

The producer's error ($\hat{P}_j$) of a given class is equal the proportion of accurate pixels in an individual column (j) of the error matrix (**Eq. 2.4**)

$$\hat{P}_j = \frac{p_{jj}}{p_j} \quad (\mathbf{2.4})$$

The user's error ($\widehat{U}_i$) of a given class is equal the proportion of accurate pixels in an individual row (i) of the error matrix (**Eq. 2.5**)

$$\widehat{U}_i = \frac{p_{ii}}{p_i} \quad (\mathbf{2.5})$$

The overall accuracy of a class was defined as the sum of uncertainties for each land classification (**Eq. 2.6**).

$$O = \sum_{j=1}^{q} p_{ij} \quad \textbf{(2.6)}$$

Where q is the number of classes, and p_{ij} is the proportion of a class's accurately classified pixels as a proportion of its total area relative to the total area of the classification (w) (**Eq. 2.7**).

$$\hat{p}_{ij} = w_i \frac{p_{ii}}{p_i} \quad \textbf{(2.7)}$$

The error-adjusted area of a class is given as A_j (**Eq. 2.8**).

$$\widehat{A_j} = A_{tot}\hat{p}_j \quad \textbf{(2.8)}$$

The error margins ($S(\widehat{p_j})$) of the error-adjusted area (**Eq. 2.8**) can also, as shown in **Eq. 2.9.,** where n is the number of points validated.

$$S(\widehat{p_j}) = \sqrt{\sum_{i=1}^{8} W_i^2 \frac{\frac{n_{ij}}{n_i}\left(1-\frac{n_{ij}}{n_i}\right)}{n_i - 1}} \quad \textbf{(2.9)}$$

Finally, the 95 % error margin of the error-adjusted area is calculated using a z-score of 1.96 (cf. Olofsson et al., 2014) (**Eq. 2.10**)

$$\hat{A}_j = \pm 1.96 \times S(\hat{p} \cdot j) \quad \textbf{(2.10)}$$

The classes of turbid water and wet ice were particularly problematic because they typically comprised episodic sediment plumes and snow/ice melt. Therefore, they were combined with water and ice respectively for the purposes of accuracy assessment. A 10 km resolution grid to display the spatial variability in the accuracy of this classification (as a proxy for confidence) was also produced, with each cell colour-coded according to the percentage of accurate assessment points within it.

2.3. Results and discussion

2.3.1. The land classes

The land class with greatest coverage across all sites is ice, which is unsurprising given the number of glaciers in these regions. While mapping ice masses was not the primary goal of this study, the high accuracy of the ice class (see section 2.3.4) makes this dataset a potentially useful resource to assess changes in the small, land-terminating glaciers within the study sites (**Figure 2.2**).

Of the sedimentary classes, coarse/wet sediment is the predominant land class at four of the six sites, particularly on South Georgia and Byers Peninsula, where it represents 57 % and 56 % respectively of the proglacial land cover (**Figure 2.3**). This coarse/wet land class includes the major surface drainage networks of Antarctica and it accurately depicts the major rivers of the

Bohemian Stream and Abernethy River on James Ross Island (**Figure 2.4**) and the Onyx River in the McMurdo Dry Valleys (cf. Chinn and Mason, 2016). The coverage of fine and dry sediment class varies inversely to that of the coarse/wet sediment. For example, on South Georgia, the 57 % coverage of coarse/wet sediment is in comparison to a 33 % coverage of fine and dry sediment. On Deception Island, where fine and dry sediments are the dominant land class (53 %), there is only 26 % coverage of coarse/wet sediment (**Figure 2.3**). At all of the sites, between 70 % and 80 % of the proglacial surface is covered by sediment.

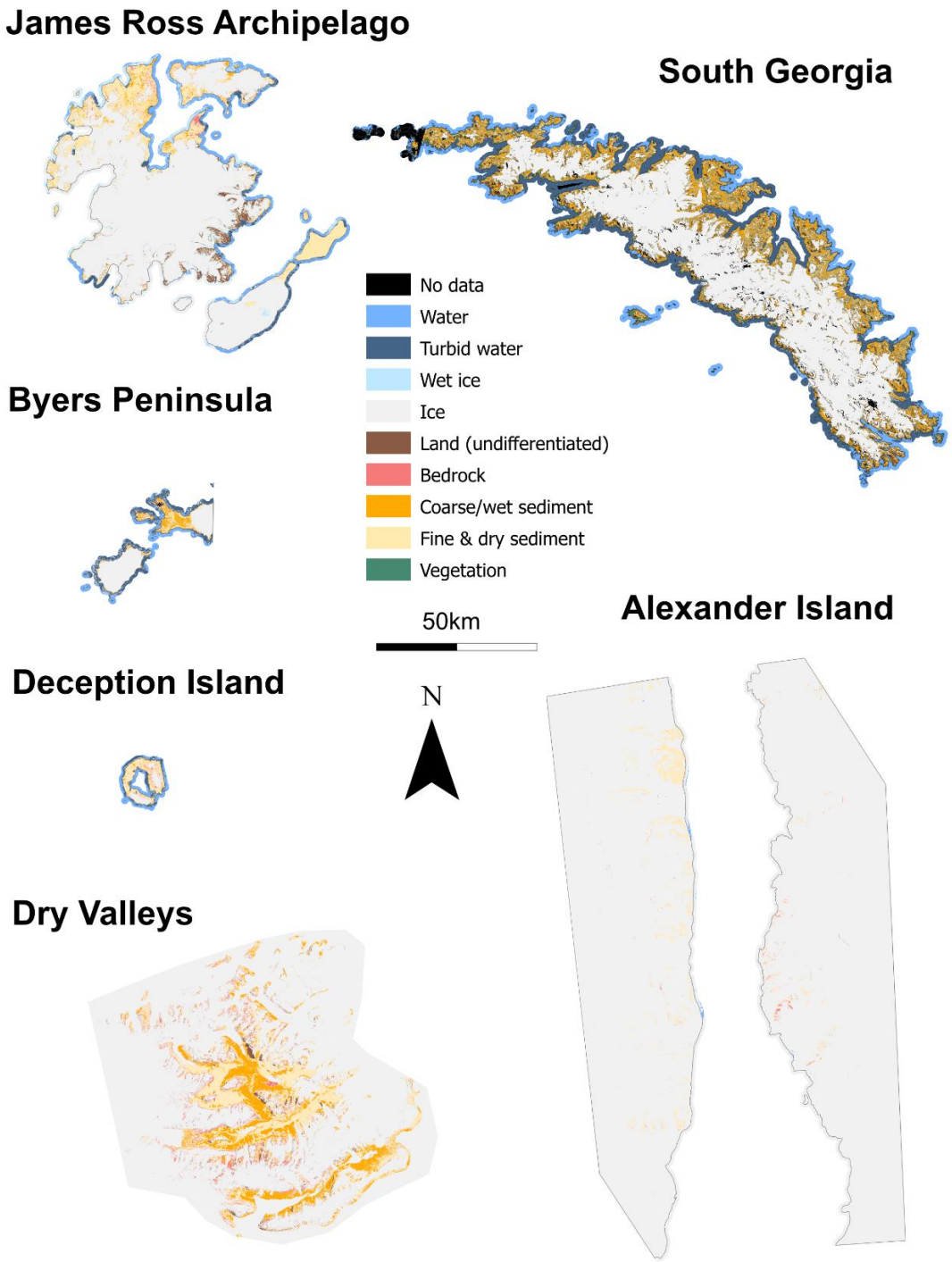

Figure 2.2: *Land cover maps of the six sites, including 10 classes, which describe eight distinct surfaces, "no data", and "land (non-differentiated)".*

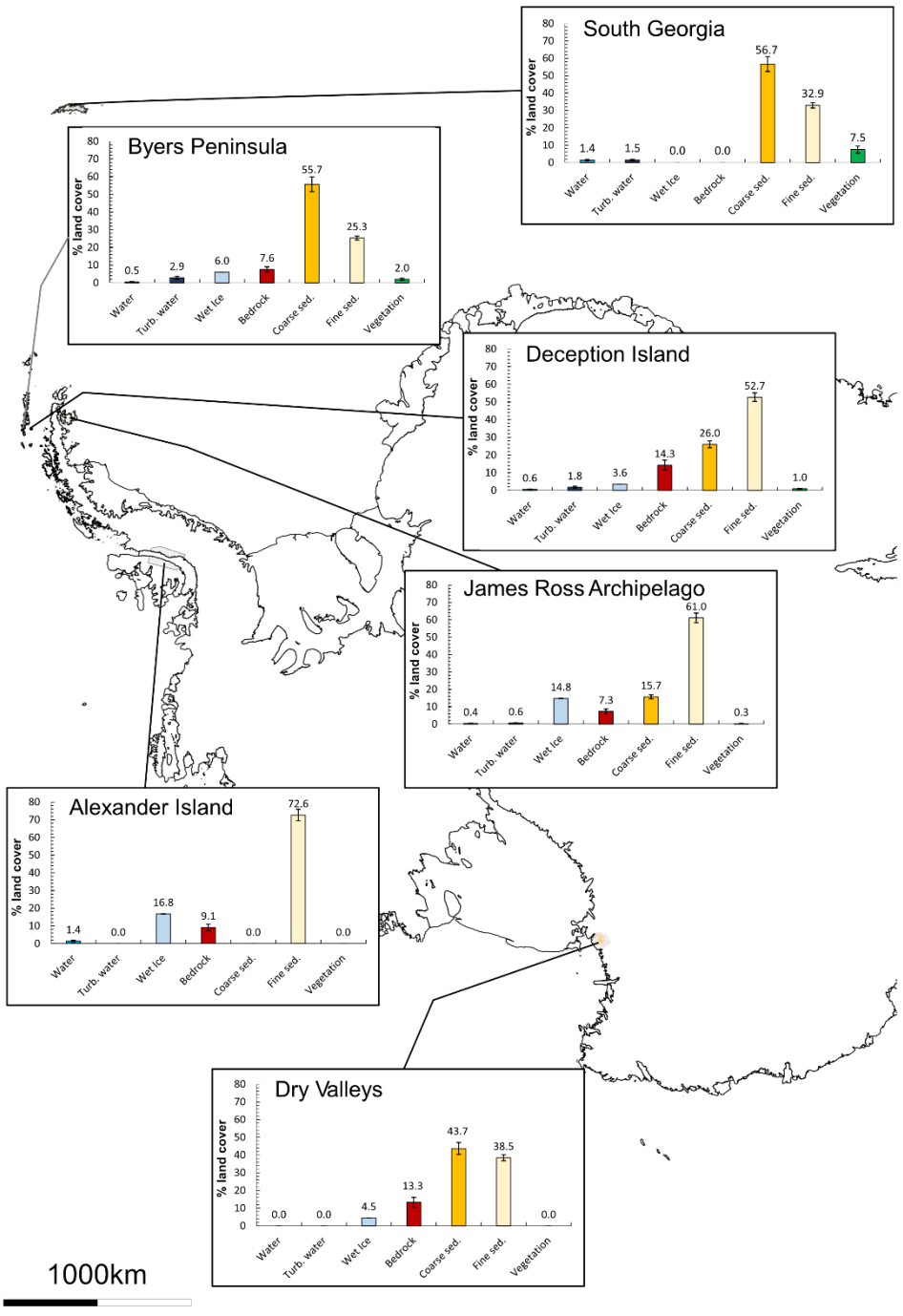

***Figure 2.4**: Percentage land cover values (excluding ice, no data and land (undifferentiated)) for each site, overlaying the coastline of Antarctica (coastline sourced from BAS). Error bars indicate the 95% confidence intervals, which were calculated using the equations in section 2.2.3.*

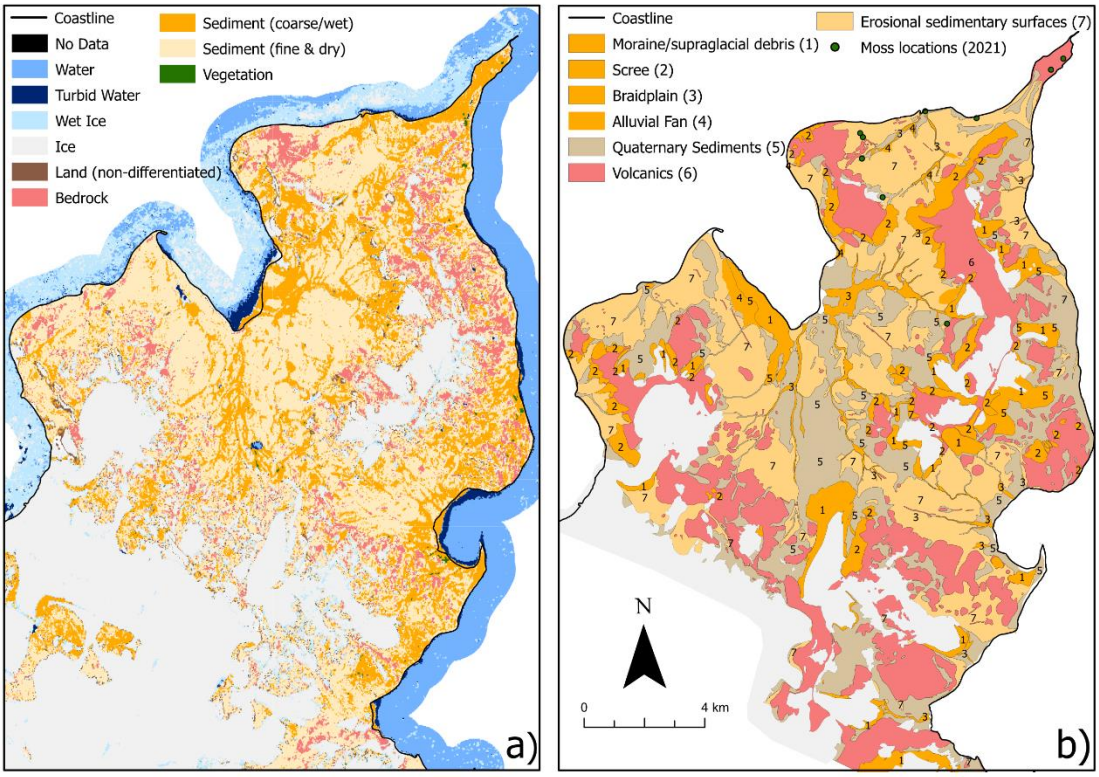

Figure 2.5: *Two classifications of the Ulu Peninsula on James Ross Island,* ***a)*** *produced in this study;* ***b)*** *adapted from Jennings et al. (2021) and displaying data collected through remote sensing and fieldwork. Vegetation locations as collected by Jan Kavan (of the Czech Antarctic Research Programme) in 2021 are also displayed. Note the similarities in the ice class, locations of river systems, and scree slopes. NB: the colours in panel b have been adapted to allow a more direct comparison with the map produced in this study (a).*

The bedrock class, which primarily describes igneous and metamorphic rock surfaces, is most abundant on Deception Island, covering 14 % of its proglacial areas (**Figure 2.3**). In the Dry Valleys, bedrock covers 13 % of the area and the performance of the classification is particularly notable for its ability to pick out an exposed basement sill (Petford and Mirhadizadeh, 2017) in Wright Valley. In other studies (e.g. Jennings et al., 2021), bedrock classes are often over-represented (**Figure 2.4b**) because the study aims to map geomorphology or geology, rather than surface characteristics such as physical weathering and in situ production of block fields. Moreover, field observations show that boulders and other glacigenic sediments overlie many of the large igneous extrusions. Therefore, the classification performed in this thesis gives a better sense of mostly thin surface coverage of exposed solid bedrock.

Classes relating to water (water, turbid water, wet ice) vary in spatial coverage across all of the sites, and may represent transient features (e.g. seasonal melt water/sediment plumes). The wet-ice class proved to be a little ambiguous to interpret from clusters and represents saturated firn and ‘slush’ ice (i.e. partially melted ice or partially frozen water). Wet ice is most

abundant on Alexander Island, with 17 % coverage (**Figure 2.3**), and highlights the record-high surface melt observed around the King George VI Ice Shelf in late 2019 (Banwell et al., 2021). This large amount of wet ice is comparable to the James Ross Archipelago (15 %), where a large proportion of wet ice is accounted for by a melt event that resulted in a large area of saturated firn on Snow Hill Island (**Figure 2.5**). This transient nature of wet ice is also seen with the turbid water class, which can pick out sediment plumes (**Figure 2.5**).

This land classification also provides the first large-scale map of vegetation in Antarctica and the sub-Antarctic. Notably, this includes extensive areas of vegetation on South Georgia, which covers 8 % of its proglacial surface (**Figure 2.3**) and are clearly identifiable in satellite images. Several sites of vegetation were also identified on the South Shetland Islands; especially those on Deception Island (total 1 % surface coverage, **Figure 2.3**) within ASPA 140 (subsite B) on Deception Island (Secretariat of the Antarctic Treaty, 2022). In some cases, it has been possible to identify very small areas of vegetation such as those located on James Ross Island, which were verified in the field (**Figure 2.4**).

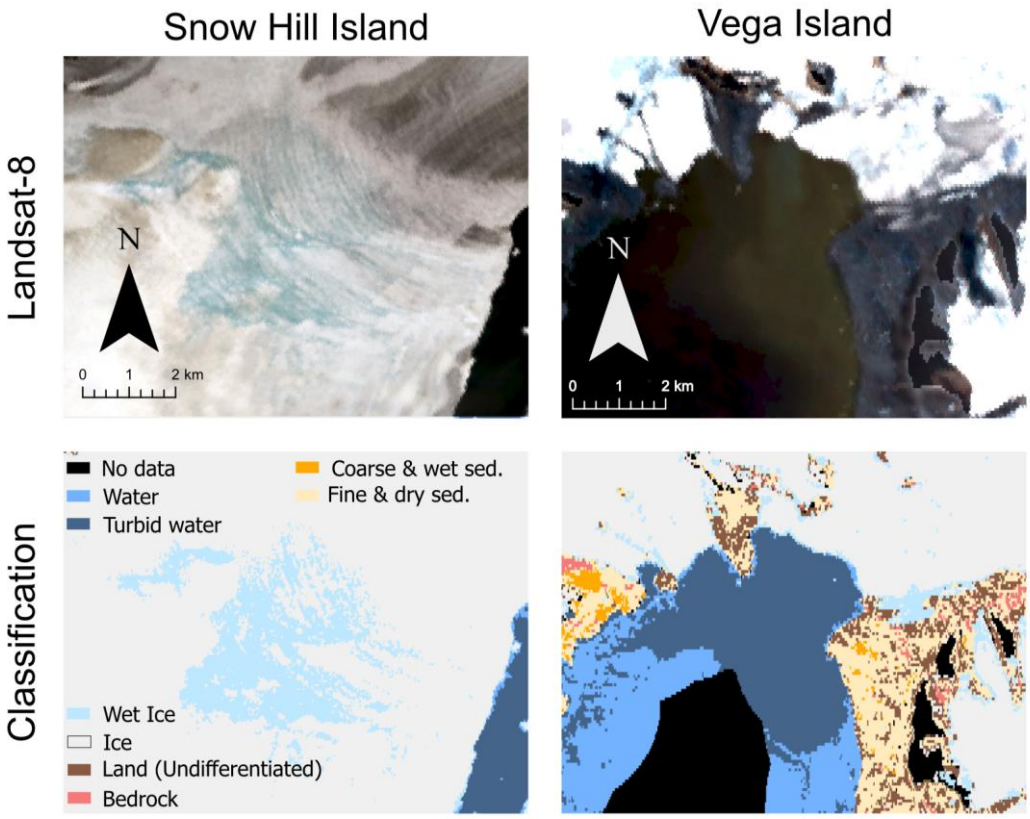

***Figure 2.6**: How the wet ice and turbid water classes compare to the images they are derived from, with a large area of saturated firn on Snow Hill Island (64°28'S, 57°4W) , and a sediment plume off the coast of Vega Island (63°52'S, 57°16'W)*

2.3.2. Spatial variations

A spatial variation in land cover can be observed between the sites (**Figure 2.3**). There is typically less coarse/wet sediment at southwards; this is offset by a general increase in fine and dry sediments. The second most southern site, Alexander Island, has 0 % of its proglacial surface covered by coarse/wet sediment, compared with 57 % on South Georgia (**Figure 2.3**). However, the most southerly site of the Dry Valleys is an exception to this trend, with 44 % of its land covered by coarse/wet sediments.

Unlike other land classes, the proportion of the (inland) water and wet ice classes appears to be more evenly spread across the sites. There is a slight apparent latitudinal pattern in these data, with more (inland) water at the sites further to the north, and variability between the east and west (i.e. when comparing the South Shetland Islands with James Ross Archipelago, **Figure 2.3**). South Georgia and Byers' Peninsula have the largest amount of liquid water present (when joining the water and turbid water classes together), around 3 %. James Ross Archipelago has significantly less (1 %) and Alexander Island has 1 % of its surfaces classified as water, owing to a large amount of supraglacial water at the time of image acquisition. Some of this melt has been classified as water, rather than wet ice, as it was unambiguously liquid when inspected and the clusters were interpreted. Much of these inter-site differences in liquid water likely represent differences in climatic setting; those sites with the greatest proportion of the water class are in milder, maritime climates; with higher temperatures and more of its precipitation falling as rain (cf. section 1.2). The bedrock class does not show a clear latitudinal pattern and is most abundant in Deception Island (14 %) and the McMurdo Dry Valleys (13 %).

A latitudinal pattern in the presence of vegetation is also present, with the largest proportions of vegetation coverage observed on South Georgia and the South Shetland Islands, and no coverage on Alexander Island or the McMurdo Dry Valleys. This is consistent with observations made in Arctic regions, where regions closer to the poles have significantly less vegetation coverage (Walker et al., 2018). Although no vegetation was detected on Alexander Island or in the McMurdo Dry Valleys, small areas of vegetation have previously been described (Heywood et al., 1977; Pannewitz et al., 2003), though they are typically below the resolution of the classification. The most northern site of South Georgia had significantly more vegetation than any other site (7 % of the proglacial regions are covered by vegetation, **Figure 2.3**), while the McMurdo Dry Valleys and Alexander Island have no detectable vegetation coverage. James Ross Island has very little vegetation cover (< 1 %), while the South Shetland Islands show 2 % coverage on Byer's Peninsula and 1 % on Deception Island.

2.3.3. Potential drivers of variability

The spatial pattern in sedimentary classes are consistent with the expectation that, in polar regions, greater runoff should occur with higher temperatures (Syvitski, 2002). Increased runoff would result in a greater proportion of the surface being covered by the coarse/wet sediment class. However, the Dry Valleys are an exception to this, with 44 % of the land covered by coarse or wet sediments (Fig. 4). This is likely due to the high relief of the region, allowing for greater mass movement and scree formation (Kirkby and Statham, 1975; Doran et al., 2002). Furthermore, consistent solar radiation during the austral summer facilitates glacier melt and, in combination with subglacial drainage, permits the formation of large rivers such as the Onyx River (Gooseff et al., 2011; Conovitz et al., 2013; Badgeley et al., 2017). No coarse sediment was identified on Alexander Island. The reasoning for this is two-fold: **i)** an apparent lack of major drainage networks, and; **ii)** the scree slopes in this region appear to be small and thin. When viewed from higher resolution Sentinel-2 images, only small-size scree slopes and very few streams could be observed, consistent with observations made by Heywood et al. (1977), who noted that many scree slopes were composed of fine sediments. Alexander Island, in particular, was difficult to classify due to a lack of supporting material to aid cluster interpretations; the most recent geological map is from 1981 (British Antarctic Survey, 1981) and only limited geomorphological maps of the region exist (e.g. Salvatore, 2001). This highlights the need to collect more high-quality ground data in Antarctica, in order to improve our wider understanding of proglacial environments in the southernmost continent. Even projects to produce high-quality maps in small areas of these remote regions would improve the performance of remote techniques, such as those described in this study.

The spatial patterns in the inland bodies of wet ice, water and turbid water classes show more water at the sites further to the north, and variability between the east and west, likely due to climatic conditions favouring liquid water on the South Shetland Islands and South Georgia. The disproportionately large amount of water and wet ice on Alexander Island and the James Ross Archipelago captures the exceptional melt that occurred in these areas (Banwell et al., 2021). The bedrock class is most abundant on Deception Island and McMurdo Dry Valleys, owing to ongoing volcanism on Deception Island (Smellie et al., 2002; Rosado et al., 2019) and extensive volcanic history of the McMurdo Dry Valleys (Petford and Mirhadizadeh, 2017; Smellie and Martin, 2021). This class is also associated with volcanic rocks on James Ross Island (Mlčoch et al., 2020; Jennings et al., 2021), Byers Peninsula (Gao et al., 2018) and metamorphic rock outcrops on Alexander Island (British Antarctic Survey, 1981).

Whilst latitude accounts for some of the variation in vegetation coverage, it is not the only factor. The sparse vegetation coverage on James Ross Island, despite its relatively low latitude,

is consistent with field observations and is logical given its semi-arid climate and high wind speeds (Barták et al., 2015; Nývlt et al., 2016; Váczi and Barták, 2022). The high vegetation coverage of Byers Peninsula and South Georgia is also logical given the milder, maritime climates of the South Shetland Islands and South Georgia, compared to the drier continental climate of Alexander Island and the McMurdo Dry Valleys, where there is very little vegetation coverage. Deception Island has less vegetation than the neighbouring Byers' Peninsula, perhaps due to the impact of ongoing volcanic activity on the island and relatively recent eruptions resulting in unfavourable conditions (Collins, 1969; Smith, 1988; Smith, 2005).

2.3.4. Data accuracy

The overall accuracy of the land cover classification is 95.9 %. However, this overall value should be taken with caution, since a large proportion of the study sites are covered by ice. This high accuracy represents the fact that the approach taken is very effective at differentiating ice from land and water. The accuracy of each land class individually provides a more informative assessment; each proglacial land class has a relatively large standard error, owing to the small number of pixels that were checked (**Table 2.3**). Full details of this calculation (i.e. full error matrix) can be seen in **Table 2.5.**

Table 2.3: *Accuracy assessment of all land classes. NB: n<3000 as several points landed on cloud-covered parts of the reference images. % error refers to the size of the 95% confidence bounds, relative to the error-adjusted area.*

Class	Error-adjusted area (km^2)	95% confidence (km^2)	% Area	% error	n
Water	99.1	45.5	0.2	45.9	9
Ice	44 001.5	219.6	92.2	0.5	2 595
Bedrock	231.3	174.2	0.5	75.3	27
Fine & dry sediment	2 131.5	195.9	4.5	9.2	134
Coarse/wet sediment	1 156.6	174.2	2.4	15.1	114
Vegetation	115.7	56.4	0.2	48.8	10

The overall accuracy of the proglacial component of the classification is 77.0%, with the greatest percentage uncertainty in the smaller-sized land classes (water and vegetation). This overall accuracy is slightly lower than some products (e.g. Malinowski et al., 2020; Pazúr et al., 2022), which have achieved accuracy values of 85 % and 84 % respectively. It should be noted that the accuracy of the data in this chapter was achieved without the availability of extensive training data, making it more comparable with the more modest accuracies achieved by Chen

et al. (2015) (80%), or Grimes et al. (2024) (81 %). The sediment classes typically perform well, with relatively small percentage errors (**Table 2.5**). Full details of this calculation (i.e. full error matrix) can be seen in **Table 2.6.**

Table 2.4: *Accuracy assessment of proglacial classes. NB: n<1000 as several points landed on cloud-covered parts of the reference images. % error refers to the size of the 95% confidence bounds, relative to the error-adjusted area.*

Class	*Error-adjusted area (km²)*	*95% confidence (km²)*	*% Area*	*% error*	*n*
Water	85.7	26.4	2.0	30.9	15
Bedrock	285.5	56.7	6.6	19.9	45
Fine & dry sediment	2 375.5	106.9	54.7	4.5	371
Coarse/wet sediment	1 444.7	108.8	33.3	7.5	257
Vegetation	148.5	40.1	3.4	27.0	34

Since it was not possible to assess the accuracy of the turbid and wet ice classes, an example of a classification of each land class has been provided to allow for a qualitative assessment of its accuracy (**Figure 2.5**).

A map of confidence in the land cover produced was also produced (**Figure 2.6**), which is notable for its spatial homogeneity; no individual site appears to be more or less accurate than any other is. The McMurdo Dry Valleys have the most “very low confidence” cells, but this is a function of it being the second largest site analysed, with the largest coverage of proglacial land. Since proglacial classes are less accurate than ice (**Tables 2.3 & 2.4**), it is to be expected that the greatest amount of “very low confidence” cells would be present here.

Additionally, many of these “very low confidence” cells contain only one or two assessment points. This means that just one inaccurate point may result in the cell being classified as “very low confidence”, when in fact further analysis may reveal it performs better than is represented here.

It is also of note that the highest accuracy, i.e. the regions with the highest density of “very high confidence” cells, are within the ice sheets at each site, which is consistent with the accuracy assessment (**Table 2.3**). This is particularly clear on South Georgia and Alexander Island. The regions with “no points” are primarily over the large ice sheets, particularly to the centre of James Ross Island, Alexander Island and the Dry Valleys. Because of the large

coverage of ice, many cells were not checked during the accuracy assessment because the random point algorithm does not generate regularly spaced points. However, in reality, there should be high confidence of cells within the centre of ice sheets: they are clearly ice when inspected and the 92.4% accuracy of the ice class (**Table 2.3**) suggests they are very likely to be accurate.

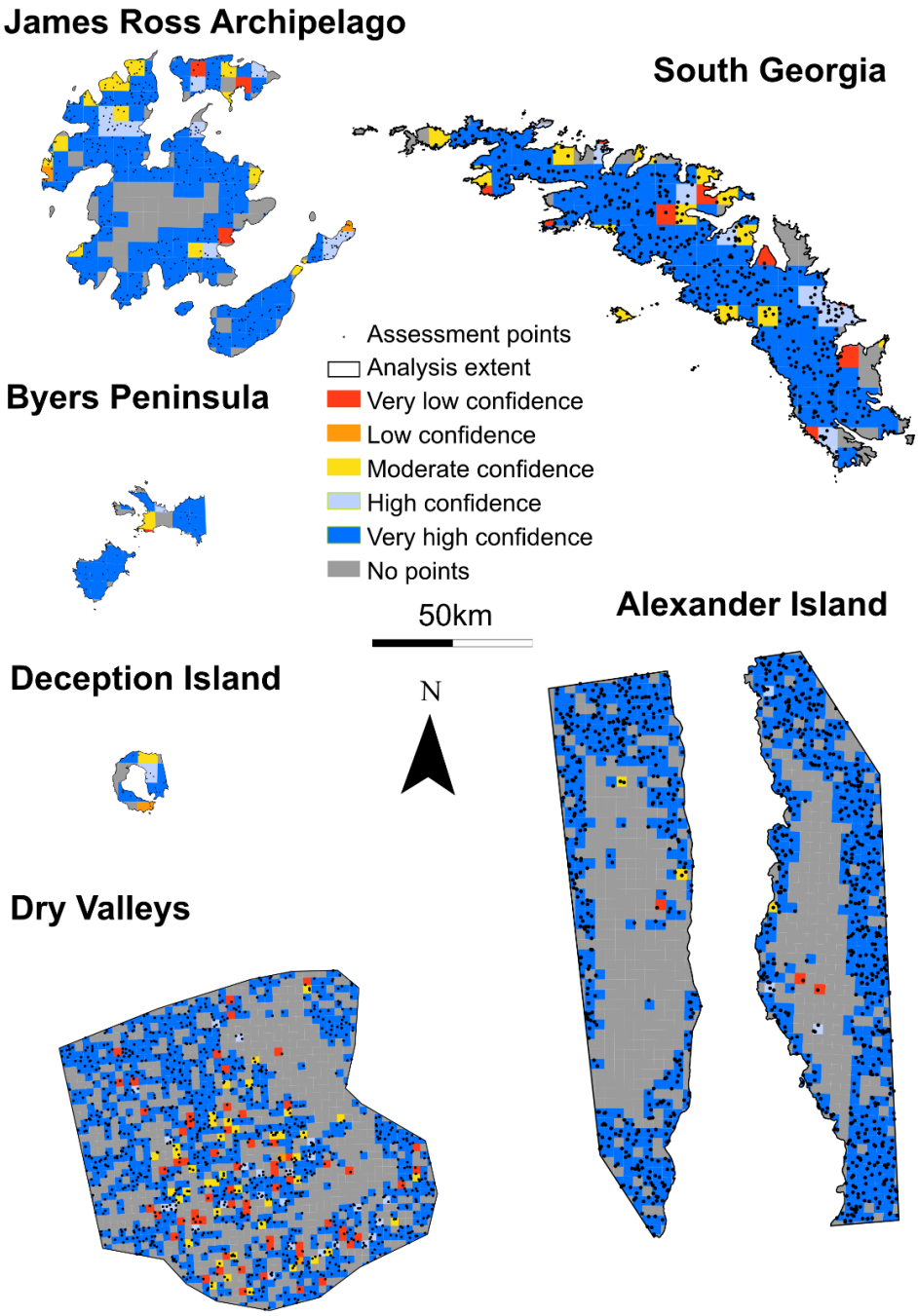

Figure 2.7: *Maps of each site indicating the spatial variability in confidence. Very low confidence = <20% of points were accurate; low confidence = 21 to 40%; medium confidence = 41 to 60%; high confidence = 61% to 80%; very high confidence = >80%*

Table 2.5: *Error matrix for the first accuracy assessment (all land classes), see section 2.2.3. for notations and methodology*

	Reference classes									
Class	Water (1)	Ice (4)	Bedrock (6)	Coarse Sed (7)	Fine Sed (8)	Veg (9)	Total (ni)	Total area (km^2)	Wi	Wi2
Water	5	3	0	0	0	1	9	91.75	0.00	0.00
Ice	1	2588	0	4	2	0	2595	43395.90	0.91	0.83
Bedrock	0	4	11	4	7	1	27	236.49	0.00	0.00
Coarse Sed	0	48	0	55	11	0	114	1461.23	0.03	0.00
Fine Sed	0	20	3	4	107	0	134	2397.77	0.05	0.00
Veg	0	0	0	3	2	5	10	152.66	0.00	0.00
Total (nj)	6	2663	14	70	129	7	2889	47735.7975		
No data	0	65	1	22	22	3				

Class	Water	Ice	Bedrock	Coarse	Fine	Veg	Total (p̂i)	Ûi	p̂j
Water	0.00	0.00	0.00	0.00	0.00	0.00	0.00	0.56	0.83
Turbid	0.00	0.90	0.00	0.00	0.00	0.00	0.90	1.00	0.97
Bedrock	0.00	0.00	0.00	0.00	0.00	0.00	0.01	0.41	0.79
Fine Sed	0.00	0.02	0.00	0.02	0.00	0.00	0.04	0.48	0.79
Coarse Sed	0.00	0.01	0.00	0.00	0.04	0.00	0.05	0.80	0.83
Veg	0.00	0.00	0.00	0.00	0.00	0.00	0.00	0.50	0.71
Total (p̂j)	0.00	0.92	0.00	0.02	0.04	0.00	1.00	3.74	4.92

Class	Error adjusted area (km^2)	95% confidence	% Area	% error	n
Water	99	46	0.21%	45.92%	9
Ice	44,002	220	92.18%	0.50%	2,595
Bedrock	231	174	0.48%	75.32%	27
Fine Sed	2,132	196	4.47%	9.19%	134
Coarse Sed	1,157	174	2.42%	15.06%	114
Veg	116	56	0.24%	48.76%	10
Total	47,735.80				

Overall accuracy	95.92%

Table 2.6: *Error matrix for the first accuracy assessment (proglacial classes only), see section 2.2.3. for notations and methodology*

	Reference classes									
Class	Water (1)	Ice (4)	Bedrock (6)	Coarse Sed (7)	Fine Sed (8)	Veg (9)	Total (ni)	Total area (km^2)	Wi	Wi2
Water	11	0	0	1	2	1	15	91.75	0.02	0.00
Ice	2	0	3	16	16	1	38	0.00	0.00	0.00
Bedrock	0	0	30	12	3	0	45	236.49	0.05	0.00
Coarse Sed	2	0	14	190	51	0	257	1461.23	0.34	0.11
Fine Sed	0	0	3	28	335	5	371	2397.77	0.55	0.31
Veg	0	0	0	6	9	19	34	152.66	0.04	0.00
Total (nj)	15	0	50	253	416	26	760	4339.899		
No data	7		5	84	197	10				

Class	Water	Ice	Bedrock	Coarse	Fine	Veg	Total (p̂i)	Ûi	p̂j
Water	0.01	0.00	0.00	0.00	0.00	0.00	0.02	0.73	0.73
Ice	0.00	0.00	0.00	0.02	0.02	0.00	0.05	0.00	0.00
Bedrock	0.00	0.00	0.04	0.02	0.00	0.00	0.06	0.67	0.60
Fine Sed	0.00	0.00	0.02	0.25	0.07	0.00	0.34	0.74	0.75
Coarse Sed	0.00	0.00	0.00	0.04	0.44	0.01	0.49	0.90	0.81
Veg	0.00	0.00	0.00	0.01	0.01	0.03	0.04	0.56	0.73
Total (p̂j)	0.02	0.00	0.07	0.33	0.55	0.03	1.00	3.60	3.62

Class	Error adjusted area km^2)	95% confidence	% Area	% error	n
Water	86	26	1.97%	30.87%	15
Bedrock	286	57	6.58%	19.86%	45
Fine Sed	2,376	107	54.74%	4.50%	371
Coarse Sed	1,445	109	33.29%	7.53%	257
Veg	148	40	3.42%	26.99%	34
Total	4,340				

Overall accuracy	76.97%

2.4. Conclusions

In this chapter, a land cover map of the major proglacial regions of the Antarctic Peninsula Region, sub-Antarctic, and the McMurdo Dry Valleys has been presented. Given the lack of consistent land cover or geomorphology maps in Antarctica, an unsupervised K-means clustering approach was used to classify 30 m resolution Landsat-8 OLI images by interpreting clusters in a hierarchical approach using a combination of published maps, field knowledge and direct interpretation of satellite images. Information has been presented on the coverage of nine land cover classes: turbid water, water, wet ice, ice, land (non-differentiated), bedrock, fine sediment, coarse sediment, and vegetation. Ten land classes were mapped at 30 m resolution that describe eight distinct surfaces (as well as “no data” and “land (undifferentiated)” classes) at an accuracy of 77.0 % for proglacial classes, and 92.2% for ice. The spatial pattern of the land classes, notably in vegetation and coarse/wet sediment, which are typically more abundant in sites that are more northerly located. This dataset provides a first step in understanding the make-up of Antarctica’s important proglacial regions. It also highlights the need for greater ground-verified data to improve the accuracy of future Antarctic land classifications.

2.5. Data and code availability

Code: Christopher D Stringer. (2022). Contemporary (2016–2020) land cover across West Antarctica and the McMurdo Dry Valleys [Code] (Version 1). Zenodo. https://doi.org/10.5281/zenodo.6720051

Data: Stringer, C. (2022). Contemporary (2016 - 2020) land cover classification across West Antarctica and the McMurdo Dry Valleys (Version 1.0) [Data set]. NERC EDS UK Polar Data Centre. https://doi.org/10.5285/5A5EE38C-E296-48A2-85D2-E29DB66E5E24

3. Land cover change of major proglacial regions across the Antarctic Peninsula, sub-Antarctic Islands and the McMurdo Dry Valleys during the 21st Century

3.1. Introduction

Information on how land cover is changing is essential to furthering our understanding of how terrestrial environments evolve, particularly in the context of a warming climate (Zhao et al., 2023). Land cover can change or respond to climatic forcing in different ways, depending on physical and chemical properties of the land (GCOS, 2010). Owing to the frequent return period and extensive areas covered by satellite images, change detection of landscapes is increasingly being conducted using remote-sensing techniques (Tewkesbury et al., 2015; Xu et al., 2018).

Maps of land cover change are particularly important for Antarctica, owing to its dynamic landscape and great rate of environmental change (Davies et al., 2013; Kavan et al., 2021). Glaciers are receding rapidly across the Antarctic Peninsula, as they respond to warming temperatures (Cook and Vaughan, 2010; Joughin et al., 2021; Engel et al., 2023). This ice mass loss has enlarged proglacial regions, as well as increasing the quantity of meltwater entering streams, and the size and number of proglacial lakes (Rosa et al., 2022; Kavan et al., 2023).

Understanding how Antarctica's proglacial regions are changing is important because they are a source of water, sediment and solutes, whose dynamics are sensitive to climatic change (Carrivick et al., 2018). Additionally, changes in vegetation cover can have wide-ranging impacts on wildlife. In a warming climate, the natural range of indigenous species may increase (Convey and Smith, 2007). Similarly, people visiting the APR and sub-Antarctic may introduce invasive species (Galera et al., 2021; Tejedo et al., 2022). The establishment of invasive species can expand the vegetated area, displace indigenous biota, increase competition and alter food web linkages, potentially threatening indigenous species' survival (Molina-Montenegro et al., 2012; Hughes et al., 2020). It is, therefore, essential to measure the rate at which these changes are occurring. Furthermore, understanding how proglacial landscapes have responded to recent ecological and climatic change is also vital for understanding how these systems may evolve in the future.

This chapter aims to quantify land cover change across key proglacial sites in the APR, sub-Antarctic, and the McMurdo Dry Valleys. Much like the previous chapter, this mapping involved simultaneous observation and interpretation, and in this case of land cover type changes, patterns of change, and potential reasons for those patterns, which will be described and discussed in a combined "Results and Discussion" section.

3.2. Methodology

3.2.1. Image selection and pre-processing

A pair of images were collated for each study site (see section 1.2 and **Figure 1.3**) to measure how landcover has change over proglacial regions in the APR, sub-Antarctic and McMurdo Dry Valleys.

The Landsat-8 images used for change detection were the same as those used to produce a map of land cover in the previous chapter (section 2.2.1, **Table 2.1**). Landsat-7 Enhanced Thematic Mapper plus (ETM+) TOA imagery (30 m resolution) was chosen to analyse images from the early 2000s (**Table 3.1**). Analysis of land cover changes pre-dating the Landsat 7 era was precluded by the poor availability and quality of imagery from earlier sensors. In particular, those that were available typically contained substantial errors relating to image quality and geo-registration (e.g. warping). As with the images described in the previous chapter (section 2.2.1), images were filtered in GEE to minimise cloud cover and snow cover, normalised difference bands (**Eq. 2.1, 2.2, 2.3**) were added and the scenes were then processed with a topographic correction, and mosaicked. Change detection could not be conducted over Deception Island, as no suitable images were available for the early 2000s, owing to frequent cloud cover. This search resulted in a pair of image mosaics for five sites, comprising a mosaic from the early 2000s (Landsat-7), and a mosaic from close to 2020 (Landsat-8).

Images were preferentially selected to ensure that they were captured at the same time of year in both time periods. This was to make sure they represented the same part of the growth and hydrological season. In some cases, poor image availability meant that some image pairs were not collected from the same time of the year (though the difference was minimised). Images were inspected to confirm key features such as flowing rivers and unfrozen lakes, were present in the images from both periods. The image pairs were then manually inspected at each site to ensure they were co-registered using the "Georeference" package in ArcGIS Pro.

***Table 3.1**: Images used to quantify land cover change*

Site	Image	Date	Cloud cover %
McMurdo Dry Valleys	LANDSAT/LE07/C02/T2_TOA/LE07_059115_20011228	28/12/2000	1
Alexander Island	LANDSAT/LE07/C02/T2_TOA/LE07_213111_20020104	04/01/2002	1
	LANDSAT/LE07/C02/T2_TOA/LE07_217111_20021202	02/12/2002	1
	LANDSAT/LE07/C02/T2_TOA/LE07_218110_20010104	04/01/2001	1

	LANDSAT/LE07/C02/T2_TOA/LE07_218111_20030211	11/02/2003	1
	LANDSAT/LE07/C02/T2_TOA/LE07_214110_20030130	30/01/2003	2
	LANDSAT/LE07/C02/T2_TOA/LE07_218110_20030211	11/02/2003	2
	LANDSAT/LE07/C02/T2_TOA/LE07_219109_20011229	29/12/2001	2
	LANDSAT/LE07/C02/T2_TOA/LE07_132133_20001123	23/11/2000	3
	LANDSAT/LE07/C02/T2_TOA/LE07_216111_20030112	12/01/2003	3
	LANDSAT/LE07/C02/T2_TOA/LE07_217111_20010214	14/02/2001	3
	LANDSAT/LE07/C02/T2_TOA/LE07_214110_20020127	27/01/2002	4
	LANDSAT/LE07/C02/T2_TOA/LE07_217110_20021202	02/12/2002	4
	LANDSAT/LE07/C02/T2_TOA/LE07_218111_20010104	04/01/2001	4
James Ross Island	LANDSAT/LE07/C02/T2_TOA/LE07_216105_20000221	21/02/2000	15
Deception Island	No images available		
Byers Peninsula	LANDSAT/LE07/C02/T2_TOA/LE07_219104_20020130	30/01/2002	17
South Georgia	LANDSAT/LE07/C02/T1_TOA/LE07_206098_20020103	03/01/2002	65
	LANDSAT/LE07/C02/T1_TOA/LE07_206098_20030207	07/02/2003	17

3.2.2. Change detection

Following co-registration, the image pairs were analysed to quantify the differences between them. There are several ways that change detection can be conducted, and these methods have previously been the subject of comprehensive literature reviews (e.g. Lu et al., 2004; Tewkesbury et al., 2015). There are five key techniques, as well as further techniques, which use a hybrid of two or more of these techniques. These are:

1) Layer arithmetic
2) Transformation
3) Post classification change (PCC)
4) Direct classification
5) Change vector analysis (CVA)

Each of these methods has its merits, but some are limited either by their simplicity, or by issues concerning error propagation.

Layer Arithmetic typically subtracts band values on a pixel-by-pixel basis, and is effective at showing where change is, but not necessarily the composition of that change (Tewkesbury et al., 2015); it is typically most effective when identifying areas of change in a single land cover

type, such vegetation change (e.g. Coulter et al., 2011). Similarly, transformation techniques uses PCA or mean absolute deviation to identify uncorrelated bands that are typically indicative of change (but not necessarily the type of change) (Tewkesbury et al., 2015).

The most widely used method change detection is PCC (Tewkesbury et al., 2015). This technique involves creating a land cover classification of images in two time periods, and then directly comparing the change in classes. Although this method is intuitive, it is flawed because its overall accuracy is reliant on the accuracy of the two land cover products. Individual errors in each land cover map are compounded in the final map of change, resulting in unacceptably high uncertainty values (Lu et al., 2004; Tewkesbury et al., 2015). Change vector analysis determines the changes in the spectral properties of images over time, which allows for a classification that allows the specific type of change to be identified (Bovolo and Bruzzone, 2007). Whilst CVA has been criticised for being difficult to interpret (Carvalho Júnior et al., 2011), recent advances in this methodology mean that the method has increased the usability of the technique, as well as its ability to identify different types of change (Xu et al., 2018). CVA determines the change in the position of image pixels within an image feature space over time, specifically by measuring the magnitude and direction of change. These can be defined by the Euclidean distance (ED) between pixel values, a vector direction angle (DA), and a spectral angle mapper (SAM). DA is indicative of the type of change that has occurred (Xu et al., 2018), while SAM is a measure of similarity between two pixels, and has been shown to be suitably complimentary to CVA (Carvalho Júnior et al., 2011; Tewkesbury et al., 2015). Together, these three factors provide a good basis for classifying areas that have: changed, and the type of change that has occurred.

Consequently, the CVA method developed by Xu et al. (2018) was implemented in Google Earth Engine (**Figure 3.1**). Each image pair was merged to create an 18-band image with spectral information from both images (i.e. $Band1_{L7}$, $Band1_{L8}$, $Band2_{L7}$, $Band2_{L8}$ …). Three further bands were added to show the ED (**Eq. 3.1**), DA (**Eq. 3.2**), and SAM (**Eq. 3.3**).

$$ED = \sqrt{\sum_{i=1}^{n} d_i^2}, ED \in [0, max(ED)] \quad (\mathbf{3.1})$$

$$DA = \cos^{-1}\left[\frac{\sum_i^n d_i}{\sqrt{n} * ED}\right], \alpha \in [0, \pi] \quad (\mathbf{3.2})$$

$$SAM = \cos^{-1}\left[\frac{\sum_i^n Y_i * X_i}{\|Y_i\| \|X_i\|}\right] \quad (\mathbf{3.3})$$

Where:

- d_i is the difference in values for each spectral pair.
- X_i represent the spectral information of the first image
- Y_i represent the spectral information of the second image
- || || represents the length of each vector

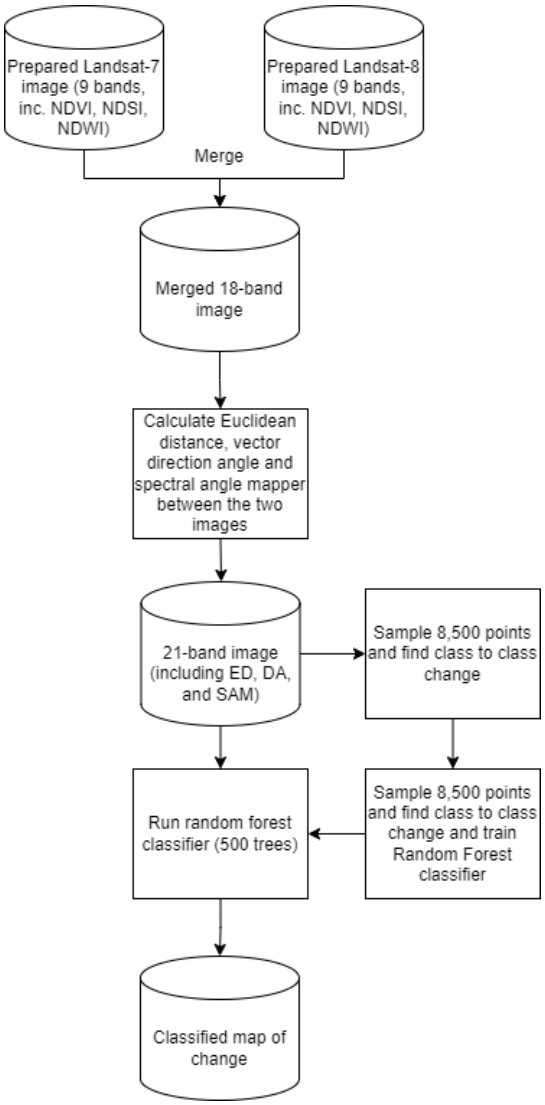

Figure 3.1: *Approach taken to classify the change between image pairs*

This 21-band image was then classified using a random forest classifier. The training data set for this classifier was produced over Byers Peninsula, where a land classification of the Landsat-7 image mosaic was produced using the approach laid out in Chapter 2 (section 2.2, i.e. two step K-means). Byers Peninsula was chosen as the ideal site for this training data set to be produced because it had the greatest variety of land classes in the contemporary classification (**Figure 2.3**).

Across this site, 8,500 points were randomly selected an the land cover at each point from both time-periods and assigned each a class-to-class (ClTCl) change value based on their land cover classification in the Landsat 7 (L7) image and Landsat 8 (L8) image (i.e. L7TL8). Any ClTCl changes that represented less than 1 % of the points were removed to reduce the risk of misclassification. The remaining points described 12 change classes (**Table 3.2**).

The band values at each point were extracted and used to train a random forest classifier. The classifier was parameterised to have 500 trees because errors have been shown to be stable around this value (Lawrence et al., 2006; Xu et al., 2018). This training dataset was modified at each site to ensure that the classifier could only predict changes between classes that were present in the modern land classification.

ClTCl changes represent both an absolute change in land cover, but are also indicative of a change in geomorphology. For example, the CTT class represents a change from coarse/wet sediment to turbid water. However, it also more generally represents a process of surface water ponding or lake formation. In the case of Alexander Island, there is no coarse sediment land cover or turbid water in its land classification. However, the Random Forest classifier was permitted to identify the CTT class in this case. This is because there was visibly surface ponding of water that the classifier was unable to identify without this class present; this is likely because the training data was biased based on cases on Byers Peninsula, where surface water ponding primarily occurred on coarse/wet sediment. Therefore, it was important to allow the CTT class to be present on Alexander Island so that it accurately identified a land cover change that was clearly visible in satellite images.

Table 3.2: *Class to class changes and their abbreviations*

Class to class change	***Abbreviation***
Wet ice to coarse/wet sediment	WITC
Ice to fine & dry sediment	ITF
Ice to coarse/wet sediment	ITC
Ice to turbid water	ITT
Coarse/wet sediment to turbid water	CTT
Coarse/wet sediment to wet ice	CTWI
Fine & dry sediment to bedrock	FTB
Coarse/wet sediment to bedrock	CTB
Coarse/wet sediment to fine & dry sediment	CTF
Coarse/wet sediment to vegetation	CTV
Bedrock to coarse/wet sediment	BTC
Fine & dry sediment to coarse/wet sediment	FTC

3.2.3. Accuracy assessment

Two types of accuracy assessment were conducted to ensure the change detection classification was accurate and robust: **i)** estimation of resubstitution error, and; **ii)** data validation. Resubstitution error assesses the differences between the training data classes and

predictions the classifier makes. This shows the accuracy of the model based on the training data made available to it and is an indicator of how well a classifier is theoretically able to make predictions; it is a good first step to ensure the classifier works as intended (Sakizadeh, 2015). The change maps were validated using a 70:30 split between training points for a classifier and for validation. This meant that 70 % of pixels were used to produce a map of land cover change, whilst 30 % were classified independently and compared against the predicted change classification. This approach is regularly used to assess the accuracy of land cover and change products in the absence of external independent data (Xu et al., 2018; Prasad et al., 2022), and this ratio between training data and validation has been shown to be most reliable (Adelabu et al., 2015; Gholamy et al., 2018). By splitting the data 70/30 between training and validation, the 30 % of pixels used for validation are "independent" of those used by the classifier. To ensure this split was unbiased, the training/validation points were randomly sorted before splitting them.

3.3. Results and discussion

3.3.1. The changing landscape

Four of the five sites had similar landscape stability with between 64.2 % and 68.2 % of the land cover remaining unchanged during the study period (**Figure 3.2**). Alexander Island, however, varies from this trend with a no change proportion of just 50.2 %. This is primarily due to the exceptional melt of snow and ice in the region at the time of the second image (2019), with more sediment being exposed (ITF) and some lakes and supraglacial lakes (ITT) forming in their place (**Table 3.3**). 84 % of the change on Alexander Island is due to ice melt; i.e. ice has been replaced by a new land cover type (**Table 3.3, Figure 3.3**). This dramatic change in land cover coincides with sustained positive-degree temperatures that occurred in 2019 for the contemporary image and also led to exceptional melt on the George VI ice shelf (Banwell et al., 2021). Alexander Island is also the exception to a general pattern observed of the loss of ice across Antarctica. In general, there is a latitudinal pattern in the loss of ice across the study sites.

Three change classes (**Table 3.2**) describe this loss of ice: ITT, ITC, and ITF. 45 % of the land cover change on South Georgia is associated with these classes (**Table 3.3, Figure 3.3**), compared with less than 1 % in the Dry Valleys. This pattern of ice loss occurs in tandem with a southward increase in the proportion of land cover change associated with sedimentary changes (FTC, CTB, or CTF).

Table 3.3: *The proportion of land cover change classes at each site. See* ***Table 3.2*** *for a list of abbreviations.*

	South Georgia	Byers Peninsula	James Ross Island	Alexander Island	Dry Valleys
WITC	1.0%	3.3%	2.4%	5.4%	0.0%
ITT	15.8%	1.5%	7.9%	32.4%	0.0%
ITC	22.5%	10.9%	1.3%	0.0%	0.1%
ITF	6.2%	5.5%	1.9%	51.7%	0.3%
BTC	0.0%	1.4%	0.5%	0.0%	0.0%
CTT	3.1%	1.2%	1.3%	0.6%	0.0%
CTWI	20.8%	4.1%	0.4%	9.8%	0.0%
CTB	0.0%	15.7%	1.1%	0.0%	0.1%
CTF	20.5%	15.3%	67.5%	0.0%	89.4%
CTV	0.5%	1.8%	0.4%	0.0%	0.0%
FTB	0.0%	0.5%	0.0%	0.0%	0.0%
FTC	9.7%	38.8%	15.2%	0.0%	10.1%

The FTC class is possibly a consequence of changes in hydrological routing, or mass movement, which may be a consequence of increased glacial melt or permafrost degradation due to rising temperatures (Kavan et al., 2017; Kňažková et al., 2021; Kavan et al., 2023). However, these changes may also be the consequence of normal inter-annual variability in surface drainage, which is consistent with it being most abundant on Byers Peninsula, where episodic changes in the flow of streams occurs as a consequence is high rate of precipitation (Bañón et al., 2013). Given care was taken to ensure images were from the same part of the hydrological season (cf. section 3.2.1), the effects of any episodic events should be minimal. Some of these differences in sedimentary class may also be accounted for by the stabilising and moisture-retaining properties of vegetation coverage (Aalto et al., 2013; Klaar et al., 2015) , which is higher at the more northerly sites (**Figure 2.3**). The CTB class should represent erosive processes, though large blocky material may be misclassified as bedrock, depending on its size. Nevertheless, CTB is most abundant on Byers Peninsula where there are several streams present in steep basins with high erosional power (Mink et al., 2014). The CTF class appears to represent dust deposition or sediment drying in most cases, which is consistent with it being most abundant in the semi-arid and hyper arid James Ross Archipelago and McMurdo Dry Valleys, where dust storms are frequent (Kavan, Nývlt, et al., 2020). Of the three sites where vegetation was identified in the land cover product, and where change detection was conducted (Byers Peninsula, South Georgia, and James Ross Island), the greatest change was seen on the Byers' Peninsula; with 2 % of its total change accounted for by the CTV class. This is consistent with

previous research which has noted the increase in vegetation coverage in the South Shetland Islands (Hughes, 2000; Torres-Mellado et al., 2011; Cavieres et al., 2016).

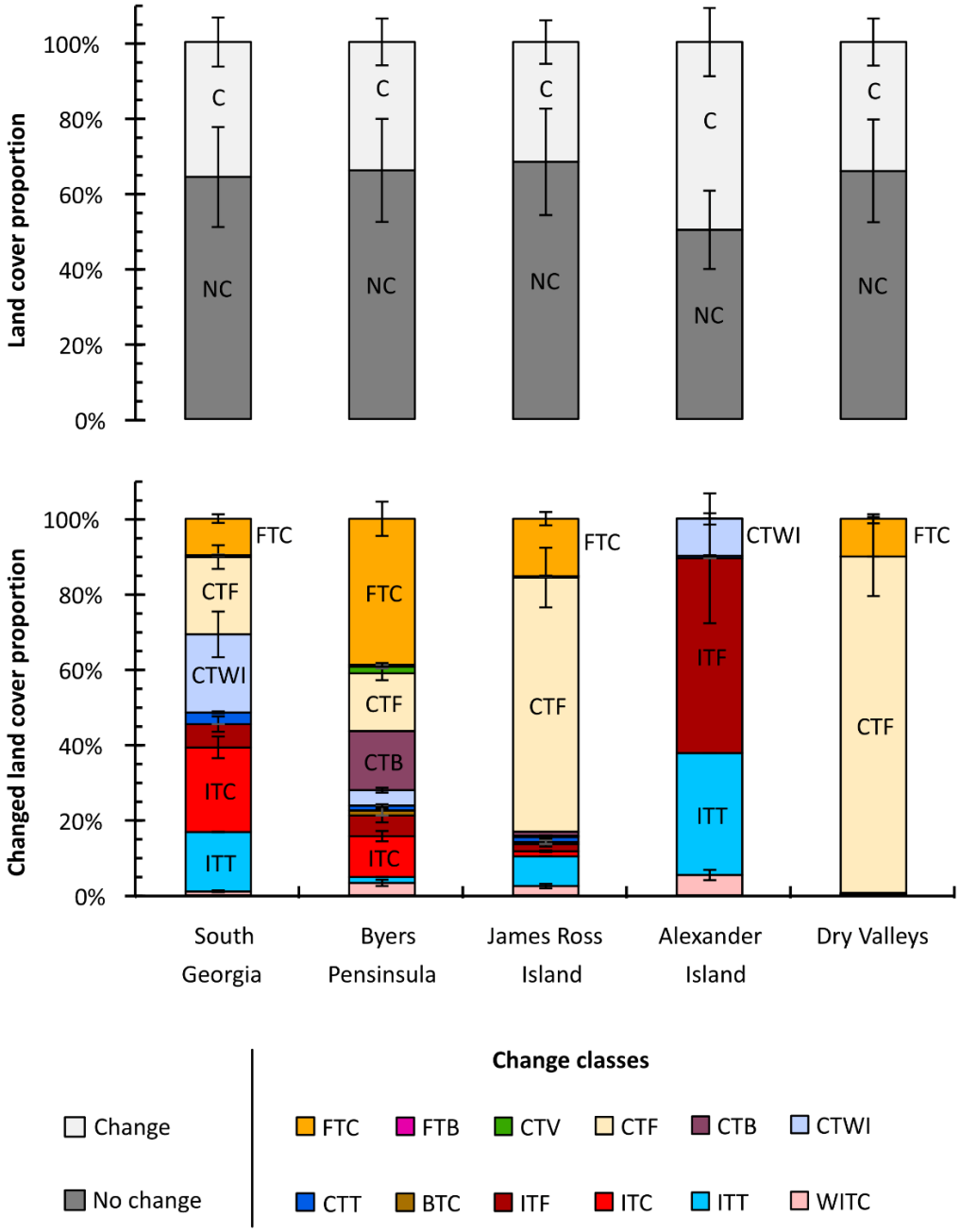

Figure 3.2: *The proportion of the proglacial landscape that has changed at each site analysed, and the make-up of those changed regions. See* ***Table 3.2*** *for list of abbreviations.*

3.3.2. Data accuracy

The resubstitution accuracy of the training data was 100.0 %, and the total validation accuracy was 80.1 %. This compares to 69 % for a similar study of land cover change conducted in Greenland (Grimes et al., 2024), and 96 % accuracy for a study conducted using CVA (Xu et al.,

2018). The latter of these studies achieved such high accuracy because it used a more accurate training dataset than that used in this chapter. The accuracy varies by class (**Table 3.4**), with the most accurate class being ITT and FTB, albeit from a low sample size. The least accurate class is the coarse/wet sediment to turbid water (CTT) class. However, as stated in section 3.2.2, it is also important to consider the geomorphological processes that the change classes represent. When classes that represent the same process as CTT (i.e. formation of a lake/formation of a wet area) are merged into a single class, the error reduces from 60.0 % to 5.9 % (**Table 3.4**).

Table 3.4: *Accuracy assessment of land cover change. % error denotes the proportion of pixels misclassified within that land class. Geomorphological process (GP error denotes the error of the geomorphological process represented by one or more change classes.*
*NB: * denotes that there are two possible ways in which classes can be represented as a GP: either as lake formation and slush-ice formation, or both could be represented as one lake formation class – this affects the resultant GP error, therefore two GP errors are displayed.*

Change Class	Geomorphological process (GP)	% error	GP % error	n
No change	No change	20.7	20.7	1563
Wet ice to coarse/wet sediment	Ice melt (land)	25.0	2.8	8
Ice to turbid water	Ice melt (water)	0.0	0.0	13
Ice to coarse/wet sediment	Ice melt (land)	12.7	2.8	79
Ice to fine & dry sediment	Ice melt (land)	33.3	2.8	21
Bedrock to coarse/wet sediment	Sediment deposition	6.7	6.7	15
Coarse/wet sediment to turbid water	Lake formation*	60.0	60.0/5.9	10
Coarse/wet sediment to wet ice	Slush-ice formation/ lake formation*	29.2	29.2/5.9	24
Coarse/wet sediment to bedrock	Erosion	32.3	21.6	127
Coarse/wet sediment to fine & dry sediment	Drying	15.3	15.3	98
Coarse/wet sediment to vegetation	Vegetation formation	30.8	30.8	13
Fine & dry sediment to bedrock	Erosion	0.0	21.6	1
Fine & dry sediment to coarse/wet sediment	Wetting	11.7	11.7	290

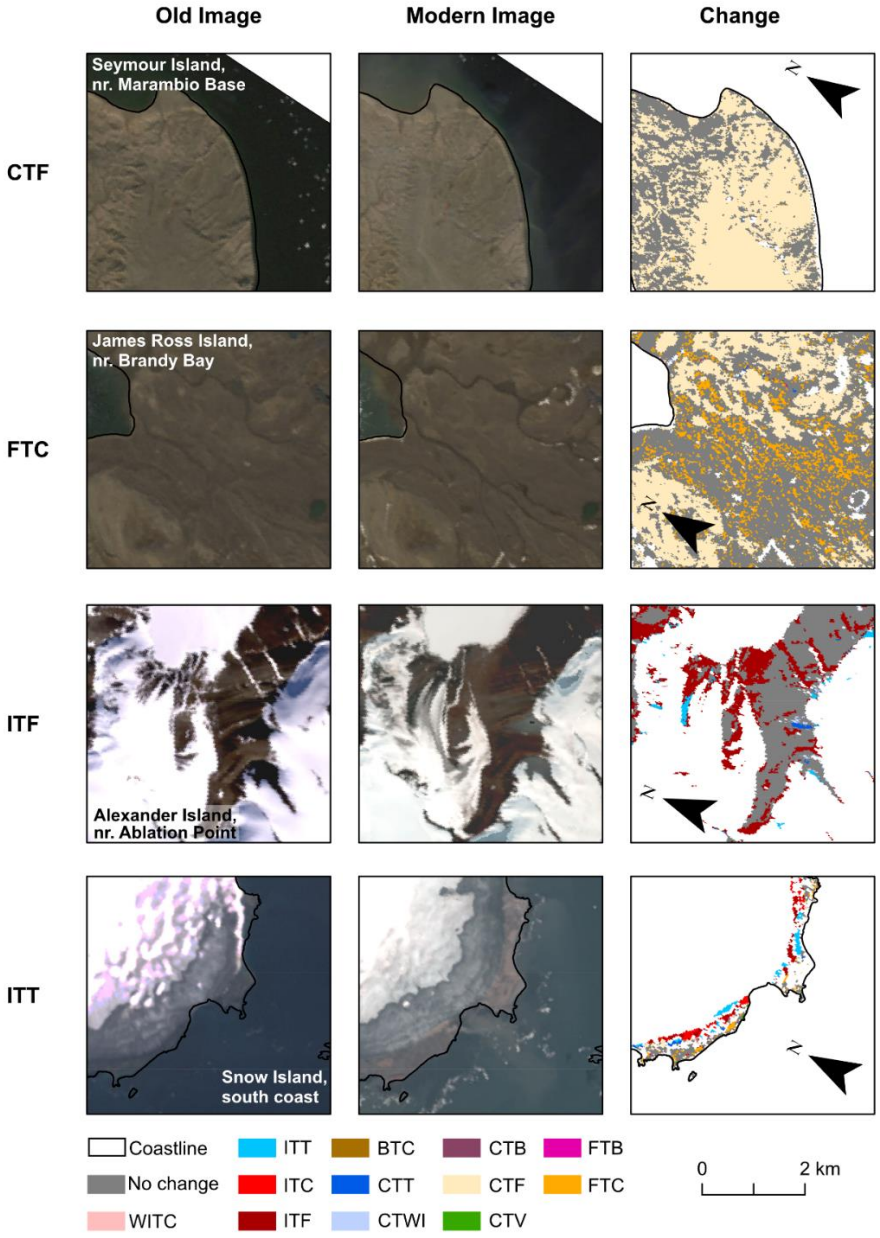

***Figure 3.3**: Examples of the four most frequently observed change classes, which describe 86 % of the change identified in the land cover data. The CTF example shows less active river channels in the modern image associated with drier sediments on Seymour Island. FTC shows the opposite, with more active river channels associated with wetter sediments on James Ross Island. The ITF example shows a reduction in the extent of glaciers and snow cover on Alexander Island, while the ITT example shows the development of proglacial lakes following glacier retreat on Snow Island in the South Shetland Islands. While these four panel sets are designed to highlight the four main change classes, all change classes can be seen within these panels.*

Changes in land cover can also be seen visually, which allows for a qualitative assessment of land cover change (**Figure 3.4**). The change detection is good at detecting phase changes, such as melting ice (ITF and ITT); in the case of Alexander Island, this highlights the exposure of new sediments, while on Snow Island (Byers Peninsula site) this highlights the formation of new proglacial lakes. More subtle changes in the flow of streams and changes in the moisture

content of soils can also be detected on James Ross Island (increased river activity, shown by FTC) and Seymour Island (James Ross Archipelago site) with reduced river activity and possible dust deposits.

Whilst efforts were made to minimise the differences in the time of year between the two sets of image mosaics, poor image availability meant image mosaics were sometimes acquired at slightly different times of the growing and hydrological season, or may be impacted by different weather events. This is a particularly important consideration given the short summer season in Antarctica and may mean that some of the land cover changes described are a product of the image acquisition dates, rather than a lasting change. However, steps were taken, such as ensuring there was water present in rivers and that lakes were unfrozen (particularly in more northern sites), to minimise these uncertainties and are also useful in improving the reliability of change detection in Antarctica and other regions where image availability is poor. Future studies should seek to ensure their images are acquired as close to those used in this study as possible.

3.4. Conclusions

This chapter has described land cover changes occurring during the 21st Century across five major proglacial regions of the Antarctic Peninsula Region, sub-Antarctic, and the McMurdo Dry Valleys. This change detection has been achieved using a CVA approach at an accuracy of 80.1 %. Through this analysis of land cover change, a latitudinal pattern in ice loss has been highlighted; the proportion of land cover change on South Georgia due to the loss of ice is two orders of magnitude greater than that in the Dry Valleys. Conversely, the opposite pattern is evident in the sediment class changes; this is possibly also influenced by an increase in vegetation coverage in more northerly sites. The extensive landscape change that has occurred on Alexander Island has also been highlighted, where 50 % of the proglacial coverage has changed this century, likely because of recent dramatic warming events around the George VI ice shelf. Overall, this dataset and analysis provides a first step in understanding the how Antarctica's important proglacial regions have changed, and provide an important first insight into how proglacial landscapes are evolving as a consequence of rising temperatures and glacier recession.

3.5 Data and code availability

Code: Christopher D Stringer. (2023). 21st century land cover change across the major proglacial regions of West Antarctica and the McMurdo Dry Valleys [Code]. (Version v1). Zenodo. https://doi.org/10.5281/zenodo.7991208

Data: Stringer, C. (2023). 21st century land cover change across the major proglacial regions of West Antarctica and the McMurdo Dry Valleys https://ramadda.data.bas.ac.uk/repository/entry/show?entryid=d6721952-a9ab-4021-adc6-1ccb4d52f1f9

4. Quantifying sediment sources, pathways, and controls on fluvial transport dynamics on James Ross Island, Antarctica

4.1. Introduction

Rivers are the primary transporter of sediment in proglacial regions (Overeem et al., 2017) and they are shaped by the interplay of glacial meltwater that erodes, transports, and deposits sediment, as well as hillslope activity that provides new sediment to the system during mass transport events (Carrivick and Heckmann, 2017; **Figure 1.2**). In a warming climate, both sets of processes result in greater sediment discharge, provided peak water (Huss and Hock, 2018) has not yet been reached (Ballantyne, 2008; Staines et al., 2015; Carrivick et al., 2018).

Permafrost underlies an extensive part of these proglacial regions, particularly in sub-polar environments, and permafrost-affected soils (active layer) can be an additional source of water and sediment when ground temperatures are above freezing; particularly in catchments with limited glacier cover (Humlum et al., 2003; Costa et al., 2018; Łepkowska and Stachnik, 2018).

Glacier recession and enlargement of proglacial regions affects the quantity, spatio-temporal pattern and composition of sediment discharged from Antarctica's rivers and hence the diversity of aquatic life present in its seas, lakes and rivers (Gonçalves et al., 2022), with potential implications for carbon sequestration (García-Rodríguez et al., 2021). Despite their importance, very few studies consider river transport dynamics in Antarctic rivers. Even fewer studies have explored the spatio-temporal variability in sediment delivery or compiled a comprehensive source-to-sink description of sediment transportation.

To address this, this chapter aims to take a holistic approach to consider sediment production and transportation in two largely deglaciated catchments on James Ross Island, from source to sink. The low areal coverage of glacier ice in these catchments is unusual in an Antarctic context and therefore provides an insight into what many other catchments may look like in the future as glaciers recede. Hydrological, sedimentological and geochemical measurements were taken whilst on fieldwork and have been analysed in the context of meteorological and active layer observations to investigate the: **i)** transport of water and sediment in two Antarctic catchments; **ii)** the source of sediments in the catchments.

4.1.2. General overview of rivers and study site

The catchments that have been studied in this chapter are the Bohemian Stream catchment and Algal Stream catchment, situated on the northern point of James Ross Island's Ulu Peninsula (**section 1.2.3, Figure 1.3**). They are situated close to the Johann Gregor Mendel Station (JGM) making them easily accessible for study (**Figure 4.1**).

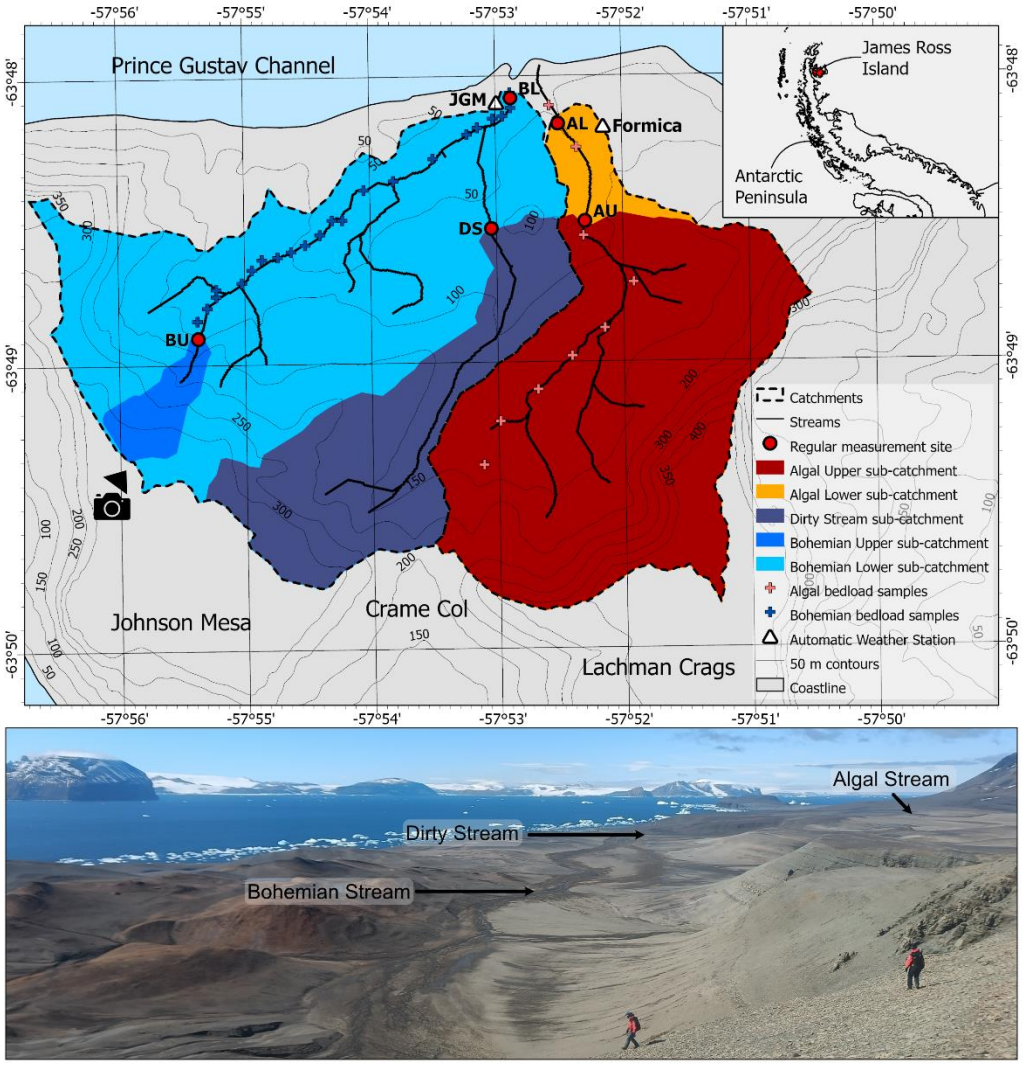

Figure 4.1: *Location of study sites on James Ross Island, Antarctic Peninsula. River channel and catchments were extracted using the flow accumulation and watershed tools in ArcGIS Pro using the REMA DSM (Howat et al., 2019); some very small channels are not delimited. Coastlines and map of Antarctica are from Gerrish et al. (2020), contours are from the Czech Geological Survey (2009). NB: JGM = Johann Gregor Mendel Station. Photo was taken by CS on the slopes of Johnson Mesa, as highlighted on the map, looking north-east. BL = Bohemian Lower (sub catchment = 6.7 km^2); BU = Bohemian Upper (sub catchment = 0.3 km^2); DS = Dirty Stream (sub catchment = 2.0 km^2); AL = Algal Lower (sub catchment = 4.5 km^2); AU = Algal Upper (sub catchment = 4.2 km^2).*

The Ulu Peninsula experienced a period of rapid ice-sheet surface lowering, coincident with the initiation of the Prince Gustav Ice Stream after ~18 ka and a transition from a thick cold-based ice sheet to a warm-based active deglaciation (Glasser et al., 2014), with the lower elevation areas becoming deglaciated ~12.9 ka (Nývlt et al., 2014). Throughout the late Holocene, several small glaciers re-advanced from cirques on the sides of mesas (Carrivick et al., 2012). Both river catchments sit within a crescent of uplands; to the east, this is Lachman Crags (408 m a.s.l.) and to the west, this is Johnson Mesa (323 m a.s.l), these two prominent

features meet at Crame Col to the south (178 m a.s.l.). The Bohemian Stream is a braided river that flows towards the east with its source in the upland region of Johnson Mesa (**Figure 4.1**). The Dirty Stream, flowing towards the north (**Figure 4.1**), is also an important water and sediment source (Sroková and Nývlt, 2021) to the Bohemian Stream's total sediment budget and is its largest tributary. The Algal Stream catchment is separated from the Bohemian Stream catchment by a small ridge that runs parallel to the Dirty Stream. The upper section of the main river channel mostly flows parallel to the Bohemian Stream, while the lower section bends to flow towards the north (**Figure 4.1**).

4.1.3. Geological setting

Both catchments predominantly lie on Cretaceous marine strata (**Figure 4.2**) composed of mudstones, sandstones and conglomerates (Ineson et al., 1986; Mlčoch et al., 2020). The Cretaceous sediments in the Bohemian catchment are composed of more conglomerate and coarse-grained sandstones in comparison to the finer-grained sandstones and mudstones

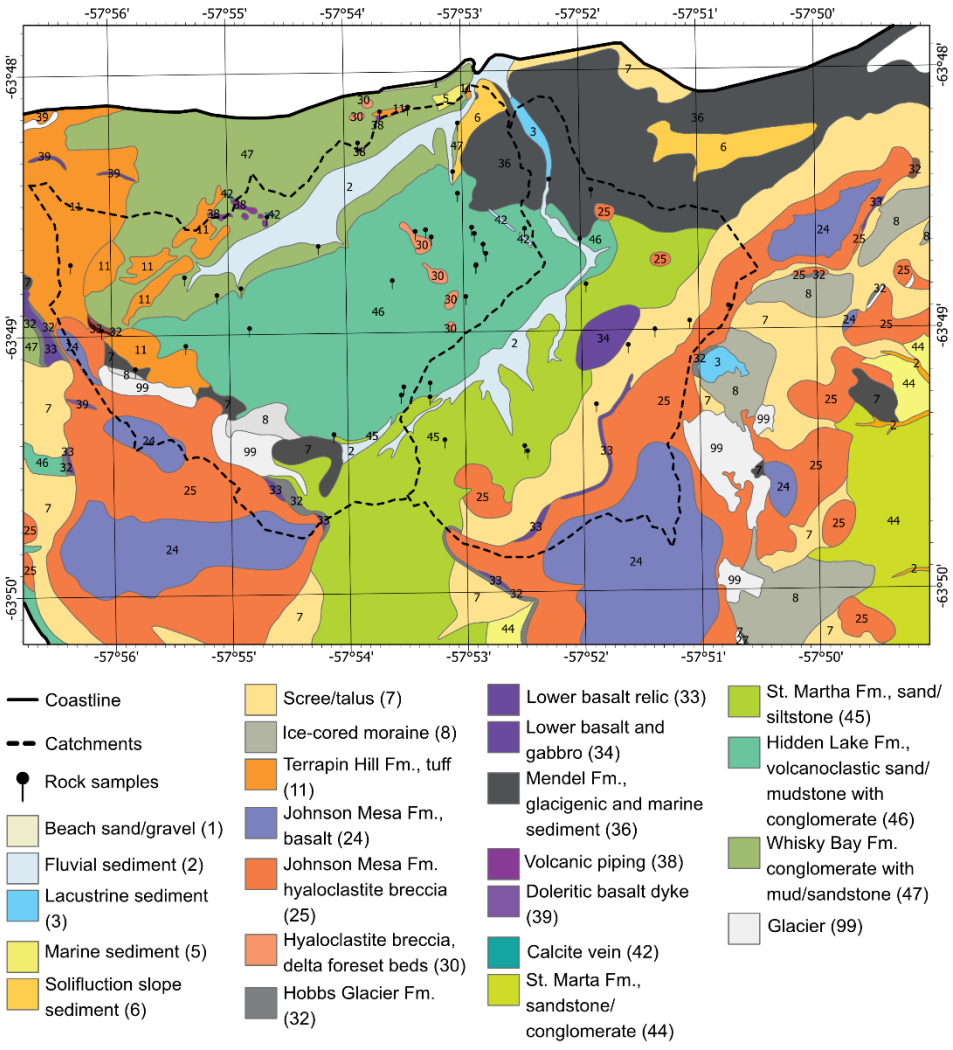

Figure 4.2: *Geological map of the Algal and Bohemian Stream catchments, based on Czech Geological Survey map* (Mlčoch et al., 2020)*. The location of rock samples collected is also displayed.*

within the Algal catchment. Parts of both catchments are underlain by Neogene igneous rocks, which are primarily hyaloclastite breccias, tuffs, and subaerial basalts (Mlčoch et al., 2020; Smellie et al., 2008). While the upland regions of both catchments contain siliciclastic and volcanoclastic sediments (Košler et al., 2009), they are finer-grained in the Algal catchment (Nehyba and Nývlt, 2014; Mlčoch et al., 2020). The lower reaches of both catchments are composed of clast-rich diamictites of Miocene to Pliocene age (Nývlt et al., 2011; Davies et al., 2013).

4.2. Methodology

4.2.1. Stream monitoring

River water discharge and suspended sediment load were measured at five "regular measurement sites" (**Figure 4.1**). These five sites were chosen to capture the water and sediment movement of the upper and lower sections of the Bohemian Stream and the Algal Stream, as well as the influence of a major tributary to the Bohemian Stream; the Dirty Stream. The lower measurement sites (Bohemian Lower: BL, and Algal Lower: AL) were placed at stable cross sections previously used for river measurements by Kavan et al. (2017) and Kavan (2021). New sampling sites were created in the upper reaches of the Algal Stream (Algal Upper: AU), the Bohemian Stream (Bohemian Upper: BU) and close to the confluence of the Bohemian and Dirty Streams (Dirty Stream: DS). The Dirty Stream site was chosen as the point closest to the Bohemian Stream confluence with a stable cross section. The Algal Upper and Bohemian Upper sites represent the point furthest upstream with a stable cross section. At each of these sites, river water discharge and suspended sediment concentration (SSC) were measured at six-hour intervals for 24 hours every two weeks for the duration of the expedition (8 weeks total study time). This resulted in 20 measurements from each of the sites over the course of the season, except for the Bohemian Upper site, which was frozen on two of the visits. Additionally, automatic discharge measurements were taken every 10 minutes at the AL and BL catchment outlet sites (at the AL and BL regular measurement sites, **Figure 4.1**).

A SonTek FlowTracker 2 handheld Acoustic Doppler Velocimeter was used to measure the discharge of the streams at each of the sites. The width of the active stream channel for each measurement was recorded, alongside the depth and velocity of the streams, approximately every 200 mm, though this varied depending on the stream flow and channel width. This equipment also generated an error assessment of each discharge measurement, which is a function of the variability in velocity and pressure in the equipment's readings. The median uncertainty was 0.001 $m^3 s^{-1}$.

Immediately after measuring discharge, a grab sample of water was taken from the centre of the channel in a pre-weighed 220 ml bottle to measure SSC. These samples were then weighed in the laboratory of JGM to calculate the total mass of water and sediment in each of the bottles at a precision of 0.01 g. From this, the volume of water in each bottle could be calculated. Using pre-weighed Whatman Grade 6 filters (3 µm), a vacuum was used to filter then samples, which were then dried in a SNOL 120/300 LSN11 drier at 80 ^{o}C for two hours. The dried sample was then weighed at a precision of 0.0001 g the concentration of suspended sediment was calculated. Median SSC uncertainty was 55 mg l^{-1}. Since many of the uncertainties are fixed, this means that some small SSC measurements are proportionally associated with very high uncertainties.

To derive a continuous record of catchment outlet river water discharge, hydrostatic pressure was continuously measured using a sensor DipperLog F100/M30 (accuracy of ± 0.05%; Heron Instruments) in a stable profile at the AL (n = 8) and BL (n = 10) regular measurement sites (Kavan et al., 2017; Kavan, 2021). These hydrostatic measurements were adjusted for local air pressure (TMAG 518 N4H barometer (accuracy ± 0.5 hPa; CRESSTO, CZ) to derive water depth and from that computed river water discharge using a stage-discharge rating curve (**Figure 4.3A,B**) constructed using manual river water discharge measurements that were independently collected over the course of the season using a SonTek FlowTracker. Using a power law relationship (Kavan et al., 2017; Kavan, 2021), the relationship between water pressure and discharge had a Root Mean Squared Error (RMSE) of 0.04 m^3 s^{-1} for AL (**Figure 4.3A**) and 0.03 m^3 s^{-1} for BL (**Figure 4.3B**), equivalent to a mean uncertainty of 21 % and 15 % respectively. Discharge measurements used in these calculations were associated with an uncertainty of 14.8 % (BL) and 11.7 % (AL), respectively.

A continuous record of suspended sediment concentration was derived from a sediment rating curve (Kavan et al., 2017; Kavan, 2021; **Figure 4.3C,D**) that was constructed using the derived discharge values and the SSC samples that were manually collected (see section 2.1.2). For the AL site (n = 18), RMSE = 590 mg l^{-1}, and for the BL (n = 13), RMSE = 820 mg l^{-1}. This is equivalent to a mean uncertainty of 56 % and 51 % respectively.

Herein, continuous measurements are described by “SSC”, but where inter-site analysis is presented, the term “sediment load” is used to account for differences in catchment area. Sediment load is defined as the mass of suspended sediment transported through a point in a given period, per square kilometre of its catchment area and it was calculated by calculating the sediment transported at a point per minute and dividing it by the catchment area; the catchment area is derived using the sub-catchments in **Figure 4.1** (BL = 6.7 km^2; BU = 0.3 km^2; DS = 2.0 km^2; AL = 4.5 km^2; AU = Algal Upper = 4.2 km^2). These sub-catchments are the up-

catchment area of each regular measurement point. This was done to ensure that any inter-site comparison is adjusted for differences in the catchment area. Suspended sediment processing was associated with an uncertainty of 4.2 % (BL) and 2.3 % (AL).

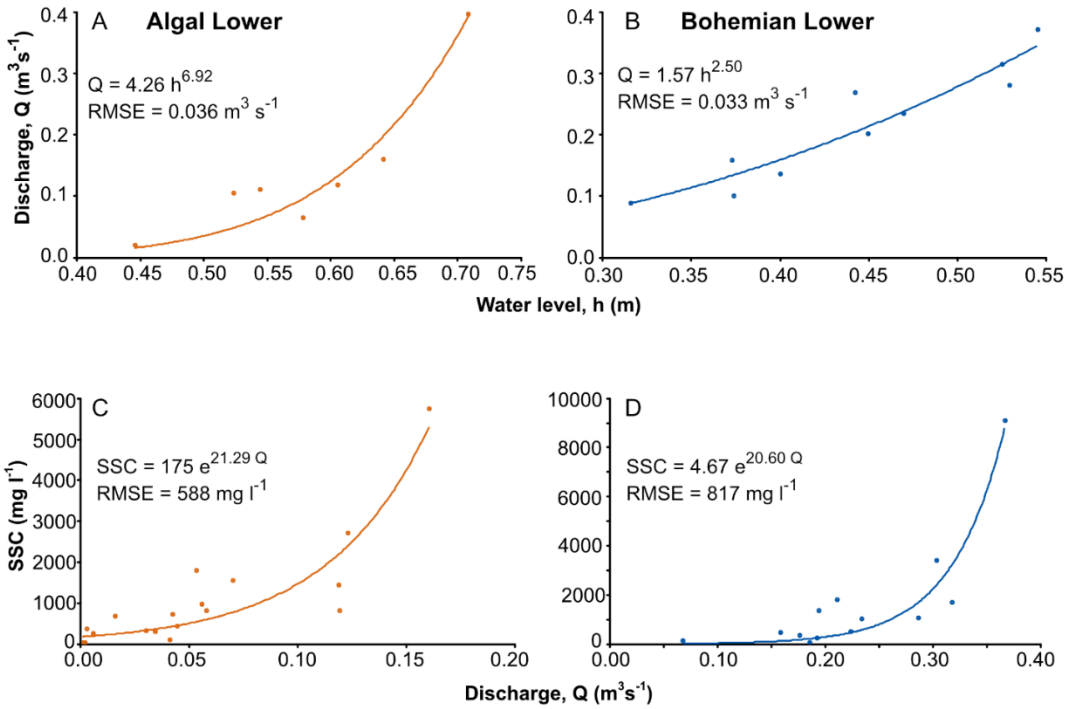

Figure 4.3: *Rating curves showing:* ***A)*** *stage-discharge relationship for the Algal Lower;* ***B)*** *stage-discharge relationship for the Bohemian Lower;* ***C)*** *Discharge and suspended sediment concentration (SSC) relationship for the Algal Lower;* ***D)*** *Discharge and suspended sediment concentration relationship for the Bohemian Lower*

4.2.2. Sampling

Samples of bed material with clasts up to gravel size were taken from the centre of the channel in the Bohemian Stream and the Algal Stream (**Figure 4.1**), for geochemical analysis. These were collected at ~ 100 m intervals (21 samples) in the Bohemian Stream. For logistical reasons, the sampling interval was set at ~300 m intervals along the Algal Stream (9 samples). Rock samples were sampled from each lithological unit in both catchments (Bohemian catchment: 28, Algal catchment: 15), as informed by the geological map of the region (Mlčoch et al., 2020), consistent with the strategy used in previous studies in this region (Kavan et al., 2017; Sroková and Nývlt, 2021). Samples largely constituted solid samples of bedrock, but in some cases were samples of surface sediments (i.e. regolith). Samples taken in the field were interpreted and their composition confirmed, to ensure there were no errors in the geological map (**Table 4.1**).

Table 4.1: *Field description of rock samples taken, with interpretation and related geological unit. Sample number runs sequentially. "(s)" denotes a sample of superficial sediments. BC = Bohemian Catchment; AC = Algal Catchment.*

Sample	***Field description***	***Interpretation***	***Geological unit (Mlčoch et al., 2020)***
G1-BC	Black, poorly sorted with lamination. Very fissile sandstone.	Sandstone	Hidden Lake Formation
G2-BC	Lighter brown material underlying black sandstone, appears fine grained with coarser (pebble to gravel) clasts, possible lamination.	Sandstone	Hidden Lake Formation
G3-BC	Clean sandstone (i.e. nothing superficial on it) samples with predominantly fine grains and clasts of very coarse sand and pebbles	Sandstone	Hidden Lake Formation
G4-BC	Found at a tributary to the Dirty Stream, where clasts were falling into the stream. Mudstone, with fissile grains. When chewed, these grains could be felt against the teeth, indicating they are silt sized. Fine sand also present. Fissile.	Silt/Mudstone	Hidden Lake Formation
G5-BC (s)	Superficial deposit near the tributary.	Surface sediment (unconsolidated)	Above Hidden Lake Formation
G6-BC	Medium grained sandstone.	Sandstone	Hidden Lake Formation
G7-BC	Big cone of volcanic breccia exposed. Large clasts of black rocks containing small, white, minerals. Otherwise fine-grained (but not glass). Andesite.	Hyaloclastite breccia	Hyaloclastite breccia (undifferentiated)
G8-Bca (s)	Superficial deposit near snow melt where there is drainage, although most of the water appears to evaporate before reaching the Bohemian	Surface sediment (unconsolidated)	Above Whisky Bay Formation

G8-BCb (s)	Superficial deposit near snow melt where there is drainage, although most of the water appears to evaporate/infiltrate before reaching the Bohemian	Surface sediment (unconsolidated)	Above Whisky Bay Formation
G9-BC (s)	Superficial deposit with large clasts of porous and crystalline rock. Slight red colour but mostly black/grey – basalt? Fine material sampled	Surface sediment (unconsolidated)	Above volcanic piping
G10-BC (s)	Possible lateral moraine, clasts do not contain pores.	Surface sediment (unconsolidated)	Above volcanic piping
G11-BC (s)	Distinct change in the colour of the drift; from brown/grey to red. Suggests, to me, a change in geochemistry. Bowl shape structure seen, I assume periglacial but unsure of its formation	Surface sediment (unconsolidated)	Above volcanic piping
G12-BC (s)	Outcrop of fine grained diamict with very few clasts, clay to fine sand sized grain. Located in a small tributary.	Surface sediment (unconsolidated)	Above Whisky Bay Formation
G13-BC (s)	Significant runoff on south slopes, fine sediment samples	Surface sediment (unconsolidated)	Above Hidden Lake Formation
G14_BC	Coarse grained, well-lithified sandstone sample taken. (in tributary)	Sandstone	Whisky Bay Formation
G15-BC (s)	Sediment from runoff channel	Surface sediment (unconsolidated)	Above Whisky Bay Formation
G16-BC (s)	Sediment from runoff channel	Surface sediment (unconsolidated)	Above Hidden Lake Formation
G17-BC (s)	Black volcanic rocks consistently seen in the dirty stream appear to be proglacial deposits from Johnson Mesa.	Surface sediment (unconsolidated)	Scree/talus
G18-BC	Black/grey fissile sandstone	Sandstone	Hidden Lake Formation
G19-BC	Yellow/brown sedimentary rock. Mud to v fine sand, some red colouring. Slightly fissile.	Mudstone	Hidden Lake Formation
G20-BC	Grey-yellow sedimentary rock from outcrop	Sandstone	Hidden Lake Formation

G21-BC	White-grey sandstone	Sandstone	Hidden Lake Formation
G22-BC	Red-grey sandstone	Sandstone	Hidden Lake Formation
G23-BC	Cobble clast dominated diamict	Conglomerate	Hidden Lake Formation
G24-BC	Very coarse sandstone/gritstone, light grey with some pebble clasts	Sandstone	Hidden Lake Formation
G25-BC	Crystalline rock with some clasts, black, no obvious crystals	Basalt	Terrapin Hill Formation
G26-BC	Sample from the moraine that dams the lakes on Johnson Mesa	Surface sediment (unconsolidated)	Ice-cored moraine
G27-BC	Red clastic with black volcanic clasts: volcanoclastic	Hyaloclastite breccia	Terrapin Hill Formation
G28-BC (s)	Block material – basalt – near lakes on JM	Surface sediment (unconsolidated)	Johnson Mesa Formation
G29-AC*	Breccia with dark clasts	hyaloclastite breccia	Johnson Mesa Formation
G30-AC	Dark breccia	hyaloclastite breccia	Scree/talus - related to JMF
G31-AC (s)	Black-purple scree below Lachman Crag	Porphyritic basalt	Scree/talus, related to lower basalt relic
G32-AC(S)	Waterfall comes down from Lachman Crag and goes underground beneath surface sediment	Surface sediment (unconsolidated)	Above scree talus
G33-AC	Fine grained crystalline rock in a linear formation below LC. Black with some shiny, white and green crystals – quartz, feldspar and olivine – basaltic dyke.	Basalt	Scree/talus, related to lower basalt relic
G34-AC	Thinly laminated, white, fine grained sedimen7	Mudstone	St Martha Formation
G35-AC	Mineral samples taken. Cubic and white crystals that appear to be calcite. One is more orangey. Fizz on contact with HCl	Calcite	Calcite veins
G36-AC	Outcrop of fine sediments with angular pebble clasts	Conglomerate	Hidden Lake Formation
G37-AC	Finely laminated grey sediments. Clay/silt sized and very fissile	Mudstone	St Martha Formation
G38-AC(S)	Mud with some large (cobble to boulder) clasts, signs of bank collapse	Surface sediment (unconsolidated)	Above St Martha Formation
G39-AC	Outcrop of hyaloclastite breccia	hyaloclastite breccia	Hyaloclastite breccia within St Martha Formation
G40-AC (s)	Cut through of diamict in runoff channel	Surface sediment (unconsolidated)	Fluvial sediment

G41-AC (s)	Sediments above snow cave	Surface sediment (unconsolidated)	Fluvial sediment
G42-AC	Medium-grained crystalline rock in stream with black, green, and white minerals present	Microgabbro	Related to Lower Basalt and gabbro
G43-AC(S)	Sample of superficial sediment	Surface sediment (unconsolidated)	Above Mendel Formation

4.2.3. Meteorological observations

Air temperature and precipitation data was measured at the automatic weather station located near JGM. Air temperature was measured using a Pt100/A resistance thermometer (accuracy of ± 0.15 °C) with a built-in EMS33H probe (EMS Brno, Czech Republic) installed at 2 m above the ground in a multi-plate radiation screen. Ground-based measurement of precipitation was carried out using a Thies laser precipitation monitor (Adolf Thies GmbH & Co., Germany) enabling both quantitative precipitation estimation (rain/snow rates and totals) and the detection of different types, i.e. drizzle, rain, hail, snow, and sleet. For the analysis, instantaneous 30-min and mean daily air temperatures were used, while daily totals and prevailing types of precipitation were calculated from 1-min observations.

4.2.4. Active layer measurements

Ground thermal regime was measured at the JGM and Formica meteorological stations, which are situated within the Bohemian Stream catchment and Algal Stream catchment, respectively (**Figure 4.1**). At both sites, the ground temperature measurements were conducted in a 2 m deep profile with measurements collected at selected depths (0.05, 0.5, 0.75, 1 m) using resistance thermometer detectors (Pt100/8, accuracy ± 0.15 °C), which measured and stored data every 30 minutes. For this analysis, daily means of near-surface ground temperature measured at a depth of 0.05 m were used. The data from deeper parts of the profile (0.50 m, 0.75 m, 1 m) were used for interpolation of the daily position of the 0 °C isotherm (e.g. Hrbáček et al., 2021) and daily thaw rate was defined as the difference in thaw depth between two consecutive days.

4.2.5. Provenance of bed material

As described, bed material was sieved to collect the < 2mm fraction. This **a)** improved the ease with which they could be manually crushed with an agate pestle and mortar, and; **b)** ensured the most mobile fraction of sediments were sampled. Fissile rock samples were crushed with an agate pestle and mortar. Agate was used as it is a resistant mineral (quartz, Mohs Hardness = 7), that is harder than most minerals. A masonry drill bit with a high Moh's hardness

(composition was probably tungsten carbide, with a Mohs Hardness of 9) was used to crush more resistant rocks samples, and the dust produced was collected for analysis. Crushing samples reduced the impact of grain size, a major component of uncertainty in sediment provenance studies, and ensured they were homogenised (Russell et al., 2019; Collins et al., 2020).

A complete analysis of provenance can be achieved by using both XRF and infrared analysis of chemical and mineralogical characteristics, respectively (Russell et al., 2019). X-ray fluorescence (XRF) was measured with a ThermoFisher Scientific Niton XL5 Plus Handheld XRF Analyzer using the mining setting and took three 120-second measurements of each bed material and rock sample. Suspended sediment samples were measured for 160 seconds, as smaller samples require a longer measuring period to ensure as many present elements as possible can be detected (Boyle, 2000; Huang et al., 2016). To calibrate the equipment and validate the readings, a standard sample was measured on any day a measurement was taken.

A Spectral Evolution PSR+ 3500 spectrometer with a fibre optic probe was used to measure infrared reflectance. Each sample was measured three times and a white reflectance standard was measured before every measurement to calibrate the equipment and validate its readings.

All bed material and rock samples were measured using both techniques. However, most of the suspended sediment samples were too small to measure, and so only 15 (5 Algal Stream catchment, 10 Bohemian Stream catchment) of these samples were measured.

Whilst many recent studies have made use of sediment un-mixing models, there are challenges associated with using these on relatively small datasets, which can lead to overfitting from the model (Lipp et al., 2021; Zhao et al., 2022). Recent studies (e.g. Shahrestani et al., 2020) have shown that the areal coverage of lithological units is a good indicator of source material. Therefore, a sub-catchment for the location of each bed material sample was calculated using the hydrology tools in ArcGIS Pro. The proportion of each lithological unit within these sub-catchments was calculated by spatially querying the most recent and digitally available geological map of the region (Mlčoch et al., 2020, **Figure 4.2**). This gave a list of potential source rocks for each sediment sample; showing: **a)** which units are up-stream of the sample, and; **b)** the potential of different units to supply sediment stream.

The infrared spectra were prepared for analysis by taking their first derivative, which has been shown to reduce the impact of unwanted physical information such as grain size on spectra (Russell et al., 2019). This was done using SpectraGryph 1.2 and a Principal Component Analysis was conducted in the Past 4.07b statistical software for each bed material sample.

From this, it was possible to produce scatter plots between the first three component scores (derived from the PCA correlation matrix) of each bed material sample and the proportion of each geological unit within its sub-catchment. The relationship between these two variables was investigated and a Spearman's Rank correlation analysis was conducted on any relationship showing an $R^2 > 0.5$. Any lithology showing a significant correlation ($p < 0.05$) was then considered as an important source rock for stream bed material. The justification for this correlation analysis was that if a unit is deemed to be an important source rock, then its contribution to sediment composition should increase in line with its proportion of the catchment area. This analysis of infrared was complimented by looking at the similarity between the chemical composition of sediment samples and important source rocks.

4.3. Results

4.3.1. Suspended sediment export and variability

The river water discharge (**Figure 4.4A**) and SSC (**Figure 4.4B**) from the Bohemian catchment at the BL site displayed three broad peaks over the course of the study period. The first of these occurred between 21 January and 24 January, with a maximum discharge of 0.51 m^3s^{-1} and a corresponding SSC of 51,837 mgl^{-1} at 17:54 (UCT) on 22 January. In the field it was observed that this maximum coincided with a large snowmelt event, during which the snow that fell on 10 January and 11 January (totalling 36 mm w.e. at JGM, **Figure 4.4C**) melted in the upland regions of the catchment, as both air and ground temperature increased (**Figure 4.4C, D**). Discharge and SSC peaked again between 7 February and 11 February (**Figure 4.4A, B**), to a maximum discharge of 0.57 m^3s^{-1} and SSC of 122,980 mgl^{-1} at 01:04 on 8 February. This was coincident with rising air and ground temperatures (**Figure 4.4C, D**), air temperature peaked on 7 February with a mean temperature of 7.5 ^oC (rising from 4.0 ^oC on the preceding day), and ground temperature increased to 8.0 ^oC on 8 February. A third peak in discharge and SSC (**Figure 4.4A, B**) occurred between 19 February and 23 February (maximum 0.37 m^3s^{-1} at 12:14 on 20 February, and an SSC = 6334 mgl^{-1}), although this broad peak was preceded by two short-duration peaks in discharge (0.51 m^3s^{-1} and 0.55 m^3s^{-1}) and SSC (49,234 mgl^{-1} and 98,143 mgl^{-1}). These two short-duration peaks are coincident with snowfall (**Figure 4.4C**). The broad peaks correspond with rising air and ground temperatures following a snowfall in the preceding days, with air temperatures rising from 0.1 ^oC on 20 February to 4.6 ^oC on 21/2, and ground temperature rising from 3.1 ^oC to 4.7 ^oC. Discharge at the BL site has a positive correlation with air temperature ($r = 0.47$, $p > 0.01$, Spearman's Rank) and ground temperature ($r = 0.53$, $p > 0.01$), as well as a weak negative correlation with precipitation ($r = -0.33$, $p = 0.02$) (**Figure 4.4D**). There is no clear relationship between active layer thaw rate and discharge in

the Bohemian Catchment (r = 0.08, p = 0.59). According to cross-correlation analysis, there is a possible correlation on a lag time of 7 days, though this is a weak negative relationship.

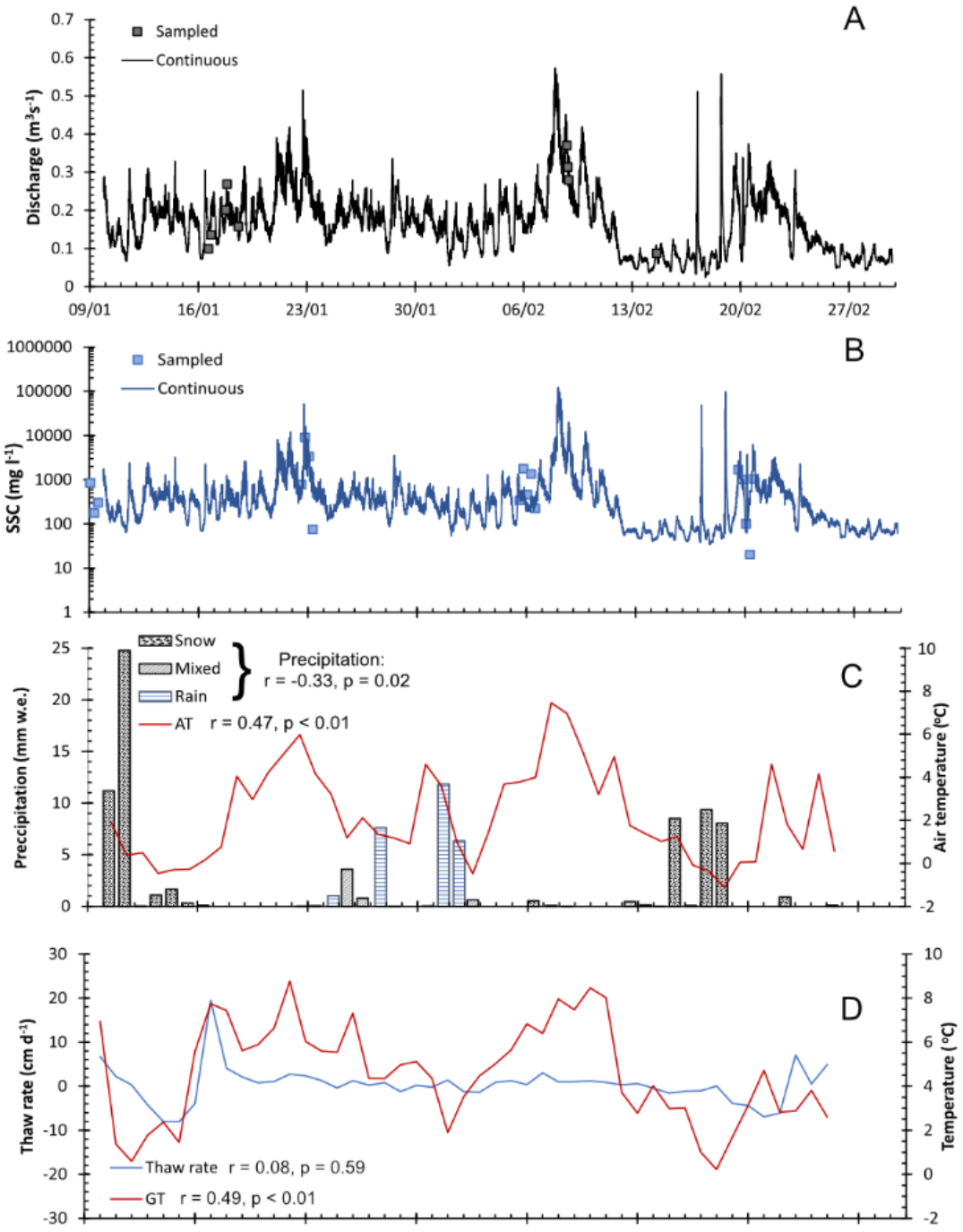

Figure 4.4: *Data from the Bohemian Lower site, describing:* ***A)*** *Discharge;* ***B)*** *Suspended sediment concentration;* ***C)*** *Precipitation and air temperature (JGM);* ***D)*** *Thaw rate (JGM) and ground temperature (JGM). Correlation is between the environmental factor and discharge, with r = correlation coefficient and p = significance.*

There were two major peaks in river water discharge and SSC from the Algal Catchment at the AL site (**Figure 4.5A, B**), between 16/01 and 24/01. The rising limb of the first peak in the Algal Stream occurred earlier in the Algal Stream than in the Bohemian Stream. During this period, a

maximum discharge of 0.66 m^3s^{-1} and SSC of 122,270 mgl^{-1} was reached at 20:16 on 17 January. This maximum discharge was coincident with an increase in thaw rate (**Figure 4.5D**), which peaked at a value of 25.7 cmd^{-1} (i.e. the active layer thawed and became thicker), and an increase in air temperature (to 4.0 °C), on 18 January. A second peak occurred later in the season, between 18 February and 23 February, with a maximum water discharge of 0.33 m^3s^{-1} at 20:26 and SSC of 31,480 mgl^{-1} on 21 February. This second peak largely coincided with an increase in discharge in the Bohemian catchment and is similarly coincident with rising temperatures following a snowfall event (**Figure 4.5C**). Unlike the Bohemian catchment, discharge in the Algal Stream shows no clear correlation with any environmental factor, other than precipitation. There is an insignificant, slight positive relationship with air temperature ($r = 0.24$, $p = 0.11$), and a negative relationship with precipitation ($r = -0.43$, $p = 0.01$). There is no correlation between thaw rate and discharge ($r = 0.03$, $p = 0.80$), though an increase in thaw rate does coincide with a large discharge between 16 February and 24 February. Similar to the Bohemian Catchment, there is a possible lag time of 5 to 6 days, though this is a weak negative relationship. The negative relationship between precipitation and discharge in both catchments is likely because the primary form of precipitation is snowfall, and there is typically a lag time of several days between peak snowfall and peak discharge as this snow melts, as well as precipitation typically coincides with lower air temperature.

Over the course of the study period, suspended sediment was exported from the Bohemian Stream at an average rate of 235 t $month^{-1}$ and the Algal Stream at 236 t $month^{-1}$. For the 50 day study period, and with a calculated area of 6.7 km^2 for the Bohemian Stream catchment and 4.5 km^2 for the Algal Stream catchment, this gives an estimated suspended sediment load of 1.18 ± 0.63 t $km^{-2}\,d^{-1}$ and 1.73 ± 1.02 t $km^{-2}\,d^{-1}$.

Daily peak air temperatures were typically recorded at ~ 16:00 UTC and this coincides with peak sediment load across all sites (**Figure 4.5**). On 22-23 January, the highest mean daily sediment load values across all three Bohemian catchment sites (BL = 14,039 kg $km^{-2}\,d^{-1}$, BU = 545,723 kg $km^{-2}\,d^{-1}$, DS = 19,083 kg $km^{-2}\,d^{-1}$), whereas the peak mean sediment load of the Algal catchment (AL = 17,558 kg $km^{-2}\,d^{-1}$, AU = 11,465 kg $km^{-2}\,d^{-1}$) fell on 8-9 January (**Figure 4.5**). The final measurement date (19-20 February) saw particularly low specific sediment load values across both catchments, with the minimum individual sediment load for the entire measurement period being measured on this day (AL = 1.61 x 10^{-4} kg $km^{-2}\,min^{-1}$, AU = 0.00 kg $km^{-2}\,min^{-1}$, BL = 3.68 x 10^{-5} kg $km^{-2}\,min^{-1}$, DS = 9.01 x 10^{-4} kg $km^{-2}\,min^{-1}$). This coincided with sub-zero air temperatures and some parts of the stream (notably AU) being partially frozen.

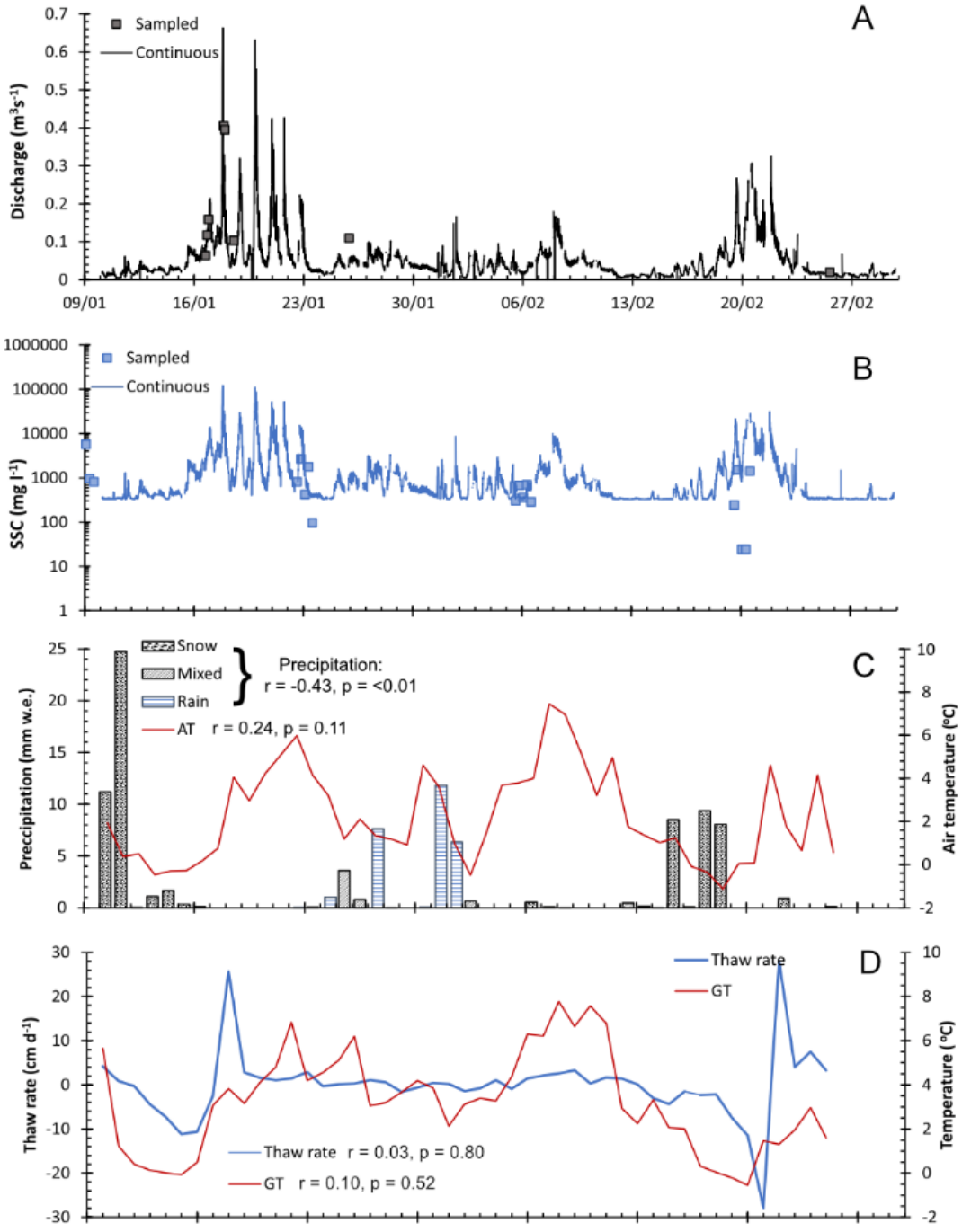

Figure 4.5: *Data from the Algal Lower site, describing:* ***A)*** *Discharge (collected every 10 min);* ***B)*** *Suspended sediment concentration (calculated by rating curve from discharge);* ***C)*** *Precipitation and air temperature (JGM);* ***D)*** *Thaw rate (JGM) and ground temperature (JGM). NB: Correlation is between the environmental factor and discharge with r = correlation coefficient and p = significance.*

Higher sediment loads were typically measured at the Bohemian catchment sites (**Figure 4.6**), especially at the lower sites (median values for the entire measurement period were: AL = 0.51 kg km^{-2} min^{-1}, AU = 0.37 kg km^{-2} min^{-1}, BL = 0.66 kg km^{-2} min^{-1}, DS = 0.45 kg km^{-2} min^{-1}, BU = 0.04 kg km^{-2} min^{-1}) with the notable exception of the 8-9 January period, when Algal catchment measurements were highest (median values for this day AL = 4.41 kg km^{-2} min^{-1}, AU = kg km^{-2}

min^{-1}, BL = 0.66 kg/min/km^2, DS = 1.25 kg km^{-2} min^{-1}, BU = 0.00 kg km^{-2} min^{-1}). In both catchments, the lower sites have the largest sediment loads, with the Dirty Stream appearing to be a major contributor of sediment to the Bohemian Stream. It should be noted that there are times in both catchments when the specific sediment load is higher in the upper parts/tributaries than in the outflow. The median sediment load uncertainty was 0.07 kg km^{-2} min^{-1}. Most of the errors were fixed, relating to the instrument and DEM precision.

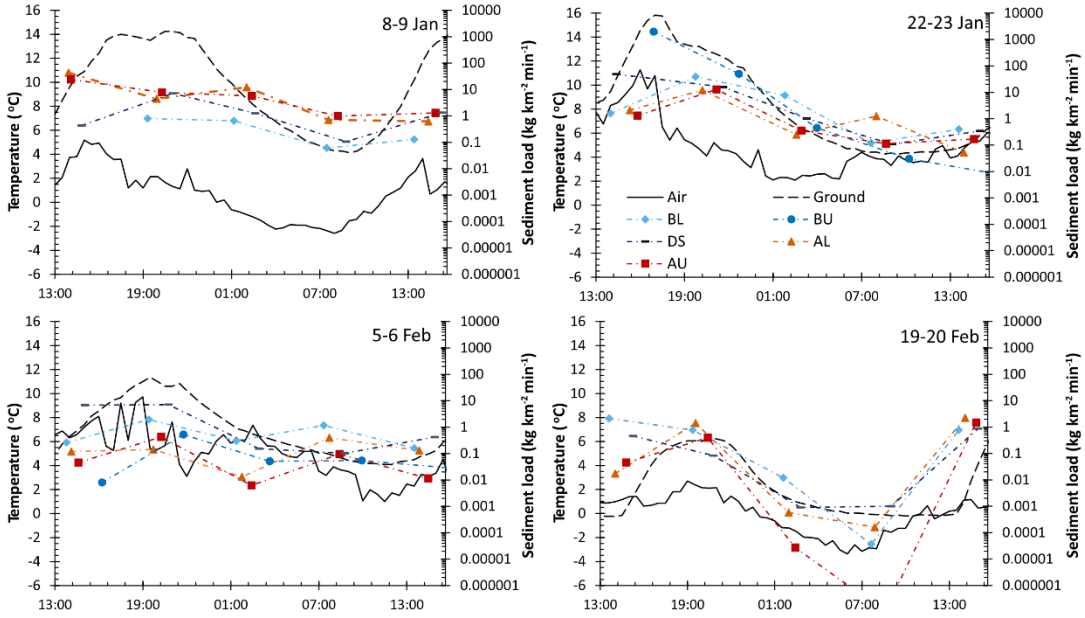

Figure 4.6: *Specific sediment load measurements from the regular measurement sites for each 24h measurement period. Plots of air and ground temperature (5 cm depth) collected from the Mendel weather station (10m a.s.l) are also presented. NB: BL = Bohemian Lower; BU = Bohemian Upper DS = Dirty Stream; AL = Algal Lower; AU = Algal Upper. All times are in UTC.*

4.3.2. Provenance of bed material

Possible sources of the Bohemian Stream's bed material are marine sediment (Holocene age), solifluction slope sediments, hyaloclastite breccia, Mendel Fm. (glacigenic, glaciomarine, and marine sediments), St. Marta Fm. (sandstone) and Whisky Bay Fm. (sandstone, conglomerate) (**Figure 4.2, 4.7A**). All lithologies present in the geological map (**Figure 4.2**, Mlčoch et al. (2020)) have been included in the analysis, including soils and drift. The coverage of each lithology changes within the sub-catchments, generally with igneous units becoming less important and sedimentary units becoming more important with distance downstream (**Figure 4.7B**).

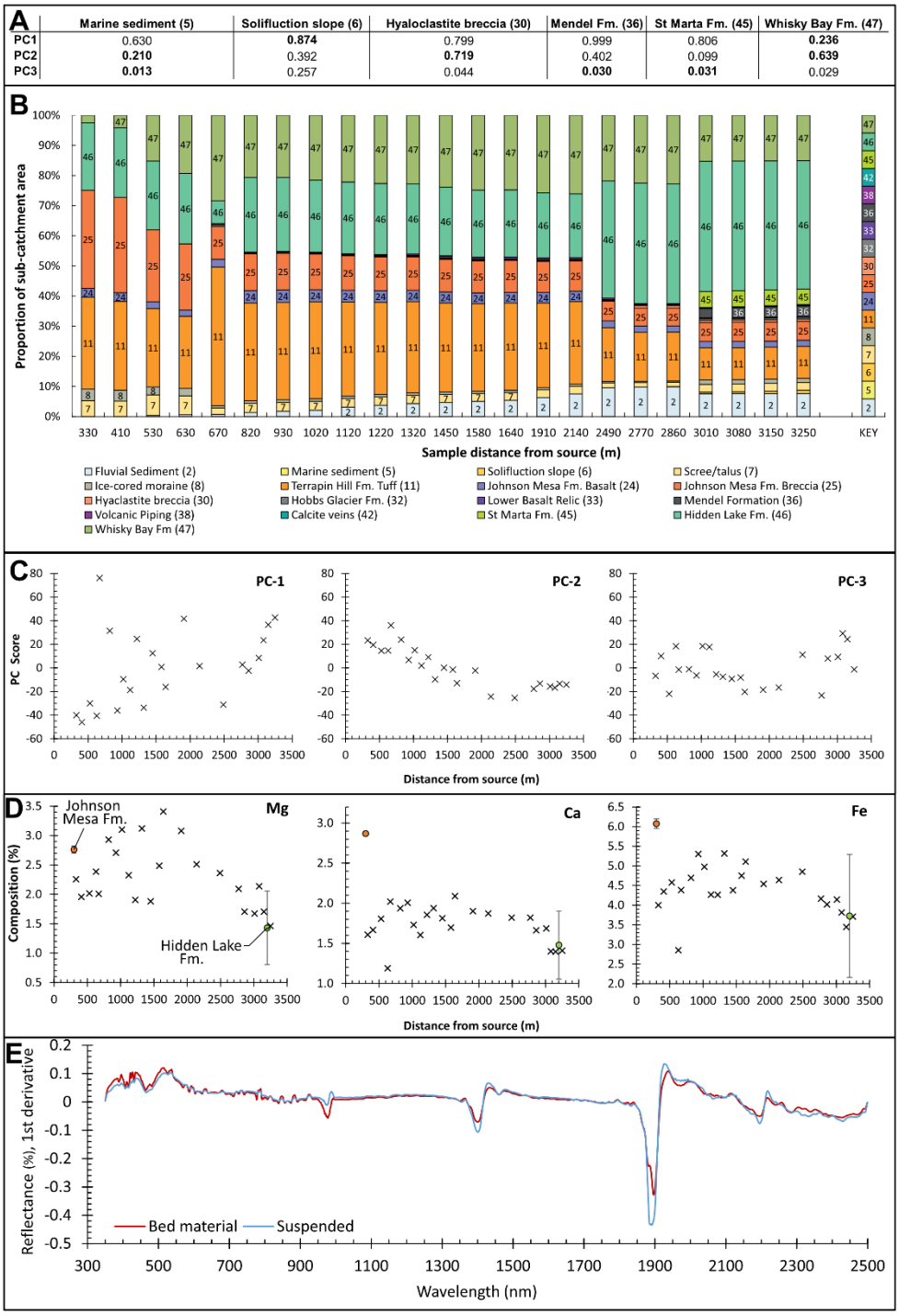

Figure 4.7: *The geochemical variation in the sediments of the Bohemian Stream.* ***A)*** *shows the R^2 value between the proportion of the sub-catchment of major lithologies and the principal component score of those samples, bold values indicate a significant correlative relations ($p < 0.05$);* ***B)*** *shows the downstream changes in the proportion of rock-types within the sub-catchment of each bed material sample, NB: the X axis is not continuous;* ***C)*** *shows the downstream changes in principal component scores;* ***D)*** *shows the downstream changes in magnesium, calcium and iron, and the % of these elements within the largest lithological unit at source and at the furthest downstream point;* ***E)*** *shows the mean first derivative reflected of bed material and suspended sediments (from across the Bohemian catchment, n = 10)*

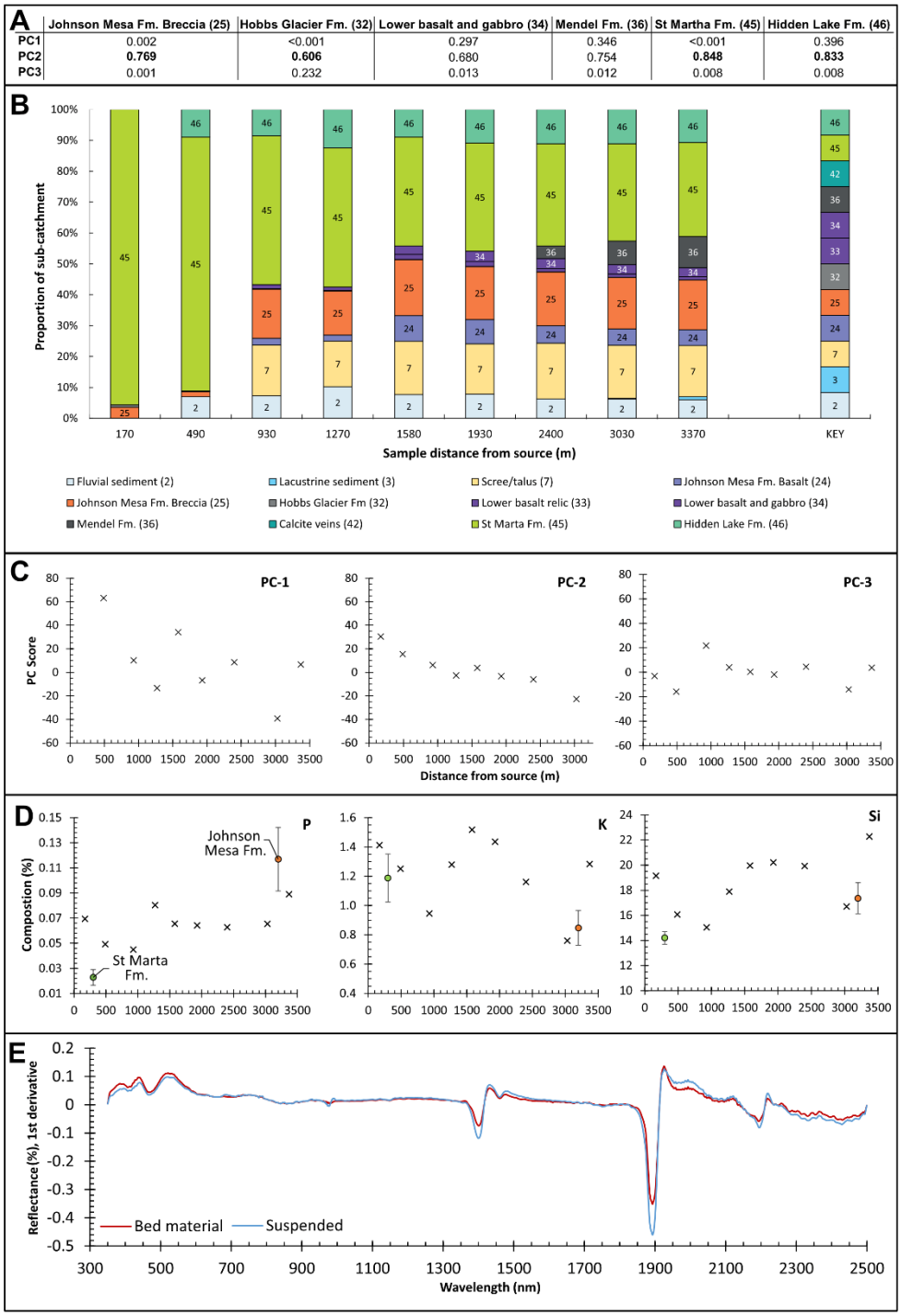

Figure 4.8: *The geochemical variation in the sediments of the Algal Stream.* ***A)*** *shows the R^2 value between the proportion of the sub-catchment of major lithologies and the principal component score of those samples, bold values indicate a significant correlative relations ($p < 0.05$);* ***B)*** *shows the downstream changes in the proportion of rock-types within the sub-catchment of each bed material sample, NB: the X axis is not continuous;* ***C)*** *shows the downstream changes in principal component scores;* ***D)*** *shows the downstream changes in Phosphorus, Potassium and Silicon, and the % of these elements within the largest lithological unit at source and the second largest at the furthest downstream point;* ***E)*** *shows the mean first derivative reflected of bed material and suspended sediments, n = 5.*

The largest downstream changes can be seen in the proportion of each sub-catchment that is composed of the Hidden Lake Fm., notably at 2490 m from the stream source. The most significant correlation between their proportion (**Figure 4.7B**) within a bed material sub-catchment and the first three principal components from the infrared spectra was seen between the Whisky Bay Fm. and PC-2 ($R^2 = 0.639$, $p < 0.001$, **Figure 4.7A**). The largest R^2 value is between Mendel Fm. and PC-1 although its relationship is not statistically significant ($R^2 = 0.999$, $p = 0.083$, **Figure 4.7A**).

Sediment composition changes downstream and this is very clear in PC-2, and to a lesser extent PC-1 of the infrared spectra data (**Figure 4.7C**). There is little downstream change in some of the minor components of the stream sediments (PC-3). The three elements present in the bed material samples with the most prominent changes in abundance downstream were magnesium, calcium and iron (Mg, Ca, Fe, **Figure 4.7D**), with each having a peak abundance around 1500 m from the stream source. The majority of suspended sediment samples collected were too small to robustly analyse. However, the composition of bed material samples can be compared with the limited number of analysed suspended sediment samples. Whilst the infrared reflectance of bed material and suspended sediment are not identical, there are similar patterns; notably in the undulation between ~ 350 to 500 nm and 500 to 600 nm, and troughs at ~ 900 nm, 1400 nm, and 1900 nm (**Figure 4.7E**).

Much like the Bohemian Stream, the composition of bed material changes in the Algal Stream is most clearly shown by PC-1 and PC-2 (**Figure 4.8C**). Few elements present in bed material samples showed a clear change downstream for the Algal catchment. Those that did show variability were phosphorus, potassium and silicon (P, K, Si, **Figure 4.8D**). P and Si increase in abundance with distance downstream, while K has a more sinuous trend, peaking around 1500 m from the stream source. P and Si also appear to have a degree of sinuosity in their downstream composition – in all cases the frequencies of these are between 1500 and 2000 m, suggesting a distinct change in bed material composition every 750 to 1000 m. There is also a distinct similarity between the bed material and infrared spectra, following a broad peak at ~ 350 to 500 nm and 500 to 600 nm, and troughs at ~ 1400 nm, and 1900 nm (**Figure 8E**). The differences between the Bohemian sediment spectra (**Figure 7E**) and Algal sediment spectra (**Figure 8E**) should be noted: with the 350 to 500 nm peak being much more variable in the Bohemian catchment's sediments and the Algal sediments lack a trough at ~ 900 nm.

4.4. Discussion

4.4.1. Provenance of bed material

In both catchments, the availability of different rock types changes downstream. This change in lithology, combined with changes in the chemical and spectral composition of the sediments (**Figure 4.7C, D; Figure 4.8C, D**), makes it likely that new sediment is being supplied into the stream. It is unlikely that the primary source of sediment is in the uplands of the catchments and that sediment composition changing as a consequence of the selective deposition of heavier minerals (Paola et al., 1992), though this likely has an impact on sediment composition as well. This interpretation is further supported by the fact that there is a statistically significant relationship between changes in lithology-type and sediment composition (**Figure 4.7A, Figure 4.8A**). The highest correlation between the proportional coverage of sub-catchment geology and bed material composition was for the geological units that underlie the main river channels (**Figure 4.2**, **Figure 4.7A**, **Figure 4.8A**). In the case of the Bohemian Stream this is the Whisky Bay Fm., while in the Algal Stream, it is the Hidden Lake Fm. and St Marta Fm.. This pattern is also further supported by the geochemistry (XRF) data, whereas there is a downstream reduction in the proportion of Mg, Ca and Fe occurs in bed material samples from 1500 m from the Bohemian Stream source (**Figure 4.7C**, **Figure 4.8C**). The igneous rocks, including basalt, breccia and tuffs, in the uplands of the Bohemian Stream catchment are enriched in these elements relative to the sedimentary rocks (e.g. Whisky Bay Fm.). This may be due to the high rate of chemical weathering that occurs in the region (Vašinka et al., 2020).

In the Algal catchment, the proportion of bed material sediment composed of P and Si increases with distance downstream. These elements are both far more abundant in igneous rocks (notably hyaloclastite breccias) in the region and suggest these rock units may have some impact on the composition of bed material in the lower reaches of the stream. The downstream increase in the proportion of these elements suggests that, although the sedimentary rocks within the catchment are likely to be the largest contributor of material to the streams, igneous rocks may have more of an impact on the Algal Stream bed material sediments than previously thought (Sroková and Nývlt, 2021). The variability in K, however, is a little less clear. Its initial high level is consistent with the dominance of the St Marta Fm. in the source area of the stream, which is relatively enriched in K. The dip in concentration around 1000 m (**Figure 4.8C**) coincides with an increase in the proportion of igneous rocks in the catchment; indeed some small tributaries come from permafrost-affected soils which overlay breccia, as well as from scree slopes with breccia and basalt clasts, which are relatively depleted in K. The subsequent increase downstream in K is consistent with the understanding that the underlying lithologies (Hidden Lake Fm. and St Marta Fm.) are primary sediment

sources. The decrease to a minimum at 3000 m (**Figure 4.8C**) from the Algal Stream source could be explained by the stream flowing over the Mendel Fm., which has slightly lower recorded K values than the Hidden Lake Fm. and St Marta Fm. The final spike in K (**Figure 4.8C**) is possibly due to the stream cutting into Holocene marine sediments. The influence of the Mendel Fm. may also account for some of the apparent importance of volcanic material in the lower reach of the Algal Stream. The Mendel Fm. is mostly glacigenic to glaciomarine in origin and is composed of clasts from the James Ross Island Volcanic Group, including Johnson Mesa Fm. breccia and basalt (Nývlt et al., 2011). Given the Algal Stream cuts through the Mendel Fm. in its lower reaches, this is a likely source of the igneous influence on Algal Stream sediments; indeed the Algal stream does erode down significantly, as it flows over this unit. Another possible source of sediment is the ice cave above the Algal Stream (**Figure 4.9**), which is covered by fine sediment and is likely to also increase sediment export on days with positive air temperatures.

Figure 4.9: *The ice cave just upstream of the AL sampling site*

For both of these catchments, the dominance of underlying strata on the composition of the streams suggests that transport capacity for bed material is low. It is likely that the river is sediment transport-limited (at least in the < 2 mm sediment fraction), and that transport distances are short (likely < 1 km), an interpretation that is consistent with the low discharge values measured in these streams and is supported by previous work in the region (Sroková

and Nývlt, 2021). Transportation of sediment within the streams was observed in the field (by traction and saltation).

Whilst the small sample sizes of suspended sediment mean an in-depth analysis of their provenance is challenging, the similarity in the spectra with bed material suggests that their sources are likely to be similar. This is also supported by the fact that the composition of suspended sediment samples varies with discharge, albeit with only a small number of data points (**Figure 4.10**). Indeed, this interpretation is statistically supported and there is a correlation between PC-1 of the IRS data and discharge; suggesting sediment composition is controlled by discharge; likely due to the transport distance of sediment entrained from the braidplain increasing with higher discharge. At BL ($r = -1.00$, $p = 0.08$, $n = 4$), and at AL ($r = -0.50$, $p = 0.66$, $n = 3$) there is a strong negative correlation (Spearman's rank), which supports interpretations made in previous studies that the braidplain is an important source of suspended sediment material (Kavan et al., 2017). Additionally, given the amount of sediment the Dirty Stream deposits onto the braidplain (**Figure 4.11A**), it also supports research suggesting the importance of the Dirty Stream as a key source of sediment exported from the Bohemian Stream (Sroková and Nývlt, 2021).

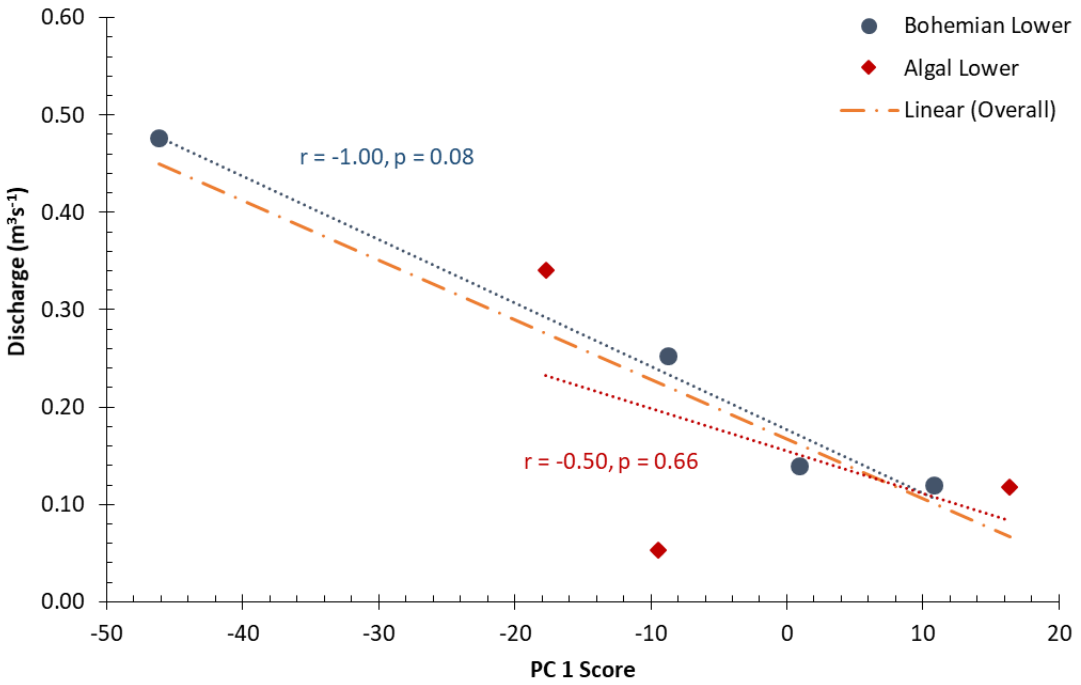

Figure 4.10: *Relationship between discharge and suspended sediment concentration, as described by PC-1 of infrared spectra.*

Sediment from outside of the catchment itself may also be an input to these streams via wind transportation (Kavan et al., 2017). Aeolian activity is especially high at the end of the summer

season when the surface is dry and a large amount of material is available for entrainment and transport (Kavan et al., 2018). Most of the material is transported a short distance. However, the deposition of long-range transported material has been identified on local glaciers (Kavan, Nývlt, et al., 2020). Preliminary analysis (Kavan and Nývlt, 2018) suggests that the braidplain and riparian zones of the Bohemian Stream act as a temporary deposition centre for fine-grained aeolian material, which is later activated and transported when the stream is flowing with a high discharge. The prevailing winds favour the transport of iron-rich material originating from the volcanic rocks of Johnson Mesa to the study catchment. This may have an impact on the geochemistry of fluvial samples and may account for the small input of volcanic sediments in the streams. The interaction of fluvial and aeolian processes has been observed in several Arctic sites (Good and Bryant, 1985; Crusius et al., 2011; Bullard and Austin, 2011; Bachelder et al., 2020), although most of the studies consider the braidplain with its fluvial sediments as a source for further aeolian transport, rather than aeolian material providing sediment to the river network.

4.4.2. Suspended sediment transport and variability

The Algal Upper site typically has a lower specific sediment load than the Algal Lower site (**Figure 4.6**). This suggests that new sediment is entrained in the lowermost part of the river, perhaps due to changes in stream gradient and the unlithified material of the Mendel Fm., which are then deposited on a small delta. The upper Algal stream is rather flat, with the lower stream cutting through the strata (**Figure 4.12**), making a steeper valley and sediment being supplied from permafrost-affected soils, slopes, and snowpacks in the lower reaches of the stream. This is consistent with the large sediment deposits in the upper parts of the Algal catchment (**Figure 4.11B-2**).

In the Bohemian catchment, the Bohemian Upper site only flowed if there had been recent warm temperatures causing snowmelt on Johnson Mesa and the surrounding uplands. However, when the water did flow, this site had significantly higher sediment loads than the Bohemian Lower site (**Figure 4.6**), which is surprising given its small area and suggests there is substantial deposition in the middle section of the Bohemian catchment; consistent with field observations. The same can be said for the tributary Dirty Stream, whose specific sediment loads are larger than that of the Bohemian Lower due to its higher gradient. Furthermore, large alluvial fans at the confluence of the Dirty Stream and Bohemian Stream and upstream (**Figure 4.11A-2**) evidence pronounced deposition to the Bohemian Stream's braidplain from several tributaries from the south east. This interpretation is consistent with the negative relationship observed between precipitation and discharge (**Figure 4.4, 4.5**) in both catchments is likely because the primary form of precipitation is snowfall, and there is typically

a lag time of several days between peak snowfall and peak discharge as this snow melts, as well as precipitation typically coinciding with lower air temperature.

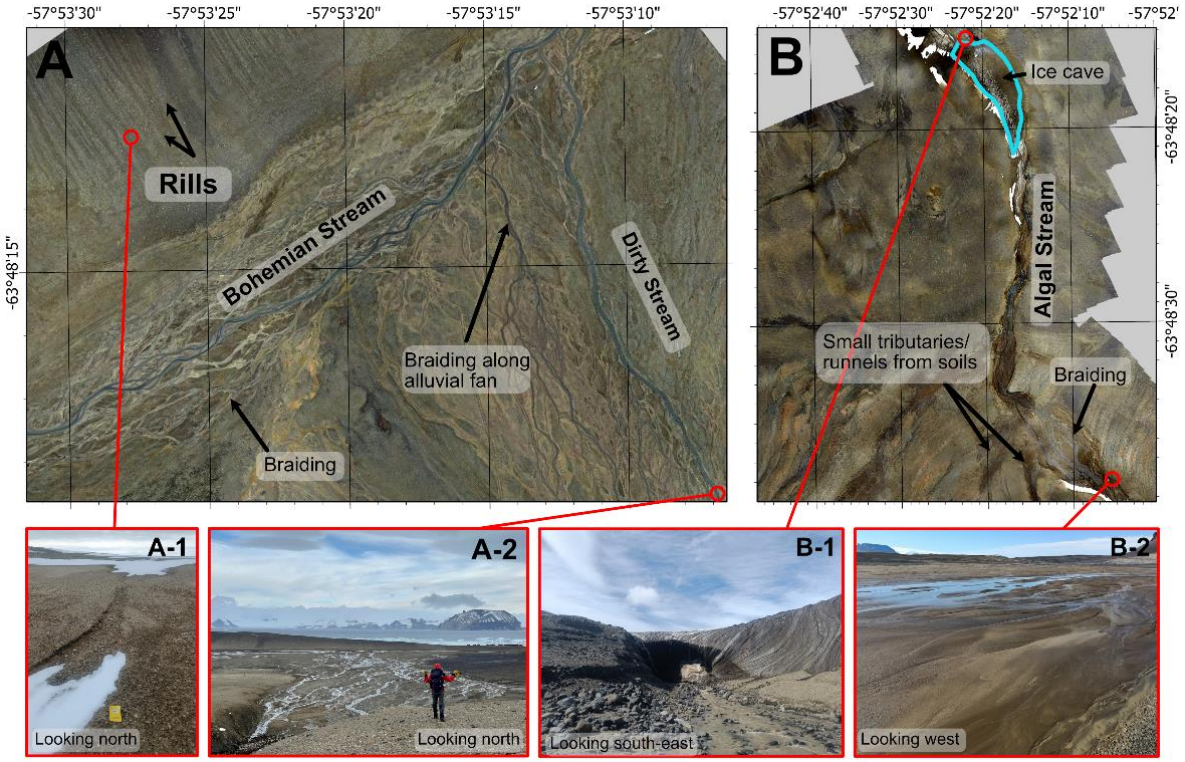

Figure 4.11: *UAV images of:* ***A)*** *the confluence between the Bohemian Stream (main channel) and Dirty Stream and;* ***B)*** *the Algal Stream, with its ice cave and braiding highlighted. Note in both catchments the large areas of unconsolidated sediments on the braidplains of all three streams.* ***A-1*** *shows rilling near the Bohemian Stream (notebook for scale),* ***A-2*** *shows the confluence of the Dirty Stream with the Bohemian Stream.* ***B-1*** *shows the ice cave front on the Algal Stream, while* ***B-2*** *shows unconsolidated sediment on an Algal Stream braidplain. Both main images were taken by MK using a DJI Mavic 2 Pro UAV. Inset photos were taken by myself, except A-2, which was taken by Lucie Ráčková.*

Data from both continuous measurement sites (**Figure 4.4, 4.5**) show that high precipitation followed by high temperatures is associated with higher rates of melt of snowfields, ice, and the active layer, and is a key control on suspended sediment concentration and, therefore, sediment load. The sediment load of both catchments is therefore highly sensitive to changes in water availability and suggests that both of the river catchments are broadly sediment transport-limited. This interpretation is consistent with the geomorphology; the presence of large sediment sinks (**Figure 4.11**), including braidplains and fans, and the high availability of unconsolidated sediments owing to it having previously been heavily glacierised (Davies et al., 2013; Jennings et al., 2021). Additionally, the local Cretaceous sedimentary rocks of this region are very friable (Ineson et al., 1986) and they remain largely unconsolidated due to James Ross Island's semi-arid climate preventing the growth of vegetation (Nývlt et al., 2016).

Figure 4.12: *Sediment being supplied to the Algal Stream from steep slopes that the stream has cut down into (Mendel Fm.).*

A transport-limited regime is further suggested by the exceptionally large specific sediment load value (1984 kg/min/km^2, **Figure 4.6**) measured at the Bohemian Upper site on 22 January. During this time, there was a brief but rapid snowmelt that increased the risk of slope failures (Decaulne et al., 2005; Kňažková et al., 2021), which was observed in the field (**Figure 4.13**), manifesting in a large volume of unconsolidated sediments and slope failure. These episodes of short-lived but very high sediment loads suggest: **i)** the sediment delivery ratio during these events was high, which is intuitive given the high slope angles of the sites and the rapid meltwater production at the time (Wan et al., 2019), and; **ii)** the fluvial energy is not sustained downstream, likely due to changes in stream gradient, and so the deposition rate was high because this very high sediment load value did not occur at the Bohemian Lower site (**Figure 4.6**). This interpretation is reinforced by field observations showing a substantial volume of deposited sediment around the Bohemian Upper site (**Figure 4.13)**. Whilst broadly transport-limited, the supply of additional aeolian sediment over the winter period to the braidplain of both streams likely results in additional sediment being available for transport, and is probably why sediment loads in the earlier parts of the summer season are higher despite similar hydrological conditions (**Figure 4.4B, 4.5B, 4.6**).

Furthermore, this interpretation is consistent with the measured “flash flood” event experienced in the Bohemian Catchment between 17 and 19 February (**Figure 4.4**) and

between 16 and 23 January in the Algal Stream (**Figure 4.5**). These kinds of rapid sediment transport events are consistent with previous work in this region (Kavan et al., 2017), which states that much of the seasonal sediment delivery happens over the course of a small number of flood events and is represented in the discharge data (**Figure 4.4, Figure 4.5**). Indeed, work in other cold regions has highlighted that a significant proportion of the sediment delivery of streams in sub-polar and alpine catchments occurs during short-duration flood events (e.g. Lenzi et al., 2003; Orwin and Smart, 2004; Willems et al., 2011; Yde et al., 2014; Eagle et al., 2021). It is of note that flash flood events appear to follow snowfall events, but not rainfall events (**Figure 4.4, 4.5**). This likely represents a difference in ground conditions in the upper parts of the catchment. Frozen ground is less porous and, as snowmelts in upland regions, infiltration rates are low and water is channelled more efficiently into the streams (Coles and McDonnell, 2018). In contrast, the rainfall events occurred after a period of sustained > 0 ^{o}C, when infiltration rates in the uplands are likely to be higher.

Figure 4.13: *Slope failure at the BU site, likely caused by melting ice in the sub-surface. This will supply additional sediment to the stream*

Whereas peaks in sediment load are associated with rising air temperatures in the Bohemian Catchment, the drivers of sediment load variability are more complicated in the Algal Catchment. Although the peak at the end of the season appears to be associated with rising air temperatures following a snowfall event, the earlier peak follows an increase in active layer thaw rate (coincident with a rise in air temperature) on 18 January. Similarly, the high

sediment load on 8-9 January for the Algal catchment sites (**Figure 4.6**) coincides with an increase in thaw rate, which rose from -7.8 cmd^{-1} on 6 January to 16.8 cmd^{-1} and 9.8 cmd^{-1} on 7 and 8 January respectively. However, due to a fault with the continuous discharge monitor, there is no continuous data from the stream at that point of the season. Both catchments had relatively short periods of sediment delivery (lasting 3-5 days), with some peaks in SSC being even shorter (e.g. preceding the 19/2 peak in the Bohemian Stream, **Figure 4.4B**). It is also of note that the suspended sediment load from the totally deglaciated Algal Catchment is greater than the Bohemian Catchment, and indeed both catchments show order of magnitude larger sediment loads compared to other catchments in Antarctica (Inbar, 1995; Mosley, 1988; Chinn and Mason, 2016; Stott and Convey, 2021). This is perhaps because the studied catchments have particularly fissile sediments (Davies et al., 2013). This highlights that even deglaciated catchments can be important sources of sediment to the Southern Ocean.

Overall, variability in SSC from the Bohemian catchment appears to be sensitive to changes in air temperature and precipitation, whilst sediment load from the Algal catchment appears to be more complicated, and shows sensitivity to active layer thaw as well as air temperature/precipitation. However, given the relatively high uncertainties in the measurements, this interpretation cannot be made with high confidence, and further research should aim to investigate this matter more closely, perhaps making use of multiple regression to better constrain the impact of different environmental factors on SSC.

A possible explanation for these differences between the catchments could be found in the presence of ice masses across the catchments. The Bohemian catchment is home to two small, unnamed glaciers on the eastern slopes of Johnson Mesa, which are sometimes unofficially referred to as Crame Col Glacier, at the source of the Dirty Stream, and Johnson Mesa Lakes Glacier, above the Bohemian Upper site at the source of the Bohemian Stream (**Figure 4.14A**). Glaciers and snowfields are sensitive to air temperature (Engel et al., 2018; Engel et al., 2023), and would be expected to be an important water source (Huss and Hock, 2018; Kavan, 2021). In contrast, no glaciers presently cover the Algal Stream catchment, and its only permanent ice is in the form of a small ice cave (**Figure 4.14B**) just upstream from the Algal Lower site.

Whilst both catchments do respond to precipitation, the magnitude of the response appears far greater in the Bohemian catchment than it is in the Algal catchment, with the most notable response in the Algal catchment being on 19 to 20 February. There is also a difference in drivers of variability at different temporal scales. The sediment load of all five sites can be seen to broadly follow changes in air temperature (**Figure 5.6**) throughout the day, but the magnitude of values on different days varies. This study proposes that these magnitudes are dependent on different environmental factors in the different catchments and can be

considered in the form of a conceptual model (**Figure 5.14**). The Bohemian Stream catchment is sensitive to changes in air temperature, which is intuitive given the presence of glaciers in

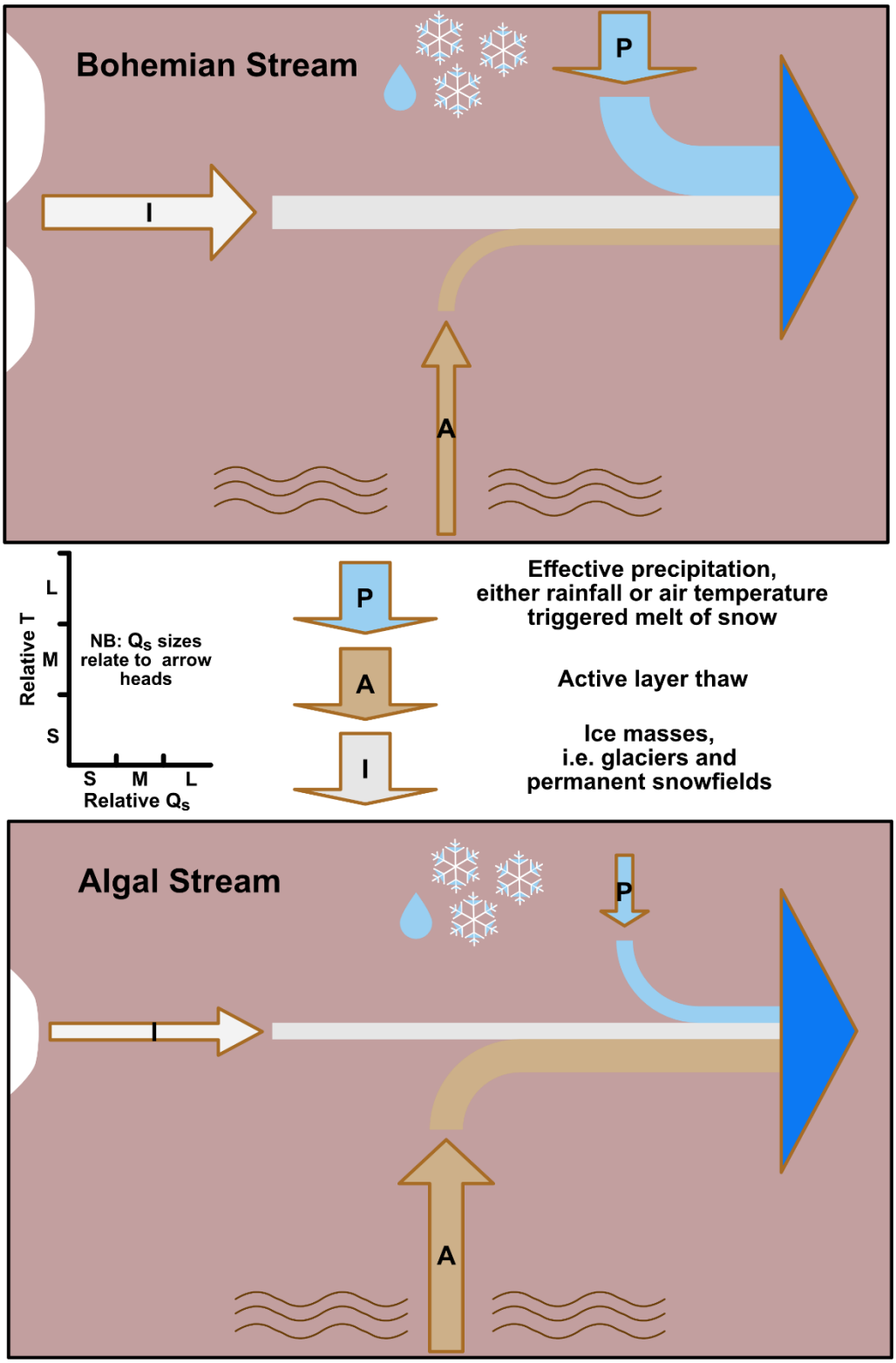

Figure 4.14: *A conceptual model of the drivers of sediment load variability in both catchments. NB: the ice mass arrows are oriented 90 degrees to the scale. S,M,L = small, medium, large. T = Time, Qs = sediment discharge. The time is relative to the melt season (approx.. 3 months), and describes the time over which each water source affects sediment discharge.*

this catchment. Whereas the Algal catchment, with an absence of ice masses, is more dependent on changes in active layer thickness, though changes in air temperature do affect discharge to some degree (**Figure 5.5**); and indeed air temperature itself controls active layer thaw (Hrbáček et al., 2023). Other studies (e.g. Kavan et al., 2017) have suggested that the Bohemian catchment is also likely to have water sourced from permafrost-affected soils. Although these data do not provide a direct agreement with this, some small-scale rills on the northern slopes of the Bohemian catchment were observed (**Figure 11 A-1**) and permafrost-affected soils are likely a small source of water and, therefore, sediment load variability in the Bohemian Stream. Indeed, the discharge of some Arctic streams are influenced by active layer thaw and permafrost degradation (Karlsson et al., 2015; Song et al., 2020; Wang et al., 2021).

Whilst this conceptual model largely confirms what is already known about Alpine and Arctic catchments (Schaefli et al., 2005; Blaen et al., 2014; Carrivick et al., 2018; Carrivick and Tweed, 2021) the spatio-temporal variability in driving mechanisms has not been unravelled for Antarctic catchments. The differences in the way two neighbouring catchments operate partly due to differences in the glacier ice cover is also particularly interesting in the context of melting glaciers and the expansion of proglacial areas in Antarctica (Lee et al., 2017; Engel et al., 2023).

4.5. Conclusions

In this chapter an in-depth analysis of river water discharge and sediment transport in two neighbouring catchments on Ulu Peninsula, James Ross Island, has been presented. Stream monitoring and provenance analysis were employed, which are very rare in Antarctica, respectively, to unravel the spatio-temporal characteristics and drivers of sediment transport controls. These data show that sediment load from the Bohemian catchment is controlled by air temperature. In contrast, sediment load in the Algal catchment appears to be sensitive to large changes in active layer thickness, as well as to air temperature and precipitation. Exceptionally high suspended sediment loads in the upper reaches of the Bohemian Stream highlight the fact that the streams in this region are sediment transport-limited and that: **i)** there is the potential for the Bohemian Stream to carry large quantities of sediment if there is sufficient water supplied to the channel, and; **ii)** the availability of this water is very sensitive to air temperature, which can result in load differences of five orders of magnitude within 24 hours. The sediment loads from these streams are exceptionally high for Antarctica (orders of magnitude higher than other regions) and this chapter estimates that the annual sediment load for the Bohemian Stream in the austral summer of 2021/2022 was 141 ± 51 t km^{-2} yr^{-1} and 208 ± 58 t km^{-2} yr^{-1} for the Algal Stream.

Bed material in both the Bohemian Stream and Algal Stream is related to the rocks they overlay, notably sedimentary strata due to the very short (< 1 km) transport distance of bedload in these rivers. However, minor components of the bed material in both streams are sourced from igneous rocks; in the Bohemian Stream, this is evident in the samples closest to the source, whereas in the Algal Stream, the importance of igneous rocks increases downstream. This is perhaps because permafrost-affected soils overlay units of hyaloclastite breccia, or due to the presence of igneous clasts within the Mendel Fm.

The Bohemian and Algal Streams give a glimpse of the future for many Antarctic catchments as glaciers retreat. The deglaciation of the catchments on James Ross Island has made a large volume of unconsolidated sediment available for transport and, even in the absence of glacial melt, large quantities of this sediment can be transported on days with positive temperatures (which are expected to become more frequent) when the active layer, snow and any other bodies of ice melt.

5. Accelerated glacier changes on the James Ross Archipelago, Antarctica, between 2010 and 2023

5.1. Introduction

Glaciers cover 132 900 km^2 around the periphery of Antarctica and represent 18 % of global glacier area, excluding the major ice sheets (Pfeffer et al., 2014). However, proportional to the total area of glaciers, few glaciological data are available for land-terminating glaciers in Antarctica compared to other World regions. Although glacier recession rates slowed down during the first decade of the 21st Century, coincident with a hiatus in warming (Oliva et al., 2017), glaciers are now receding at an enhanced rate as a consequence of rising temperatures since 2015 (Carrasco et al., 2021). Furthermore, recent extreme warming across the Antarctic Peninsula Region (APR) has led to exceptional melt rates in some places (Siegert et al., 2023), most notably on the George VI and Larsen C ice shelves (Bevan et al., 2020; Xu et al., 2021; Banwell et al., 2021).

Exceptional melt events release large volumes of freshwater, as well as sediments and solutes, into proglacial streams, lakes, and the Southern Ocean (Kavan et al., 2017; Carrivick and Tweed, 2021; Kavan and Strzelecki, 2023). More generally, the loss of glacier mass increases the size of proglacial areas, and can increase meltwater flux and the availability of sediment. In turn, this affects both water temperature and water quality and thus, the fragile marine and lacustrine ecosystems of Antarctica (Nedbalová et al., 2017; Gonçalves et al., 2022), as well as contributing to glacier accelerations (Bell et al., 2018; Tuckett et al., 2019).

Recently recorded mass losses from the peripheral glaciers of Antarctica are moderate when compared with other glacierised world regions (Hugonnet et al., 2021). However, projected melt rates across the APR and the rest of the Antarctic periphery are amongst the greatest of any world region and, due to the very large ice volume, may be highly impactful (Edwards et al., 2021; Siegert et al., 2023). Therefore, there is a pressing need to understand how recent air temperature increases and extreme warm events affect APR glaciers.

This chapter aims to present and evaluate glacier changes for the 156 glaciers on the James Ross Archipelago in response to recent and ongoing extreme air temperature warming recorded at the Johann Gregor Mendel Czech Antarctic Station (JGM). Specifically, satellite (Landsat-7, Landsat-8, Landsat-9) derived data is presented to show changes in snow line altitude (SLA), glacier area, and albedo for the James Ross Archipelago since 2010. Coincident *in-situ* measurements of ablation and accumulation for Lookalike Glacier and Davies Dome on the Ulu Peninsula, James Ross Island are also presented.

1.1. James Ross Archipelago's glaciated environment

The James Ross Archipelago has a semi-arid polar continental climate, with a mean annual air temperature of -7 °C at JGM (10 m a.s.l) (Kaplan Pastíriková and others, 2023, section 1.2.3), and a mean lapse rate of 0.43 °C 100 m^{-1} measured over glacierised sites (270 to 540 m a.s.l. between 2013 and 2016) (Ambrožová et al., 2020), and a snow depth rarely exceeding 0.35 m (Hrbáček et al., 2021) at JGM (10 m a.s.l). To consider the regional variability in climatic conditions (Morris and Vaughan, 2003), glaciers across the archipelago have been split into two groups; those closer to the considerably warmer Ulu Peninsula (north west), and those closer to the ice-bound Weddell Sea (south east) (**Figure 5.1**).

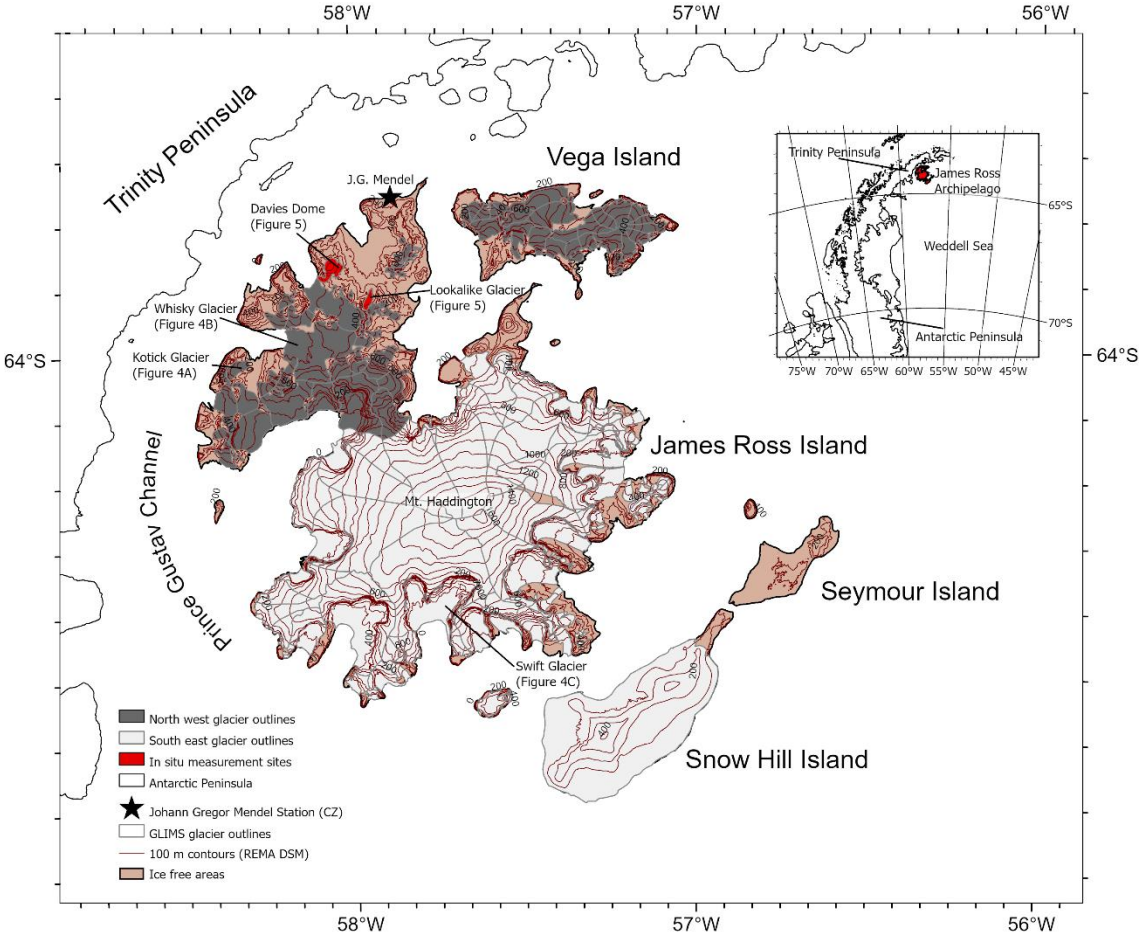

Figure 5.1: *The glacier outlines on James Ross Island, derived from the GLIMS dataset. Glaciers in the north western sector of the island are in grey, with those in the south eastern sector in white. Those glaciers with in-situ measurements (Lookalike Glacier and Davies Dome) are coloured in red; these have GLIMS IDs of G301945E63889S and G302049E63932S respectively. Glaciers that have experienced exceptional changes havce also been labelled: Whisky Glacier (G301946E63935S), Kotick Glacier (G301659E64016S), and Swift Glacier (G302228E64270S). Inset shows location of James Ross Archipelago with respect to the AP (highlighted red).*

Since the Last Glacial Maximum, when ice from the Antarctic Peninsula coalesced with James Ross Island (Glasser et al., 2014), James Ross Island has been dominated by the Mount Haddington ice cap (**Figure 5.1**), which is ~ 300 m thick and drains over steep cliffs to outlet

glaciers that are predominantly marine-terminating (Skvarca et al., 1995). Numerous small valley and cirque glaciers also exist beneath near-vertical bedrock cliffs on the Ulu Peninsula of James Ross Island and have changed in thermal regime and behaviour but relatively little in geometry during the late Holocene (Carrivick et al., 2012). Vega Island is dominated by two plateaux ice caps that feed small tidewater glaciers (Davies et al., 2012). Seymour Island is free of glacier cover. In contrast, Snow Hill Island is almost entirely covered by a marine-terminating ice cap (Davies et al., 2012).

5.2. Methodology

All satellite images (**Table 5.1**) used in this study were derived from the Landsat surface reflectance catalogue for the period 2010 to 2023. In this instance, the surface reflectance product was preferable to the TOA product (as used in Chapters 3 and 4), as a key aim of this chapter was to derive albedo measurements, which require the use of surface reflectance image (Naegeli et al., 2019). Images were selected from the austral summer (December to March) to coincide with the dates of *in-situ* measurements. Images were visually inspected and chosen on the basis of clarity, with images from later in the summer season (February, March) preferentially chosen for consistency and to ensure there was a minimum of snow cover (Hrbáček et al., 2016). In cases of poor image availability, imagery from December and January were used, which may have included snow cover in a minority of cases. Images were taken from Landsat 7 Enhanced Thematic Mapper Plus (ETM+), Landsat 8 Operational Land Imager (OLI), and Landsat 9 OLI-2 and filtered to include only those with < 50 % cloud cover. The glacier outlines were produced between 2005 and 2014 and are available from the GLIMS dataset (Raup et al., 2007). It was necessary to manually remove some erroneous polygons that seemed to correspond to frozen lakes, snow-filled river valleys, shadows, and a few spurious digitising/topology errors.

Table 5.1: *Satellite images used in this study. Specific image date is coded into the image ID.*

Month-Year	***Sensor***	***Image ID(s)***
February-2010	Landsat-7 ETM+	20100218-LE07 20100223-LE07 20100225-LE07
February/March-2011	Landsat-7 ETM+	20110219-LE07 20110307-LE07
January/February-2012	Landsat-7 ETM+	20120112-LE07 20120222-LE07 20120229-LE07
February/March-2013	Landsat-7 ETM+	20130224-LE07 20130305-LE07
January-2014	Landsat-8 OLI	20140111-LC08
December-2014 (summer 2015)	Landsat-8 OLI	20141204-LC08

January-2016	Landsat-8 OLI	20160117-LC08
February-2017	Landsat-8 OLI	20170204-LC08
January-2018	Landsat-8 OLI	20180106-LC08 20180115-LC08
March-2019	Landsat-8 OLI	20190330-LC08
January-2020	Landsat-8 OLI	20200112-LC08
December-2020 (summer 2021)	Landsat-8 OLI	20201204-LC08
February-2022	Landsat-8 OLI	20220209-LC08
February-2023	Landsat-9 OLI-2	20230204-LC09

5.2.1. Air temperature

Air temperature data were collated from the automatic weather station located near JGM (10 m a.s.l.). Air temperature was measured using a Minikin TH datalogger and EMS33H probe (EMS Brno, Czech Republic) with an accuracy of ± 0.15 °C, installed at 2 m above the ground in a multi-plate radiation screen. From the hourly air temperature observations, the annual sum of positive degree days has been calculated (Hock, 2003). A linear regression was conducted to calculate the average annual change in temperature and report the standard error of the slope of the regression line (similar to other studies, e.g. Carrasco et al., 2021).

5.2.2. In-situ Glacier changes

Glacier ablation and accumulation was measured using stakes placed on Davies Dome Glacier and Lookalike Glacier, which form part of a long-term measurement study (cf. Engel et al., 2018). The height of the stakes above the glacier surface was measured with an accuracy of ± 0.01 m using a standard tape measure during the austral summer, typically in early February. In the case of Davies Dome, the measurements in this chapter are from ablation stakes taken along a W-E transect that are less affected by snowdrifts and enhanced accumulation at the north eastern slope of the dome have been selected. These ablation measurements were split into 100 m altitude bins.

5.2.2. Snow line altitude

Google Earth Engine (GEE) was used to calculate annual end-of-summer snow line altitudes (SLA) for each glacier.

Landsat images were topographically corrected using the ALOS World 3D 30 m digital surface model (DSM) (Takaku et al., 2014), and a cloud mask was applied. Topographic correction is a routine method of image preparation that corrects for the variable illumination caused by topography (Soenen et al., 2005; Vanonckelen et al., 2013). This chapter has made of use of the ALOS DSM, instead of the Antarctic-specific REMA DSM (which was used in Chapters 3 and 4), as the analysis of SLA was derived from a broader (southern-hemisphere) analysis of SLA

(Macfee, 2023). Images were clipped to each of the glacier polygons to permit automatic quality checking and any image of a glacier that contained > 35 % invalid pixels was removed. The majority of invalid pixels arose due to cloud cover, but sensor issues (e.g. Landsat 7 scanning line error) would also result in a pixel being automatically defined as invalid.

An automated approach to determine end-of-summer SLA identification was used to ensure there was consistency in the identification of SLA between sites. To identify the boundary between snow and ice, a new band was added to the image called "NIRSWIR", as defined in equation (**Eq. 5.1**) and that was used to perform Otsu thresholding to segment the image into "ice" and "snow" pixels (e.g. Li et al., 2022; Wang et al., 2023). Otsu is a statistical algorithm used for binary image segmentation (Otsu, 1979). The method calculates glacier-specific classification thresholds, by identifying the value that creates maximum between-class variance of image pixel values. Otsu is the favoured thresholding method for automated snowline detection studies (Rastner et al., 2019; Liu et al., 2021; Li et al., 2022; Wang et al., 2023), as it offers the opportunity to adaptively identify the glacier snow-ice boundary with efficiency over large samples (Gaddam et al., 2022). This case-by-case thresholding is important as the characteristics of glacier snow cover vary spatially and temporally.

$$NIRSWIR = NIR \times \frac{NIR}{SWIR1} \quad (\mathbf{5.1})$$

Where NIR is band 4 in Landsat-7 ETM+, and band 5 in Landsat 8 OLI and Landsat-9 OLI-2. SWIR1 is band 5 in Landsat 7 ETM+ and band 6 in Landsat-8 OLI and Landsat-9 OLI-2.

Once the image had been automatically classified into "snow" and "ice" pixels, the DSM was to the glacier outlines, 20 m elevation bins were created on each glacier (cf. Rastner et al., 2019). Within each of these bins, the snow cover ratio (SCR) was, as defined (**Eq. 5.2**). Progressing from the lowermost bin upwards, when a set of five bins were found with a SCR > 0.5, the SLA was set as the average elevation of the lowest bin where snow cover was > 50 %, as recommended by the World Meteorological Organisation's definition for SLA identification (WMO, 1970; Li et al., 2022). If five bins could not be identified, the number of bins was gradually reduced to the number necessary to identify SLA. If no bin could be identified with an SCR > 0.5, it was returned as null.

$$SCR = \frac{snow\ pixel\ count}{snow\ pixel\ count + ice\ pixel\ count} \quad (\mathbf{5.2})$$

The uncertainty of the SLA was calculated as the root mean squared error (RMSE, **Eq. 5.3**), and previously implemented in other SLA studies (Racoviteanu et al., 2019)

$$U_T = \sqrt{{U_d}^2 + {U_o}^2 + {U_b}^2} \quad (\mathbf{5.3})$$

where U_T is the total uncertainty (RMSE), U_d is the vertical uncertainty of the DSM (5 m, Takaku and others, 2014), U_o is the uncertainty of the glacier outline, which is the size of a Landsat pixel (30 m), and U_b is the buffer uncertainty, defined as half of an elevation bin (10 m). This gives U_T a value of 32.0 m.

A quality assessment of the snow classification was also performed by randomly selecting 100 points from the 2020 image. A level of agreement (percentage of correctly classified points) was determined by comparing the automated snow and ice classifications to a false-colour composite image, and visually interpreting areas of snow-covered and snow-free terrain, for which an agreement of 96 % was found. Misclassification is generally due to other light absorbing materials being present within the glacier outlines beyond ice (Liu et al., 2021). This includes rocks and vegetation, representing a minor disadvantage to using an automated approach.

5.2.3. Glacier area

Glacier outlines for years 2011, 2017, and 2023 were delimited by manually editing GLIMS (years 2005 to 2014) glacier outlines (Raup et al., 2007) to digitise glacier extent visible in satellite images (see **Table 5.1**). These years were chosen for image clarity (lack of clouds and overall snow cover). Area change was then quantified for each period (2011 to 2017 and 2017 to 2023) and converted this into a percentage change relative to the initial glacier area. Error in glacier outline position is assumed to be ± 15 m, or half the size of one Landsat pixel (cf. Paul et al., 2017). This conservative estimate of the uncertainty in glacier area, assessed by creating a ± 15 m buffer on each glacier and calculating the standard deviation in those areas, produces a mean uncertainty (1 σ) in glacier area of ± 0.13 km^2, or 7 % of the glacier area, which is comparable to previous studies (Malmros et al., 2016; Taylor et al., 2022). Other sources of errors can be introduced by misidentifying debris cover or snow covered nunataks/headwalls, which are considered to be negligible and therefore accounted for within this conservative approach.

5.2.4. Albedo

GEE was also used to calculate albedo per pixel for each glacier in each year. A band was added to the Landsat image for each year to represent albedo, calculated using **Eq. 5.4** which is a narrow-to-broadband conversion calculation (Liang, 2001; Naegeli et al., 2019).

$$\alpha = 0.356_{blue} + 0.130_{red} + 0.373_{NIR} + 0.085_{SWIR1} + 0.072_{SWIR2} - 0.0018 \quad (\mathbf{5.4})$$

Where α is albedo, blue is Landsat-8 OLI, Landsat-9 OLI-2 band 2 and Landsat 7 ETM+ band 1. Red is Landsat-8 OLI, Landsat-9 OLI-2 band 3, and Landsat 7 ETM+ band 2; NIR is Landsat-8 OLI and Landsat-9 OLI-2 band 5 and Landsat 7 ETM+ band 4. SWIR1 and SWIR2 are bands 6 and 7

for Landsat-8 OLI and Landsat-9 OLI-2, and bands 5 and 7 for Landsat 7 ETM+. Each glacier was assigned a single annual albedo value using the median of all pixels per glacier. For those glaciers with *in-situ* measurements, albedo was also calculated at 100 m altitude bins.

This method of albedo measurement has previously been shown to be suitable for glaciated environments, though sometimes slightly underestimates true values (Liang, 2001; Naegeli and Huss, 2017). However, given this chapter focuses on interannual comparisons of albedo, relative changes in albedo are more important than true values. Uncertainties typically stem from saturation problems over snow-covered areas, though this is difficult to quantify and is assumed to be negligible (cf. Naegeli et al., 2019).

5.3. Results

5.3.1. Temperature, snowline altitude, and albedo changes

Both mean annual air temperature (MAAT) and the sum of positive degree days (PDD) have increased during the study period (**Figure 5.2A**). The lowest annual temperature in the period was in 2009/10, at -8.59 °C, with a maximum of -3.61 °C in 2022/23. The average warming trend was 0.24 ± 0.08 °C yr^{-1} (r^2 = 0.44, p = 0.01). PDD has also increased over the study period, with an average rate of increase of 15.0 ± 3.8 K d^{-1} yr^{-1} (r^2 = 0.56, p < 0.01). This trend is most

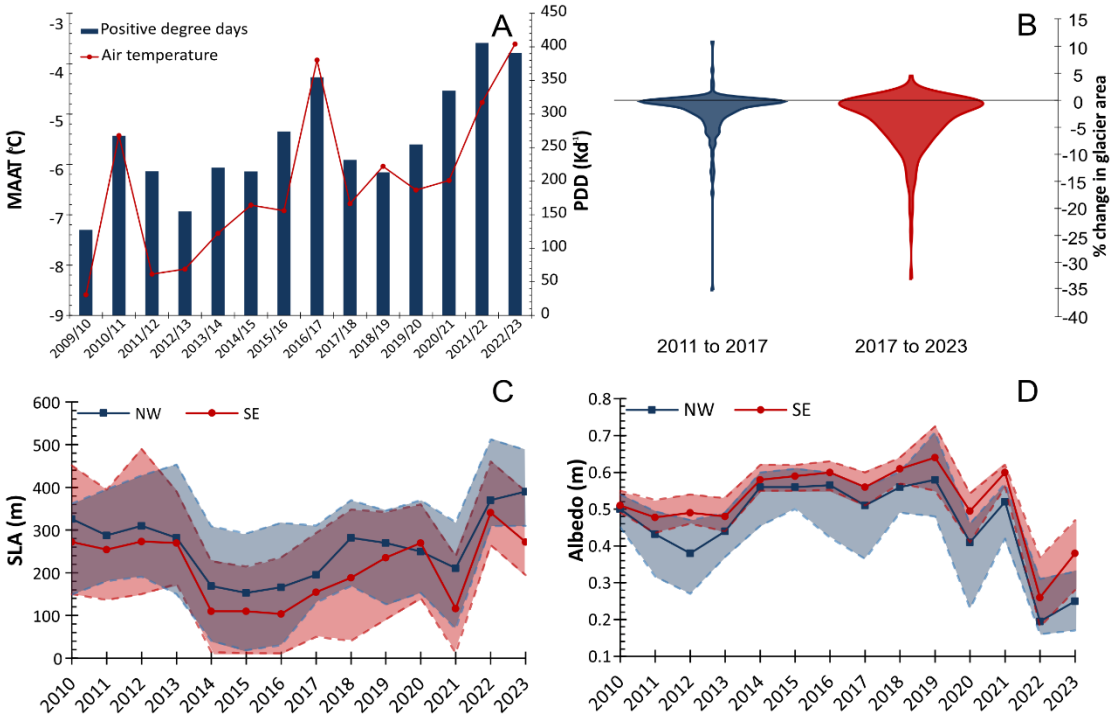

Figure 5.2: A) *Mean annual air temperature (MAAT) and annual sum of positive degree days (PDD), measured at JGM;* ***B)*** *violin plot of % glacier area change 2011–2017 and 2017–2023, the width of the plots is proportional to the number of glaciers n =156);* ***C)*** *Change in summer SLA for the NW and SE glaciers, NB: shaded area shows inter-quartile range;* ***D)*** *Change in albedo for the NW and SE glaciers, NB: shaded area shows inter-quartile range.*

clear from 2018/19 when PDD increased from 213 K d^{-1} to 406 K d^{-1} in 2021/22. Despite a slight decrease in PDD in 2022/23 relative to the previous year, with a value of 391 K d^{-1}, it had the second-highest PDD in the study period. The lowest PDD was in 2009/10, at 127 K d^{-1}.

The rate of glacier area change (decline) increased in the period from 2017 to 2023 compared to between 2011 and 2017 (**Figure 5.2B**). The median rate of glacier area loss between 2011 and 2017 was 0.06 % yr^{-1}, but then increased six-fold to 0.38 % yr^{-1} between 2017 and 2023. While the upper quartile was maintained at 0.00 % yr^{-1}, the lower quartile fell from an area loss of 0.39 % yr^{-1} to 0.94 % yr^{-1}.

The summer SLA data suggest an increase in both the NW and the SE sectors of the archipelago since 2015, from minimum median height of 153 m a.s.l. (NW, 2015) and 110 m (SE, 2016) to maximum values of 390 m a.s.l. (NW, 2023) and 341 m a.s.l. (SE, 2022) (**Figure 5.2C**). Although SLA decreased in the SE sector in 2023, it remained at a high value of 272 m, the joint second-highest elevation during the study period. Before 2015, SLA was also high but was lower than the maximum values of 326 m a.s.l. (NW) and 272 m a.s.l. (SE) in 2010. The median SLA is typically higher in the NW sector compared to the SE, but this difference is only significant (in a T-test, defined as p-value < 0.05) in 2023 ($p < 0.01$).

There are inter-annual variations in glacier-wide median albedo have generally increased in the period 2011 to 2019 (**Figure 5.2D**) from 0.43 (NW) and 0.48 (SE) to 0.58 and 0.64, respectively. Since 2019, albedo has decreased to 0.20 (NW) and 0.26 (SE), respectively. Although albedo increased slightly in 2023, it remained low at 0.25 (NW) and 0.38 (SE). Albedo in the SE is consistently higher than in the NE sector, and this is statistically significant in 10 of the 13 years studied.

5.3.2. Notable changes in glacier area

Whilst most glaciers have become smaller in surface area during the period 2011 to 2023 (**Figure 5.2B**), there have been some exceptional changes in glaciers that are worthy of note. Two glaciers have gained in areal extent: Whisky Glacier (**Figure 5.1B**), and Kotick Glacier (**Figure 5.1A**). Whisky Glacier slightly reduced in area, from 28.7 ± 0.4 km^2 to 28.2 ± 0.4 km^2 (a loss of 1.8 %) between 2011 and 2017 before the terminus advanced by ~ 800 m, increasing its area to 29.5 ± 0.4 km^2 (an increase of 4.7 %). Kotick Glacier advanced by > 800 m during the period between 2011 to 2017 when it increased in area from 5.0 ± 0.1 km^2 to 5.5 ± 0.1 km^2 (an increase of 11.0 %).

Since 2017, the terminus position of Kotick Glacier has remained approximately stable, though the glacier as a whole decreased in size to 5.2 ± 0.1 km^2 (a loss of 6.0 % of its area), with that area loss occurring primarily close to its headwall. In contrast, Swift Glacier's eastern terminus

position receded by 4 km (**Figure 5.1, Figure 5.3C**), 3 km of which has occurred since 2017. Swift Glacier, which has an accumulation area on Mount Haddington ice cap according to the GLIMS outlines (Raup et al., 2007, **Figure 5.1**), decreased in size from 178.4 ± 0.6 km^2 in 2011 to 175.9 ± 0.6 km^2 in 2017 (a loss of 1.3 % of its area) and was further reduced to 161.0 ± 0.6 km^2 in 2023 (a loss of 8.5 % of its area). Changes in the area of Swift Glacier were coincident with measurements suggesting a rise in SLA from 50 m a.s.l. in 2017 to 510 m a.s.l. in 2018.

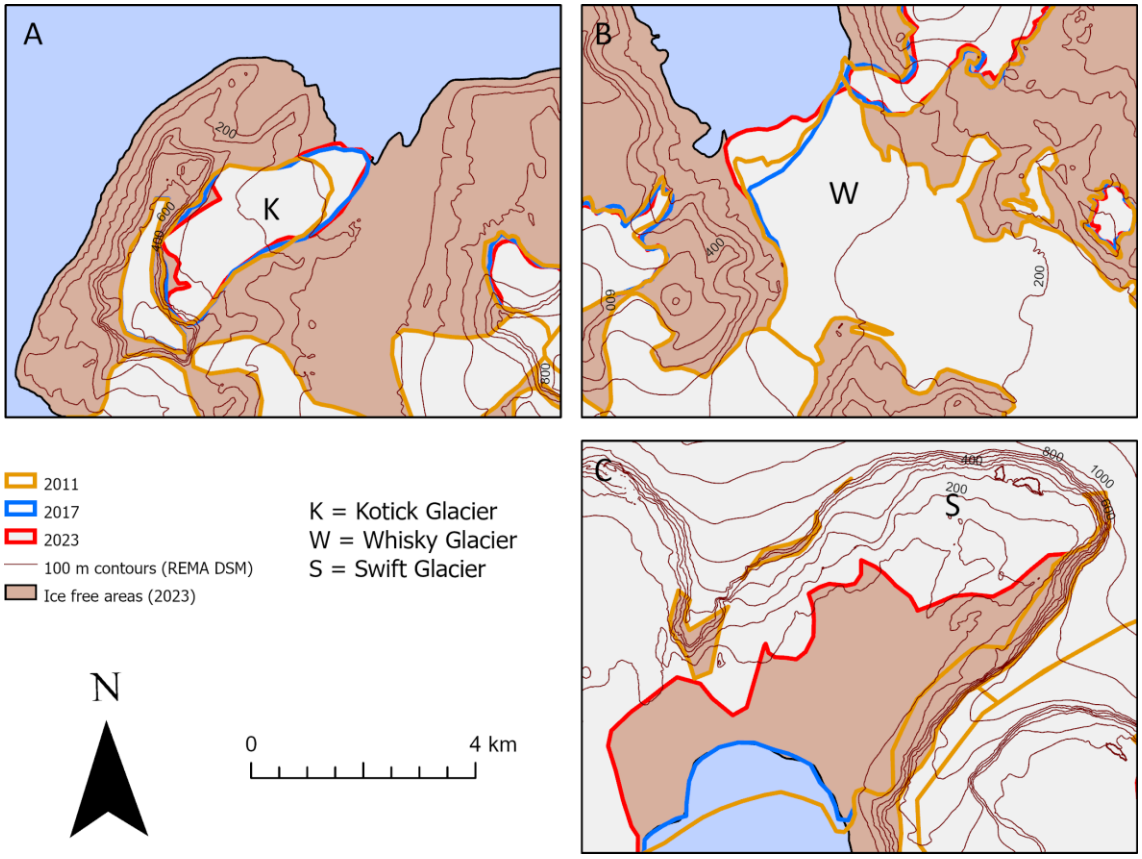

Figure 5.3: *Exceptional changes in glaciers on James Ross Island, including the advance of Kotick Glacier* ***(A)****, Whisky Glacier* ***(B)****, and the exceptional loss of area of Swift Glaciers* ***(C)****.*

5.3.3. Comparison of albedo, SLA, and dH datasets

Across the entire archipelago, there has been a visible reduction in albedo, both spatially (**Figure 5.4A**) and through time (**Figure 5.2D, Figure 5.4B**). On Davies Dome and Lookalike Glacier (**Figure 5.4B**), albedo has followed the same trend as the rest of the island, with high albedo values of 0.56 (200 to 300 m) to 0.75 (> 500 m, Davies Dome only) in 2019, down to 0.16 to 0.41 in 2022. At altitudes above 300 m, albedo continued to fall in 2022/23 (e.g. > 500 m albedo was 0.37), though the albedo at 200 to 300 m increased to 0.20. The decrease in

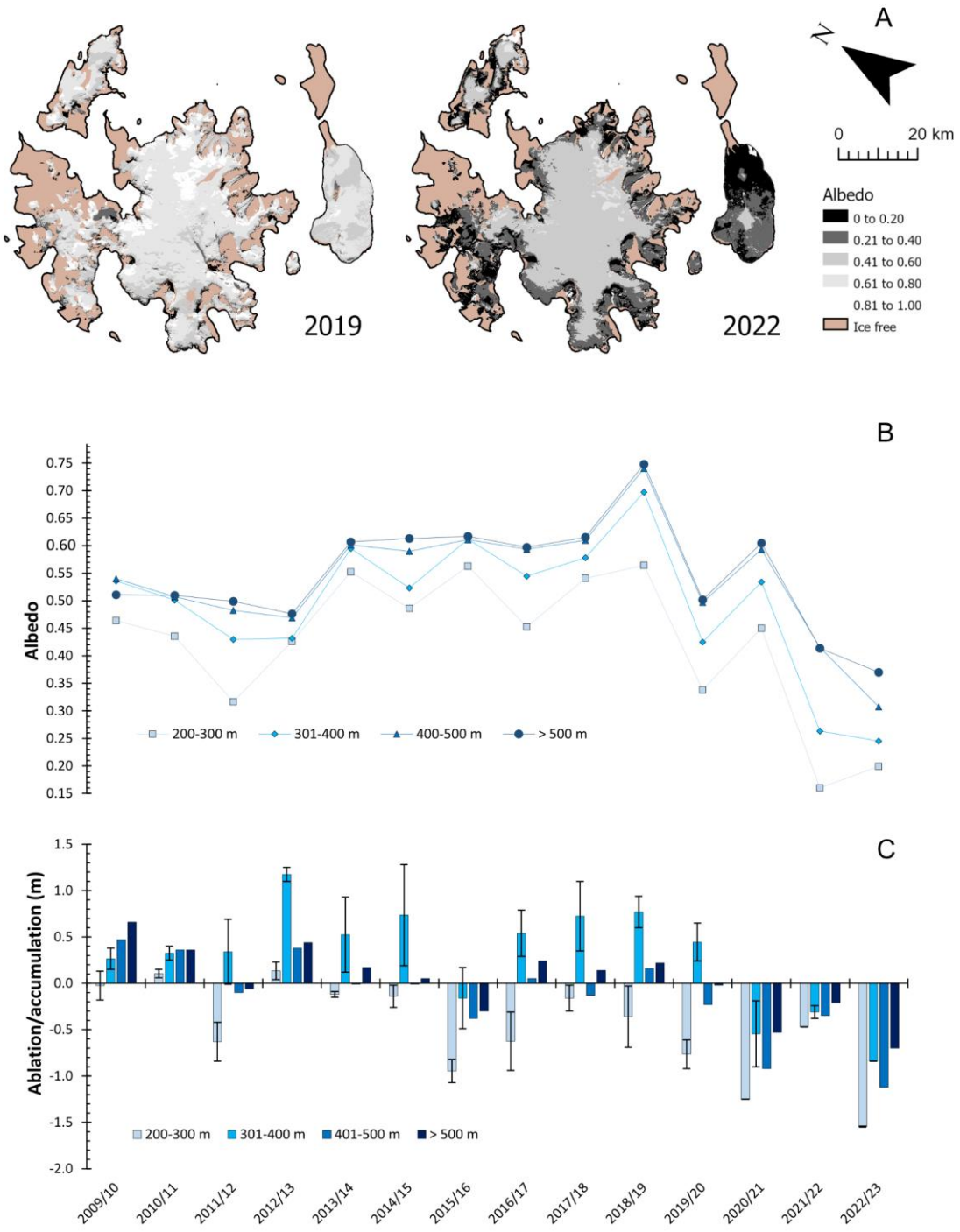

Figure 5.4: A) *The years of maximum albedo (2019) and minimum albedo (2022);* ***B)*** *Mean albedo for Lookalike Glacier and Davies Dome Glaciers (combined) at different elevations (mean standard deviation is 0.027);* ***C)*** *Mean change in ablation/accumulation (collected in-situ) of Lookalike Glacier and Davies Dome Glaciers of at different altitudes (error bars show standard deviation).*

albedo occurs in tandem with measurements showing an increase in SLA; for Davies Dome the median SLA over the study period was 280 m a.s.l, which would result in snow covering 81 % of the glacier. In contrast, in 2022 and 2023, SLA rose to 490 m a.s.l. (10 % coverage) and 470 m a.s.l. (17 %) respectively. In the case of Lookalike Glacier, the median value was 285 m a.s.l. (88 %), but this rose to 365 m a.s.l. (48 %) in 2022 and 465 m a.s.l. (2 %) in 2023. This rise in SLA is consistent with other observations across the archipelago. For example, on Snow Hill Island, SLA rose from a median value of 10 m a.s.l. to 290 m a.s.l. in 2022, resulting in a reduction in albedo (**Figure 5.4A**). A decrease in albedo corresponds with glacier ablation (**Figure 5.4C**) recorded at the ablation stakes at all altitudes. In the years 2020/21, 2021/22, and 2022/23, ablation was measured at all altitudes of both glaciers. There has been consistent ablation at all of measured points below 300 m altitude since 2012/13, except for 2018/19 when some stakes showed accumulation, and in the 400 to 500 m bin since 2019/20. Since 2009/10, only two years have seen accumulation at all altitudes (2010/11 and 2012/13). The greatest degree of ablation at every altitude was in 2022/23, with a loss of 1.5 m below 300 m, 0.8 m at 300 to 400 m, 1.1 m at 400 to 500 m and 0.7 m above 500 m.

There is a statistically significant correlation between albedo and ablation across these two glaciers, with a Pearson's r-value of 0.42 and a p-value of < 0.01. When considering a simple 1-year offset that assumes albedo responds to ablation, there is still a significant relationship with an r-value of 0.42, but over two years, this relationship switched to a weak negative relationship that was not significant. Conversely, offsets assuming ablation responds to albedo are significant on both timescales, with an r-value of 0.47 after a 1-year offset and 0.37 over a 2-year offset. There is an interlinkage between albedo and ablation but a stronger forcing of albedo on ablation, as previous studies have noted (Johnson and Rupper, 2020).

5.4. Discussion

5.4.1. Drivers of recent melt

The MAAT increase of 0.24 ± 0.08 $^{o}C\ yr^{-1}$ during the study period and an increase in PDD of 15.0 ± 3.8 $K\ d^{-1}\ yr^{-1}$ are exceptional, both by Antarctic standards (Turner and others, 2020) and in a global context. Mindful of the relatively short period of this study, and the high interannual and multidecadal variability of temperature trends in the APR, the rate of change in air temperature per year on James Ross Island can nonetheless be said to be rapid. Antarctic temperature increases at other sites have typically been in the region of an order of magnitude smaller, with Turner et al. (2020) reporting that temperatures increased at a rate of 0.3 ^{o}C $decade^{-1}$ (i.e. 0.03 $^{o}C\ yr^{-1}$) and 0.2 $^{o}C\ decade^{-1}$ (i.e. 0.02 $^{o}C\ yr^{-1}$) at the nearby Marambio and Esperanza bases respectively, albeit over a longer study period. Indeed, the temperature increases and subsequent lengthening of the summer season recorded here are more

comparable to observed changes in the Arctic, which has undergone the Earth's fastest rate of warming (Arndt et al., 2019; Gutiérrez et al., 2021; England et al., 2021).

Whilst mindful that the albedo data presented in this chapter only provide a limited insight, it appears that albedo varies interannually (**Figure 5.2D**), likely dependent on the combined effects of snowfall, aeolian transport of dust, as well as possible debris sourcing from surrounding rocks (Naegeli and Huss, 2017; Kavan, Nývlt, et al., 2020). Although a rise in air temperature (**Figure 5.2A**) would be expected to increase the rate of glacial melt, a decrease in albedo would further exacerbate melt rates (Naegeli and Huss, 2017; Johnson and Rupper, 2020; Zhang et al., 2021). Changes in albedo induce a positive feedback; whereby dust and other debris lower glacier albedo, leading to melt and thinning which reveals more debris, which acts to keep albedo low (Naegeli and Huss, 2017). The statistical difference in albedo between the north west and south east sectors of the archipelago highlights two things. Firstly the importance of the Ulu Peninsula, a large glacier-free region, a source of dust that, upon aeolian deposition, lowers albedo because large dust storms are observed frequently (Kavan et al., 2018). Dust deposits have also accumulated on Triangular Glacier (Kavan, Nývlt, et al., 2020; Engel et al., 2023, **Figure 5.5**) and Lookalike Glacier (Kavan et al., 2020) on the Ulu Peninsula. Secondly, whilst albedo and ablation influence each other in the short term, the analysis of lag times in **section 5.3.3** suggests that annual albedo has controlled glacier ablation for at least the subsequent two years.

Figure 5.6*: Triangular glacier in 2023. Note the extensive dust depots (resulting in a darkened glacier surface). Photo taken by Michael Matějka.*

More broadly, the James Ross Archipelago is home to several large proglacial areas which are abundant in fine dust (Davies et al., 2013), which is likely to contribute to darkening glacier surfaces in the north west sector, lowering albedo and thus increasing melt rates, particularly in years with less snowfall (Fassnacht et al., 2015). It is likely that the combination of persistent increases in MAAT and PDD (**Figure 5.2A**), alongside high temperatures in 2021/22 and 2022/23 (**Figure 5.2A**) and low surface albedo (**Figure 5.2D**), is likely the cause of enhanced glacier area loss and the exceptional glacier ablation (**Figure 5.2B, C**) in recent years. This loss of glacier mass is acutely shown by *in-situ* ablation data (**Figure 5.4C**), which records consistent ablation for three years. Similarly, there was a consistent thinning in both periods on Snow Hill Island and to the east of Vega Island, as well as around the periphery of James Ross Island, particularly on its southern coast (**Figure 5.4A, B**).

5.4.2. Notable changes in glacier area

Whilst most glaciers on the archipelago have undergone moderate decreases in their area since 2011 (median values of 0.06 % yr^{-1} 2011 to 2017 and 0.38 % yr^{-1} since 2017), three glaciers have shown large aerial changes (**Figure 5.3**). Swift Glacier receded from a marine-terminating environment to a land-terminating setting between 2011 and 2023. Successive years of summer Landsat images reveal that the rate of terminus recession was not linear, with the majority (~ 3 km) of this recession occurring in the austral summer of years 2018/19. This rate of recession is comparable to the highest rates (~ 5 km yr^{-1}) recorded for large tidewater glaciers in the Antarctic Peninsula region (Wallis, Hogg, van Wessem, et al., 2023). It is two orders of magnitude higher than most glacier recession rates recorded in the Arctic, which are typically between 10 and 35 m yr^{-1} (Rachlewicz et al., 2007; Kavan and Strzelecki, 2023); specifically, it is one order of magnitude greater than the highest recession rates (~ 300 m) observed on Svalbard and other glaciers in the Barent's Sea region (Błaszczyk et al., 2021; Carr et al., 2023). Indeed, it is and more akin to exceptional retreat rates (> 1 km $yr^{-}1$) observed in northern Greenland (Carr et al., 2017). This loss of mass from the Swift Glacier ablation tongue is interpreted to be due to a combination of warming air and ocean temperatures (Cook et al., 2016) (Cook et al., 2016), driving surface and subglacial melt. In addition, record low sea ice extent in the Weddell Sea also potentially causing substantial recession due to debuttressing of the ice (Jena et al., 2022; Surawy-Stepney et al., 2024).

In addition, the SLA of Swift Glacier rose to 510 m a.s.l. in 2018, the second-highest SLA recorded for this glacier in the study period. This elevation puts the SLA at the base of the glacier's headwall and would effectively mean that the Swift Glacier outlet received very little accumulation directly from snowfall. Given that the glacier receded rapidly in 2018/19, accumulation from the Ice Cap brought on by avalanching was also likely to have been

minimal. Swift Glacier's topographic setting means it is vulnerable to disconnection from the Mount Haddington Ice Cap (cf. Rippin et al., 2020; Davies et al., 2022), though without any direct observations of avalanching it is not possible to say with certainty that this has occurred. A sudden decrease in nourishment to the glacier tongue, brought on by a disconnection of the outlet glacier from its ice cap has previously been observed to cause the rapid recession of glaciers in North America (Rippin et al., 2020; Davies et al., 2022), and the cause of Swift Glacier's recession is likely to be mechanistically similar. This loss of ice flow through to the glacier tongue has resulted in substantial thinning (as highlighted by data from Hugonnet and others, 2021, **Figure 5.6**). Consequent lowering of the terminus has revealed exposed bedrock and thermokarst features (**Figure 5.7**) that are characteristic of stagnant, degrading ice masses elsewhere (Schomacker and Kjær, 2008; Błaszkiewicz et al., 2023) (e.g. Schomacker and Kjær, 2008, Błaszkiewicz and others, 2023). Whilst this has been interpreted as a substantial recession, disconnected ice masses are often covered in substantial debris cover (Davies et al., 2022) and further research should focus on collating velocity data to verify this interpretation.

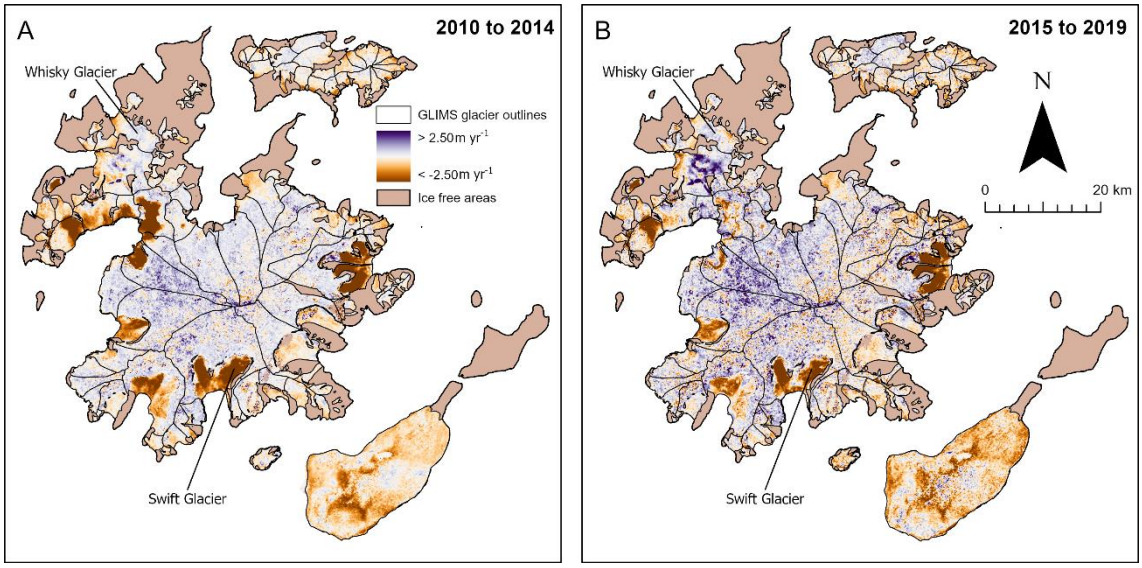

Figure 5.8: *Rate of surface elevation change for* ***A)*** *2010 to 2014 and* ***B)*** *2015 to 2019 (Hugonnet and others, 2021)*

Whisky Glacier and Kotick Glacier are both unusual due to experiencing large advances in their terminus positions. Having receded between 2011 and 2017, the Whisky Glacier terminus appears to have advanced slightly (~ 200 m) between 2017 and 2022, followed by ~ 400 m advance in a single year between 2022 and 2023. Whilst this terminus advance may represent a surge event, in the absence of surface elevation and velocity data it is difficult to make this interpretation with any certainty. This advance occurred despite calving (visible in satellite images) and thinning occurring at the terminus of the glacier (**Figure 5.6**). Further attention should be given to Whisky Glacier in the future, to determine the cause of the advance.

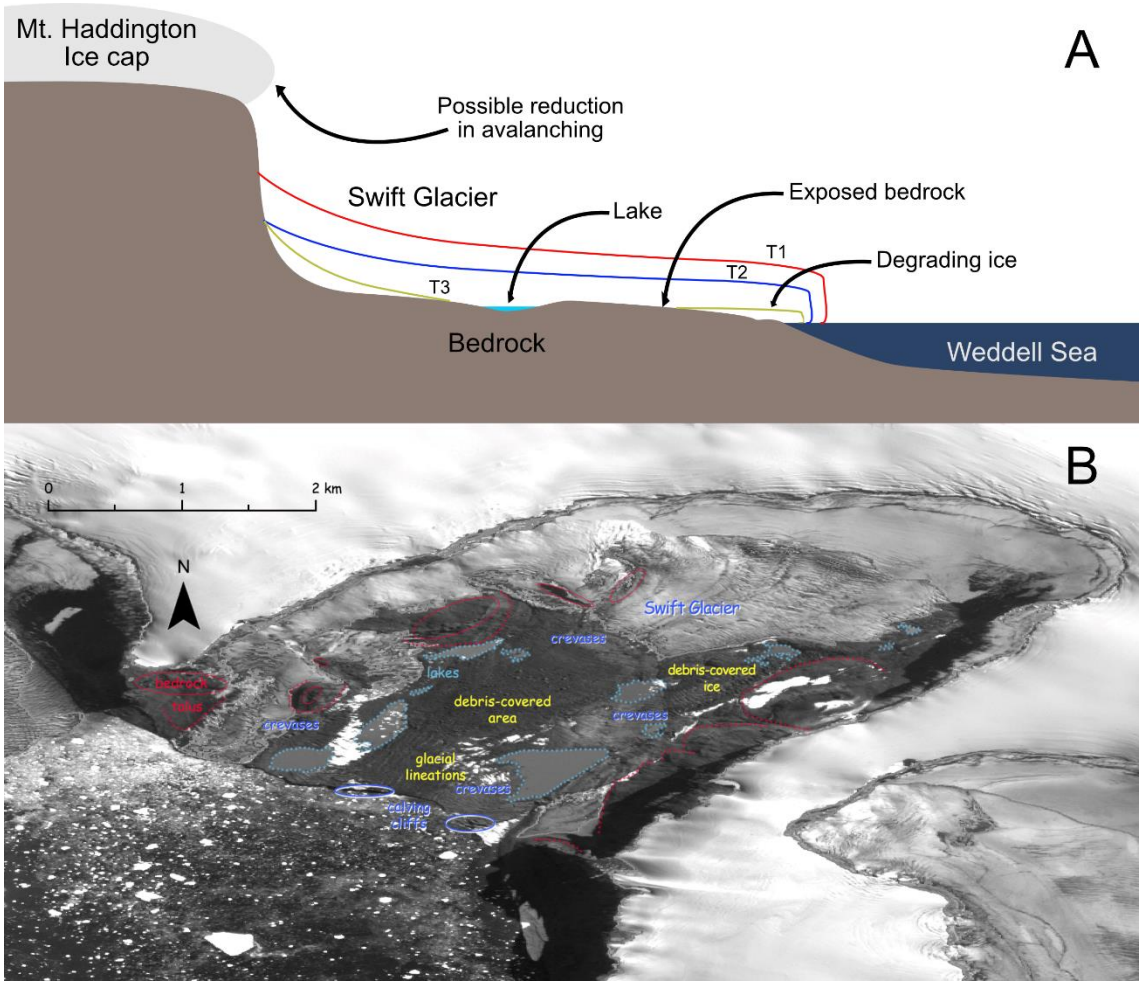

Figure 5.10: A) *A schematic of the mechanism behind Swift Glacier's rapid rate of recession (glacier thinning is exaggerated, and for a theoretical time period 1,2, and 3 (T1-3);* ***B)*** *an annotated Sentinel-2 image of Swift Glacier (2023) following its recession. Annotated image made by Zbyněk Engel.*

The terminus advance of Kotick Glacier coincides with a period for which there is ice surface velocity data (NASA MEaSUREs ITS_LIVE project data, Gardner et al., 2018) and surface elevation data (Hugonnet et al., 2021). The terminus of Kotick Glacier advanced by ~ 350 m in 2014/15 and ~ 300 m in 2015/16 (**Figure 5.3A**) and corresponds to an ice surface velocity increase from 41 m yr^{-1} to 130 m yr^{-1} (**Figure 5.8A**). This suggests that Kotick Glacier may be a surging glacier. This interpretation is further supported by the pronounced surface elevation gain (often referred to as "bulging") present at the glacier terminus, a phenomenon frequently observed as glaciers reach the active phase of a surge cycle (Clarke and Blake, 1991). A period of accelerated elevation gain occurred prior to the terminus advance (**Figure 5.8B, C**), coincident with a reduced rate of thinning upstream of the bulge. These changes occurred at the same time that glacier velocity decreased in 2016 to 121 m yr^{-1} and more obviously to 70 m yr^{-1} in 2017 as it relaxed back into a state of relative quiescence. Therefore, this appears to be the first surge-type glacier to have been identified in Antarctica. Although many glaciers in

the Antarctic Peninsula region have been observed to suddenly increase in velocity (De Angelis and Skvarca, 2003; Glasser et al., 2011), these events were associated with the collapse of the Larsen A and Prince Gustav Ice Shelves and are likely to be the consequence of de-buttressing on the glaciers (Rignot and others, 2004; Joughin and others, 2021).

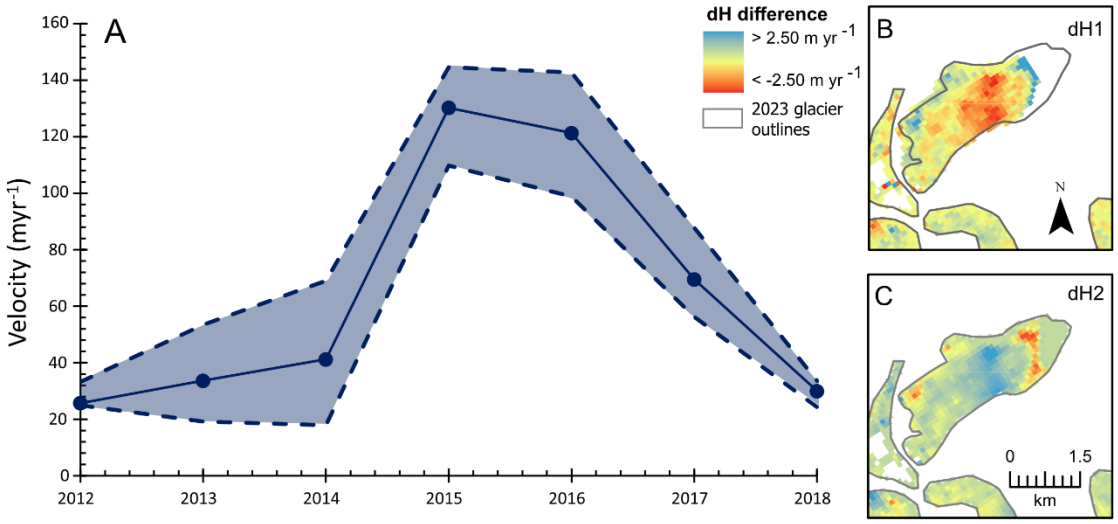

Figure 5.12: *Change in the velocity and surface elevation change rates on the bulge at the front of Kotick Glacier.* ***A)*** *Velocity is described by the median value of velocity on the bulge evident at the front of the glacier, with the shading showing the standard deviation. Insets show the change in surface elevation rates between* ***B)*** *2005 to 2009 and 2010 to 2014 (dH1), and* ***C)*** *2010 to 2014 and 2015 to 2019 (dH2).*

Previous work (Sevestre and Benn, 2015) has highlighted that glacier geometry, in particular glacier length, is correlated with surging behaviour. With a length of ~ 4000 m, a mean annual air temperature measured at the nearby JGM of – 7 °C, and a mean annual precipitation of up to 700 mm yr-1, the geometry of Kotick Glacier and the 'climatic window' are suitable for surging to occur (Sevestre and Benn, 2015; Benn et al., 2019) (Sevestre and Benn, 2015; Benn and others, 2019). Indeed, Carrivick et al. (2012) commented that, considering the environment, it was surprising that no surge-type glaciers had been observed on James Ross Island.

Whilst the velocity and surface elevation data, as well as the glacier's climatic setting and geometry, make it likely that this is a surge-type glacier, it is important to be mindful that cyclicity has not been observed due to an absence of velocity data for this region before 2012 and the low availability of satellite images from before 1990. It is feasible that recent temperature increases in the region may have made this surge event more likely by delivering more meltwater to the bed (Tuckett et al., 2019; Benn, 2021), although other glaciers in the region maintained a positive mass balance in 2015 when this surge event occurred (Engel et

al., 2018). Possible geomorphological evidence for surging has previously been described on the Antarctic Peninsula, but never directly observed (Nichols, 1973; Wellman, 1982), and further research looking for geomorphological evidence for surging around Kotick Glacier may be useful to determine if there is evidence of cyclicity.

5.5. Conclusions

In this chapter, multiple datasets have been brought together to highlight changes to glaciers on the James Ross Archipelago. Between 2010 and 2023, MAAT increased by 0.24 ± 0.08 $^{o}C\ yr^{-1}$, and PDD increased by 15.0 ± 3.8 $K\ d^{-1}\ yr^{-1}$. This has led to an increase in the rate of glacier area reduction: the median loss of glacier area between 2011 and 2017 was 0.06 % yr^{-1}, but then increased six-fold to 0.38 % yr^{-1} between 2017 and 2023. Glacier thinning has also been observed over the same period, at a maximum rate of 1.5 m yr^{-1} at 200 to 300 m a.s.l. on Lookalike Glacier and Davies Dome in 2023. Very high temperatures, combined with observation made in this study of low albedo (0.20 in the north west sector of the islands, and 0.26 in the south east sector), have caused enhanced melt rates since 2020. SLA has been gradually increasing in both sectors of the archipelago since 2015 and reached maximum positions of 341 m (SE) and 390 m (NW) in 2022 and 2023, respectively, which is an increase from a minimum position of 153 m a.s.l. (NW, 2015) and 110 m (SE, 2016). The exceptionally low albedo values, which are likely to be the consequence of low rates of snowfall and the occurrence of localised dust storms in the archipelago's extensive proglacial regions, will likely exacerbate future melt rates.

Some exceptional changes to glaciers have also been highlighted in this study. To the south west of James Ross Island, Swift Glacier has experienced an exceptional loss of area at the front of its terminus, receding by 4 km since 2011, 3 km of which largely occurred in 2018/19. This is amongst the fastest glacier recession rates observed anywhere globally. This rapid loss of ice is probably the result of rising air and ocean temperatures, as well as a rapid loss of accumulation possibly brought on by a disconnection from the Mount Haddington Ice Cap. This dramatic loss of ice highlights the positive feedbacks in these climate-glacier-topography systems and, in particular, the non-linearity of glacier recession that can be experienced by ice cap outlet glaciers draining over plateaux edges.

Anomalies to the overall terminus recession and areal loss of ice across the archipelago has also been observed at some glaciers, most notably at Kotick Glacier. Kotick Glacier increased its velocity in the terminus region from 41 m yr^{-1} to 130 m yr^{-1} between 2014 and 2015. This tripling of the frontal velocity, combined with the rapid terminus position advance, formation of a bulge near the terminus and other substantial changes in its surface elevation, indicate

that it is the first surge-type glacier to have been identified in Antarctica. The cause of another advance on Whisky Glacier is less clear, and further research should be conducted to monitor future changes in its frontal position and velocity.

6. Discussion and outlook for the future

6.1. Glacial-proglacial interactions

6.1.1. Changing land cover

Thus far, this thesis has highlighted that glaciers are receding across the Antarctic Peninsula and sub-Antarctic islands and in doing so they are exposing new proglacial surfaces. Existing proglacial land cover has been shown to be dynamic and rapidly changing. These changes in land cover have implications for local climatic conditions and the transport of sediments into the ocean. Deglaciation and land cover change is most pronounced at northerly sites, where vegetation coverage is increasing, and glacier coverage is decreasing. In turn, this impacts the local climate system via two feedback mechanisms (Mooney et al., 2020):

1) Changes to surface sensible and latent heating
2) Decreasing albedo and increasing the absorption of radiation at the surface

At high latitudes, land cover change primarily affects local climates by the absorption of radiation (Mooney et al., 2020) as glaciers recede and expose darker surfaces (**Figure 6.1**). In transitional zones between wet and dry climates (such as the Ulu Peninsula on James Ross Island), changes in soil moisture (represented as changes in the coarse and wet sediment class in Chapters 2 and 3) play an important role in sensible and latent heating. Soil moisture can reduce heat extremes through evaporative cooling (Seneviratne et al., 2018, **Figure 6.1**).

In the Arctic, similar positive feedbacks have been observed between vegetation and local climate systems. In particular, expanding woody vegetation decreases albedo (Loranty et al., 2014). However, woody plants are not present on the Antarctic Peninsula or sub-Antarctic, where observed expansion of vegetation is limited to non-vascular plants and grasses (Torres-Mellado et al., 2011; Barták et al., 2015). In the Arctic the most significant vegetation-climate feedback is related to changes in tree cover (i.e. albedo), whereas in the Antarctic it is related to sensible and latent heat fluxes. Antarctic feedbacks are associated with latent and sensible heat fluxes as a consequence of the water-retention capabilities of moss, and the role they play in insulating the ground (Hrbáček et al., 2020). The implication for the Antarctic Peninsula and sub-Antarctic islands is that the expansion of vegetation acts to buffer increases in air temperature and reduces the rate of permafrost-affected soil thaw (**Figure 6.1**). In addition to affecting local climate, vegetation will also have implications on sediment export, as vegetation stabilises sediments and reduces sediment loads in streams (Klaar et al., 2015; **Figure 6.1**).

Changes in Antarctic land cover also have other implications for the longevity of glaciers in the region. Proglacial environments are important sources of dust (Kavan, Nývlt, et al., 2020), and

the quantity of dust available for transport increases as proglacial regions expand following glacier recession (Prospero et al., 2012). This, in-turn, creates a negative feedback with glaciers; as aeolian sediment transport increases, so too does the deposition of sediment on glaciers (**Figure 5.4**). This results in lower albedo and higher rates of melt (Krinner et al., 2006; Painter et al., 2007; Zhang et al., 2021, **Figure 6.1**). The feedback mechanisms associated with deglaciation can be broadly split into two types: **i)** increased local temperatures as land surface albedo falls, and; **ii)** decreased glacier albedo from increased dust transport (**Figure 6.1**). These are only slightly tempered by the role vegetation expansion and increased meltwater have in increasing soil moisture and slightly decreasing air and ground temperatures.

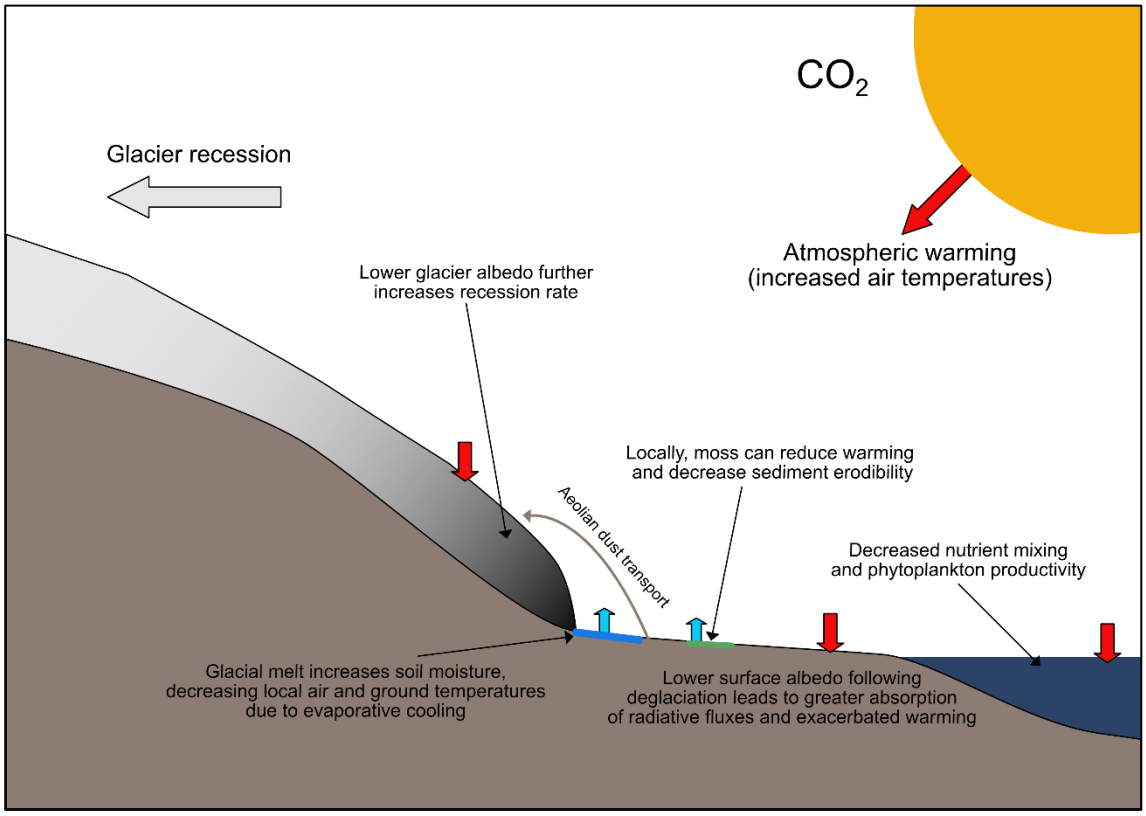

Figure 6.1: *The interplay between glacial and proglacial land systems*

Further to affecting local climate, deglaciation also affects the quantity of sediment, and therefore nutrients, delivered to the Southern Ocean. In Greenland, changes in sediment transport, and a consequential reduction in phytoplankton productivity and CO_2 uptake, has been observed as glaciers recede onto land (Meire et al., 2023). Marine terminating glaciers supply nutrients to oceans through the subsurface release of sediments (Meire et al., 2023), and through surface meltwater (Chu et al., 2009). These sediments stimulate diatom blooms, and subsurface sediments encourage mixing of the water column. However, land terminating glaciers do not play a role in ocean mixing and instead create a stratified, low light environment as pulses of sediment rich water flow into the ocean; consequently reducing

productivity (Cloern, 1987). Furthermore, a loss of marine ice reduces albedo and increases water temperatures (Riihelä et al., 2021; **Figure 6.1**). The spatial coverage of a land-terminating glacier also affects the sediment budget of a region, and increases the catchment's sensitivity to changes in air temperature (Chapter 4). Similar to other world regions (Carrivick and Tweed, 2021), the transfer of sediments is closely controlled by precipitation and air temperate and, where permafrost-affected soils are extensive, ground temperature (Kavan et al., 2017; Hrbáček et al., 2023; Kavan et al., 2023).

6.1.2. The role of extreme weather

Heatwaves are sporadic events, but are occurring at an increased frequency both globally (Perkins-Kirkpatrick and Lewis, 2020) and across Antarctica (Turner et al., 2021). Extreme temperatures in 2022 and 2023, particularly across Europe, have received extensive media attention. The clearest impact of these heatwaves on the cryosphere was in the Swiss Alps, where glacier volume decreased by over 10 % over just two years. Over these two years, the surface mass balance of Swiss glaciers were exceptionally low, due to a combination of warm temperatures and decreased winter snowfall (GLAMOS, 2023). Exceptional temperatures in Antarctica over the past few years have also led to high rates of surface melt across the APR (Banwell et al., 2021; Siegert et al., 2023). Consecutive years of warming on the James Ross Archipelago have substantially reduced glacier area (Chapter 5). An increase in the magnitude of negative surface mass balance (SMB) was measured on the Ulu Peninsula between 2015 and 2021, compared to preceding years (Engel et al., 2024), and ablation stake data indicate that the magnitude of negative SMB is likely to have further increased in 2022 and 2023 as a result of extreme weather (**Figure 5.4C**). As highlighted in Chapter 5, these extreme temperatures are often associated with substantial lowering of glacier surfaces; this in turn can expose englacial debris. The evolution of a surface debris layer can impact its response to further climatic changes – a thin layer may enhance melt rates (Naegeli and Huss, 2017) whereas a thick debris cover will insulate the ice (Pelto, 2000; Glasser et al., 2016).

Whilst long term precipitation records are sparse in Antarctica, the decrease in albedo on James Ross Island, especially on high elevation regions such as the Mount Haddington Ice Cap, indicate decreased snowfall across the James Ross Archipelago in 2022 and 2023 (**Figure 5.4A**), which ultimately contributed to enhanced glacier surface lowering. Projecting future changes in precipitation is also challenging for the Antarctic Peninsula, but it is likely that there will be a modest increase in precipitation in coastal regions of Antarctica (Vignon et al., 2021; Tewari et al., 2022). This increase in precipitation will be most pronounced on the western side, where the lengthening of the summer season will cause an increase in rainfall days, further enhancing glacier melt (Turner et al., 2005; Vignon et al., 2021). Projections for the eastern side of the

Antarctic Peninsula are more uncertain, but most suggest a slight increase in precipitation (both snowfall and rainfall), which may act to slightly temper the rate of glacier thinning.

In addition to affecting the glaciated environment, heat waves lead to pulses of activity in proglacial regions. As observed in Chapter 4, and indeed in proglacial regions globally (Carrivick and Tweed, 2021), warm temperatures change the dynamics of sediment transport such that streams transport the majority of their annual sediment load in fewer shorter-duration, higher-magnitude events. Similarly, extreme precipitation events also act to increase the availability of liquid water (González-Herrero et al., 2023). These high-magnitude events are facilitated in two ways: **i)** increased sediment delivery to the catchment by the thaw permafrost-affected soils, and; **ii)** increased liquid water into streams. Warming temperatures have also been observed to destabilise ice-cored moraines (Ravanel et al., 2018), and increase the availability of unconsolidated sediments in the catchment; indeed, a similar phenomenon was observed at the Bohemian Upper site in Chapter 4 (**Figure 4.14**). This sediment is then entrained when higher temperatures increase meltwater discharge from glaciers and snow-patches. Further water is supplied by precipitation as well as by active layer soils when air temperature, and consequently ground temperature, rises (Kavan et al., 2017; Hrbáček et al., 2021, Chapter 4), though enhanced evaporation rates in a warmer climate may decrease the proportion of this water reaching streams (Nývlt et al., 2016).

6.2. The future of proglacial regions on the Antarctic Peninsula and sub-Antarctic Islands

6.2.1. Challenges in projecting the future of the Antarctic Peninsula

Although some work has been done to investigate future proglacial habitats in Antarctica (Lee et al., 2017; Bosson et al., 2023), these studies commonly contain substantial omissions or uncertainties. Firstly, these studies (at least in part) make use of the RGI dataset, which does not cover the Antarctic continent. This is partly with good reason, as many glaciers to the south of the Antarctic Peninsula are connected to the Antarctic Ice Sheet (Windnagel et al., 2023), but this does not explain the omission of glaciers on the Antarctic Peninsula north of 70 ^{o}S, whose connectivity with the Ice Sheet is very low (Huber et al., 2017). Whilst these glaciers are mapped and available within the GLIMS data repository, most global studies make use of the RGI dataset (Pfeffer et al., 2014) for consistency, thus excluding the Antarctic Peninsula mainland (e.g. Bosson et al., 2023).

For studies that cover Antarctica, the use of the RGI dataset for large-scale modelling casts doubt on the reliability of the results of existing studies, and limits their applicability for modelling the future of river and lake networks. This is because the RGI outlines are known to

show snow-filled river valleys and frozen lakes as glaciers. These irregularities within the RGI dataset were not addressed in its most recent update (RGI Consortium, 2023) and, whilst others have attempted to address the issue (Liu et al., 2024), these improved data are not openly available. Since it is often rivers and lakes that are misrepresented by this dataset, accurately depicting their future extent (cf. Steffen et al., 2022) is not possible to do robustly. These issues are compounded, since the glacier outlines are also used to generate ice thickness estimates (Farinotti et al., 2019). Whilst Bosson et al. (2023) identify changes in freshwater ecosystems, the lack of available maps to verify this make this challenging to assess. This is not to say these data are redundant; indeed this thesis highlights that datasets covering the proglacial evolution of Antarctica are sparse, and these datasets certainly move the field forward. However, it is important to recognise that these data contain fundamental flaws, and that further work is needed if we are to improve key datasets that feed glacier models.

6.2.2. Possible future glacier evolution

In order to consider how proglacial regions on the Antarctic Peninsula and sub-Antarctic islands are likely to change in the future, it is imperative to first consider the future evolution of glaciers. Using the data collated in Chapter 5, the longevity of glaciers on the James Ross Archipelago can be considered using the SLA data described (**Figure 5.2**) in relation to glacier hypsometry. This was conducted in ArcGIS Pro by identifying glaciated land above the minimum and maximum SLAs identified in Chapter 5, based upon data from the REMA DSM (Howat et al., 2019)

Parts of glaciers below the minimum recorded median SLA in Chapter 5 (132 m a.s.l) are vulnerable to future melting (**Figure 6.2**) as temperatures increase, and include large proportions of Snow Hill Island, the southern coast of Vega Island and the periphery of James Ross Island (which have already experienced thinning in recent years). As the SLA of these regions rise, so too will the ELA (Rabatel et al., 2013). As the accumulation zone of these glaciers shrinks, ice flux will also likely reduce and, subsequently, lower regions of the glacier will thin and recede.

The Mount Haddington Ice Cap, as well as the ice caps of Vega Island, are characterised by upland plateaux surrounded by deep glacial valleys and cirques. Glaciers in this region can be separated into two sections, an upper section on the ice cap plateaux, and lower sections of "glacier tongues" in cirques. As glacier SLA, and consequently ELA, rises in a warming climate, these low-elevation glacier tongues will likely disconnect from their upper regions on the plateaux, following a decrease in ice-flux (Rippin et al., 2020). As a result, these glacier tongues will thin, with the underlying bedrock topography playing a greater role in controlling ice flow,

resulting in stagnant ice tongues with increased crevassing, decreased velocity and increased debris cover, which further increases the thermal energy stored within the ice (Davies et al., 2022). These glacier tongues will subsequently recede into smaller ice-masses, concomitantly increasing the proglacial area, only persisting in heavily shaded areas and primarily nourished by wind-blown snow (Boston and Lukas, 2019). The lower parts of glaciers to the south of James Ross Island are, therefore, likely to significantly reduce in size in the coming decades, resulting in a substantial loss of ice above that which is already expected (Lee et al., 2017; Engel et al., 2019). In the future, parts of north west James Ross Island and Vega Island are also likely to be vulnerable to disconnection. Recent surface lowering has revealed steep

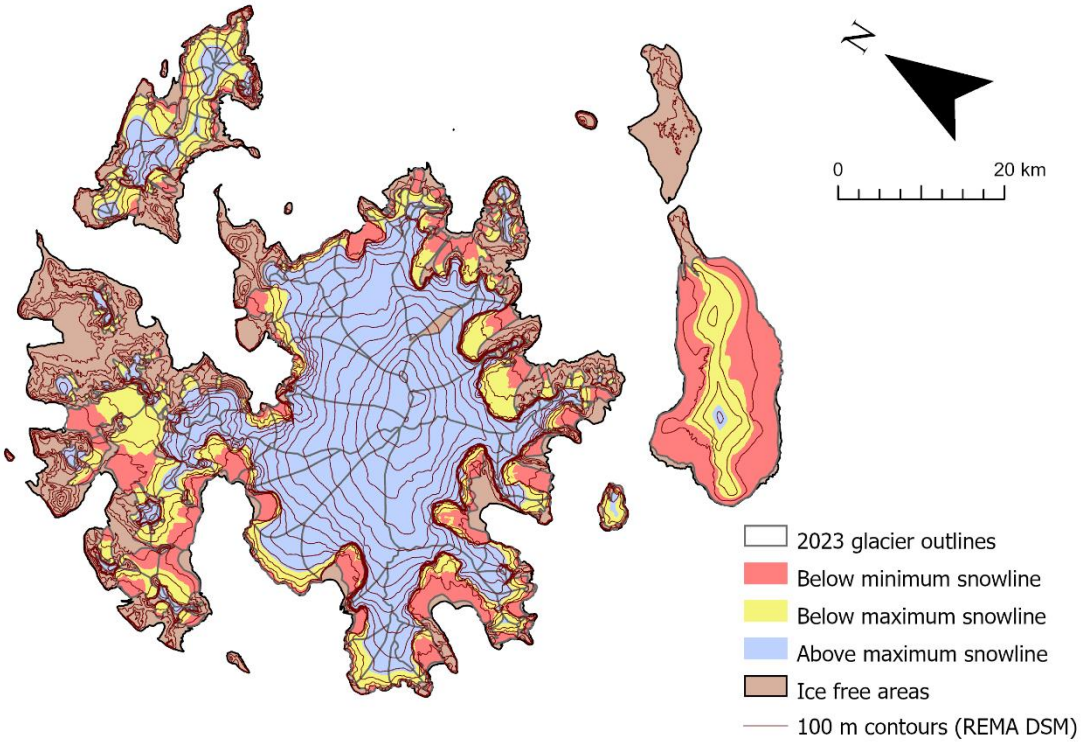

Figure 6.2: *Map of regions with elevation below the minimum and maximum snowlines and above the maximum snowline according to REMA (Howat and others, 2019). The minimum of these values was 132 m, and the maximum was 355 m.*

topography at the glacier bed that would make several more glaciers in the archipelago vulnerable to disconnections in the more distant future.

Vulnerability to glacier disconnections is not limited to James Ross Island, and indeed other parts of the Antarctic Peninsula are likely to be vulnerable to these processes. Given that the Antarctic Peninsula is projected to experience temperature increases up to 4^{o}C by 2100 (Hughes et al., 2021), it is reasonable to assume that the changes that have been experienced on the James Ross Archipelago will migrate poleward with rising temperatures (González-

Herrero et al., 2024). Whilst projections of the future extent of proglacial areas in Antarctica have been previously investigated (Lee et al., 2017; Bosson et al., 2023), they typically do not consider the role that hypsometry, and other non-linear feedbacks (e.g. changes in debris cover, albedo, and glacier velocity), may play in accelerating future accelerated mass losses. Work done in Alaska (notably by Davies et al., 2022), has highlighted that glacier disconnections primarily occur where a steep slope (mean of 26^{o}) intersects a plateaux (a high elevation region with shallow slopes of <10^{o}). These values are broadly consistent with the Swift Glacier recession/disconnection described in Chapter 5 (cf. **Figure 5.3C**).

Using this research, areas of the Antarctic Peninsula that may be vulnerable to future disconnection can be identified by making use of the REMA DSM (Howat et al., 2019), and the GLIMS glacier outlines covering the Antarctic Peninsula (Raup et al., 2007; Huber et al., 2017). This can be achieved in ArcGIS Pro by:

1) Identifying plateau regions within REMA, defined as > 1000 m a.s.l., with a slope of < 10^{o}.
2) Finding steep slopes, for a conservative estimate this is defined as > 30^{o} (a 500 m buffer was created around these steep regions, to account for gaps in DEMs that are common in steep terrain).
3) Finding the intersect between the plateaux and steep slopes and querying the glacier inventory for glaciers that intersect these points and have a mean elevation > 1000 m a.s.l.

Although this is a relatively crude approach, and possibly an overestimation, it highlights that 1/3 of the glaciated area of the Antarctic Peninsula may be vulnerable to disconnection (**Figure 6.3**) and, thus, rapid mass loss through surface lowering and frontal recession is possible (**Figure 5.7**). In particular, it highlights the potential for accelerated glacier mass loss to increase proglacial area beyond what is already projected. Glacier area around the periphery of Antarctica is expected to decrease by between 8 and 26 % by 2100, though much of this is expected to be below sea level (Bosson et al., 2023). Between 2 and 9 % of present day glacier area is expected to become terrestrial or lacustrine proglacial area, accounting for a total area of between 2,500 km^2 and 11,000 km^2 (Bosson et al., 2023). Across the entirety of Antarctica, proglacial area could increase by up to 17,300 km^2 (Lee et al., 2017). Both of these studies highlight that the northern parts of the Antarctic Peninsula are expected to undergo the greatest amount of change. Neither model accounts for the potential for non-linear recession because of glacier disconnection events, which the northern tip of the Antarctic Peninsula appears to be most susceptible to (**Figure 6.3**), and, therefore, current estimations for future proglacial area may be an underestimation.

Other non-linear feedbacks are also often not considered in glacier evolution models. First, a rise in SLA (such as that observed on the James Ross Archipelago) will likely increase the equilibrium line altitude (ELA) of the glaciers which will, due to the low slope of plateaux and ice cap accumulation areas, significantly reduce the size of the accumulation zone, and lead to enhanced melt (Åkesson and others, 2017; McGrath and others, 2017). As ELA rises, so does the area of bare ice, which has a lower albedo than snow and exacerbates melt further (Johnson and Rupper, 2020). Indeed, the initial melt of the glacier may itself be enhanced by dust deposits that reduce albedo, as may be the case for the ablation observed at Davies Dome and Lookalike Glacier (**Figure 5.5**). Furthermore, as glaciers recede they expose large proglacial sites that are themselves new sources of dust. This adds an additional component of non-linearity to glacier recession, as dust from these regions can be deposited on glaciers; lowering albedo and further accelerating glacier melt (Oerlemans et al., 2009; Kavan et al., 2020). If glaciers darken, in combination with rises in SLA, these non-linear feedbacks are likely to affect many glaciers across the Antarctic Peninsula and could lead to substantial melt, particularly if ELA rises above the maximum elevation of some glaciers (McGrath and others, 2017). Plateaux, such at the Mount Haddington Ice Cap will likely sit above the maximum SLA for the foreseeable future, and so are at low risk of ablation. However, their relatively low relief means that they are sensitive to rising air temperatures and rising SLAs, and could therefore experience widespread melt with only minimal warming (Boston and Lukas, 2019), similar to that occurring on Snow Hill Island (**Figure 5.6**). Whilst this may be offset by modest increases in snowfall in the eastern Antarctic Peninsula, increased liquid precipitation in the western part of the Antarctic Peninsula may further enhance this effect.

Whilst warmer temperatures will lead to glacier thinning, and potentially decrease glacier velocities in some parts (Carrivick et al., 2023), many glaciers on the Antarctic Peninsula are likely to respond with increased velocities as enhanced glacier melt increases the supply of water to the bed of glaciers (Tuckett et al., 2019; Wallis, Hogg, van Wessem, et al., 2023). In turn, this can lead to enhanced rates of recession (Wallis, Hogg, Meredith, et al., 2023).

6.2.3. Future evolution of proglacial environments

As glaciers retreat, proglacial areas will expand (**Figure 6.3**), and many more marine-terminating glaciers are likely to recede onto land as glacier SMBs decrease as a consequence of rising temperatures and changes in precipitation. As a glacier recedes from its initial marine terminus, onto land, several key transitions in the land system occur:

1) Glaciers give way to new “ice free” coastal habitats
2) Meltwater is channelled into newly formed streams and rivers
3) New lakes form where there are closed topographic basins or glacial overdeepenings.

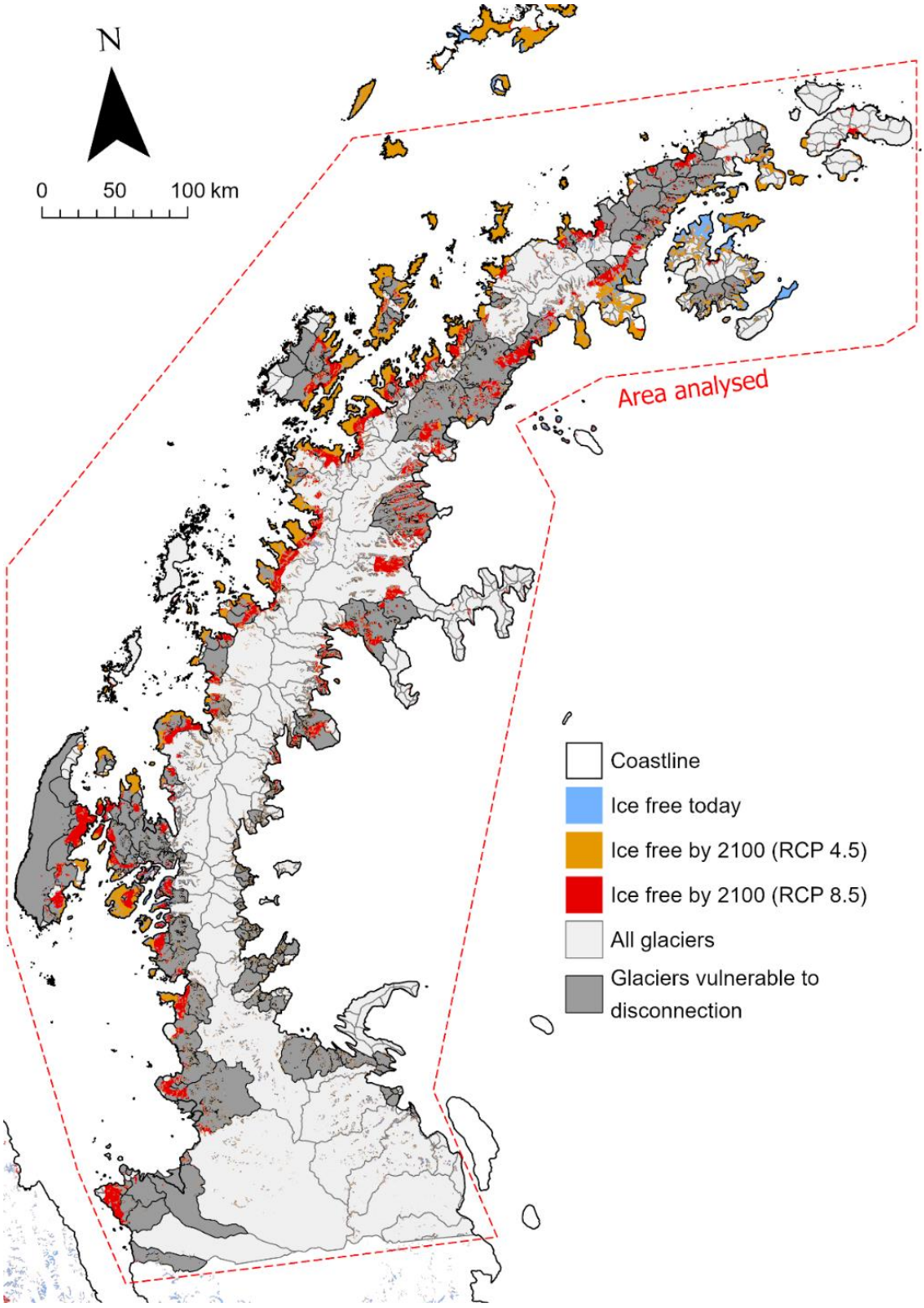

Figure 6.3: *Proglacial area on the northern Antarctic Peninsula for the present day (blue), and as projected for RCP 4.5 (orange) and 8.5 by 2100 (red), from Lee et al. (2017). Glaciers potentially vulnerable to disconnection, and subsequent accelerated glacier recession, are highlighted in dark grey.*

At each of these transitions, changes occur in the transport of sediment and nutrients from the land. The first of these has been well documented in the Arctic, especially on Svalbard (Kavan and Strzelecki, 2023), where the terrestrial coastline has increased in length by 16.4 %. Glacier recession will change the habitats in the region; in the Arctic, the loss of tidewater glaciers has been detrimental to the populations of many mammals and seabirds (Lydersen and others, 2014). Furthermore, it will cause a loss of productivity in coastal regions. Whilst the exposure of new land surfaces is likely to be positive for lichens and plants (depending on the availability of liquid water), some of these species may be invasive (Heller and Zavaleta 2009; Golledge and others, 2010; Olech and Chwedorzewska, 2011). Some parts of Antarctica are greening, particularly more northern sites such as Byers Peninsula (South Shetland Islands, cf. Chapter 3, **Table 3.3**). It may be the case that the drier, eastern sector of the Antarctic Peninsula region sees sediment yields increase from proglacial regions as glaciers recede, whereas the warmer and wetter west side may be more suitable for relatively dense vegetation (Fretwell et al., 2011) that could stabilise sediments. Conversely, in dry summers, the eastern Peninsula would have lower sediment yields with less meltwater availability. However, liquid precipitation is also projected to increase across Antarctica, particularly on the northern and western Antarctic Peninsula (Vignon et al., 2021), which is also likely to increase sediment yields (cf. Chapter 4).

Progressive deglaciation means that landscapes presently covered by glacier ice will become proglacial with rivers fed by diminishing glaciers and perhaps eventually looking similar to the rivers discussed in Chapter 4, specifically the Bohemian Stream catchment and the Dirty Stream that is directly fed by Crame Col Glacier. Streams that are in newly-deglaciated catchments are characterised by unconsolidated sediments (Davies et al., 2013), with high connectivity and relatively high sediment loads (Carrivick and Tweed, 2021). These sites are typically characterised by several active channels with braiding (Overeem et al., 2017). Sediment load decreases as vegetation colonises a region and glacier area decreases (Klaar et al., 2015; Brown et al., 2015). Following this stabilisation, and as meltwater creates more pronounced, incised, channels, connectivity decreases; which in turn decreases sediment load (Carrivick and Tweed, 2021). It is of note that, despite total deglaciation, the Algal Stream (cf. Chapter 4), still has relatively high sediment loads. This is, at least in part, because James Ross Island's harsh environment makes it a challenging place for vegetation to colonise (Nývlt et al., 2016). However, warming temperatures may make James Ross Island more habitable in the near future (Barták et al., 2015; Siegert et al., 2019), depending on the availability of liquid water.

Sediment loads to the Southern Ocean will also be tempered by the creation of new lakes. Proglacial lakes form when glaciers receded, revealing topographic overdeepinings that are

filled by meltwater. These lakes are an important consideration in proglacial systems, as they affect the stability of glaciers, and interrupt the delivery of meltwater and sediment to the ocean (Carrivick and Tweed, 2013). In recent years, there has been an increase in both the number and size of lakes on sub-Antarctic Islands (Rosa et al., 2022), an observation that is supported by this thesis (**Figure 3.3**), where new lakes have been observed to have formed on Snow Island. Modelling of Alpine catchments (Steffen et al., 2022) highlights that the number of proglacial lakes will increase as temperatures rise and glaciers recede. These lakes act as sediment traps (Carrivick and Tweed, 2013), decreasing sediment loads into the Southern Ocean. Often, these lakes are shallow, transient features that are either infilled by sediments, or drain as their ice-cored moraine dams melt (Tomczyk et al., 2020; Steffen et al., 2022). Theoretically, this should subsequently increase sediment loads, however these changes will occur over several decades, and the loss of lakes must also be balanced against other changes to land cover (e.g. channelisation and vegetation expansion), which will decrease sediment yields.

6.3. Future research directions

In this thesis, the glacial and proglacial evolution of the sub-Antarctic and Antarctic Peninsula have been explored. Through this analysis, further questions have been raised as to: **a)** how proglacial regions have evolved in the more distant past (i.e. 20th Century), and; **b)** how proglacial areas may advance in the future (**Figure 6.3**). It has also highlighted the need to collect more field data, so that Antarctic proglacial regions may be more adequately monitored.

Chapter 2 highlighted the dearth of literature available to understand more remote parts of Antarctica, particularly on Alexander Island. Whilst a great deal of scientific progress can be made through modelling efforts and remote-sensing, the importance of *in-situ* observations, such as geomorphological mapping, should not be overlooked (**Figure 6.4**). Although a robust land cover map of six proglacial regions in Antarctica was presented in Chapter 2, these data would undoubtedly be improved with the availability of better field data and maps that describe the land surface. Efforts to improve field observations of land-surface types would improve the availability of training data, and thus the accuracy and reliability, of future land cover maps.

There is also a lack of data surrounding sediment export from proglacial regions in Antarctica, largely owing to the logistical challenges of transporting stream monitoring equipment. Chapter 4, in part, takes a small step in improving this. Furthermore, the use of equipment such as the SonTek FlowTracker (cf. section 4.2.1) makes stream monitoring more accessible,

since this equipment is small enough to be transported on a commercial flight in a standard suitcase. Although this approach only allows for spot measurements, these can be combined with continuous monitoring of stream stage height as a powerful tool to widen the monitoring of Antarctic streams (**Figure 6.4**). This would create a wider knowledge of how sediment fluxes respond to different climatic factors, and therefore the potential impacts of climate change in transferring nutrients to the Southern Ocean. In glaciated catchments, this would have the additional impact of providing a continuous record of glacier ablation (cf. Kavan et al., 2023).

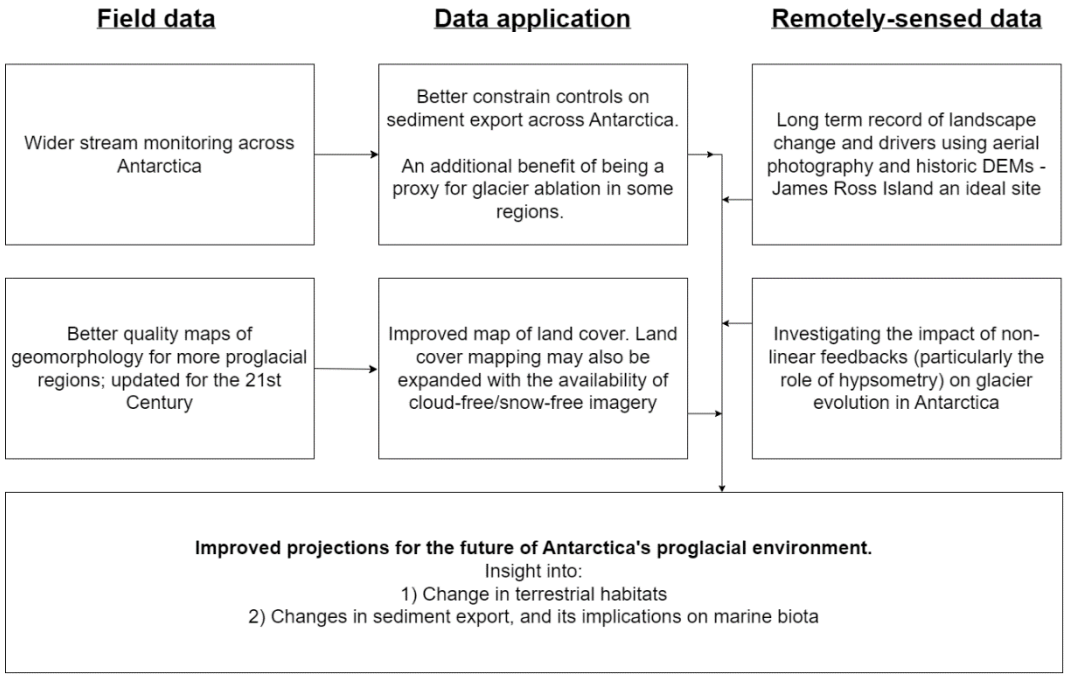

Figure 6.4: *Potential future research directions, and how they come together to improve our knowledge of Antarctica's proglacial environment and potential evolution*

Although the change in proglacial regions since 2000 has been quantified in this thesis (Chapter 3), information on land cover before this time is lacking. This is because Landsat images from before 2000 are sparse, and often geometrically inadequate. However, many parts of Antarctica, notably (but not limited to) James Ross Island, have been surveyed and photographed aerially over the last 50 years by the Royal Navy and BAS; indeed these images have been processed into DEMs (Czech Geological Survey, 2009) (**Figure 6.4**). This permits an exploration historic changes in both the glacial environment (e.g. Geyman et al., 2022), as well as changes in the proglacial environment, such as changes in the river channels, and degradation of ice-cored moraines (e.g. Tonkin, 2023). This research will be essential for understanding how Antarctic proglacial regions have evolved in the past and, therefore, how they are likely respond to future warming. Crucially, it would allow glacial and proglacial environments to be considered holistically; jointly supplying water, nutrients, and habitat

space to a wide-range of organisms. There may also be further information available in written historical archives (e.g. Headland et al., 2023).

Chapter 5 and section 6.2.1. highlight the potential implications of non-linear feedbacks on accelerating glacier recession rates on the Antarctic Peninsula. Given these factors are typically not typically included in glacier evolution models; there is a need to quantify the potential implication of non-linear feedbacks, particularly glacier disconnection events, on the future evolution of Antarctica (**Figure 6.4**). Since disconnected glaciers typically recede at an accelerated rate (Boston and Lukas, 2019; Rippin et al., 2020; Davies et al., 2022), understanding the potential for these non-linear responses in the future will have important implications on future sea-level rise projections, as well as improving our understanding of habitat evolution in the future.

7. Summary and conclusions

7.1. Research summary

This thesis has documented the composition and ever-evolving dynamics of the proglacial environment in the Antarctic Peninsula Region and sub-Antarctic islands. This has been achieved by combining remote sensing techniques and fieldwork to reveal the dynamic nature of the Antarctic landscape.

Chapter 1 of this thesis outlined the importance of proglacial regions globally, and that relatively little is known about these environments in Antarctica. This thesis sought to rectify that knowledge gap, and four research objectives were to set (section 1.3) to provide a framework in which some of the key "unknowns" could explored.

Objective 1: *"Use the existing maps of Antarctica to design the first unified land cover classification of the major proglacial regions of the Antarctic Peninsula and sub-Antarctic islands using optical satellite images."*

Chapter 2 of this thesis made use of several published maps to classify the proglacial landscape of several major proglacial areas across the Antarctic Peninsula and sub-Antarctic islands, as well as the McMurdo Dry Valleys. This was conducted using a K-means approach to classify Landsat-8 OLI TOA images, which has been demonstrated to be an ideal approach to classifying regions where there is limited training data available. Ten land cover classes were mapped: turbid water, water, wet ice, ice, land (non-differentiated), bedrock, fine sediment, coarse sediment, and vegetation. They were mapped at 30 m resolution at an accuracy of 77.0 %. **This study identified a latitudinal trend in the coverage of different land types, notably that vegetation and coarse/wet sediment are typically more abundant in sites that are more northerly located**. This work provides a first step in understanding the composition of Antarctica's important proglacial regions. It was also highlighted that there is a need for greater ground-verified data to improve the accuracy of future Antarctic land classifications.

Objective 2: *"Investigate how the land cover has changed on Antarctic Peninsula and sub-Antarctic islands during the 21st century."*

Change-vector analysis was used in Chapter 3 to investigate how the major proglacial regions of the Antarctic Peninsula and sub-Antarctic islands, as well as the McMurdo Dry Valleys, have evolved over the past two decades. This was achieved at an accuracy of 80 % and highlighted a latitudinal pattern of ice loss and the consequent expansion of proglacial regions. For example, the proportion of landscape change on South Georgia due to the loss of ice is two orders of magnitude greater than that in the Dry Valleys. Furthermore, extensive land cover change was

highlighted on Alexander Island, where 50 % of the proglacial coverage has changed this century, likely because of recent dramatic warming events around the George VI ice shelf. **The key finding of this chapter is that both the glacial and proglacial landscapes of the Antarctic Peninsula and sub-Antarctic Islands are changing rapidly, particularly in warmer regions with more glacial melt.** The dataset provides a first step in understanding how Antarctica's important proglacial regions have changed, and provides an important first insight into how proglacial landscapes are evolving because of rising temperatures and glacier recession.

Objective 3: "*Explore how different environmental factors and ground conditions influence sediment export from two river catchments on James Ross Island."*

An in-depth analysis of river water discharge and sediment transport in two neighbouring catchments on Ulu Peninsula, James Ross Island, was presented in Chapter 4. Stream monitoring and provenance techniques highlight that largely deglaciated catchments on James Ross Island are sensitive to changes in air temperature (specifically in melting ice and snow) for their water delivery, whilst the supply of sediment is largely controlled by underlying lithology. It also highlighted the role that permafrost-affected soils play in supplying water to deglaciated catchments. The studied streams (Bohemian and Algal Streams) give a glimpse of the future for many Antarctic catchments as glaciers retreat. **The study highlights that deglaciation of the catchments on James Ross Island has made a large volume of unconsolidated sediment available for transport and, even in the absence of glacial melt, large quantities of this sediment can be transported on days with positive temperatures when the active layer, snow and any other bodies of ice melt.**

Objective 4: *"Quantify how glaciers have changed in recent decades on the James Ross Archipelago"*.

Multiple datasets were brought together in Chapter 5 to highlight changes to glaciers on the James Ross Archipelago between 2010 and 2023. Over this period, the rate of glacier area reduction increased six-fold, from 0.06 % yr^{-1} between 2011 and 2017 to 0.38 % yr^{-1} between 2017 and 2023. Over the same period, ablation was also observed, at a maximum rate of 1.5 m yr^{-1} at 200 to 300 m a.s.l. on Lookalike Glacier and Davies Dome in 2023. This accelerated loss of glacier mass is probably due to an increase in temperatures, which increased by 0.24 ± 0.08 $^{o}C\ yr^{-1}$ over the study period, combined with a decrease in albedo (in part likely due to decreased levels of snowfall), which reached a low of 0.20 in 2022. Some exceptional changes to glaciers were also highlighted. Swift Glacier experienced a dramatic loss of area at the front of its terminus, receding by 4 km since 2011; likely as a product of substantial thinning following its disconnection from the Mount Haddington Ice Cap. Further abnormalities were

identified on Whisky Glacier and Kotick Glacier, whose total area increased over the study period. The latter of these is interpreted to be due to a surge-event. **In summary, chapter 5 highlights that the James Ross Archipelago is undergoing a period of rapid glacial melt and recession, associated with increased temperatures, decreased albedo, and, in part, this is influenced by hypsometry.**

7.2. Concluding remarks

Through an analysis of land cover, sediment transport dynamics, and recent rapid glacier recession, this has highlighted that Antarctica's landscape is dynamic, and has undergone rapid changes in recent years. **The key overall finding of this thesis is that both the glacial and proglacial landscapes of the Antarctic Peninsula and sub-Antarctic Islands are changing rapidly, affecting sediment transport and export from these regions.**

Furthermore, this thesis has also emphasised glacial and proglacial changes do not occur in isolation, but are rather part of a broader, interconnected system. The interactions between glaciers and proglacial systems, combined with glacier hypsometry, create a complex pattern of non-linear feedback mechanisms, which have implications for glacier longevity. These factors are not presently well understood or considered in Antarctica, and there is a pressing need for further research into these mechanisms, fitting into a broader theme of improving our understanding of the future evolution of proglacial areas in Antarctica.

A key component of future research of these mechanisms will be to ensure a holistic approach is taken. At present, many studies focus on either glacier or proglacial dynamics, but few consider these as part of a broader land-system and, ultimately, an interconnected series of habitats and life-support systems. Receding glaciers have multiple impacts on habitats in their wider environments by changing water temperature and sediment/nutrient flux in streams, lakes, and coastal waters and their recessions creates new terrestrial habitats, which includes the formation of new lake and river habitats. This is particularly apparent when marine-terminating glacier recede onto land, and create new habitats for animals and plants alike, some of which may be invasive. Furthermore, the melt of ice is not limited to glaciers, and indeed the recession of glaciers is ultimately a sentinel for broader landscape degradation, including the thickening of permafrost-affected (active layer) soils, and the melt-out of ice-cored moraines, amongst other periglacial features that supply further water and sediment to habitats. To ensure the protection of its precious landscape and ecosystems (**Figure 7.1**), we must first understand how its different land-systems interact with each other.

Figure 7.1: *Antarctica's special landscape: Two Gentoo penguins pose for a picture on a moss-clad beach to the north east of Edgell Bay (Nelson Island), with the island's ice cap at one of its marine termini in the background; note the small beach recently exposed to the bottom left of the glacier and the eroding cliff above it.*

References

Aalto, J., le Roux, P.C. and Luoto, M. 2013. Vegetation mediates soil temperature and moisture in arctic-alpine environments. *Arctic, Antarctic, and Alpine Research*. **45**(4), pp.429–439.

Adelabu, S., Mutanga, O. and Adam, E. 2015. Testing the reliability and stability of the internal accuracy assessment of random forest for classifying tree defoliation levels using different validation methods. *Geocarto International*. **30**(7), pp.810–821.

Ahmed, M., Seraj, R. and Islam, S.M.S. 2020. The k-means algorithm: A comprehensive survey and performance evaluation. *Electronics (Switzerland)*. **9**(8), pp.1–12.

Åkesson, H., Nisancioglu, K.H., Giesen, R.H. and Morlighem, M. 2017. Simulating the evolution of Hardangerjøkulen ice cap in southern Norway since the mid-Holocene and its sensitivity to climate change. *Cryosphere*. **11**(1), pp.281–302.

Ambrožová, K., Hrbáček, F. and Láska, K. 2020. The summer surface energy budget of the ice-free area of northern james ross island and its impact on the ground thermal regime. *Atmosphere*. **11**(8), p.877.

De Angelis, H. and Skvarca, P. 2003. Glacier surge after ice shelf collapse. *Science*. **299**(5612), pp.1560–1562.

Arndt, K.A., Santos, M.J., Ustin, S., Davidson, S.J., Stow, D., Oechel, W.C., Tran, T.T.P., Graybill, B. and Zona, D. 2019. Arctic greening associated with lengthening growing seasons in Northern Alaska. *Environmental Research Letters*. **14**(12), p.125018.

Arrigo, K.R., Dijken, G.L., Castelao, R.M., Luo, H., Rennermalm, Å.K., Tedesco, M., Mote, T.L., Oliver, H. and Yager, P.L. 2017. Melting glaciers stimulate large summer phytoplankton blooms in southwest Greenland waters. *Geophysical Research Letters*. **44**(12), pp.6278–6285.

Attal, M., Mudd, S.M., Hurst, M.D., Weinman, B., Yoo, K. and Naylor, M. 2015. Impact of change in erosion rate and landscape steepness on hillslope and fluvial sediments grain size in the Feather River basin (Sierra Nevada, California). *Earth Surface Dynamics*. **3**(1), pp.201–222.

Bachelder, J., Cadieux, M., Liu-Kang, C., Lambert, P., Filoche, A., Galhardi, J.A., Hadioui, M., Chaput, A., Bastien-Thibault, M.-P., Wilkinson, K.J., King, J. and Hayes, P.L. 2020. Chemical and microphysical properties of wind-blown dust near an actively retreating glacier in

Yukon, Canada. *Aerosol Science and Technology*. **54**(1), pp.2–20.

Badgeley, J.A., Pettit, E.C., Carr, C.G., Tulaczyk, S., Mikucki, J.A. and Lyons, W.B. 2017. An englacial hydrologic system of brine within a cold glacier: Blood Falls, McMurdo Dry Valleys, Antarctica. *Journal of Glaciology*. **63**(239), pp.387–400.

Ballantyne, C.K. 2008. After the Ice: Holocene Geomorphic Activity in the Scottish Highlands. *Scottish Geographical Journal*. **124**(1), pp.8–52.

Ballantyne, C.K., Sandeman, G.F., Stone, J.O. and Wilson, P. 2014. Rock-slope failure following Late Pleistocene deglaciation on tectonically stable mountainous terrain. *Quaternary Science Reviews*. **86**, pp.144–157.

Ban, Y., Gong, P. and Giri, C. 2015. Global land cover mapping using Earth observation satellite data: Recent progresses and challenges. *ISPRS Journal of Photogrammetry and Remote Sensing*. **103**, pp.1–6.

Bannister, D. and King, J. 2015. Föhn winds on South Georgia and their impact on regional climate. *Weather*. **70**(11), pp.324–329.

Bannister, D. and King, J.C. 2020. The characteristics and temporal variability of föhn winds at King Edward Point, South Georgia. *International Journal of Climatology*. **40**(5), pp.2778–2794.

Bañón, M., Justel, A., Velázquez, D. and Quesada, A. 2013. Regional weather survey on Byers Peninsula, Livingston Island, South Shetland Islands, Antarctica. *Antarctic Science*. **25**(2), pp.146–156.

Banwell, A.F., Tri Datta, R., Dell, R.L., Moussavi, M., Brucker, L., Picard, G., Shuman, C.A. and Stevens, L.A. 2021. The 32-year record-high surface melt in 2019/2020 on the northern George VI Ice Shelf, Antarctic Peninsula. *Cryosphere*. **15**(2), pp.909–925.

Barták, M., Váczi, P., Stachoň, Z. and Kubešová, S. 2015. Vegetation mapping of moss-dominated areas of northern part of James Ross Island (Antarctica) and a suggestion of protective measures. *Czech Polar Reports*. **5**(1), pp.75–87.

Bartolini, S., Geyer, A., Martí, J., Pedrazzi, D. and Aguirre-Díaz, G. 2014. Volcanic hazard on Deception Island (South Shetland Islands, Antarctica). *Journal of Volcanology and Geothermal Research*. **285**, pp.150–168.

Bell, R.E., Banwell, A.F., Trusel, L.D. and Kingslake, J. 2018. Antarctic surface hydrology and impacts on ice-sheet mass balance. *Nature Climate Change*. **8**(12), pp.1044–1052.

Benn, D.I. 2021. Surging glaciers in Scotland. *Scottish Geographical Journal*. **137**(1–4), pp.1–40.

Benn, D.I., Fowler, A.C., Hewitt, I. and Sevestre, H. 2019. A general theory of glacier surges. *Journal of Glaciology*. **65**(253), pp.701–716.

Bentley, M.J., Evans, D.J.A., Fogwill, C.J., Hansom, J.D., Sugden, D.E. and Kubik, P.W. 2007. Glacial geomorphology and chronology of deglaciation, South Georgia, sub-Antarctic. *Quaternary Science Reviews*. **26**(5–6), pp.644–677.

Bentley, M.J., Hodgson, D.A., Smith, J.A., Cofaigh, C.., Domack, E.W., Larter, R.D., Roberts, S.J., Brachfeld, S., Leventer, A., Hjort, C., Hillenbrand, C.-D. and Evans, J. 2009. Mechanisms of Holocene palaeoenvironmental change in the Antarctic Peninsula region. *The Holocene*. **19**(1), pp.51–69.

Bevan, S., Luckman, A., Hendon, H. and Wang, G. 2020. The 2020 Larsen C Ice Shelf surface melt is a 40-year record high. *The Cryosphere*. **14**(10), pp.3551–3564.

Blaen, P.J., Hannah, D.M., Brown, L.E. and Milner, A.M. 2014. Water source dynamics of high Arctic river basins. *Hydrological Processes*. **28**(10), pp.3521–3538.

Błaszczyk, M., Jania, J.A., Ciepły, M., Grabiec, M., Ignatiuk, D., Kolondra, L., Kruss, A., Luks, B., Moskalik, M., Pastusiak, T., Strzelewicz, A., Walczowski, W. and Wawrzyniak, T. 2021. Factors Controlling Terminus Position of Hansbreen, a Tidewater Glacier in Svalbard. *Journal of Geophysical Research: Earth Surface*. **126**(2), e2020JF005763.

Błaszkiewicz, M., Andrzejewski, L., Dudek, J., Sobota, I. and Czarnecki, K. 2023. The role of dead ice in transforming glacier forelands under the rapid climate warming of recent decades, Oscar II Land, Svalbard. *Land Degradation and Development*. **34**(14), pp.4328–4345.

Bojinski, S., Verstraete, M., Peterson, T.C., Richter, C., Simmons, A. and Zemp, M. 2014. The Concept of Essential Climate Variables in Support of Climate Research, Applications, and Policy. *Bulletin of the American Meteorological Society*. **95**(9), pp.1431–1443.

Bosson, J.B., Huss, M., Cauvy-Fraunié, S., Clément, J.C., Costes, G., Fischer, M., Poulenard, J. and Arthaud, F. 2023. Future emergence of new ecosystems caused by glacial retreat. *Nature*. **620**(7974), pp.562–569.

Boston, C.M. and Lukas, S. 2019. Topographic controls on plateau icefield recession: insights from the Younger Dryas Monadhliath Icefield, Scotland. *Journal of Quaternary Science*. **34**(6), pp.433–451.

Bovolo, F. and Bruzzone, L. 2007. A theoretical framework for unsupervised change detection

based on change vector analysis in the polar domain. *IEEE Transactions on Geoscience and Remote Sensing*. **45**(1), pp.218–236.

Boyle, J.F. 2000. Rapid elemental analysis of sediment samples by isotope source XRF. *Journal of Paleolimnology*. **23**(2), pp.213–221.

British Antarctic Survey 1981. British Antarctic Territory geological map : scale 1:500,000 , Sheet 4 G. B. D. of O. Surveys, ed.

Brooks, S.M., Anderson, M.G. and Collison, A.J.C. 1995. Modelling the role of climate, vegetation and pedogenesis in shallow translational hillslope failure. *Earth Surface Processes and Landforms*. **20**(3), pp.231–242.

Brown, C.F., Brumby, S.P., Guzder-Williams, B., Birch, T., Hyde, S.B., Mazzariello, J., Czerwinski, W., Pasquarella, V.J., Haertel, R., Ilyushchenko, S., Schwehr, K., Weisse, M., Stolle, F., Hanson, C., Guinan, O., Moore, R. and Tait, A.M. 2022. Dynamic World, Near real-time global 10 m land use land cover mapping. *Scientific Data*. **9**(1), p.251.

Brown, L.E., Dickson, N.E., Carrivick, J.L. and Füreder, L. 2015. Alpine river ecosystem response to glacial and anthropogenic flow pulses. *Freshwater Science*. **34**(4), pp.1201–1215.

Brussaard, C.P.D., Wilhelm, S.W., Thingstad, F., Weinbauer, M.G., Bratbak, G., Heldal, M., Kimmance, S.A., Middelboe, M., Nagasaki, K., Paul, J.H., Schroeder, D.C., Suttle, C.A., Vaqué, D. and Wommack, K.E. 2008. Global-scale processes with a nanoscale drive: the role of marine viruses. *The ISME Journal*. **2**(6), pp.575–578.

Bullard, J.E. and Austin, M.J. 2011. Dust generation on a proglacial floodplain, West Greenland. *Aeolian Research*. **3**(1), pp.43–54.

Bullard, J.E., Baddock, M., Bradwell, T., Crusius, J., Darlington, E., Gaiero, D., Gassó, S., Gisladottir, G., Hodgkins, R., McCulloch, R., McKenna-Neuman, C., Mockford, T., Stewart, H. and Thorsteinsson, T. 2016. High-latitude dust in the Earth system. *Reviews of Geophysics*. **54**(2), pp.447–485.

Burton-Johnson, A., Black, M., Fretwell, P.T. and Kaluza-Gilbert, J. 2016. An automated methodology for differentiating rock from snow, clouds and sea in Antarctica from Landsat 8 imagery: a new rock outcrop map and area estimation for the entire Antarctic continent. *The Cryosphere*. **10**(4), pp.1665–1677.

Carlson, T.N. and Ripley, D.A. 1997. On the relation between NDVI, fractional vegetation cover, and leaf area index. *Remote Sensing of Environment*. **62**(3), pp.241–252.

Carr, J.R., Stokes, C.R. and Vieli, A. 2017. Threefold increase in marine-terminating outlet glacier retreat rates across the Atlantic Arctic: 1992–2010. *Annals of Glaciology*. **58**(74), pp.72–91.

Carr, R., Murphy, Z., Nienow, P., Jakob, L. and Gourmelen, N. 2023. Rapid and synchronous response of outlet glaciers to ocean warming on the Barents Sea coast, Novaya Zemlya. *Journal of Glaciology*., pp.1–35.

Carrasco, J.F., Bozkurt, D. and Cordero, R.R. 2021. A review of the observed air temperature in the Antarctic Peninsula. Did the warming trend come back after the early 21st hiatus? *Polar Science*. **28**, p.100653.

Carrivick, J.L., Davies, B.J., Glasser, N.F., Nývlt, D. and Hambrey, M.J. 2012. Late-Holocene changes in character and behaviour of land-terminating glaciers on James Ross Island, Antarctica. *Journal of Glaciology*. **58**(212), pp.1176–1190.

Carrivick, J.L. and Heckmann, T. 2017. Short-term geomorphological evolution of proglacial systems. *Geomorphology*. **287**, pp.3–28.

Carrivick, J.L., Heckmann, T., Turner, A. and Fischer, M. 2018. An assessment of landform composition and functioning with the first proglacial systems dataset of the central European Alps. *Geomorphology*. **321**, pp.117–128.

Carrivick, J.L., Smith, M.W., Sutherland, J.L. and Grimes, M. 2023. Cooling glaciers in a warming climate since the Little Ice Age at Qaanaaq, northwest Kalaallit Nunaat (Greenland). *Earth Surface Processes and Landforms*. **48**(13), pp.2446–2462.

Carrivick, J.L., Sutherland, J.L., Huss, M., Purdie, H., Stringer, C.D., Grimes, M., James, W.H.M. and Lorrey, A.M. 2022. Coincident evolution of glaciers and ice-marginal proglacial lakes across the Southern Alps, New Zealand: Past, present and future. *Global and Planetary Change*. **211**, p.103792.

Carrivick, J.L. and Tweed, F.S. 2021. Deglaciation controls on sediment yield: Towards capturing spatio-temporal variability. *Earth-Science Reviews*. **221**, p.103809.

Carrivick, J.L. and Tweed, F.S. 2013. Proglacial Lakes: Character, behaviour and geological importance. *Quaternary Science Reviews*. **78**, pp.34–52.

Carvalho Júnior, O.A., Guimarães, R.F., Gillespie, A.R., Silva, N.C. and Gomes, R.A.T. 2011. A new approach to change vector analysis using distance and similarity measures. *Remote Sensing*. **3**(11), pp.2473–2493.

Cary, S.C., McDonald, I.R., Barrett, J.E. and Cowan, D.A. 2010. On the rocks: The microbiology of Antarctic Dry Valley soils. *Nature Reviews Microbiology*. **8**(2), pp.129–138.

Cavieres, L.A., Sáez, P., Sanhueza, C., Sierra-Almeida, A., Rabert, C., Corcuera, L.J., Alberdi, M. and Bravo, L.A. 2016. Ecophysiological traits of Antarctic vascular plants: their importance in the responses to climate change. *Plant Ecology*. **217**(3), pp.343–358.

Chakrapani, G.J. and Subramanian, V. 1990. Factors controlling sediment discharge in the Mahanadi River Basin, India. *Journal of Hydrology*. **117**(1), pp.169–185.

Chasmer, L., Mahoney, C., Millard, K., Nelson, K., Peters, D., Merchant, M., Hopkinson, C., Brisco, B., Niemann, O., Montgomery, J., Devito, K. and Cobbaert, D. 2020. Remote Sensing of Boreal Wetlands 2: Methods for Evaluating Boreal Wetland Ecosystem State and Drivers of Change. *Remote Sensing*. **12**(8), p.1321.

Chen, Jun, Chen, Jin, Liao, A., Cao, X., Chen, L., Chen, X., He, C., Han, G., Peng, S., Lu, M., Zhang, W., Tong, X. and Mills, J. 2015. Global land cover mapping at 30m resolution: A POK-based operational approach. *ISPRS Journal of Photogrammetry and Remote Sensing*. **103**, pp.7–27.

Chen, W., Li, X. and Wang, L. 2019. Fine Land Cover Classification in an Open Pit Mining Area Using Optimized Support Vector Machine and WorldView-3 Imagery. *Remote Sensing*. **12**(1), p.82.

Chinn, T. and Mason, P. 2016. The first 25 years of the hydrology of the Onyx River, Wright Valley, Dry Valleys, Antarctica. *Polar Record*. **52**(1), pp.16–65.

Chu, V.W., Smith, L.C., Rennermalm, A.K., Forster, R.R., Box, J.E. and Reeh, N. 2009. Sediment plume response to surface melting and supraglacial lake drainages on the Greenland ice sheet. *Journal of Glaciology*. **55**(194), pp.1072–1082.

Clapperton, C.M. (Chalmers M. 1971. *Geomorphology of the Stromness Bay-Cumberland Bay area, South Georgia* . London: British Antarctic Survey.

Clarke, G.K.C. and Blake, E.W. 1991. Geometric and thermal evolution of a surge-type glacier in its quiescent state: Trapridge Glacier, Yukon Territory, Canada, 1969–89. *Journal of Glaciology*. **37**(125), pp.158–169.

Cloern, J.E. 1987. Turbidity as a control on phytoplankton biomass and productivity in estuaries. *Continental Shelf Research*. **7**(11–12), pp.1367–1381.

Coles, A.E. and McDonnell, J.J. 2018. Fill and spill drives runoff connectivity over frozen ground.

Journal of Hydrology. **558**, pp.115–128.

Colesie, C., Walshaw, C. V., Sancho, L.G., Davey, M.P. and Gray, A. 2023. Antarctica's vegetation in a changing climate. *Wiley Interdisciplinary Reviews: Climate Change*. **14**(1), p.e810.

Collins, A.L., Blackwell, M., Boeckx, P., Chivers, C.A., Emelko, M., Evrard, O., Foster, I., Gellis, A., Gholami, H., Granger, S., Harris, P., Horowitz, A.J., Laceby, J.P., Martinez-Carreras, N., Minella, J., Mol, L., Nosrati, K., Pulley, S., Silins, U., da Silva, Y.J., Stone, M., Tiecher, T., Upadhayay, H.R. and Zhang, Y. 2020. Sediment source fingerprinting: benchmarking recent outputs, remaining challenges and emerging themes. *Journal of Soils and Sediments*. **20**(12), pp.4160–4193.

Collins, N.J. 1969. The effects of volcanic activity on the vegetation of Deception Island. *British Antarctic Survey Bulletin*. **21**, pp.79–94.

Conovitz, P.A., Mcknight, D.M., Macdonald, L.H., Fountain, A.G. and House, H.R. 2013. Hydrologic Processes Influencing Streamflow Variation in Fryxell Basin, Antarctica *In*: Ecosystem Dynamics in a Polar Desert: the McMurdo Dry Valleys, Antarctica, J.C. Priscu (Ed.)., pp.93–108.

Consortium, R. 2023. Randolph Glacier Inventory: A dataset of global glacier outlines, version 7.0, digital media. Available from: https://doi.org/10.5067/F6JMOVY5NAVZ.

Convey, P. and Smith, R.I.L. 2007. Responses of terrestrial Antarctic ecosystems to climate change *In*: J. Rozema, R. Aerts and H. Cornelissen, eds. *Plants and Climate Change*. Dordrecht: Springer Netherlands, pp.1–12.

Cook, A.J., Holland, P.R., Meredith, M.P., Murray, T., Luckman, A. and Vaughan, D.G. 2016. Ocean forcing of glacier retreat in the western Antarctic Peninsula. *Science*. **353**(6296), pp.283–286.

Cook, A.J., Poncet, S., Cooper, A.P.R., Herbert, D.J. and Christie, D. 2010. Glacier retreat on South Georgia and implications for the spread of rats. *Antarctic Science*. **22**(3), pp.255–263.

Cook, A.J. and Vaughan, D.G. 2010. Overview of areal changes of the ice shelves on the Antarctic Peninsula over the past 50 years. *Cryosphere*. **4**(1), pp.77–98.

Costa, A., Molnar, P., Stutenbecker, L., Bakker, M., Silva, T.A., Schlunegger, F., Lane, S.N., Loizeau, J.L. and Girardclos, S. 2018. Temperature signal in suspended sediment export from an Alpine catchment. *Hydrology and Earth System Sciences*. **22**(1), pp.509–528.

Coulter, L.L., Hope, A.S., Stow, D.A., Lippitt, C.D. and Lathrop, S.J. 2011. Time–space radiometric normalization of TM/ETM+ images for land cover change detection. *International Journal of Remote Sensing*. **32**(22), pp.7539–7556.

Cox, S.C., Morin, P. and Smith Lyttle, B. 2019. GeoMAP on Rema. Abstract A253 & Poster *In*: *13th International Symposium on Antarctic Earth Sciences, 22-26 July 2019, Incheon, Republic of Korea.*

Cox, S.C., Smith Lyttle, B., Elkind, S., Smith Siddoway, C., Morin, P., Capponi, G., Abu-Alam, T., Ballinger, M., Bamber, L., Kitchener, B., Lelli, L., Mawson, J., Millikin, A., Dal Seno, N., Whitburn, L., White, T., Burton-Johnson, A., Crispini, L., Elliot, D., Elvevold, S., Goodge, J., Halpin, J., Jacobs, J., Martin, A.P., Mikhalsky, E., Morgan, F., Scadden, P., Smellie, J. and Wilson, G. 2023. A continent-wide detailed geological map dataset of Antarctica. *Scientific Data*. **10**(1).

Crusius, J., Schroth, A.W., Gassó, S., Moy, C.M., Levy, R.C. and Gatica, M. 2011. Glacial flour dust storms in the Gulf of Alaska: Hydrologic and meteorological controls and their importance as a source of bioavailable iron. *Geophysical Research Letters*. **38**(6).

Czech Geological Survey 2009. *Map of Northern Part of James Ross Island*.

Davies, B., Bendle, J., Carrivick, J., McNabb, R., McNeil, C., Pelto, M., Campbell, S., Holt, T., Ely, J. and Markle, B. 2022. Topographic controls on ice flow and recession for Juneau Icefield (Alaska/British Columbia). *Earth Surface Processes and Landforms*. **47**(9), pp.2357–2390.

Davies, B.J., Carrivick, J.L., Glasser, N.F., Hambrey, M.J. and Smellie, J.L. 2012. Variable glacier response to atmospheric warming, northern Antarctic Peninsula, 1988-2009. *Cryosphere*. **6**(5), pp.1031–1048.

Davies, B.J., Glasser, N.F., Carrivick, J.L., Hambrey, M.J., Smellie, J.L. and Nývlt, D. 2013. Landscape evolution and ice-sheet behaviour in a semi-arid polar environment: James Ross Island, NE Antarctic Peninsula. *Geological Society, London, Special Publications*. **381**(1), pp.353–395.

Davies, B.J., Hambrey, M.J., Glasser, N.F., Holt, T., Rodés, A., Smellie, J.L., Carrivick, J.L. and Blockley, S.P.E. 2017. Ice-dammed lateral lake and epishelf lake insights into Holocene dynamics of Marguerite Trough Ice Stream and George VI Ice Shelf, Alexander Island, Antarctic Peninsula. *Quaternary Science Reviews*. **177**, pp.189–219.

Decaulne, A., Sæmundsson, P. and Pétursson, O. 2005. Debris flow triggered by rapid snowmelt: A case study in the Gleidarhjalli area, northwestern Iceland. *Geografiska*

Annaler, Series A: Physical Geography. **87**(4), pp.487–500.

Dibbern, J.S. 2010. Fur seals, whales and tourists: A commercial history of deception Island, Antarctica. *Polar Record*. **46**(3), pp.210–221.

Dickens, J., Hollyman, P.R., Hart, T., Clucas, G. V., Murphy, E.J., Poncet, S., Trathan, P.N. and Collins, M.A. 2021. Developing UAV Monitoring of South Georgia and the South Sandwich Islands' Iconic Land-Based Marine Predators. *Frontiers in Marine Science*. **8**, p.654215.

Doran, P.T., McKay, C.P., Clow, G.D., Dana, G.L., Fountain, A.G., Nylen, T. and Lyons, W.B. 2002. Valley floor climate observations from the McMurdo dry valleys, Antarctica, 1986-2000. *Journal of Geophysical Research Atmospheres*. **107**(24), p.4772.

Duda, T. and Canty, M. 2002. Unsupervised classification of satellite imagery: Choosing a good algorithm. *International Journal of Remote Sensing*. **23**(11), pp.2193–2212.

Eagle, L.J.B., Carrivick, J.L., Milner, A.M., Brown, L.E. and Klaar, M.J. 2021. Repeated high flows drive morphological change in rivers in recently deglaciated catchments. *Earth Surface Processes and Landforms*. **46**(7), pp.1294–1310.

Edwards, T.L., Nowicki, S., Marzeion, B., Hock, R., Goelzer, H., Seroussi, H., Jourdain, N.C., Slater, D.A., Turner, F.E. and Smith, C.J. 2021. Projected land ice contributions to twenty-first-century sea level rise. *Nature*. **593**(7857), pp.74–82.

Engel, Z., Kropáček, J.A.N. and Smolíková, J. 2019. Surface elevation changes on Lachman Crags ice caps (north-eastern Antarctic Peninsula) since 1979 indicated by DEMs and ICESat data. *Journal of Glaciology*. **65**(251), pp.410–421.

Engel, Z., Láska, K., Kavan, J. and Smolíková, J. 2023. Persistent mass loss of Triangular Glacier, James Ross Island, north-eastern Antarctic Peninsula. *Journal of Glaciology*. **69**(273), pp.27–39.

Engel, Z., Láska, K., Nývlt, D. and Stachoň, Z. 2018. Surface mass balance of small glaciers on James Ross Island, north-eastern Antarctic Peninsula, during 2009-2015. *Journal of Glaciology*. **64**(245), pp.349–361.

Engel, Z., Láska, K., Smolíková, J. and Kavan, J. 2024. Recent Change in Surface Mass-Balance Trends of Glaciers on James Ross Island, North-Eastern Antarctic Peninsula. *Journal of Glaciology*., pp.1–15.

England, M.R., Eisenman, I., Lutsko, N.J. and Wagner, T.J.W. 2021. The Recent Emergence of Arctic Amplification. *Geophysical Research Letters*. **48**(15), e2021GL094086.

Farías-Barahona, D., Sommer, C., Sauter, T., Bannister, D., Seehaus, T.C., Malz, P., Casassa, G., Mayewski, P.A., Turton, J. V. and Braun, M.H. 2020. Detailed quantification of glacier elevation and mass changes in South Georgia. *Environmental Research Letters*. **15**(3), p.34036.

Farinotti, D., Huss, M., Fürst, J.J., Landmann, J., Machguth, H., Maussion, F. and Pandit, A. 2019. A consensus estimate for the ice thickness distribution of all glaciers on Earth. *Nature Geoscience*. **12**(3), pp.168–173.

Farr, T.G., Rosen, P.A., Caro, E., Crippen, R., Duren, R., Hensley, S., Kobrick, M., Paller, M., Rodriguez, E., Roth, L., Seal, D., Shaffer, S., Shimada, J., Umland, J., Werner, M., Oskin, M., Burbank, D. and Alsdorf, D. 2007. The Shuttle Radar Topography Mission. *Reviews of Geophysics*. **45**(2), p.RG2004.

Fassnacht, S.R., Cherry, M.L. and Venable, N.B.H. 2015. Snow and albedo climate change impacts across the United States Northern Great Plains. *Cryosphere Discussions*. **9**(3), pp.3331–3349.

Fountain, A.G., Levy, J.S., Gooseff, M.N. and Van Horn, D. 2014. The McMurdo Dry Valleys: A landscape on the threshold of change. *Geomorphology*. **225**(C), pp.25–35.

Fretwell, P.T., Convey, P., Fleming, A.H., Peat, H.J. and Hughes, K.A. 2011. Detecting and mapping vegetation distribution on the Antarctic Peninsula from remote sensing data. *Polar Biology*. **34**(2), pp.273–281.

Friedl, M.A., Sulla-Menashe, D., Tan, B., Schneider, A., Ramankutty, N., Sibley, A. and Huang, X. 2010. MODIS Collection 5 global land cover: Algorithm refinements and characterization of new datasets. *Remote Sensing of Environment*. **114**(1), pp.168–182.

Friedlander, A.M., Goodell, W., Salinas-de-León, P., Ballesteros, E., Berkenpas, E., Capurro, A.P., Cárdenas, C.A., Hüne, M., Lagger, C., Landaeta, M.F., Muñoz, A., Santos, M., Turchik, A., Werner, R. and Sala, E. 2020. Spatial patterns of continental shelf faunal community structure along the Western Antarctic Peninsula J. M. Riascos, ed. *PLOS ONE*. **15**(10), p.e0239895.

Frohn, R.C., Reif, M., Lane, C. and Autrey, B. 2009. Satellite remote sensing of isolated wetlands using object-oriented classification of Landsat-7 data. *Wetlands*. **29**(3), pp.931–941.

Gaddam, V.K., Boddapati, R., Kumar, T., Kulkarni, A. V. and Bjornsson, H. 2022. Application of "OTSU"—an image segmentation method for differentiation of snow and ice regions of

glaciers and assessment of mass budget in Chandra basin, Western Himalaya using Remote Sensing and GIS techniques. *Environmental Monitoring and Assessment*. **194**(5), p.337.

Galera, H., Znój, A., Chwedorzewska, K.J. and Wódkiewicz, M. 2021. Evaluation of factors influencing the eradication of annual bluegrass (Poa annua L.) from Point Thomas Oasis, King George Island, Maritime Antarctica. *Polar Biology*. **44**(12), pp.2255–2268.

Gao, L., Zhao, Y., Yang, Z., Liu, J., Liu, X., Zhang, S.H. and Pei, J. 2018. New Paleomagnetic and 40Ar/39Ar Geochronological Results for the South Shetland Islands, West Antarctica, and Their Tectonic Implications. *Journal of Geophysical Research: Solid Earth*. **123**(1), pp.4–30.

García-Rodríguez, F., Piccini, C., Carrizo, D., Sánchez-García, L., Pérez, L., Crisci, C., Oaquim, A.B.J., Evangelista, H., Soutullo, A., Azcune, G. and Lüning, S. 2021. Centennial glacier retreat increases sedimentation and eutrophication in Subantarctic periglacial lakes: A study case of Lake Uruguay. *Science of the Total Environment*. **754**, p.142066.

Gardner, A.S., Moholdt, G., Scambos, T., Fahnstock, M., Ligtenberg, S., Van Den Broeke, M. and Nilsson, J. 2018. Increased West Antarctic and unchanged East Antarctic ice discharge over the last 7 years. *The Cryosphere*. **12**(2), pp.521–547.

GCOS 2010. Implementation plan for the global observing system for climate in support of the UNFCCC (2010 update). , p.186.

Gerrish, L., Fretwell, P., & Cooper, P. 2021. Medium resolution vector polygons of the Antarctic coastline (Version 7.4) [Data set]. *UK Polar Data Centre, Natural Environment Research Council, UK Research & Innovation*.

Gerrish, L., Fretwell, P. and Cooper, P. 2020. High resolution vector polygons of Antarctic rock outcrop (7.3) [Data set]. *UK Polar Data Centre, Natural Environment Research Council, UK Research & Innovation*.

Geyman, E.C., J. J. van Pelt, W., Maloof, A.C., Aas, H.F. and Kohler, J. 2022. Historical glacier change on Svalbard predicts doubling of mass loss by 2100. *Nature*. **601**(7893), pp.374–379.

Gholamy, A., Kreinovich, V. and Kosheleva, O. 2018. Why 70/30 Or 80/20 Relation Between Training And Testing Sets : A Pedagogical Explanation. *Departmental Technical Reports (CS)*. **1209**, pp.1–6.

Gil-Delgado, J.A., González-Solís, J. and Barbosa, A. 2013. Populations of breeding birds in Byers Peninsula, Livingston Island, South Shetland Islands. *Antarctic Science*. **25**(2),

pp.303–306.

Gil-Delgado, J.A., Villaescusa, J.A., Diazmacip, M.E., Velazquez, D., Rico, E., Toro, M., Quesada, A. and Camacho, A. 2013. Minimum population size estimates demonstrate an increase in southern elephant seals (Mirounga leonina) on Livingston Island, maritime Antarctica. *Polar Biology*. **36**(4), pp.607–610.

GLAMOS 2023. *GLAMOS 1880-2021, The Swiss Glaciers 1880-2021, Glaciological Reports No 1-142.* VAW / ETH Zurich.

Glasser, N.F., Davies, B.J., Carrivick, J.L., Rodés, A., Hambrey, M.J., Smellie, J.L. and Domack, E. 2014. Ice-stream initiation, duration and thinning on James Ross Island, northern Antarctic Peninsula. *Quaternary Science Reviews*. **86**, pp.78–88.

Glasser, N.F., Holt, T.O., Evans, Z.D., Davies, B.J., Pelto, M. and Harrison, S. 2016. Recent spatial and temporal variations in debris cover on Patagonian glaciers. *Geomorphology*. **273**, pp.202–216.

Glasser, N.F., Scambos, T.A., Bohlander, J., Truffer, M., Pettit, E. and Davies, B.J. 2011. From ice-shelf tributary to tidewater glacier: continued rapid recession, acceleration and thinning of Röhss Glacier following the 1995 collapse of the Prince Gustav Ice Shelf, Antarctic Peninsula. *Journal of Glaciology*. **57**(203), pp.397–406.

Golledge, N.R., Everest, J.D., Bradwell, T. and Johnson, J.S. 2010. Lichenometry on adelaide island, antarctic peninsula: size-frequency studies, growth rates and snowpatches. *Geografiska Annaler: Series A, Physical Geography*. **92**(1), pp.111–124.

Gonçalves, V.N., de Souza, L.M.D., Lirio, J.M., Coria, S.H., Lopes, F.A.C., Convey, P., Carvalho-Silva, M., de Oliveira, F.S., Câmara, P.E.A.S. and Rosa, L.H. 2022. Diversity and ecology of fungal assemblages present in lake sediments at Clearwater Mesa, James Ross Island, Antarctica, assessed using metabarcoding of environmental DNA. *Fungal Biology*. **126**(10), pp.640–647.

Gong, P., Li, X., Wang, J., Bai, Y., Chen, B., Hu, T., Liu, X., Xu, B., Yang, J., Zhang, W. and Zhou, Y. 2020. Annual maps of global artificial impervious area (GAIA) between 1985 and 2018. *Remote Sensing of Environment*. **236**, p.111510.

González-Herrero, S., Navarro, F., Pertierra, L.R., Oliva, M., Dadic, R., Peck, L. and Lehning, M. 2024. Southward migration of the zero-degree isotherm latitude over the Southern Ocean and the Antarctic Peninsula: Cryospheric, biotic and societal implications. *Science of the Total Environment*. **912**, p.168473.

González-Herrero, S., Vasallo, F., Bech, J., Gorodetskaya, I., Elvira, B. and Justel, A. 2023. Extreme precipitation records in Antarctica. *International Journal of Climatology*. **43**(7), pp.3125–3138.

Good, T.R. and Bryant, I.D. 1985. Fluvio-Aeolian Sedimentation—An Example from Banks Island, N.W.T., Canada. *Geografiska Annaler: Series A, Physical Geography*. **67**(1–2), pp.33–46.

Gooseff, M.N. and Lyons, W.B. 2007. *Trends in discharge and flow season timing of the Onyx River, Wright Valley, Antarctica since 1969.* Reston, VA.

Gooseff, M.N., McKnight, D.M., Doran, P., Fountain, A.G. and Lyons, W.B. 2011. Hydrological Connectivity of the Landscape of the McMurdo Dry Valleys, Antarctica. *Geography Compass*. **5**(9), pp.666–681.

Gorelick, N., Hancher, M., Dixon, M., Ilyushchenko, S., Thau, D. and Moore, R. 2017. Google Earth Engine: Planetary-scale geospatial analysis for everyone. *Remote Sensing of Environment*. **202**, pp.18–27.

Grimes, M., Carrivick, J.L., Smith, M.W. and Comber, A.J. 2024. Land cover changes across Greenland dominated by a doubling of vegetation in three decades. *Scientific Reports*. **14**(1), p.3120.

Gutiérrez, J.M., Jones, R.G., Narisma, G.T., Alves, L.M., Amjad, M., Gorodetskaya, I.V., Grose, M., Klutse, N.A.B., Krakovska, S., Li, J., Martínez-Castro, D., Mearns, L.O., Mernild, S.H., Ngo-Duc, T., Hurk, B. van den and Yoon, J.-H. 2021. IPCC Interactive Atlas. *In Climate Change 2021: The Physical Science Basis. Contribution of Working Group I to the Sixth Assessment Report of the Intergovernmental Panel on Climate Change*.

Harangozo, S.A., Colwell, S.R. and King, J.C. 1997. An analysis of a 34-year air temperature record from Fossil Bluff (71°S, 68°W), Antarctica. *Antarctic Science*. **9**(3), pp.355–363.

Headland, R. 1984. *The Island of South Georgia*. CUP Archive.

Headland, R.K., Hughes, N.E. and Wilkinson, J.P. 2023. Historical occurrence of Antarctic icebergs within mercantile shipping routes and the exceptional events of the 1890s. *Journal of Glaciology*., pp.1–13.

Heller, N.E. and Zavaleta, E.S. 2009. Biodiversity management in the face of climate change: a review of 22 years of recommendations. *Biological conservation*. **142**(1), pp.14–32.

Heywood, R.B., Fuchs, V.E. and Laws, R.M. 1977. A limnological survey of the Ablation Point

area, Alexander Island, Antarctica. *Philosophical Transactions of the Royal Society of London. B, Biological Sciences*. **279**(963), pp.39–54.

Hock, R. 2003. Temperature index melt modelling in mountain areas. *Journal of Hydrology*. **282**(1–4), pp.104–115.

Howat, I.M., Porter, C., Smith, B.E., Noh, M.-J. and Morin, P. 2019. The Reference Elevation Model of Antarctica. *The Cryosphere*. **13**(2), pp.665–674.

Hrbáček, F., Cannone, N., Kňažková, M., Malfasi, F., Convey, P. and Guglielmin, M. 2020. Effect of climate and moss vegetation on ground surface temperature and the active layer among different biogeographical regions in Antarctica. *Catena*. **190**, p.104562.

Hrbáček, F., Engel, Z., Kňažková, M. and Smolíková, J. 2021. Effect of summer snow cover on the active layer thermal regime and thickness on CALM-S JGM site, James Ross Island, eastern Antarctic Peninsula. *Catena*. **207**, p.105608.

Hrbáček, F., Láska, K. and Engel, Z. 2016. Effect of Snow Cover on the Active-Layer Thermal Regime – A Case Study from James Ross Island, Antarctic Peninsula. *Permafrost and Periglacial Processes*. **27**(3), pp.307–315.

Hrbáček, F., Oliva, M., Hansen, C., Balks, M., O'Neill, T.A., de Pablo, M.A., Ponti, S., Ramos, M., Vieira, G., Abramov, A., Kaplan Pastíriková, L., Guglielmin, M., Goyanes, G., Francelino, M.R., Schaefer, C. and Lacelle, D. 2023. Active layer and permafrost thermal regimes in the ice-free areas of Antarctica. *Earth-Science Reviews*. **242**, p.104458.

Hrbáček, F. and Uxa, T. 2020. The evolution of a near-surface ground thermal regime and modeled active-layer thickness on James Ross Island, Eastern Antarctic Peninsula, in 2006–2016. *Permafrost and Periglacial Processes*. **31**(1), pp.141–155.

Huang, J.J., Löwemark, L., Chang, Q., Lin, T.Y., Chen, H.F., Song, S.R. and Wei, K.Y. 2016. Choosing optimal exposure times for XRF core-scanning: Suggestions based on the analysis of geological reference materials. *Geochemistry, Geophysics, Geosystems*. **17**(4), pp.1558–1566.

Huber, J., Cook, A.J., Paul, F. and Zemp, M. 2017. A complete glacier inventory of the Antarctic Peninsula based on Landsat 7 images from 2000 to 2002 and other preexisting data sets. *Earth System Science Data*. **9**(1), pp.115–131.

Hughes, K.A., Convey, P. and Turner, J. 2021. Developing resilience to climate change impacts in Antarctica: An evaluation of Antarctic Treaty System protected area policy. *Environmental Science and Policy*. **124**, pp.12–22.

Hughes, K.A., Pescott, O.L., Peyton, J., Adriaens, T., Cottier-Cook, E.J., Key, G., Rabitsch, W., Tricarico, E., Barnes, D.K.A., Baxter, N., Belchier, M., Blake, D., Convey, P., Dawson, W., Frohlich, D., Gardiner, L.M., González-Moreno, P., James, R., Malumphy, C., Martin, S., Martinou, A.F., Minchin, D., Monaco, A., Moore, N., Morley, S.A., Ross, K., Shanklin, J., Turvey, K., Vaughan, D., Vaux, A.G.C., Werenkraut, V., Winfield, I.J. and Roy, H.E. 2020. Invasive non-native species likely to threaten biodiversity and ecosystems in the Antarctic Peninsula region. *Global Change Biology*. **26**(4), pp.2702–2716.

Hughes, L. 2000. Biological consequences of global warming: Is the signal already apparent? *Trends in Ecology and Evolution*. **15**(2), pp.56–61.

Hugonnet, R., McNabb, R., Berthier, E., Menounos, B., Nuth, C., Girod, L., Farinotti, D., Huss, M., Dussaillant, I., Brun, F. and Kääb, A. 2021. Accelerated global glacier mass loss in the early twenty-first century. *Nature*. **592**(7856), pp.726–731.

Humlum, O., Instanes, A. and Sollid, J.L. 2003. Permafrost in Svalbard: a review of research history, climatic background and engineering challenges. *Polar Research*. **22**(2), pp.191–215.

Huss, M., Funk, M. and Ohmura, A. 2009. Strong Alpine glacier melt in the 1940s due to enhanced solar radiation. *Geophysical Research Letters*. **36**(23).

Huss, M. and Hock, R. 2018. Global-scale hydrological response to future glacier mass loss. *Nature Climate Change*. **8**(2), pp.135–140.

Inbar, M. 1995. Fluvial Morphology and Streamflow on Deception Island, Antarctica. *Geografiska Annaler. Series A, Physical Geography*. **77**(4), pp.221–230.

Ineson, J.R., Crame, J.A. and Thomson, M.R.A. 1986. Lithostratigraphy of the Cretaceous Strata of West James Ross Island, Antarctica. *Cretaceous Research*. **7**(2), pp.141–159.

Jena, B., Bajish, C.C., Turner, J., Ravichandran, M., Anilkumar, N. and Kshitija, S. 2022. Record low sea ice extent in the Weddell Sea, Antarctica in April/May 2019 driven by intense and explosive polar cyclones. *Npj Climate and Atmospheric Science*. **5**(1), p.19.

Jennings, S.J.A., Davies, B.J., Nývlt, D., Glasser, N.F., Engel, Z., Hrbáček, F., Carrivick, J.L., Mlčoch, B. and Hambrey, M.J. 2021. Geomorphology of Ulu Peninsula, James Ross Island, Antarctica. *Journal of Maps*. **17**(2), pp.125–139.

Johnson, E. and Rupper, S. 2020. An Examination of Physical Processes That Trigger the Albedo-Feedback on Glacier Surfaces and Implications for Regional Glacier Mass Balance Across High Mountain Asia. *Frontiers in Earth Science*. **8**.

Joughin, I., Shapero, D., Smith, B., Dutrieux, P. and Barham, M. 2021. Ice-shelf retreat drives recent Pine Island Glacier speedup. *Science Advances*. **7**(24), p.eabg3080.

Kaplan Pastíriková, L., Hrbáček, F., Uxa, T. and Láska, K. 2023. Permafrost table temperature and active layer thickness variability on James Ross Island, Antarctic Peninsula, in 2004–2021. *Science of the Total Environment*. **869**, p.161690.

Karlsson, J.M., Jaramillo, F. and Destouni, G. 2015. Hydro-climatic and lake change patterns in Arctic permafrost and non-permafrost areas. *Journal of Hydrology*. **529**, pp.134–145.

Kavan, J. 2021. Fluvial transport in the deglaciated Antarctic catchment–Bohemian Stream, James Ross Island. *Geografiska Annaler, Series A: Physical Geography*. **104**(1), pp.1–10.

Kavan, J., Dagsson-Waldhauserova, P., Renard, J.B., Láska, K. and Ambrožová, K. 2018. Aerosol concentrations in relationship to local atmospheric conditions on James Ross Island, Antarctica. *Frontiers in Earth Science*. **6**.

Kavan, J., Hrbáček, F. and Stringer, C.D. 2023. Proglacial streams runoff dynamics in Devil´s Bay, Vega Island, Antarctica. *Hydrological Sciences Journal*. **68**(7), pp.967–981.

Kavan, J., Láska, K., Nawrot, A. and Wawrzyniak, T. 2020. High latitude dust transport altitude pattern revealed from deposition on snow, Svalbard. *Atmosphere*. **11**(12), pp.1–17.

Kavan, J., Nedbalová, L., Nývlt, D., Čejka, T. and Lirio, J.M. 2021. Status and short-term environmental changes of lakes in the area of Devil's Bay, Vega Island, Antarctic Peninsula. *Antarctic Science*. **33**(2), pp.150–164.

Kavan, J. and Nývlt, D. 2018. Where does the Antarctic fluvial suspended sediment come from? [Poster].

Kavan, J., Nývlt, D., Láska, K., Engel, Z. and Kňažková, M. 2020. High-latitude dust deposition in snow on the glaciers of James Ross Island, Antarctica. *Earth Surface Processes and Landforms*. **45**(7), pp.1569–1578.

Kavan, J., Ondruch, J., Nývlt, D., Hrbáček, F., Carrivick, J.L. and Láska, K. 2017. Seasonal hydrological and suspended sediment transport dynamics in proglacial streams, James Ross Island, Antarctica. *Geografiska Annaler: Series A, Physical Geography*. **99**(1), pp.38–55.

Kavan, J. and Strzelecki, M.C. 2023. Glacier decay boosts the formation of new Arctic coastal environments—Perspectives from Svalbard. *Land Degradation and Development*. **34**(12), pp.3467–3474.

Kendall, K.A., Ruhl, H.A. and Wilson, R.C. 2003. Distribution and abundance of marine bird and pinniped populations within Port Foster, Deception Island, Antarctica. *Deep-Sea Research Part II: Topical Studies in Oceanography*. **50**(10–11), pp.1873–1888.

Kirkby, M.J. and Statham, I. 1975. Surface Stone Movement and Scree Formation. *The Journal of Geology*. **83**(3), pp.349–362.

Klaar, M.J., Kidd, C., Malone, E., Bartlett, R., Pinay, G., Chapin, F.S. and Milner, A. 2015. Vegetation succession in deglaciated landscapes: implications for sediment and landscape stability. *Earth Surface Processes and Landforms*. **40**(8), pp.1088–1100.

Kňažková, M., Nývlt, D. and Hrbáček, F. 2021. Slope processes connected with snow patches in semi-arid ice-free areas of James Ross Island, Antarctic Peninsula. *Geomorphology*. **373**, p.107479.

Košler, J., Magna, T., Mlčoch, B., Mixa, P., Nývlt, D. and Holub, F. V 2009. Combined Sr, Nd, Pb and Li isotope geochemistry of alkaline lavas from northern James Ross Island (Antarctic Peninsula) and implications for back-arc magma formation. *Chemical Geology*. **258**(3), pp.207–218.

Krinner, G., Boucher, O. and Balkanski, Y. 2006. Ice-free glacial northern Asia due to dust deposition on snow. *Climate Dynamics*. **27**(6), pp.613–625.

Lai, J. and Anders, A.M. 2021. Climatic controls on mountain glacier basal thermal regimes dictate spatial patterns of glacial erosion. *Earth Surface Dynamics*. **9**(4), pp.845–859.

Lawrence, R.L., Wood, S.D. and Sheley, R.L. 2006. Mapping invasive plants using hyperspectral imagery and Breiman Cutler classifications (randomForest). *Remote Sensing of Environment*. **100**(3), pp.356–362.

Lee, J.R., Raymond, B., Bracegirdle, T.J., Chadès, I., Fuller, R.A., Shaw, J.D. and Terauds, A. 2017. Climate change drives expansion of Antarctic ice-free habitat. *Nature*. **547**(7661), pp.49–54.

Leeuwe, M.A., Webb, A.L., Venables, H.J., Visser, R.J.W., Meredith, M.P., Elzenga, J.T.M. and Stefels, J. 2020. Annual patterns in phytoplankton phenology in Antarctic coastal waters explained by environmental drivers. *Limnology and Oceanography*. **65**(7), pp.1651–1668.

Lenzi, M.A., Mao, L. and Comiti, F. 2003. Interannual variation of suspended sediment load and sediment yield in an alpine catchment. *Hydrological Sciences Journal*. **48**(6), pp.899–915.

Łepkowska, E. and Stachnik, Ł. 2018. Which Drivers Control the Suspended Sediment Flux in a

High Arctic Glacierized Basin (Werenskioldbreen, Spitsbergen)? *Water*. **10**(10), p.1408.

Levy, J. 2013. How big are the McMurdo Dry Valleys? Estimating ice-free area using Landsat image data. *Antarctic Science*. **25**(1), pp.119–120.

Li, X., Wang, N. and Wu, Y. 2022. Automated Glacier Snow Line Altitude Calculation Method Using Landsat Series Images in the Google Earth Engine Platform. *Remote Sensing*. **14**(10), p.2377.

Liang, S. 2001. Narrowband to broadband conversions of land surface albedo I algorithms. *Remote Sensing of Environment*. **76**(2), pp.213–238.

Lipp, A.G., Roberts, G.G., Whittaker, A.C., Gowing, C.J.B. and Fernandes, V.M. 2021. Source Region Geochemistry From Unmixing Downstream Sedimentary Elemental Compositions. *Geochemistry, Geophysics, Geosystems*. **22**(10), e2021GC009838.

Liu, C., Li, Z., Zhang, P., Tian, B., Zhou, J. and Chen, Q. 2021. Variability of the snowline altitude in the eastern Tibetan Plateau from 1995 to 2016 using Google Earth Engine. *Journal of Applied Remote Sensing*. **15**(04), p.48505.

Liu, X., An, L., Hai, G., Xie, H. and Li, R. 2024. Updating glacier inventories on the periphery of Antarctica and Greenland using multi-source data. *Annals of Glaciology*., pp.1–18.

Lopez-Martinez, J., Thomson, M.R.A., Arche, A., Bjorck, S., Ellis-Evans, J.C., Hathway, B., Hernandez-Cifuentes, F., Hjort, C., Ingolfsson, O., Ising, J., Lomas, S., Martinez de Pison, E., Serrano, E., Zale, R. and King, S. 1996. Geomorphological map of Byers Peninsula, Livingston Island 1:25 000. *Geomorphological map of Byers Peninsula, Livingston Island 1:25 000*.

Loranty, M.M., Berner, L.T., Goetz, S.J., Jin, Y. and Randerson, J.T. 2014. Vegetation controls on northern high latitude snow-albedo feedback: Observations and CMIP5 model simulations. *Global Change Biology*. **20**(2), pp.594–606.

Lu, D., Mausel, P., Brondízio, E. and Moran, E. 2004. Change detection techniques. *International Journal of Remote Sensing*. **25**(12), pp.2365–2401.

Lydersen, C., Assmy, P., Falk-Petersen, S., Kohler, J., Kovacs, K.M., Reigstad, M., Steen, H., Strøm, H., Sundfjord, A., Varpe, Ø., Walczowski, W., Weslawski, J.M. and Zajaczkowski, M. 2014. The importance of tidewater glaciers for marine mammals and seabirds in Svalbard, Norway. *Journal of Marine Systems*. **129**, pp.452–471.

Maat, D.S., Visser, R.J.W. and Brussaard, C.P.D. 2019. Virus removal by glacier-derived

suspended fine sediment in the Arctic. *Journal of Experimental Marine Biology and Ecology*. **521**, p.151227.

Macfee, M.W. 2023. *Spatio-temporal variability in Southern Hemisphere glacier snowline altitudes from 2000-2020*. MSc by research thesis, University of Leeds, White Rose Repository, p.110.

Malinowski, R., Lewiński, S., Rybicki, M., Gromny, E., Jenerowicz, M., Krupiński, Michał, Nowakowski, A., Wojtkowski, C., Krupiński, Marcin, Krätzschmar, E. and Schauer, P. 2020. Automated Production of a Land Cover/Use Map of Europe Based on Sentinel-2 Imagery. *Remote Sensing*. **12**(21), p.3523.

Malmros, J.K., Mernild, S.H., Wilson, R., Yde, J.C. and Fensholt, R. 2016. Glacier area changes in the central Chilean and Argentinean Andes 1955-2013/14. *Journal of Glaciology*. **62**(232), pp.391–401.

Martin, A.R. and Richardson, M.G. 2019. Rodent eradication scaled up: Clearing rats and mice from South Georgia. *Oryx*. **53**(1), pp.27–35.

Matthews, J.A. and Briffa, K.R. 2005. The 'Little Ice Age': Re-evaluation of an evolving concept. *Geografiska Annaler, Series A: Physical Geography*. **87**(1), pp.17–36.

McGrath, D., Sass, L., O'Neel, S., Arendt, A. and Kienholz, C. 2017. Hypsometric control on glacier mass balance sensitivity in Alaska and northwest Canada. *Earth's Future*. **5**(3), pp.324–336.

Meire, L., Paulsen, M.L., Meire, P., Rysgaard, S., Hopwood, M.J., Sejr, M.K., Stuart-Lee, A., Sabbe, K., Stock, W. and Mortensen, J. 2023. Glacier retreat alters downstream fjord ecosystem structure and function in Greenland. *Nature Geoscience*. **16**(8), pp.671–674.

Mink, S., López-Martínez, J., Maestro, A., Garrote, J., Ortega, J.A., Serrano, E., Durán, J.J. and Schmid, T. 2014. Insights into deglaciation of the largest ice-free area in the South Shetland Islands (Antarctica) from quantitative analysis of the drainage system. *Geomorphology*. **225**, pp.4–24.

Mlčoch, B., Nývlt, D. and Mixa, P. 2020. *Geological map of James Ross Island–Northern part 1: 25,000*.

Mohd Hasmadi, I., Pakhriazad, H.Z. and Shahrin, M.F. 2009. Evaluating supervised and unsupervised techniques for land cover mapping using remote sensing data. *Malaysia nJournal of Society and Space*. **5**(1), pp.1–10.

Molina-Montenegro, M.A., Carrasco-Urra, F., Rodrigo, C., Convey, P., Valladares, F. and Gianoli, E. 2012. Occurrence of the Non-Native Annual Bluegrass on the Antarctic Mainland and Its Negative Effects on Native Plants. *Conservation Biology*. **26**(4), pp.717–723.

Mooney, P.A., Sobolowski, S. and Lee, H. 2020. Designing and evaluating regional climate simulations for high latitude land use land cover change studies. *Tellus, Series A: Dynamic Meteorology and Oceanography*. **72**(1), pp.1–17.

Moosdorf, N., Cohen, S. and von Hagke, C. 2018. A global erodibility index to represent sediment production potential of different rock types. *Applied Geography*. **101**, pp.36–44.

Morris, E.M. and Vaughan, D.G. 2003. Spatial and Temporal Variation of Surface Temperature on the Antarctic Peninsula And The Limit of Viability of Ice Shelves. *Antarctic Research Series*. **79**(10.1029), pp.61–68.

Mosley, M. 1988. Bedload transport and sediment yield in the Onyx River, Antarctica. *Earth Surface Processes and Landforms*. **13**, pp.51–67.

Mosley, M.P. 1980. Mapping sediment sources in a New Zealand Mountain Watershed. *Environmental Geology*. **3**(2), pp.85–95.

Motschmann, A., Huggel, C., Carey, M., Moulton, H., Walker-Crawford, N. and Muñoz, R. 2020. Losses and damages connected to glacier retreat in the Cordillera Blanca, Peru. *Climatic Change*. **162**(2), pp.837–858.

Moura, P.A., Francelino, M.R., Schaefer, C.E.G.R., Simas, F.N.B. and de Mendonça, B.A.F. 2012. Distribution and characterization of soils and landform relationships in Byers Peninsula, Livingston Island, Maritime Antarctica. *Geomorphology*. **155**–**156**, pp.45–54.

Mulvaney, R., Abram, N.J., Hindmarsh, R.C.A., Arrowsmith, C., Fleet, L., Triest, J., Sime, L.C., Alemany, O. and Foord, S. 2012. Recent Antarctic Peninsula warming relative to Holocene climate and ice-shelf history. *Nature*. **489**(7414), pp.141–144.

Naegeli, K. and Huss, M. 2017. Sensitivity of mountain glacier mass balance to changes in bare-ice albedo. *Annals of Glaciology*. **58**(75), pp.119–129.

Naegeli, K., Huss, M. and Hoelzle, M. 2019. Change detection of bare-ice albedo in the Swiss Alps . *The Cryosphere*. **13**(1), pp.397–412.

Naveen, R., Lynch, H.J., Forrest, S., Mueller, T. and Polito, M. 2012. First direct, site-wide penguin survey at Deception Island, Antarctica, suggests significant declines in breeding

chinstrap penguins. *Polar Biology*. **35**(12), pp.1879–1888.

Nedbalová, L., Nývlt, D., Lirio, J.M., Kavan, J. and Elster, J. 2017. Current distribution of Branchinecta gaini on James Ross Island and Vega Island. *Antarctic Science*. **29**(4), pp.341–342.

Nehyba, S. and Nývlt, D. 2014. Deposits of pyroclastic mass flows at Bibby Hill (Pliocene, James Ross Island, Antarctica). *Czech Polar Reports*. **4**, pp.103–122.

Nichols, R.L. 1973. Antarctic glacial surges? *Journal of Glaciology*. **12**(66), pp.524–525.

Nylen, T.H., Fountain, A.G. and Doran, P.T. 2004. Climatology of katabatic winds in the McMurdo dry valleys, southern Victoria Land, Antarctica. *Journal of Geophysical Research: Atmospheres*. **109**(3), p.3114.

Nývlt, D., Braucher, R., Engel, Z. and Mlčoch, B. 2014. Timing of the Northern Prince Gustav Ice Stream retreat and the deglaciation of northern James Ross Island, Antarctic Peninsula during the last glacial-interglacial transition. *Quaternary Research (United States)*. **82**(2), pp.441–449.

Nývlt, D., Fišáková, M.N., Barták, M., Stachoň, Z., Pavel, V., Mlčoch, B. and Láska, K. 2016. Death age, seasonality, taphonomy and colonization of seal carcasses from Ulu Peninsula, James Ross Island, Antarctic Peninsula. *Antarctic Science*. **28**(1), pp.3–16.

Nývlt, D., Košler, J., Mlčoch, B., Mixa, P., Lisá, L., Bubík, M. and Hendriks, B.W.H. 2011. The Mendel Formation: Evidence for Late Miocene climatic cyclicity at the northern tip of the Antarctic Peninsula. *Palaeogeography, Palaeoclimatology, Palaeoecology*. **299**(1–2), pp.363–384.

Obryk, M.K., Doran, P.T., Fountain, A.G., Myers, M. and McKay, C.P. 2020. Climate From the McMurdo Dry Valleys, Antarctica, 1986–2017: Surface Air Temperature Trends and Redefined Summer Season. *Journal of Geophysical Research: Atmospheres*. **125**(13), e2019JD032180.

Oerlemans, J., Giesen, R.H. and Van Den Broeke, M.R. 2009. Retreating alpine glaciers: Increased melt rates due to accumulation of dust (Vadret da Morteratsch, Switzerland. *Journal of Glaciology*. **55**(192), pp.729–736.

Olech, M. and Chwedorzewska, K.J. 2011. Short note: the first appearance and establishment of an alien vascular plant in natural habitats on the forefield of a retreating glacier in Antarctica. *Antarctic Science*. **23**(2), pp.153–154.

Oliva, M., Hrbacek, F., Ruiz-Fernández, J., de Pablo, M.Á., Vieira, G., Ramos, M. and Antoniades, D. 2017. Active layer dynamics in three topographically distinct lake catchments in Byers Peninsula (Livingston Island, Antarctica). *Catena*. **149**, pp.548–559.

Oliva, M., Navarro, F., Hrbáček, F., Hernández, A., Nývlt, D., Pereira, P., Ruiz-Fernández, J. and Trigo, R. 2017. Recent regional climate cooling on the Antarctic Peninsula and associated impacts on the cryosphere. *Science of the Total Environment*. **580**, pp.210–223.

Olofsson, P., Foody, G.M., Herold, M., Stehman, S. V, Woodcock, C.E. and Wulder, M.A. 2014. Good practices for estimating area and assessing accuracy of land change. *Remote Sensing of Environment*. **148**, pp.42–57.

Olofsson, P., Foody, G.M., Stehman, S. V and Woodcock, C.E. 2013. Making better use of accuracy data in land change studies: Estimating accuracy and area and quantifying uncertainty using stratified estimation. *Remote Sensing of Environment*. **129**, pp.122–131.

Orwin, J.F. and Smart, C.C. 2004. Short-term spatial and temporal patterns of suspended sediment transfer in proglacial channels, Small River Glacier, Canada. *Hydrological Processes*. **18**(9), pp.1521–1542.

Otsu, N. 1979. Threshold Selection Method From Gray-Level Histograms. *IEEE Trans Syst Man Cybern*. **SMC**-**9**(1), pp.62–66.

Overeem, I., Hudson, B.D., Syvitski, J.P.M., Mikkelsen, A.B., Hasholt, B., van den Broeke, M.R., Noël, B.P.Y. and Morlighem, M. 2017. Substantial export of suspended sediment to the global oceans from glacial erosion in Greenland. *Nature Geoscience*. **10**(11), pp.859–863.

Painter, T.H., Barrett, A.P., Landry, C.C., Neff, J.C., Cassidy, M.P., Lawrence, C.R., McBride, K.E. and Farmer, G.L. 2007. Impact of disturbed desert soils on duration of mountain snow cover. *Geophysical Research Letters*. **34**(12), p.L12502.

Palerme, C., Genthon, C., Claud, C., Kay, J.E., Wood, N.B. and L'Ecuyer, T. 2017. Evaluation of current and projected Antarctic precipitation in CMIP5 models. *Climate Dynamics*. **48**(1), pp.225–239.

Pannewitz, S., Green, T.G.A., Scheidegger, C., Schlensog, M. and Schroeter, B. 2003. Activity pattern of the moss Hennediella heimii (Hedw.) Zand. in the Dry Valleys, Southern Victoria Land, Antarctica during the mid-austral summer. *Polar Biology*. **26**(8), pp.545–551.

Paola, C., Parker, G., Seal, R., Sinha, S.K., Southard, J.B. and Wilcock, P.R. 1992. Downstream Fining by Selective Deposition in a Laboratory Flume. *Science*. **258**(5089), pp.1757–1760.

Paola, C. and Voller, V.R. 2005. A generalized Exner equation for sediment mass balance. *Journal of Geophysical Research*. **110**(F4), p.F04014.

Paul, F., Bolch, T., Briggs, K., Kääb, A., McMillan, M., McNabb, R., Nagler, T., Nuth, C., Rastner, P., Strozzi, T. and Wuite, J. 2017. Error sources and guidelines for quality assessment of glacier area, elevation change, and velocity products derived from satellite data in the Glaciers_cci project. *Remote Sensing of Environment*. **203**, pp.256–275.

Pavel, V. and Weidinger, K. 2013. First records of the white-rumped sandpiper and brown-hooded gull south-east of the Antarctic Peninsula. *Antarctic Science*. **25**(3), pp.387–388.

Pazúr, R., Huber, N., Weber, D., Ginzler, C. and Price, B. 2022. A national extent map of cropland and grassland for Switzerland based on Sentinel-2 data. *Earth System Science Data*. **14**(1), pp.295–305.

Pelto, M.S. 2000. Mass balance of adjacent debris-covered and clean glacier ice in the North Cascades, Washington. *IAHS-AISH Publication*., pp.35–42.

Perkins-Kirkpatrick, S.E. and Lewis, S.C. 2020. Increasing trends in regional heatwaves. *Nature Communications*. **11**(1), p.3357.

Petford, N. and Mirhadizadeh, S. 2017. Image-based modelling of lateral magma flow: the Basement Sill, Antarctica. *Royal Society Open Science*. **4**(5), p.161083.

Pfeffer, W.T., Arendt, A.A., Bliss, A., Bolch, T., Cogley, J.G., Gardner, A.S., Hagen, J.O., Hock, R., Kaser, G., Kienholz, C., Miles, E.S., Moholdt, G., Mölg, N., Paul, F., Radić, V., Rastner, P., Raup, B.H., Rich, J., Sharp, M.J., Andreassen, L.M., Bajracharya, S., Barrand, N.E., Beedle, M.J., Berthier, E., Bhambri, R., Brown, I., Burgess, D.O., Burgess, E.W., Cawkwell, F., Chinn, T., Copland, L., Cullen, N.J., Davies, B., De Angelis, H., Fountain, A.G., Frey, H., Giffen, B.A., Glasser, N.F., Gurney, S.D., Hagg, W., Hall, D.K., Haritashya, U.K., Hartmann, G., Herreid, S., Howat, I., Jiskoot, H., Khromova, T.E., Klein, A., Kohler, J., König, M., Kriegel, D., Kutuzov, S., Lavrentiev, I., Le Bris, R., Li, X., Manley, W.F., Mayer, C., Menounos, B., Mercer, A., Mool, P., Negrete, A., Nosenko, G., Nuth, C., Osmonov, A., Pettersson, R., Racoviteanu, A., Ranzi, R., Sarikaya, M.A., Schneider, C., Sigurdsson, O., Sirguey, P., Stokes, C.R., Wheate, R., Wolken, G.J., Wu, L.Z. and Wyatt, F.R. 2014. The randolph glacier inventory: A globally complete inventory of glaciers. *Journal of Glaciology*. **60**(221), pp.537–552.

Phiri, D. and Morgenroth, J. 2017. Developments in Landsat land cover classification methods: A review. *Remote Sensing*. **9**(9), p.967.

Prasad, P., Loveson, V.J., Chandra, P. and Kotha, M. 2022. Evaluation and comparison of the earth observing sensors in land cover/land use studies using machine learning algorithms. *Ecological Informatics*. **68**, p.101522.

Prospero, J.M., Bullard, J.E. and Hodgkins, R. 2012. High-latitude dust over the North Atlantic: Inputs from Icelandic proglacial dust storms. *Science*. **335**(6072), pp.1078–1082.

Quesada, A., Camacho, A. and Lyons, W.B. 2013. Multidisciplinary research on Byers Peninsula, Livingston Island: A future benchmark for change in Maritime Antarctica. *Antarctic Science*. **25**(2), pp.123–127.

Rabatel, A., Letréguilly, A., Dedieu, J.P. and Eckert, N. 2013. Changes in glacier equilibrium-line altitude in the western Alps from 1984 to 2010: Evaluation by remote sensing and modeling of the morpho-topographic and climate controls. *Cryosphere*. **7**(5), pp.1455–1471.

Rachlewicz, G., Szczuciński, W. and Ewertowski, M. 2007. Post-"Little Ice Age" retreat rates of glaciers around Billefjorden in central Spitsbergen, Svalbard. *Polish Polar Research*. **28**(3), pp.159–186.

Racoviteanu, A.E., Rittger, K. and Armstrong, R. 2019. An Automated Approach for Estimating Snowline Altitudes in the Karakoram and Eastern Himalaya From Remote Sensing. *Frontiers in Earth Science*. **7**.

Rastner, P., Prinz, R., Notarnicola, C., Nicholson, L., Sailer, R., Schwaizer, G. and Paul, F. 2019. On the automated mapping of snow cover on glaciers and calculation of snow line altitudes from multi-temporal Landsat data. *Remote Sensing*. **11**(12), p.1410.

Raup, B., Racoviteanu, A., Khalsa, S.J.S., Helm, C., Armstrong, R. and Arnaud, Y. 2007. The GLIMS geospatial glacier database: A new tool for studying glacier change. *Global and Planetary Change*. **56**(1–2), pp.101–110.

Ravanel, L., Duvillard, P.A., Jaboyedoff, M. and Lambiel, C. 2018. Recent evolution of an ice-cored moraine at the Gentianes Pass, Valais Alps, Switzerland. *Land Degradation and Development*. **29**(10), pp.3693–3708.

Righetti, D., Vogt, M., Gruber, N., Psomas, A. and Zimmermann, N.E. 2019. Global pattern of phytoplankton diversity driven by temperature and environmental variability. *Science Advances*. **5**(5), p.eaau6253.

Rignot, E., Casassa, G., Gogineni, P., Krabill, W., Rivera, A. and Thomas, R. 2004. Accelerated ice discharge from the Antarctic Peninsula following the collapse of Larsen B ice shelf.

Geophysical Research Letters. **31**(18), p.L18401.

Riihelä, A., Bright, R.M. and Anttila, K. 2021. Recent strengthening of snow and ice albedo feedback driven by Antarctic sea-ice loss. *Nature Geoscience*. **14**(11), pp.832–836.

Rippin, D.M., Sharp, M., Van Wychen, W. and Zubot, D. 2020. 'Detachment' of icefield outlet glaciers: catastrophic thinning and retreat of the Columbia Glacier (Canada). *Earth Surface Processes and Landforms*. **45**(2), pp.459–472.

Rodriguez-Galiano, V.F., Ghimire, B., Rogan, J., Chica-Olmo, M. and Rigol-Sanchez, J.P. 2012. An assessment of the effectiveness of a random forest classifier for land-cover classification. *ISPRS Journal of Photogrammetry and Remote Sensing*. **67**(1), pp.93–104.

Roman, M., Nedbalová, L., Kohler, T.J., Lirio, J.M., Coria, S.H., Kopáček, J., Vignoni, P.A., Kopalová, K., Lecomte, K.L., Elster, J. and Nývlt, D. 2019. Lacustrine systems of Clearwater Mesa (James Ross Island, north-eastern Antarctic Peninsula): geomorphological setting and limnological characterization. *Antarctic Science*. **31**(4), pp.169–188.

Rosa, K.K. da, Oliveira, M.A.G. de, Petsch, C., Auger, J.D., Vieira, R. and Simões, J.C. 2022. Expansion of glacial lakes on Nelson and King George Islands, Maritime Antarctica, from 1986 to 2020. *Geocarto International*. **37**(15), pp.4454–4464.

Rosa, K.K. da, Perondi, C., Veettil, B.K., Auger, J.D. and Simões, J.C. 2020. Contrasting responses of land-terminating glaciers to recent climate variations in King George Island, Antarctica. *Antarctic Science*. **32**(5), pp.398–407.

Rosado, B., Fernández-Ros, A., Berrocoso, M., Prates, G., Gárate, J., de Gil, A. and Geyer, A. 2019. Volcano-tectonic dynamics of Deception Island (Antarctica): 27 years of GPS observations (1991–2018). *Journal of Volcanology and Geothermal Research*. **381**, pp.57–82.

Ruiz-Fernández, J., Oliva, M. and García-Hernández, C. 2017. Topographic and geomorphologic controls on the distribution of vegetation formations in Elephant Point (Livingston Island, Maritime Antarctica). *Science of The Total Environment*. **587**–**588**, pp.340–349.

Russell, F.E., Boyle, J.F. and Chiverrell, R.C. 2019. NIRS quantification of lake sediment composition by multiple regression using end-member spectra. *Journal of Paleolimnology*. **62**(1), pp.73–88.

Sakizadeh, M. 2015. Assessment the performance of classification methods in water quality studies, A case study in Karaj River. *Environmental Monitoring and Assessment*. **187**(9), pp.1–12.

Salvatore, M.C. 2001. Geomorphological sketch map of the Fossil Bluff area (Alexander Island, Antarctica) mapped from aerial photographs. *Antarctic Science*. **13**(1), pp.75–78.

Schaefli, B., Hingray, B., Niggli, M. and Musy, A. 2005. A conceptual glacio-hydrological model for high mountainous catchments. *Hydrology and Earth System Sciences*. **9**(1–2), pp.95–109.

Schiel, R., Güpner, F. and Spitzenberger, H.J. 2019. Population size and condition of the emperor penguin Aptenodytes forsteri colony of Snow Hill Island, Weddell sea, Antarctica: Observations from 29 December 2018. *Marine Ornithology*. **47**(2), pp.189–192.

Schomacker, A. and Kjær, K.H. 2008. Quantification of dead-ice melting in ice-cored moraines at the high-Arctic glacier Holmströmbreen, Svalbard. *Boreas*. **37**(2), pp.211–225.

Schrott, L., Hufschmidt, G., Hankammer, M., Hoffmann, T. and Dikau, R. 2003. Spatial distribution of sediment storage types and quantification of valley fill deposits in an alpine basin, Reintal, Bavarian Alps, Germany. *Geomorphology*. **55**(1–4), pp.45–63.

Secretariat of the Antarctic Treaty 2022. ASPA 140: Parts of Deception Island, South Shetland Islands.

Selkowitz, D.J. and Forster, R.R. 2016. An automated approach for mapping persistent ice and snow cover over high latitude regions. *Remote Sensing*. **8**(1), p.16.

Seneviratne, S.I., Wartenburger, R., Guillod, B.P., Hirsch, A.L., Vogel, M.M., Brovkin, V., Van Vuuren, D.P., Schaller, N., Boysen, L., Calvin, K. V., Doelman, J., Greve, P., Havlik, P., Humpenöder, F., Krisztin, T., Mitchell, D., Popp, A., Riahi, K., Rogelj, J., Schleussner, C.F., Sillmann, J. and Stehfest, E. 2018. Climate extremes, land-climate feedbacks and land-use forcing at 1.5°C. *Philosophical Transactions of the Royal Society A: Mathematical, Physical and Engineering Sciences*. **376**(2119), p.20160450.

Sevestre, H. and Benn, D.I. 2015. Climatic and geometric controls on the global distribution of surge-type glaciers: Implications for a unifying model of surging. *Journal of Glaciology*. **61**(228), pp.646–662.

Shahrestani, S., Mokhtari, A.R. and Fatehi, M. 2020. The use of unmixing technique in stream sediment geochemical exploration. *Journal of Geochemical Exploration*. **208**, p.106339.

Siegert, M., Atkinson, A., Banwell, A., Brandon, M., Convey, P., Davies, B., Downie, R., Edwards, T., Hubbard, B., Marshall, G., Rogelj, J., Rumble, J., Stroeve, J. and Vaughan, D. 2019. The Antarctic Peninsula Under a 1.5°C Global Warming Scenario. *Frontiers in Environmental*

Science. **7**, p.102.

Siegert, M.J., Bentley, M.J., Atkinson, A., Bracegirdle, T.J., Convey, P., Davies, B., Downie, R., Hogg, A.E., Holmes, C., Hughes, K.A., Meredith, M.P., Ross, N., Rumble, J. and Wilkinson, J. 2023. Antarctic extreme events . *Frontiers in Environmental Science* . **11**.

Simms, A.R., Bentley, M.J., Simkins, L.M., Zurbuchen, J., Reynolds, L.C., DeWitt, R. and Thomas, E.R. 2021. Evidence for a "Little Ice Age" glacial advance within the Antarctic Peninsula – Examples from glacially-overrun raised beaches. *Quaternary Science Reviews*. **271**, p.107195.

Skvarca, P., Rott, H. and Nagler, T. 1995. Satellite imagery, a base line for glacier variation study on James Ross Island, Antarctica. *Annals of Glaciology*. **21**, pp.291–296.

Smellie, J.L. 2013. Geological Map of James Ross Island 1 . James Ross Island Volcanic Group. *BAS GEOMAP 2 Series, Sheet 5, British Antarctic Survey, Cambridge.*

Smellie, J.L., Johnson, J.S., McIntosh, W.C., Esser, R., Gudmundsson, M.T., Hambrey, M.J. and van Wyk de Vries, B. 2008. Six million years of glacial history recorded in volcanic lithofacies of the James Ross Island Volcanic Group, Antarctic Peninsula. *Palaeogeography, Palaeoclimatology, Palaeoecology*. **260**(1–2), pp.122–148.

Smellie, J.L., Lopez-Martinez Geomorphological, J., Lopez-Martinez, J., Serrano, E., Rey, J., Headland, R.K., Hernandez-Cifuentes, F., Maestro, A., Millar, I.L., Somoza, L., Thomson, J.W. and Thomson, M.R.A. 2002. *Geology and geomorphology of Deception Island*. British Antarctic Survey.

Smellie, J.L. and Martin, A.P. 2021. Chapter 5.2a Erebus Volcanic Province: volcanology. *Geological Society, London, Memoirs*. **55**(1), pp.415–446.

Smith, R.I.L. 1988. Botanical survey of Deception Island. *British Antarctic Survey Bulletin*. (80), pp.129–136.

Smith, R.I.L. 2005. The thermophilic bryoflora of Deception Island: Unique plant communities as a criterion for designating an Antarctic Specially Protected Area. *Antarctic Science*. **17**(1), pp.17–27.

Soenen, S.A., Peddle, D.R. and Coburn, C.A. 2005. SCS+C: A modified sun-canopy-sensor topographic correction in forested terrain. *IEEE Transactions on Geoscience and Remote Sensing*. **43**(9), pp.2148–2159.

Song, C., Wang, G., Mao, T., Dai, J. and Yang, D. 2020. Linkage between permafrost distribution

and river runoff changes across the Arctic and the Tibetan Plateau. *Science China Earth Sciences*. **63**(2), pp.292–302.

Speirs, J.C., Steinhoff, D.F., McGowan, H.A., Bromwich, D.H. and Monaghan, A.J. 2010. Foehn winds in the McMurdo Dry Valleys, Antarctica: The origin of extreme warming events. *Journal of Climate*. **23**(13), pp.3577–3598.

Sroková, S. and Nývlt, D. 2021. Bedload geochemical and petrophysical signature of the Algal and Bohemian streams, James Ross Island, Antarctic Peninsula. *Czech Polar Reports*. **11**, pp.203–214.

Staines, K.E.H., Carrivick, J.L., Tweed, F.S., Evans, A.J., Russell, A.J., Jóhannesson, T. and Roberts, M. 2015. A multi-dimensional analysis of pro-glacial landscape change at Sólheimajökull, southern Iceland. *Earth Surface Processes and Landforms*. **40**(6), pp.809–822.

Steffen, T., Huss, M., Estermann, R., Hodel, E. and Farinotti, D. 2022. Volume, evolution, and sedimentation of future glacier lakes in Switzerland over the 21st century. *Earth Surface Dynamics*. **10**(4), pp.723–741.

Stott, T. and Convey, P. 2021. Seasonal hydrological and suspended sediment transport dynamics and their future modelling in the Orwell Glacier proglacial stream, Signy Island, Antarctica. *Antarctic Science*. **33**(2), pp.192–212.

Strother, S.L., Salzmann, U., Roberts, S.J., Hodgson, D.A., Woodward, J., Van Nieuwenhuyze, W., Verleyen, E., Vyverman, W. and Moreton, S.G. 2015. Changes in Holocene climate and the intensity of Southern Hemisphere Westerly Winds based on a high-resolution palynological record from sub-Antarctic South Georgia. *The Holocene*. **25**(2), pp.263–279.

Surawy-Stepney, T., Hogg, A.E., Cornford, S.L., Wallis, B.J., Davison, B.J., Selley, H.L., Slater, R.A.W., Lie, E.K., Jakob, L., Ridout, A., Gourmelen, N., Freer, B.I.D., Wilson, S.F. and Shepherd, A. 2024. The effect of landfast sea ice buttressing on ice dynamic speedup in the Larsen B embayment, Antarctica. *Cryosphere*. **18**(3), pp.977–993.

Syakur, M.A., Khotimah, B.K., Rochman, E.M.S. and Satoto, B.D. 2018. Integration K-Means Clustering Method and Elbow Method For Identification of The Best Customer Profile Cluster. *IOP Conference Series: Materials Science and Engineering*. **336**(1), p.12017.

Syvitski, J.P.M. 2002. Sediment discharge variability in Arctic rivers: implications for a warmer future. *Polar Research*. **21**(2), pp.323–330.

Takaku, J., Tadono, T. and Tsutsui, K. 2014. Generation of high resolution global DSM from

ALOS PRISM. *International Archives of the Photogrammetry, Remote Sensing and Spatial Information Sciences - ISPRS Archives*. **40**(4), pp.243–248.

Taylor, L.S., Quincey, D.J., Smith, M.W., Potter, E.R., Castro, J. and Fyffe, C.L. 2022. Multi-Decadal Glacier Area and Mass Balance Change in the Southern Peruvian Andes. *Frontiers in Earth Science*. **10**.

Tejedo, P., Benayas, J., Cajiao, D., Albertos, B., Lara, F., Pertierra, L.R., Andrés-Abellán, M., Wic, C., Luciáñez, M.J., Enríquez, N., Justel, A. and Reck, G.K. 2016. Assessing environmental conditions of Antarctic footpaths to support management decisions. *Journal of Environmental Management*. **177**, pp.320–330.

Tejedo, P., Benayas, J., Cajiao, D., Leung, Y.-F., De Filippo, D. and Liggett, D. 2022. What are the real environmental impacts of Antarctic tourism? Unveiling their importance through a comprehensive meta-analysis. *Journal of Environmental Management*. **308**, p.114634.

Tejedo, P., Gutiérrez, B., Pertierra, L.R. and Benayas, J. 2015. Analysis of published scientific research from Deception Island, South Shetland Islands. *Antarctic Science*. **27**(2), pp.134–149.

Tewari, K., Mishra, S.K., Salunke, P. and Dewan, A. 2022. Future projections of temperature and precipitation for Antarctica. *Environmental Research Letters*. **17**(1), p.14029.

Tewkesbury, A.P., Comber, A.J., Tate, N.J., Lamb, A. and Fisher, P.F. 2015. A critical synthesis of remotely sensed optical image change detection techniques. *Remote Sensing of Environment*. **160**, pp.1–14.

Tomczyk, A.M., Ewertowski, M.W. and Carrivick, J.L. 2020. Geomorphological impacts of a glacier lake outburst flood in the high arctic Zackenberg River, NE Greenland. *Journal of Hydrology*. **591**, p.125300.

Tonkin, T.N. 2023. The paraglacial adjustment of an Alpine lateral moraine, Bas Glacier d'Arolla, Switzerland. *Physical Geography*. **44**(5), pp.643–659.

Torres-Mellado, G.A., Jaña, R. and Casanova-Katny, M.A. 2011. Antarctic hairgrass expansion in the South Shetland archipelago and Antarctic Peninsula revisited. *Polar Biology*. **34**(11), pp.1679–1688.

Tuckett, P.A., Ely, J.C., Sole, A.J., Livingstone, S.J., Davison, B.J., Melchior van Wessem, J. and Howard, J. 2019. Rapid accelerations of Antarctic Peninsula outlet glaciers driven by surface melt. *Nature Communications*. **10**(1), p.4311.

Turner, J., Lachlan-Cope, T., Colwell, S. and Marshall, G.J. 2005. A positive trend in western Antarctic Peninsula precipitation over the last 50 years reflecting regional and Antarctic-wide atmospheric circulation changes. *Annals of Glaciology*. **41**, pp.85–91.

Turner, J., Lu, H., King, J., Marshall, G.J., Phillips, T., Bannister, D. and Colwell, S. 2021. Extreme temperatures in the Antarctic. *Journal of Climate*. **34**(7), pp.2653–2668.

Turner, J., Marshall, G.J., Clem, K., Colwell, S., Phillips, T. and Lu, H. 2020. Antarctic temperature variability and change from station data. *International Journal of Climatology*. **40**(6), pp.2986–3007.

USGS 2024. Landsat Collection 2 Surface Reflectance. [Accessed 1 February 2024]. Available from: https://www.usgs.gov/landsat-missions/landsat-collection-2-surface-reflectance.

Váczi, P. and Barták, M. 2022. Multispectral aerial monitoring of a patchy vegetation oasis composed of different vegetation classes. UAV-based study exploiting spectral reflectance indices. *Czech Polar Reports*. **12**(1), pp.131–142.

Vanonckelen, S., Lhermitte, S. and Van Rompaey, A. 2013. The effect of atmospheric and topographic correction methods on land cover classification accuracy. *International Journal of Applied Earth Observation and Geoinformation*. **24**, pp.9–21.

Vašinka, M., Krmíček, L., Všianský, D., Hrbáček, F. and Nývlt, D. 2020. Chemical weathering in Antarctica: an example of igneous rock particles in Big Lachman Lake sediments, James Ross Island. *Environmental Earth Sciences*. **79**(8), p.186.

Vaughan, D.G., Marshall, G.J., Connolley, W.M., Parkinson, C., Mulvaney, R., Hodgson, D.A., King, J.C., Pudsey, C.J. and Turner, J. 2003. Recent Rapid Regional Climate Warming on the Antarctic Peninsula. *Climatic Change*. **60**(3), pp.243–274.

Vignon, É., Roussel, M.-L., Gorodetskaya, I. V, Genthon, C. and Berne, A. 2021. Present and Future of Rainfall in Antarctica. *Geophysical Research Letters*. **48**(8), e2020GL092281.

Walker, D.A., Daniëls, F.J.A., Matveyeva, N. V, Šibík, J., Walker, M.D., Breen, A.L., Druckenmiller, L.A., Raynolds, M.K., Bültmann, H., Hennekens, S., Buchhorn, M., Epstein, H.E., Ermokhina, K., Fosaa, A.M., Heiðmarsson, S., Heim, B., Jónsdóttir, I.S., Koroleva, N., Lévesque, E., MacKenzie, W.H., Henry, G.H.R., Nilsen, L., Peet, R., Razzhivin, V., Talbot, S.S., Telyatnikov, M., Thannheiser, D., Webber, P.J. and Wirth, L.M. 2018. Circumpolar Arctic Vegetation Classification. *Phytocoenologia*. **48**(2), pp.181–201.

Wallis, B.J., Hogg, A.E., Meredith, M.P., Close, R., Hardy, D., McMillan, M., Wuite, J., Nagler, T. and Moffat, C. 2023. Ocean warming drives rapid dynamic activation of marine-

terminating glacier on the west Antarctic Peninsula. *Nature Communications*. **14**(1), p.7535.

Wallis, B.J., Hogg, A.E., van Wessem, J.M., Davison, B.J. and van den Broeke, M.R. 2023. Widespread seasonal speed-up of west Antarctic Peninsula glaciers from 2014 to 2021. *Nature Geoscience*. **16**(3), pp.231–237.

Wan, D., Li, F., Yu, W., Chen, C. and Gao, Y. 2019. Sediment delivery of partially-unfrozen loam soil rill by snow/glacier meltwater flow. *Scientific Reports*. **9**(1), p.3954.

Wang, J., Tang, Z., Deng, G., Hu, G., You, Y. and Zhao, Y. 2023. Landsat Satellites Observed Dynamics of Snowline Altitude at the End of the Melting Season, Himalayas, 1991–2022. *Remote Sensing*. **15**(10), p.2534.

Wang, P., Huang, Q., Pozdniakov, S.P., Liu, S., Ma, N., Wang, T., Zhang, Y., Yu, J., Xie, J., Fu, G., Frolova, N.L. and Liu, C. 2021. Potential role of permafrost thaw on increasing Siberian river discharge. *Environmental Research Letters*. **16**(3), p.34046.

Wellman, P. 1982. Surging of Fisher Glacier, Eastern Antarctica: Evidence From Geomorphology. *Journal of Glaciology*. **28**(98), pp.23–28.

Willems, B.A., Powell, R.D., Cowan, E.A. and Jaeger, J.M. 2011. Glacial outburst flood sediments within Disenchantment Bay, Alaska: implications of recognizing marine jökulhlaup deposits in the stratigraphic record. *Marine Geology*. **284**(1–4), pp.1–12.

Windnagel, A., Hock, R., Maussion, F., Paul, F., Rastner, P., Raup, B. and Zemp, M. 2023. Which glaciers are the largest in the world? *Journal of Glaciology*. **69**(274), pp.301–310.

WMO 1970. *Seasonal snow cover: a guide for measurement compilation and assemblage of data*. Champaign, IL.

Xu, H. 2006. Modification of normalised difference water index (NDWI) to enhance open water features in remotely sensed imagery. *International Journal of Remote Sensing*. **27**(14), pp.3025–3033.

Xu, M., Yu, L., Liang, K., Vihma, T., Bozkurt, D., Hu, X. and Yang, Q. 2021. Dominant role of vertical air flows in the unprecedented warming on the Antarctic Peninsula in February 2020. *Communications Earth & Environment*. **2**(1), p.133.

Xu, R., Lin, H., Lü, Y., Luo, Y., Ren, Y. and Comber, A. 2018. A Modified Change Vector Approach for Quantifying Land Cover Change. *Remote Sensing*. **10**(10), p.1578.

Yde, J.C., Knudsen, N.T., Hasholt, B. and Mikkelsen, A.B. 2014. Meltwater chemistry and solute

export from a Greenland ice sheet catchment, Watson River, West Greenland. *Journal of Hydrology*. **519**, pp.2165–2179.

Zhang, Y., Gao, T., Kang, S., Shangguan, D. and Luo, X. 2021. Albedo reduction as an important driver for glacier melting in Tibetan Plateau and its surrounding areas. *Earth-Science Reviews*. **220**, p.103735.

Zhao, S., Liu, M., Tao, M., Zhou, W., Lu, X., Xiong, Y., Li, F. and Wang, Q. 2023. The role of satellite remote sensing in mitigating and adapting to global climate change. *Science of the Total Environment*. **904**, p.166820.

Zhao, Y., Gao, G., Ding, G., Zhou, Q., Zhang, Y., Wang, J. and Zhou, J. 2022. Improving the performance of an unmixing model in sediment source apportionment using synthetic sediment mixtures and an adaptive boosting algorithm. *Catena*. **217**, p.106491.